The University of Manitoba

APPLICATION OF THE IMPEDANCE BOUNDARY CONDITIONS TO THE NUMERICAL SOLUTION OF CORRUGATED AND RECEIVER HORNS

BY

KAMAL AZMY ISKANDER

A Thesis

Submitted to the Faculty of Graduate Studies

In Partial Fulfillment of the Requirements For The

Degree of Doctor of Philosophy

DEPARTMENT OF ELECTRICAL ENGINEERING

Winnipeg, Manitoba

Canada

SEPTEMBER 1980

APPLICATION OF THE IMPEDANCE BOUNDARY CONDITIONS TO THE NUMERICAL SOLUTION OF CORRUGATED AND RECEIVER HORNS

BY

KAMAL AZMY ISKANDER

A thesis submitted to the Faculty of Graduate Studies of
the University of Manitoba in partial fulfillment of the requirements
of the degree of

DOCTOR OF PHILOSOPHY

©1980

Permission has been granted to the LIBRARY OF THE UNIVERSITY OF MANITOBA to lend or sell copies of this thesis, to the NATIONAL LIBRARY OF CANADA to microfilm this thesis and to lend or sell copies of the film, and UNIVERSITY MICROFILMS to publish an abstract of this thesis.

The author reserves other publication rights, and neither the thesis nor extensive extracts from it may be printed or otherwise reproduced without the author's written permission.

To My Daughter, Mary-Ann

ABSTRACT

An integral equation approach is used to study the scattering properties of corrugated surfaces used in corrugated horn design. Corrugations are replaced by a proper impedance boundary to reduce the labour of computation in a moment method solution of the integral equation. Two-dimensional prisms with impedance walls are used to represent the E-plane walls of a corrugated pyramidal horn. The excitation is due to magnetic line sources which provide a field similar to that of the incident mode on the horn waveguide junction. For three-dimensional problems, scalar and vector potentials are used to obtain the desired integral equation. Symmetry properties of bodies of revolution are used and the formulation is applied to rotationally symmetric corrugated horns. Radiation patterns for these horns are obtained by substituting for the corrugations by an anisotropic surface impedance. The waveguide excitation is simulated by the field of a Hertzian dipole situated near the waveguide termination. The same formulation is used to study the scattering properties of horns in the receiver mode. In this case the waveguide termination is an isotropic surface impedance and the exciting dipole is placed at a far distance from the scattering horn.

For bigger horns, Green's functions used for the integral equations in two dimensions were replaced by the field of a dipole or a quadrupole. The elements of the coefficient matrix obtained through the application of the moment method to the new equations are studied. They were found to decay at a faster rate away from the diagonal elements as

the order of multiplicity of the Green's source is increased. Condition numbers and pivot ratio of the new matrices showed that ill-conditioned solutions resulting at frequencies of internal resonance can be avoided.

ACKNOWLEDGEMENTS

The author wishes to express his sincere appreciation to Dr. L. Shafai of the Electrical Engineering Department, University of Manitoba, for his guidance, continuous interest and encouragement throughout all phases of this work.

Special thanks are due to my wife Mervat, for her assistance and understanding through the years which made this work possible.

Special acknowledgement go to Dr. N. Sultan for his constructive criticism which led to a number of clarifications and other improvements.

Extended thanks are expressed to my colleagues A. Shoamanesh and A. Ittipiboon for long hours of helpful discussions, and to Mrs. P. Hyland for her skilful typing of the manuscript.

The financial support provided in the form of a National Research Council Scholarship and a University of Manitoba fellowship are gratefully acknowledged.

TABLE OF CONTENTS

			Page
ABSTRACT			i
ACKNOWLEDGEMENTS			iii
TABLE OF CONTENTS			iv
LIST OF SYMBOLS			vii
LIST OF FIGURES			xiv
LIST OF TABLES			xx
CHAPTER	I	INTRODUCTION	1
	1.1	Recent Developments in Electromagnetic Horns	1
	1.2	Resumé	10
CHAPTER	II	LITERATURE REVIEW	13
	2.1	Introduction	13
	2.2	Solution of the Corrugated Conical Horn by the Method of Separation of Variables	13
	2.2.1	The Characteristic Equation of the TM Mode in the Grooves	17
	2.2.2	Corrugation Depths for Symmetrical Patterns	18
	2.2.3	Boundary Conditions at the Wall of the Corrugated Horn	19
	2.2.4	The Electromagnetic Field in the Corrugated Horn	20
	2.2.5	The Radiation Pattern of the Corrugated Conical Horn Antenna	22
	2.3	Pattern Analysis Using the Geometrical Theory of Diffraction [GTD]	23
	2.3.1	H-Plane Edge Diffraction	24
	2.3.2	Horn with E-Plane Magnetic Conducting Walls	27
	2.3.3	Horn with E-Plane Corrugated Walls	28
	2.4	Special Techniques and Investigations	29
	2.4.1	The Choked Waveguide Feed [39]	29
	2.4.2	Study of the Properties of Corrugated Surfaces for Corrugated Horn Design	31
	2.5	Conclusion	33

			Page
CHAPTER	III	THE IMPEDANCE REPRESENTATION OF CORRUGATED SURFACES	34
	3.1	Introduction	34
	3.2	The Scattering Surface	37
	3.3	The Surface Current Integral Equation	40
	3.4	The Impedance Representation	42
	3.5	Solution of the Integral Equation for the Surface Current	43
	3.6	The Scattered Field	47
	3.7	Numerical Results	49
	3.8	The E-Plane Dihedral Horn	60
	3.9	Conclusion	67
CHAPTER	IV	SCATTERING FROM BODIES OF REVOLUTION WITH IMPEDANCE BOUNDARY CONDITIONS	70
	4.1	Introduction	70
	4.2	Modelling, and the Solution Technique	71
	4.3	The Scattering Geometry	78
	4.4	The Integral Equation for the Electric Current Density on the Surface of a Scatterer with Impedance Boundary Conditions	82
	4.5	Solution of the Integral Equation (4.21)	85
	4.5.1	Contributions of the Terms $j\omega\bar{A}$ and ∇V to the Impedance Matrix	90
	4.5.2	Contribution of the Term $\nabla x\bar{F}$ to the Impedance Matrix	93
	4.5.3	The Impedance Matrix for the mth Mode on a Body of Revolution with Impedance Boundary Conditions	99
	4.6	Numerical Evaluation of the Impedance Matrix $[Z_m]$	100
	4.7	The Excitation Matrix	106
	4.8	The Measurement Coefficients	110
	4.9	Symmetric Properties of $[Z_m]$	115
	4.10	Mode Dependence of $[Z_m]$	117
	4.11	Mode Dependence of the Measurement Coefficients R_m^{pq}	118
	4.12	Evaluation of the Total Surface Current and the Total Scattered Field	119
	4.13	Conclusion and General Remarks on the Computer Program	120
CHAPTER	V	RADIATION AND SCATTERING FROM ELECTROMAGNETIC HORNS	123
	5.1	Introduction	123
	5.2	The Numerical Solution	124
	5.3	Co-polar and Cross-polar Radiation from rotationally Symmetric Corrugated Horns	124

Page

	5.4	The Impedance Representation for the rotationally Symmetric Corrugated Horn	126
	5.5	The Precise Modelling of the Rotationally Symmetric Corrugated Horn	128
	5.6	Scattering from Electromagnetic Horns	147
	5.7	The Numerical Output	154
	5.8	Conclusion	169
CHAPTER	VI	FORMULATION OF THE INTEGRAL EQUATIONS USING NEW GREEN'S FUNCTIONS	174
	6.1	Introduction	174
	6.2	E-Field and H-Field Integral Equations in Two Dimensions	179
	6.3	The Modified Electric Field Integral Equation	182
	6.3.1	The Dipole Source	182
	6.3.2	The Quadrupole Source	186
	6.4	The Modified Magnetic Field Integral Equation	189
	6.5	Numerical Results	190
	6.6	Conclusion	220
CHAPTER	VII	DISCUSSION AND CONCLUSION	222
APPENDIX	A	INTEGRAL FUNCTIONS USED IN APERTURE INTEGRATION AND GTD ANALYSIS OF CORRUGATED HORNS	230
APPENDIX	B	DERIVATION OF EQUATION (3.2)	234
APPENDIX	C	DERIVATION OF EQUATION (4.38)	235
APPENDIX	D	DERIVATION OF EQUATION (4.41)	236
APPENDIX	E	ON THE DERIVATION OF EQUATION (4.37)	239
APPENDIX	F	DERIVATION OF EQUATION (4.53)	240
APPENDIX	G	DERIVATION OF EQUATION (4.68)	242
APPENDIX	H	ELEMENTS OF MATRIX [B] IN EQUATION (4.102)	244
APPENDIX	I	NEAR FIELD AND FAR FIELD COMPONENTS OF AN X-DIRECTED HERTZIAN DIPOLE	245
REFERENCES			247

LIST OF SYMBOLS

Unless otherwise stated, the symbols most commonly used in this thesis have the following meaning:

(x, y, z)	Coordinates of a cartezian system with unit vectors $\hat{a}_x, \hat{a}_y, \hat{a}_z$.
(ρ, ϕ, z)	Coordinates of a circular cylindrical system with unit vectors $\hat{u}_\rho, \hat{u}_\phi, \hat{u}_z$.
(r, θ, ϕ)	Coordinates of a spherical system with unit vectors $\hat{i}_r, \hat{i}_\theta, \hat{i}_\phi$.
(t, ϕ)	Coordinates tangential to the surface of a body of revolution, with unit vectors $\hat{u}_t$ and $\hat{u}_\phi$.
$\bar{A}$	Electric vector potential.
$\bar{A}_d$	Electric vector potential due to a current element.
a	Half length separation between the parallel plates of a dihedral horn. (Chapter III).
a	Inner radius of circular waveguide. (Chapter V).
a	Radius of a circular scattering cylinder. (Chapter VI).
B	Square matrix with elements equal to Z_t or Z_ϕ .
b^t_{mn}, b^ϕ_{mn}	Constant coefficients in the expansion of the magnetic current M^t and M^ϕ .

C_{mm}	Elements of a square coefficient matrix.
c	Linear integration path.
D_m	Elements of a column matrix.
d	Depth of rectangular corrugation slot. (Chapters II to V).
d_{zi}	Distance between two points $\bar{t}_{2i}$ and $\bar{t}_{2i+1}$ on the generating curve of a body of revolution.
d	Distance between two points along the normal to the scattering surface. (Chapter VI).
$\bar{E}$	Electric field vector.
$\bar{E}_c$	Transverse component of electric field tangential to the scatterer cross-section.
$\bar{E}^{inc}$	Incident electric field.
$\bar{E}^{sc}$	Scattered electric field.
$\bar{E}^{sc}_{\bar{J}}$	Scattered electric field due to $\bar{J}$
$\bar{E}^{sc}_{\bar{F}}$	Scattered electric field due to $\bar{M}$
$\bar{E}_{cross}$	Cross-polar electric field.
e	Base of naperian logarithm.
$\bar{F}$	Magnetic vector potential.
$F_1(\theta, \phi)$	Angular dependence of scattered field in θ direction.

$F_2(\theta, \phi)$	Angular dependence of scattered field in ϕ direction.
$f(t)$	Basis expansion function used in the moment method of solution.
G	Two-dimensional Green's function.
$G_1, G_2, \ldots, G_6$	Integral functions.
G'	Function defined in (4.54).
g	Width of a rectangular corrugation slot.
$\bar{H}$	Magnetic field vector.
$H_0^{(2)}$	Hankel function of second kind and order zero.
$H_1^{(2)}$	Hankel function of second kind and order 1 .
h_i	Distance between two points with ρ and z coordinates (ρ_i^-, z_i^-) and $(\rho_{i+1}^-, z_{i+1}^-)$ on the surface of a body of revolution.
I_{mn}^t, I_{mn}^ϕ	Constant coefficients in the expansion of the electric currents J^t and J^ϕ .
J_n	Bessel function of first kind and order n .
$\bar{J}$	Surface electric current density.
J_{mn}^t, J_{mn}^ϕ	Expansion functions for the currents J^t and J^ϕ .
j	$= \sqrt{-1}$.

K_1 , K_2	Magnetic line currents phasors.
k	wave number.
L	Waveguide length.
ℓ	Horn wall length (Figure III.12).
ℓ_{mn}	Elements of a coefficient matrix.
$\bar{M}$	Surface magnetic current density.
M^t_{mn}, M^ϕ_{mn}	Expansion functions for the currents M^t and M^ϕ .
Nl	Number of matching points over a section.
NP	Number of matching points on the generating curve of a body of revolution.
$\hat{n}$	Unit outward normal to the scatterer.
$\bar{P}$	Vector function.
p	Permutation of t or ϕ . (Used as superscript).
p	Index used in the expansion of a triangular function or its derivative. (Chapter IV).
p	Constant coefficient used in Figure V.13(c).
$\bar{Q}$	A vector function.
q	Permutation of t and ϕ . (Used as superscript).
q	Index used in the expansion of a triangular function or its derivative. (Chapter IV).

R	Distance between field and source points.
$(R_m^{pq})_j$	Measurement coefficient due to the jth azimuthal mode current on the mth segment of the generating curve of a body of revolution. $p = t$ or ϕ ; $q = \theta$ or ϕ .
$(\tilde{R}_m^{pq})_j$	Measurement coefficient with ϕ dependence omitted.
$\bar{r}$, $\bar{r}'$	Position vectors of field and source points respectively.
$\bar{r}_0$	Unit vector in the direction from origin to a field point.
S_{00}	Antenna reflection coefficient.
s	Scattering surface.
T	Weighting function in the expansion of a triangle basis function.
T'	Weighting function in the expansion of the derivative of a triangle basis function.
TH	Thickness of a scatterer.
t	Time.
U_m	Elements of a column matrix.
V	Electric scalar potential.
V^P	Inner product, $P = t$ or ϕ . (Defined in 4.32).

v_{mi}^{p}	Function defined in (4.39).
$\bar{W}$	Vector function.
Z_c	Surface impedance in a direction tangential to the scatterer cross-section (Chapter III).
Z_t, Z_ϕ	Surface impedances in directions t and ϕ tangential to a body of revolution.
$[Z]$	(Generalized) Impedance matrix.
$[Z_m^{pq}]$	Submatrices of $[Z]$. $p = t$ or ϕ ; $q = t$ or ϕ .
$[Z_m^{pq,\bar{J}}]$	Portions of $[Z_m^{pq}]$ due to $\bar{J}$.
$[Z_m^{pq,\bar{F}}]$	Portions of $[Z_m^{pq}]$ due to $\bar{F}$ (or $\bar{M}$).
$[\tilde{Z}_m^{pq,\bar{F}}]$	Submatrices with elements proportional to those of $[Z_m^{pq,\bar{F}}]$ (p and q in those two matrices are not necessarily the same).
$Z_0^{TE_{11}}$	Characteristic impedance of the dominant circular waveguide mode, TE_{11} .
α	Horn flare angle.
α_n	Constant coefficients in the expansion of the current J_z
β_n	Constant coefficients in the expansion of the current J_c
Γ_L	Load reflection coefficient.

γ	Euler's constant.
δ	Tooth width in rectangular corrugations.
$\delta(t-t')$	Impulse function defined at $t = t'$.
ε_0	Permittivity of free space.
η	Characteristic impedance of free space.
Θ	Inner product defined in (4.58).
λ	Wavelength.
μ_0	Permeability of free space.
ν	Angle between $\hat{u}_t$ and the z direction.
ν_{mn}	Angle defined by the difference vector $\lvert\bar{\rho}_m - \bar{\rho}_n\rvert$ and the normal to the scattering cross-section (Chapter III).
σ	Surface electric charge density.
τ	Inner product defined in (4.66).
Φ	A scalar function used in identities (4.8a) and (4.49).
Φ	Free space Green's function.
Φ_d	Electric scalar potential due to a current element.
Ψ	Inner product defined in (4.37).
ω	Radian frequency.

LIST OF FIGURES

Figure		Page
I.1	Multimode Feeding of Conical Horns for Achieving Axial Symmetry	3
I.2	A Dielectric Loaded Horn	3
I.3	A Corrugated Horn	3
II.1	Corrugated Horns with Corrugations	26
	(a) Perpendicular to Horn Axis	
	(b) Perpendicular to Horn Walls	
	(c) Deformed to Fit Spherical Coordinate System	
II.2	Terminology used for GTD Analysis of Pyramidal Corrugated Horns	26
	(a) Side View of the Corrugated Horn	
	(b) Top View of the Corrugated Horn	
II.3	Thick Edge Model of Corrugated Horn E-Plane Wall	32
II.4	Choked Waveguide Feed	32
II.5	Scattering Model for Corrugated Horn Wall	32
III.1	(a) Rectangular Prism with Corrugations	39
	(b) Rectangular Prism with Corrugations Replaced by an Impedance Surface	
	(c) Wall Model with Rectangular Corrugations Considered by Mentzer and Peters [35]	
	(d) Wall Model with V-Corrugations Considered by Mentzer and Peters [36]	
III.2	Cross Section of Scattering Cylinder	50

Figure		Page
III.3	Current Distribution over the Corrugated Surface with $g/g+\delta = 0.9$ and Different Values for d/λ	50
III.4	Current Distribution over the Corrugated Surface with $d/\lambda = 0.375$ and Different Values for $g/g+\delta$	51
III.5	Current Distribution over the Corrugated Surface with $d/\lambda = 0.251$ and Different Values for $g/g+\delta$	51
III.6	Total Radiation Pattern for the Line Sources Illuminating the Corrugated Prism; $g/g+\delta = 0.9$ and $d/\lambda = 0.251$; 0.3125; 0.375; 0.4375	57
III.7	Total Radiation Pattern for the Line Sources Illuminating the Corrugated Prism; $g/g+\delta = 0.9$ and $d/\lambda = 0.251$; 0.2501; 0.25001; 0.250001	57
III.8	Total Radiation Pattern for the Line Sources Illuminating the Corrugated Prism; $g/g+\delta = 0.85$ and $d/\lambda = 0.251$; 0.313; 0.5	58
III.9	Current Distribution over the Corrugated Surface with $g/g+\delta = 0.85$ and $d/\lambda = 0.5$; 0.437; 0.375; 0.313	58
III.10	Total Radiation Pattern for the Line Sources Illuminating the Corrugated Prism; $d/\lambda = 0.375$ and $g/g+\delta = 0.5$; 0.6; 0.7; 0.8	59
III.11	Total Radiation Pattern for the Line Sources Illuminating the Corrugated Prism; $d/\lambda = 0.251$ and $g/g+\delta = 0.5$; 0.6; 0.7; 0.8	59
III.12	(a) The E-Plane Dihedral Horn	62
	(b) Equivalent Scatterer with Surface Impedance	
III.13	Radiation Patterns of the E-Plane Dihedral Horn with $\alpha = 30^{\circ}$; $\ell = 2.15\lambda$; $L = 1.89\lambda$; $TH = 0.32\lambda$; 1 Division = 5dB	66
	(a) $d/\lambda = 0.0$ and 0.25	
	(b) $d/\lambda = 0.33$ and 0.41	

Figure			Page
IV.1	(a)	Rotationally Symmetric Corrugated Horn with excitation for TE_{11} Circular Waveguide Mode	76
	(b)	Equivalent Scatterer with Impedance Surfaces	76
	(c)	Smooth Wall Counterpart	77
IV.2		Geometry of Body Revolution	81
IV.3	(a)	Triangle Function (solid) and Four Impulse Approximation (arrows)	102
	(b)	Derivative of Triangle Function (solid) and Four Impulse Approximation (arrows)	
V.1	(a)	Unsuccessful Modelling of Corrugated Horn	129
	(b)	Unsuccessful Modelling of Corrugated Horn	130
	(c)	Unsuccessful Modelling of Corrugated Horn	131
V.2	(a)	Thick Wall Modelling of Corrugated Horn. (Horn Geomtery)	133
	(b)	Thick Wall Modelling of Corrugated Horn. (Radiation Patterns)	134
V.3	(a)	Co-polar Radiation Pattern for Corrugated Horn with $a/\lambda = 0.32$; $d/\lambda = 0.15$; $\alpha = 90^{o}$; NP = 60. Single and Double Precision Calculations	135
	(b)	Cross-Polar Radiation Pattern for Corrugated Horn with $a/\lambda = 0.32$; $d/\lambda = 0.15$; $\alpha = 90^{o}$; NP = 60 Single and Double Precision Calculations	136
V.4	(a)	Co-polar Radiation Patterns for Smooth Wall Horn ($d/\lambda = 0.0$) with $a/\lambda = 0.36$; $\alpha = 90^{o}$ and NP = 30; 35; 50; 60	137
	(b)	Cross-Polar Radiation Patterns for Smooth Wall Horn ($d/\lambda = 0.0$) with $a/\lambda = 0.36$; $\alpha = 90^{o}$ and NP = 30; 35; 50; 60	138
V.5	(a)	Co-polar Radiation Pattern for Corrugated Horn with $a/\lambda = 0.32$; $d/\lambda = 0.15$; $\alpha = 90^{o}$ and NP = 30; 35; 40; 50; 60	141

Figure		Page
	(b) Cross-Polar Radiation Pattern for Corrugated Horn with $a/\lambda = 0.32$; $d/\lambda = 0.15$; $\alpha = 90^{o}$ and NP = 30; 35; 40; 50; 60	142
V.6	(a) Co-polar Radiation Pattern for Corrugated Horn with $a/\lambda = 0.36$; $\alpha = 90^{o}$; and $d/\lambda = 0.0$; 0.15; 0.249; 0.251; 0.35; 0.45	143
	(b) Cross-Polar Radiation Pattern for Corrugated Horn with $a/\lambda = 0.36$; $\alpha = 90^{o}$ and $d/\lambda = 0.0$; 0.15; 0.249; 0.251; 0.35; 0.45	144
V.7	(a) Co-polar Radiation Pattern for Corrugated Horn with $a/\lambda = 0.36$; $\alpha = 30^{o}$ and $d/\lambda = 0.0$; 0.15; 0.251; 0.35; 0.45	145
	(b) Cross-Polar Radiation Pattern for Corrugated Horn with $a/\lambda = 0.36$; $\alpha = 30^{o}$ and $d/\lambda = 0.0$; 0.15; 0.251; 0.35; 0.45	146
V.8	(a) Co-polar Radiation Pattern for Optimum Horn with $a/\lambda = 0.32$; $\alpha = 90^{o}$ and $d/\lambda = 0.13$; 0.14; 0.15; 0.16; 0.17	148
	(b) Cross-Polar Radiation Pattern for Optimum Horn with $a/\lambda = 0.32$; $\alpha = 90^{o}$ and $d/\lambda = 0.13$; 0.14; 0.15; 0.16; 0.17	149
V.9	Scattering Model of receiver horn used by Frandsen [91]	153
V.10	Scattering Model Using Impedance boundaries	153
V.11	(a) Induced Current I_t on a Waveguide Section with $L/\lambda = 1.0$; $a/\lambda = 0.35$; $TH/\lambda = 0.1$; $Z_t = Z_\phi = 0.0$; NP = 50; 100	156
	(b) Induced Current I_ϕ on a Waveguide Section with $L/\lambda = 1.0$; $a/\lambda = 0.35$; $TH/\lambda = 0.1$; $Z_t = Z_\phi = 0.0$; NP = 50; 100	157
	(c) Scattering Pattern from a Waveguide Section with $L/\lambda = 1.0$; $a/\lambda = 0.35$; $Z_t = Z_\phi = 0.0$; NP = 50; 100	158

Figure		Page
V.12	(a) Induced Current I_t on a Waveguide Section with $L/\lambda = 2.7$; $a/\lambda = 0.35$; $TH/\lambda = 0.1$; $Z_t = Z_\phi = Z_0^{TE_{11}}$; NP = 60; 120	159
	(b) Induced Current I_ϕ on a Waveguide Section with $L/\lambda = 2.7$; $a/\lambda = 0.35$; $TH/\lambda = 0.1$; $Z_t = Z_\phi = Z_0^{TE_{11}}$; NP = 60; 120	160
	(c) Scattering Pattern from a Waveguide Section with $L/\lambda = 2.25$; $a/\lambda = 0.35$; $TH/\lambda = 0.1$; $Z_t = Z_\phi = Z_0^{TE_{11}}$; NP = 60; 120	161
V.13	(a) Induced Current I_t on a Waveguide Section with $L/\lambda = 1.75$; $a/\lambda = 0.35$; $TH/\lambda = 0.1$; $Z_t = Z_\phi = 0$ and $Z_t = Z_\phi = Z_0^{TE_{11}}$	162
	(b) Induced Current I_ϕ on a Waveguide Section with $L/\lambda = 1.75$; $a/\lambda = 0.35$; $TH/\lambda = 0.1$; $Z_t = Z_\phi = 0.0$ and $Z_t = Z_\phi = Z_0^{TE_{11}}$	163
	(c) Scattering Pattern from a Waveguide Section with $L/\lambda = 2.0$; $a/\lambda = 0.35$; $TH/\lambda = 0.1$; $Z_t = Z_\phi = p\, Z_0^{TE_{11}}$; p = 0.0; 0.4; 0.7; 1.0; 1.3; 1.6	164
V.14	(a) Induced Current I_t on a Waveguide Section with $L/\lambda = 2.5$; $a/\lambda = 0.35$; $TH/\lambda = 0.1$; NP = 150; $Z_t = Z_\phi = Z_0^{TE_{11}}$	165
	(b) Induced Current I_ϕ on a Waveguide Section with $L/\lambda = 2.5$; $a/\lambda = 0.35$; $TH/\lambda = 0.1$; NP = 150; $Z_t = Z_\phi = Z_0^{TE_{11}}$	166

Figure		Page
V.15	(a) Induced Current I_t on a Waveguide Section with $L/\lambda = 2.5$; $a/\lambda = 0.35$; $TH/\lambda = 0.2$; $NP = 120$; $Z_t = Z_\phi = Z_0^{TE}11$	167
	(b) Induced Current I_ϕ on a Waveguide Section with $L/\lambda = 2.5$; $a/\lambda = 0.35$; $TH/\lambda = 0.2$; $NP = 120$; $Z_t = Z_\phi = Z_0^{TE}11$	168
V.16	Scattering Patterns from a Waveguide Section with $L/\lambda = 2.5$; $a/\lambda = 0.35$; $TH/\lambda = 0.1$	170
VI.1	Scatterer Cross-Section. Green's Function is the Field of a Point Source Located at "a"	188
VI.2	Scatterer Cross-Section. Green's Function is the Field of a Dipole Source "ab"	188
VI.3	Scatterer Cross-Section. Green's Function is the Field of a Quadrupole Source "abe"	188
VI.4	Relative Decay of Matrix Elements in the EFIE and its Modified Forms (ka = 1.5)	192
VI.5	Relative Decay of Matrix Elements in the MFIE and its Modified Forms (ka = 1.5)	204
VI.6	Relative Decay of Matrix Elements in the MFIE and its Modified Forms (ka = 4.5)	205
VI.7	Variation of Condition Number with ka for the EFIE and its Modified Forms (kd = 0.001) (Point Source, Dipole Source and Quadrupole Source)	213
VI.8	Variation of the Pivot Ratio with ka for the EFIE and its Modified Form (Dipole source with kd = 0.001)	214
VI.9	Variation of Condition Number with ka for the EFIE and its Modified Form (Dipole Source with kd = 0.001; 0.01; 0.1)	215

LIST OF TABLES

Table		Page
VI.1(a)	Induced Current (J_z) on Cylinder. TM Case. Comparison between Analytical and Moment Method Solutions of the EFIE and its modified forms. ka = 1.5; kd = 0.001; N1 = 40	195
VI.1(b)	Induced Current (J_z) on Cylinder. TM Case. Comparison between Analytical and Moment Method Solutions of the modified EFIE ka = 1.5; kd = 0.01; N1 = 40	196
VI.1(c)	Induced Current (J_z) on Cylinder. TM Case. Comparison between Analytical and Moment Method Solutions of the modified EFIE ka = 1.5; kd = 0.1; N1 = 40	197
VI.2(a)	Induced Current Magnitude (J_z) on Cylinder. TM Case. Comparison between Analytical and Moment Method Solutions of the EFIE and its modified forms. ka = 2.405; kd = 0.145×10^{-2}	198
VI.2(b)	Scattered Field Magnitude (E_z) from Cylinder. TM Case. Comparison between Analytical and Moment Method Solutions of the EFIE and its modified forms. ka = 2.405; kd = 0.145×10^{-2}	200
VI.3(a)	Induced Current (J_c) on Cylinder. TE Case. Comparison between Analytical and Moment Method Solutions of the MFIE and its modified forms. ka = 1.5; kd = 0.2; N1 = 40	206
VI.3(b)	Induced Current (J_c) on Cylinder. TE Case. Comparison between Analytical and Moment Method Solutions of the modified MFIE ka = 1.5; kd = 0.8; N1 = 40	207

Table		Page
VI.4(a)	Induced Current (J_c) on Cylinder. TE Case. Comparison between Analytical and Moment Method Solutions of the MFIE and its modified forms. ka = 4.5; kd = 0.2; Nl = 40	208
VI.4(b)	Induced Current (J_c) on Cylinder. TE Case. Comparison between Analytical and Moment Method Solutions of the modified MFIE ka = 4.5; kd = 0.8; Nl = 40	209
VI.5	Variation of Condition Number and Pivot Ratio with ka. EFIE and its modified forms are considered with small values of kd	216
VI.6	Variation of Condition Number and Pivot Ratio with ka. EFIE and its modified forms are considered with large values of kd	218

CHAPTER I

INTRODUCTION

1.1 Recent Developments in Electromagnetic Horns

Electromagnetic horns, in general, are characterized by their ability to affect a transition from a medium supporting a small number of propagating modes, such as a waveguide to one supporting a large or infinite number of modes, such as free space. They represent a means of approximating the ideal wavefront needed for good directivity, with the advantage of being able to accommodate a broad band of frequencies. These forms of radiators can hardly said to be new, but they certainly represent a field which has been anything but dormant in recent years. The impetus for activity in the design of new types of horns, has stemmed, of course, from the need to wring out every last fraction of decibel in gain from the large satellite communication and radio astronomy reflectors that are in use all over the world today.

By the end of the 1950's, almost all horn designs known to the antenna engineer were lacking the properties needed to make maximum use of the received energy in a large aperture antenna using paraboloid reflectors. Since the early 1960's, therefore, much of antenna research was dedicated to the development of horn radiators having broad band performances, and possessing rotationally symmetric radiation patterns, low side and backlobes, low input voltage standing wave ratio (V S W R), as well as a low level of cross-polarization and a well defined phase center. Such horns were intended to be used as primary feeds for the

high cost reflector antennas. The precise uniformity of the power pattern around the axis of the horn is needed for the efficient illumination of parabolic antennas, reducing, in this way, spillover and cross-polarization losses, and increasing the aperture efficiency. This same property is also essential in polarization measurements of the celestial source distribution in radio astronomy applications. There, a telescope should "see" the same area in the sky when its feed horn is effectively, or actually, rotated through 90° so as to measure two perpendicular polarizations. On the other hand, frequency reuse, whereby two separate data channels within the same frequency band are transmitted (or received) with different polarizations, in order to increase the data capacity of a satellite communication link, requires adequate ($\simeq$ 30 dB) isolation between orthogonal radiation beams, hence the need for antennas with low levels of cross-polarization.

Three high performance horns, whose developments have been stimulated by the need to optimize the performance of reflector antennas were introduced, therefore, during the last two decades. These sophisticated versions of horn radiators are the multimode, Figure I.1, the dielectric-loaded, Figure I.2, and the corrugated horn antennas, Figure I.3.

The original concept for the first of these new horns appears to have been due to P.D.Potter. In his paper [1], published in 1963, he describes a technique for generating and combining a TM_{11} mode field with that of a dominant TE_{11} field in a conical horn in such a way as to create a high degree of axial symmetry, along with E-plane side-

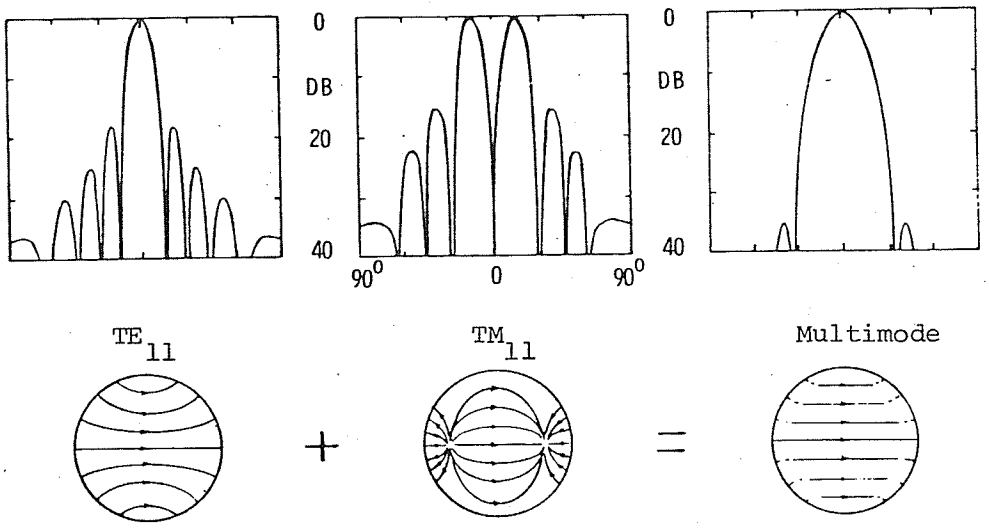

Fig. I.1. Multimode Feeding of Conical Horns for achieving Axial Symmetry.

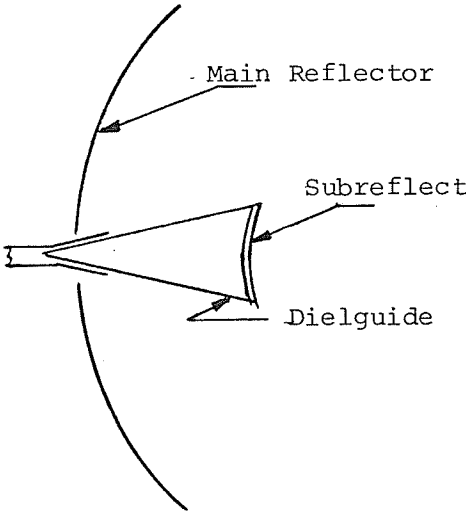

Fig. I.2. A Dielectric Loaded Horn.

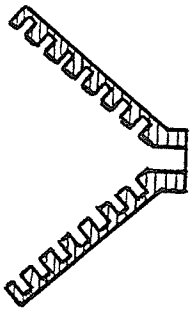

Fig. I.3. A Corrugated Horn.

lobe suppression in the radiated beam. A few months later, Potter and Ludwig [2] analyzed the possibilities of beam shaping through the superposition of higher order modes in conical horns. About the same time, Jensen [3] described the extension of the multimode technique to pyramidal horns. In this case, the dominant mode, of course, is the TE_{10}, while the appropriate higher mode, (hence the counterpart of the TM_{11} mode in the conical horn), is a mixture of the TE_{12} and the TM_{12} modes. This single, hybrid mode, was called EM_{12} by Drabowitz [4] in recognition of the fact that the TE_{12} and TM_{12} modes have the same cutoff frequency and hence propagate with the same phase velocity. In 1966, Ludwig gave a definitive development of pattern synthesis for circular aperture horns. In his work [5], he shows that the θ and ϕ components of the radiated field may be synthesized, respectively, from TM and TE circular waveguide modes, and gives examples in which up to four modes are used. Turrin [6] combined a very compact TM_{11} mode transducer and a circular horn to form a small prime focus feed possessing all the attributes of a multimode horn. Generation of the TM_{11} mode occurs due to an abrupt flare angle change in the guide. Cohn [7], showed how to apply flare angle changes to generate the hybrid $TE_{12} + TM_{12}$ mode in a pyramidal horn, and hence a tapered aperture field in the E-plane aperture distribution. He also gave an example of a feed for a large Cassegrain system. The same techniques were applied by Han and Wickert [8] in their paper describing a multimode rectangular aperture horn. The latter radiates a circularly polarized beam of elliptical cross section that is useful for continental area coverage from orbiting satellites.

Since the dominant mode and the desired higher modes propagate with different velocities as they travel from the point of mode generation to the horn aperture, they will arrive in the correct phase relationship at only one frequency. For this reason, bandwidth is quite limited, and this appears to be the principal shortcoming of the multimode horns.

The dielectric loaded horns, on the other hand, were first introduced by Bartlett and Moseley [9]. They used a low permittivity dielectric cone (dielguide), extending beyond the horn and all the way to the subreflector of a Cassegrain antenna, to compromise between illumination uniformity and the amount of energy lost in spillover. They explained using ray-optic concepts, how most of the radiation from the feedhorn can be made to intercept the subreflector, Fig.I.2, due to the total internal reflection at the dielectric-air interface. After reflection at the subreflector, the rays pass through the dielectric-air boundary almost without effect, as the angle of incidence is then less than the critical angle. Experimental patterns show that the radiation patterns of such antennas exhibit a large degree of symmetry, and antennas efficiencies of 75 to 80 percent were reported. Later, Tsandoulas and Fitzgerald [10] described the use of dielectric wedges inside the walls of rectangular and pyramidal horns to create a dominant longitudinal section electric (LSE) mode. Their objective was to increase the aperture efficiency of the radiator from the usual 81 percent to a value close to 100 percent. Such radiators would presumably be more useful in array applications than as feed horns.

Hamid et al [11] reported some experimental results for the case of a dielectric plug in the end of a circular waveguide to narrow the radiation pattern and increase the gain. A disadvantage of the dielectric-loaded horn for certain applications, however, lies in the effects of the atmospheric moisture upon the dielectric and the deterioration of the radiator performance over long periods in an all-weather environment.

Finally, the corrugated horn which also possesses many of the desirable characteristics of an ideal feed horn for a paraboloid reflector, originated simultaneously in two widely separated regions. In the United States, Kay [12] came to the realization that if the same boundary conditions could be obtained inside the horn in the E and H planes, the field would have the same pattern in both planes. A metallic surface corrugated with many closely-spaced parallel transverse grooves will present a reactive boundary which approaches the same boundary condition for TM and TE waves at grazing incidence. According to some empirical studies by Simmons and Kay [13], it was reasoned that if these grooves were made deep enough so that the surface reactance is capacitive, surface waves cannot be supported. While reporting some of their experimental results, they concluded that for these horns, the radiated energy is confined to the angular sector determined by the horn flare angle rather than by the aperture size in wavelengths, as is the case for a conventional diffraction limited horn, and that in addition, the beamwidth is constant over a wide frequency band. The bandwidth limitation appeared to be due to the waveguide excitation at the throat.

At about the same time, research at the Commonwealth Scientific and Industrial Research Organization (CSIRO) in Australia showed that the focal region field of a paraboloid reflector consisted of a superposition of cylindrical hybrid modes. Hence, Minnet and Thomas [14] were able to prove from a focal region-analysis that a uniform, linearly polarized wave incident normally on the aperture of a paraboloid, produces balanced hybrid modes at the focal plane. In these modes, the $\bar{E}$ and $\bar{H}$ fields were found to be identical in form and satisfy the relation $\bar{E} = j\,\eta\,\bar{H}$ where η is the intrinsic impedance of free space. A study of the structure of these fields also led to the hypothesis that the waves could be confined in a cylindrical metal tube, provided that the walls were corrugated either circumferentially or longitudinally with resonant slots. They found, in particular, that the required surface reactance X_ϕ and X_z on the inner wall of the supporting waveguide, defined as

$$X_\phi = -j\,E_\phi/H_z \qquad \text{and} \qquad X_z = j\,E_z/H_\phi \tag{1.1}$$

where the subscripts refer to a circular cylindrical system of coordinates (ρ, ϕ, z), should satisfy the relation $X_\phi X_z = -\eta^2$. Thus to match X_ϕ and X_z at every point, the boundary must be anisotropic. This requirement may be realized in practice with corrugated metal surfaces. For example, a cylindrical surface with circumferential slots may be designed so that $H_\phi = 0$ at the surface (zero longitudinal current). Also the edges of flanges between slots require $E_\phi = 0$. With sufficient slots per wavelength, the structure approximates a continuous anisotropic surface with

$X_\phi = 0$ and $X_z = \infty$. It will be noted that these boundaries affect the $\bar{E}$ and $\bar{H}$ fields in the same way, in agreement with the fact that the fields are identical. A second result followed immediately by reciprocity: balanced hybrid modes radiating from the focal plane must illuminate the paraboloid aperture without cross-polarization. Consequently, the radiation fields of these modes had to possess axial symmetry of polarization. A detailed study of boundary conditions, formulated in terms of anisotropic surface reactances and assuming only the lowest slot mode, confirmed the original hypothesis that the balanced hybrid modes would propagate in a cylindrical corrugated tube with slots tuned to resonance and excellent experimental radiation patterns were reported in [14]. These successful results were relevant to Rumsey's theoretical studies of fields which everywhere satisfy the relationship $\bar{E} = \pm j \eta \bar{H}$ [15]; the latter had been found to be characteristic of propagation over anisotropic surfaces, for which the boundary conditions on $\bar{E}$ and $\bar{H}$ are the same. Subsequently, Rumsey deduced by general electromagnetic arguments, that the axially symmetric fields were of the same type [16]. Later, Clarricoats and Saha [17], and Jansen et al [18] presented analytical studies useful for the design of corrugated horns.

When looking back at the concept of operation of the three kinds of horns just discussed above, it might seem at a first glance, that the multimode and corrugated horns accomplish similar results, namely axisymmetric radiation patterns, by quite different means. In reality, the modal contents of the fields in the two cases are, with one important

difference, the same. In Potter's multimode horn, TE_{11} and TM_{11} modes have different phase velocities by virtue of the fact that the modes have different cutoffs, since the boundary conditions on $\bar{E}$ and $\bar{H}$ are not the same. In the corrugated horn, however, a hybrid mixture of TE_{11} and TM_{11} waves behaves as a single mode, in which both components propagate with the same velocity, resulting of course in a wider operating bandwidth. For the same reason, pattern synthesis using normal circular waveguide as presented by Ludwig and Potter, will need the independent generation of double the number of corresponding hybrid modes in a corrugated waveguide to accomplish a similar radiation pattern.

It becomes clear therefore from the above considerations, and from further theoretical studies grouped in an IEEE press publication edited by Love [19], that the corrugated horn stands indeed as a very competitive candidate in reflector antennas applications. As a matter of fact, it has been designed in different forms for several projects for satellite communications and unattended earth terminals [20, 21, 22] . The drawback of this horn, lies however, not in its electrical performance, but in its massive size and difficulty in fabrication. A design engineer would need therefore, a helpful tool to test his design of a corrugated horn before being involved with much man-hour work and expenses. This seems more to be the case when he modifies his design or tests several prototype antennas. Available theoretical investigations however, are based on many approximations and can hardly be extended to study the effect of geometrical changes for the improvement of its characteristics. In addition, some valuable informations, as for example the back scattering from

these types of horns cannot be obtained using the old techniques. It is the object of the present work therefore to devise a new method for studying corrugated horns, so as to come up with a valuable tool for the horn antenna designer in particular, and for those involved in the field of electromagnetic wave scattering, in general.

In short, the technique we will be adopting, is that of considering the problem of radiation from the corrugated horn as one of electromagnetic scattering from a body with impedance boundaries. The excitation is obtained from a source with proper location and polarization so as to induce the possible waveguide mode incident on the waveguide-horn junction. Hence, assuming a proper mode of propagation inside the slots, a value for the surface reactance could be defined and an integral equation for the currents on the waveguide and horn walls can be obtained. Using the moment method of solution [23], the integral equation is solved for the currents and most of the electrical properties of the horn are then determined from their appropriate formulae.

1.2 Resumé

Chapter II of the thesis will include a literature review on the subject of corrugated horns, where the main techniques of solution and design are presented with particular emphasis on the approximations involved. Before proceeding to the lengthy solution of the corrugated circular horns, we include Chapter III where the study on the effectiveness

of representing the corrugations by an impedance surface in the numerical solution of a simplified model in two dimensions is reported. The results are also applied to the case of dihedral corrugated horns. Chapter IV is an extension of the work to three dimensions, to apply to the case of corrugated circular horns. The same numerical technique used in the preceeding chapter is adopted here, but the solution is becoming more complicated since we use both triangular and azimuthal mode representation for the unknown surface currents. This formulation is then used in Chapter V to calculate the radiation and the cross-polarization patterns for several corrugated horn models. In the same chapter, we show how the same numerical study we have developed can be applied to investigate the scattering properties of horns. This is a problem of general concern to the antenna engineer, but nothing was found in the literature concerning the backscattering from corrugated horns. As for smooth wall horns, we became aware of only one method which could well serve this purpose, and was published [24] at the time of the final preparation of this thesis. Although our technique for determining the backscattering is applicable to both corrugated and smooth wall horns, we preferred to include the study on the second type only. In this way, it will be more useful to designers who are not particularly interested in the corrugated horn.

Chapter VI includes a closer look at the moment method of solution which has been used extensively throughout our investigation. It was noticed that the size of the impedance matrix to be inverted was

becoming quite large when the number of matching points was increased to obtain accurate solutions. In addition, horns larger than the moderate size ones we have considered, will result in even larger matrices. Since the impedance matrix obtained is usually dense, round-off errors might become serious during inversion. Resonance effects might also result in false predictions when small errors happen in computing the elements of the matrix. Different Green's functions with asymptotic decay as R^{-1} and R^{-2}, where R is the distance between source and field points, are therefore investigated in this section in the hope of obtaining a predominantly diagonal matrix. The behaviour of the matrix coefficients and solutions for these cases are also reported.

Finally, the work is concluded in Chapter VII by a general discussion of the results and possible extensions to related problems.

CHAPTER II

LITERATURE REVIEW

2.1 Introduction

The excellent electromagnetic performance of horn radiators using corrugated walls as demonstrated independently by Simmons and Kay [25] in the U.S.A., and Minnet and Thomas [26] in Australia, has stimulated considerable interest in the study of the properties of these devices. Because of the complicated shape of their boundaries, however, a rigorous theoretical analysis for such structures is difficult to derive, and some approximations are necessary in the course of any attempt to solve for their electromagnetic characteristics. Although investigations in this field were not quite general, they have indeed contributed a great deal to the understanding of the operating behaviour of corrugated horns.

The analytical approaches used were usually based on either the method of separation of variables followed by an aperture integration technique to determine the fields inside and outside the horn, or the application of the Geometrical Theory of Diffraction for the pattern analysis in the major planes of radiation. While the first technique was used for the analysis of both the pyramidal and conical corrugated horns, the second method, however, was reported in conjunction with the solution of pyramidal horns only. Hence, for horns of conical shape, Clarricoats and Saha [27] used a cylindrical modal analysis when the flare semiangle

is 5° or less, and a spherical modal analysis for angles in the range 9° - 70° . Jansen, Jenken and Lambrechtse [28] carried a similar analysis by first investigating the possible modes in the slots of the corrugations. Solutions by these investigators, however, were applicable only to the case of resonant slots. The limitations of their method was not considered serious since it was believed, at the beginning, that the corrugations are effective mainly when the anisotropic wall impedance is zero in the azimuthal direction and infinite along the other normal coordinate. Later, Narasimhan [29] was able to solve for the propagation modes inside the horn for slot depths ranging from 0.25 to 0.5 of the operating wavelength, by treating the corrugations as an impedance boundary. His analysis was reported to be valid when the circular waveguide exciting the horn is proportioned to carry the dominant TE_{11} mode. Further, it was assumed that the thickness of the fins forming the corrugated boundary is very small compared with the spacing between any two adjacent fins and that the number of corrugations within one wavelength of the operating frequency is large enough such that space harmonics in the axial region may be ignored. Impedance representation was also used in a separation of variables solution of the corrugated E-plane sectoral horn (Narasimhan and Rao, [30]), but there, the wall impedances had to satisfy special conditions before the field in the axial region could be expressed in terms of separable modes.

In calculating the radiated field, Kirchhoff-Huygen's integration method was usually adopted as in [27, 28]. For the same purpose,

Clarricoats and Saha [27] used a modal expansion method valid for the determination of both the near and the far field radiation patterns. Narasimhan and Rao [31, 32] included the effect of phase error as a perturbation and have obtained good agreement with experimental results for horns with semiangles up to 30° . The semi-rigorous method employing the Geometrical Theory of Diffraction (GTD) was used by Lawrie and Peters [33] to explain the diffraction mechanism in corrugated horns. This method, which tends to give a physical insight into the process that prevents a uniform aperture distribution was also used by Mentzer and Peters [34] to evaluate the far out side- and backlobes of a corrugated pyramidal horn. As no diffraction coefficient was known for a wedge with capacitive surface having an arbitrary reactance value, they used instead an approximate coefficient evaluated for thick wedges with infinite impedance walls.

On the other hand, numerical investigations related to corrugated horns are very limited and less general. The reason being the large perimeter of the corrugated horn which imposes excessive computer time and storage requirements when known numerical methods are used. Hence, Mentzer and Peters [35, 36] were able to study only the properties of the two-dimensional surfaces used in horn design, by means of an integral equation formulation. Terzuoli et al [37, 38] used a similar equation to study the shielding effectiveness of the corrugations and the VSWR properties of small E-plane dihedral horns. Later, Elliot and Hockam [39] presented a numerical solution valid for waveguides with corrugated flanges in which they used a normal mode expansion for the

fields in the slots. The original idea of using the impedance boundary conditions in conjunction with the scattering properties of bodies of revolution for the study of the radiation characteristics of corrugated conical horns is due to Shafai and Hansen [40, 41].

Finally, experimental studies on corrugated horns are reported by T.B. Vu and Q.H. Vu [42] for optimum feed design, and by Vu and Hien [43] for corrugated monopulse feed. Thomas [44] presented some results on corrugated cylindrical waveguides used for mode conversion while Jenken [45] and then Jenken and Lambrechtse [46] gave experimental radiation patterns for corrugated conical horn antennas with small and wide flare angles. Some design charts for corrugated conical horns are reported by B. Thomas in [47].

In the following sections, a brief review on the main approaches mentioned above will be introduced. Approximations involved, which restrict the range of validity of each solution will be pointed out. We include in particular, Jansen's et al solution [28] using the method of separation of variables and the pattern analysis by the GTD as reported by Mentzer and Peters [34]. Special techniques by Elliot and Hockham [39] and by Mentzer and Peters [35, 36] will also be discussed for a complete presentation of the subject.

2.2 Solution of the Corrugated Conical Horn by the Method of Separation of Variables

2.2.1 The Characteristic Equation of the TM Mode in the Grooves

The computation of the electromagnetic fields in a groove is a difficult task, since the boundaries of the groove do not coincide with a coordinate system in which Maxwell's equations can be easily solved. For a groove which is not too close to the apex of the cone, however, we can change the shape of these boundaries to make them coincide with a spherical system of coordinates (r, θ, ϕ), (Figure II.1). The TM mode in the groove can be derived from a potential $A_r(r,\theta,\phi)$, given by

$$A_r(r,\theta,\phi) = kr \{[y_n(kr_1) + kr_1\ y_n'(kr_1)]\ j_n(kr) - [j_n(kr_1) + kr_1\ j_n'(kr_1)]\ y_n(kr)\} \times \times [Q_n^m(\cos\theta_2)\ P_n^m(\cos\theta) - P_n^m(\cos\theta_2)\ Q_n^m(\cos\theta)] \times \times (e_m \cos m\phi + f_m \sin m\phi) \ . \qquad (2.1)$$

upon application of the boundary conditions $E_\phi = 0$ at $r = r_1$ and $E_r = 0$ at $\theta = \theta_2$. In this expression, $j_n(kr)$ and $y_n(kr)$ are the spherical Bessel and Neuman functions, $P_n^m(\cos\theta)$ and $Q_n^m(\cos\theta)$ are the associated Legendre functions of the first and second kind, k is the usual wave number and e_m and f_m are constants to be determined from the boundary conditions and the strength of the electromagnetic field at the opening of the groove, $\theta = \theta_0$. Primes mean derivative with respect to the argument and m is an index whose value depends on the way in which the electromagnetic field in the groove is excited. In most practical cases $m = 1$. When the

width of the groove g is small compared to the wavelength, then the condition $E_\phi = 0$ at the boundaries I and III (Figure II.1c) also gives

$$n = -\frac{1}{2} \pm \left[\frac{1}{4} + (kr_1)^2\right]^{1/2} \tag{2.2}$$

Hence

$$n \simeq kr_1 \qquad \text{if} \quad kr_1 >> 1 \quad \text{and} \quad kg << 1 \tag{2.3}$$

It can be concluded therefore that the TM mode can exist in the groove even if its width is small compared to the wavelength. A similar investigation would prove that TE modes cannot propagate in a groove having a width which is less than half a wavelength [48] .

2.2.2 Corrugation Depths for Symmetrical Patterns

If we start by assuming the boundary conditions $E_\phi = 0$ and $\eta H_\phi = 0$, then, as will be seen in Section 2.2.5, the resulting radiation pattern becomes rotationally symmetric. Using (2.1), we see that the second condition will be satisfied if we can find a value of θ_0 such that

$$P_n^{m'}(\cos\theta_0)\, Q_n^m(\cos\theta_2) - P_n^m(\cos\theta_2)\, Q_n^{m'}(\cos\theta_0) = 0 \tag{2.4}$$

If $kr_1 >> 1$ and $kg << 1$ then (2.3) shows that $n >> 1$. Hence using the asymptotic expansions for $P_n^m(\cos\theta)$ and $Q_n^m(\cos\theta)$ and the recurrence

relations for the associated Legendre functions, one can finally deduce from (2.4) that for large θ_0 ,

$$d = r_1\theta_1 = \frac{\lambda}{4}(2\ell+1) \quad ; \quad \ell = 0,1,2,3, \ldots. \tag{2.5}$$

where d is the depth of the groove and λ is the operating wavelength. Equation (2.5) shows that the grooves can all be made $\lambda/4$ deep when they are far enough from the apex of the cone. For small values of θ_0 , (2.5) is not valid, and a computation to determine the groove depths can be carried out starting from the Runge-Kutta method as described in [48] . The following conclusions are generally deduced:

(i) Groove depths can be found from (2.5) when $n > 15$.

(ii) When $5 < n < 15$, groove depths are virtually independent of θ_0 if $\theta_0 \geq 30$.

(iii) Grooves characterized by low values of n and θ_0 have depths which are functions of both of them.

2.2.3 Boundary Conditions at the Wall of the Corrugated Horn

The electromagnetic field at the opening of a narrow groove consists of a dominant TM mode plus evanescent modes which are usually neglected due to their small effect. Assuming that there are many grooves per wavelength, then the boundary conditions at $\theta = \theta_0$ can be formulated in terms of two impedances Z_ϕ and Z_r defined as

$$E_\phi = Z_\phi H_r \qquad \text{and} \qquad E_r = Z_r H_\phi \tag{2.6}$$

While E_ϕ is zero at the opening of the grooves and the dams, currents in the ϕ direction, however, are possible. Hence we have $Z_\phi = 0$ but $H_r \neq 0$. Assuming the width of the dam to be negligibly thin, then

$$Z_r = \frac{E_r}{H_\phi} = \frac{-1}{j\omega\varepsilon_0} \frac{n(n+1)}{r} A_r \left(\frac{\partial A_r}{\partial \theta}\right)^{-1} \tag{2.7}$$

with j being equal to $\sqrt{-1}$, ω the radian frequency and ε_0, the permittivity of free space. Using (2.1) and (2.2) in (2.7), one can show that

$$Z_r = - j\eta \tan(kd) \tag{2.8}$$

2.2.4 The Electromagnetic Field in the Corrugated Horn

In general, the electromagnetic field in the region $\theta' < \theta_0$ is a spherical hybrid mode, and can be determined from the potentials:

$$A_r(r',\theta',\phi') = A_1 P_\nu^1(\cos\theta') \cos\phi' h_\nu^{(2)}(kr') \tag{2.9a}$$

$$F_r(r',\theta',\phi') = A_2 P_\nu^1(\cos\theta') \sin\phi' h_\nu^{(2)}(kr') \tag{2.9b}$$

in which $h_\nu^{(2)}$ represents the spherical Hankel function of the second kind. Prime coordinates are used for the description of the field in

the axial region of the horn while fields in the grooves are described in terms of unprimed coordinates. The unknowns in equation (2.9) are the value of ν and the ratio of A_1/A_2. Application of the boundary conditions $Z_\phi = 0$ and $E'_r = Z_r H'_\phi$ gives rise to the equations:

$$\frac{P_\nu^1(\cos\theta)}{\sin\theta} + (d)\cdot \frac{d\, P_\nu^1(\cos\theta)}{d\theta}\Bigg|_{\theta=\theta_0} = 0 \qquad (2.10a)$$

and

$$\frac{-\nu(\nu+1)}{jkr'}\,\frac{\eta}{Z_r}\,P_\nu^1(\cos\theta)\,\frac{d\, P_\nu^1(\cos\theta)}{d\theta} - \left[\frac{d\, P_\nu^1(\cos\theta)}{d\theta}\right]^2 + \left[\frac{P_\nu^1(\cos\theta)}{\sin\theta}\right]^2\Bigg|_{\theta=\theta_0} = 0\,. \qquad (2.10b)$$

Equation (2.10a) contains the variable r' which implies that ν is a function of r'. However, this is not possible because in (2.9) the assumption has been made that the method of separation of variables can be applied. Hence (2.10a) can be solved only if we assume $Z_r = \infty$ or a depth of $\lambda/4$ for the grooves. For this special case we find $A_2 = \pm \eta\, A_1$. Consequently, two classes of modes can propagate in the corrugated conical horn. Modes for which $A_2 = +\eta\, A_1$, are called $HE_{1\nu}^{(1)}$ while the others are called $HE_{1\nu}^{(2)}$ - modes;(Clarricoats proposes a different nomenclature in [27]). From the expressions for the transverse electric and magnetic fields,it can be shown that the first type gives a

maximum in the radiation pattern in the boresight direction, $\theta' = 0$, while the second gives a null at this angle.

2.2.5 The Radiation Pattern of the Corrugated Conical Horn Antenna

The radiation field can be computed using the aperture integration method. Hence for a point p defined by the position vector $\bar{r}$,

$$\bar{E}(\bar{r}) = \text{curl}_p \int_{S_A} [\hat{n}' x \bar{E}(\bar{r}')] \, \Phi(\bar{r},\bar{r}') \, ds + \frac{1}{j\omega\varepsilon_0} \text{curl}_p \, \text{curl}_p \int_{S_A} [\hat{n}' x \bar{H}(\bar{r}')] \, \Phi(\bar{r},\bar{r}') \, ds \tag{2.11a}$$

and

$$\bar{H}(\bar{r}) = \text{curl}_p \int_{S_A} [\hat{n}' x \bar{H}(\bar{r}')] \, \Phi(\bar{r},\bar{r}') \, ds - \frac{1}{j\omega\mu_0} \text{curl}_p \, \text{curl}_p \int_{S_A} [\hat{n}' x \bar{E}(\bar{r}')] \, \Phi(\bar{r},\bar{r}') \, ds \tag{2.11b}$$

with $\Phi(\bar{r},\bar{r}') = \frac{1}{4\pi} \frac{e^{-jk\,|\bar{r}-\bar{r}'|}}{|\bar{r}-\bar{r}'|}$ and μ_0 being the permeability of free space. These expressions are valid when the outside of the horn is perfectly conducting and carries zero current. The horn aperture S_A is part of a sphere of radius r, with outward normal $\hat{n}'$. Using far field approximations, and the relation $A_2 = \eta A_1$ for $HE_{1\nu}^{(1)}$ modes we arrive at

$$E_\theta = \frac{-jk}{4} \frac{e^{-jkr}}{r} A_1 \eta \frac{h_\nu^{(2)}(kr')}{r'} (r')^2 \cos\phi \, F(\theta, \theta_0, kr') \qquad (2.12a)$$

$$E_\phi = \frac{jk}{4} \frac{e^{-jkr}}{r} A_1 \eta \frac{h_\nu^{(2)}(kr')}{r'} (r')^2 \sin\phi \, F(\theta, \theta_0, kr') \qquad (2.12b)$$

where $F(\theta, \theta_0, kr')$ is an integral function and is given in Appendix A. From (2.12a and b) we find that $|E_\theta|^2 + |E_\phi|^2$ is independent of ϕ. Hence, the radiation pattern of a corrugated conical horn is symmetrical provided the depth of the grooves is a quarter of a wavelength.

2.3 Pattern Analysis Using the Geometrical Theory of Diffraction (GTD)

The GTD was applied by Mentzer and Peters to the problem of radiation from pyramidal horns with corrugated E-plane walls [34]. For the model shown in Figure (II.2), they assumed an aperture magnetic field of the form

$$\bar{H}^a = \hat{y} H_0 \cos\frac{\pi x}{b} \cos\frac{\pi y}{a} \exp\left[jk\left(\rho_E \cos\theta_E - \sqrt{x^2+y^2} + (\rho_E \cos\theta + z)^2\right)\right] \qquad (2.13)$$

in which $\hat{y}$ is a unit vector in the direction y, a and b are the aperture dimensions, and ρ_E and θ_E are as shown in the figure. This cosine distribution was checked through a series of measurements. The radiation pattern near the main beam is represented using the aperture integration method. Hence the main portion of the horn pattern will be given by

$$E_\theta^A = \frac{jk}{4\pi} \frac{e^{-jkR}}{R} \cos\phi \ (1+\cos\theta) \int_{-a/2}^{a/2} \int_{-b/2}^{b/2} E_x^a(x',y') \ e^{jk\sin\theta \ (x'\cos\phi + y'\sin\phi)} \ dx' \ dy' \tag{2.14a}$$

$$E_\phi^A = \frac{-jk}{4\pi} \frac{e^{-jkR}}{R} \sin\phi \ (1+\cos\theta) \int_{-a/2}^{a/2} \int_{-b/2}^{b/2} E_x^a(x',y') \ e^{jk\sin\theta \ (x'\cos\phi + y'\sin\phi)} \ dx' \ dy' \tag{2.14b}$$

where

$$E_x^a(x,y) = \eta \ |\bar{H}^a| \tag{2.15}$$

The far out sidelobes and backlobes are to be found using the GTD. When properly computed, these far out regions of the pattern should connect smoothly to the near axial pattern as computed from (2.14a and b).

2.3.1 H-Plane Edge Diffraction

For a two-dimensional (dihedral) horn, the pattern may be obtained from the GTD using slope diffraction analysis [49, 50] . Hence

$$E_x = \cos\left(\frac{\pi}{b} \rho_H \cos\theta_H \tan\theta\right) \frac{e^{-jkr}}{\sqrt{r}} \exp[-jk\rho_H \cos(\theta_H - \theta)]$$

$$+jk\eta \ H_\rho^i \ \frac{e^{-jkr}}{\sqrt{r}} \{D_s(180^\circ - \theta_H + \theta) + D_s(180^\circ - \theta_H - \theta)$$

$$\exp[-j2k\rho_H \sin\theta_H \sin\theta]\} \tag{2.16}$$

where the first term is included for $|\theta| < \theta_H$, the second term is in-

cluded for $-90^{\circ} < \theta < 180^{\circ} + \theta_H$, the third term is included for $-180^{\circ} - \theta_H < \theta < 90^{\circ}$, and

$$D_s(\psi) = \frac{-e^{j(\pi/4)}}{4\sqrt{2\pi}\, k^{3/2}} \frac{\sin \psi/2}{(\cos \psi/2)^2} \tag{2.17}$$

as obtained by Keller [51]. H_ρ^i is given by

$$H_\rho^i = \frac{-1}{j\omega\mu_0} \hat{a}_\rho \cdot (\nabla \times \bar{E}^a)\Big|_{\text{edge}} \tag{2.18}$$

Equation (2.16) can be used to compute the radiation fields in the side- and backlobe regions by omitting the first term. Using the geometry of Figure (II.2) and the equivalent current concept [50, 52], the line source amplitudes are evaluated in terms of the diffracted fields. In this case, since the fields parallel to the edge at all four walls go to zero, the slope diffraction formulation is used for all four of the equivalent currents on the aperture edges. The H-plane edge contribution to the radiation pattern is given by

$$E_\theta^H = \frac{-jk\eta}{4\pi} \frac{e^{-jkR}}{R} \cos\theta \cos\phi \, (I_1+I_2) \tag{2.19a}$$

$$E_\phi^H = \frac{jk\eta}{4\pi} \frac{e^{-jkR}}{R} \sin\phi \, (I_1+I_2) \tag{2.19b}$$

I_1 and I_2, as given in Appendix A, are integrals involving the $\hat{x}$-directed equivalent electric currents on the H-plane edges at $y = \pm a/2$.

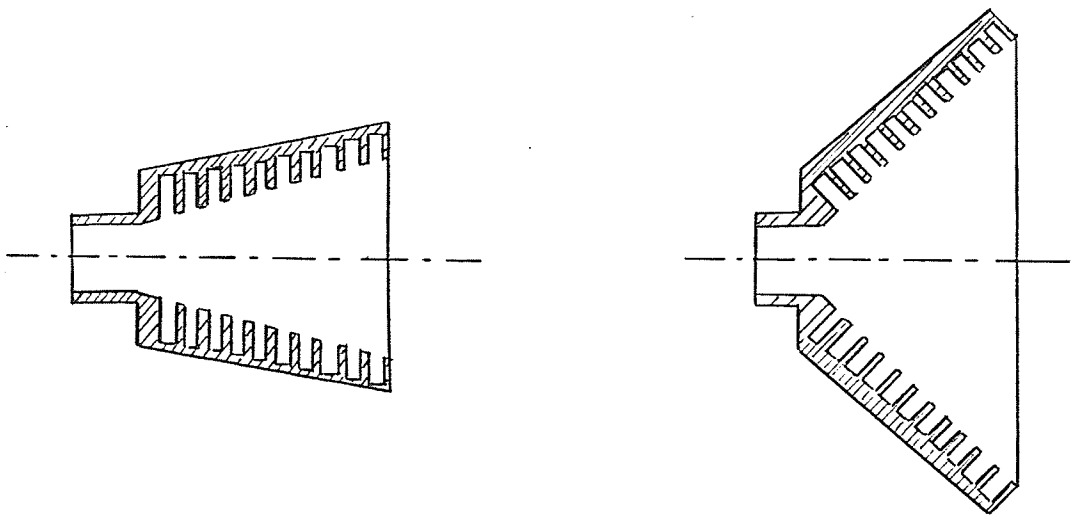

(a) (b)

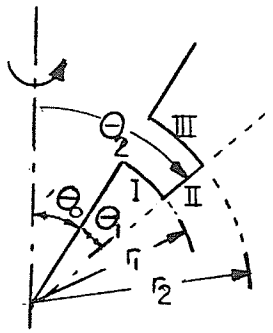

(c)

Fig. II.1. Corrugated Horns with corrugations:

(a) Perpendicular to horn axis.

(b) Perpendicular to horn walls.

(c) Deformed to fit spherical coordinate system.

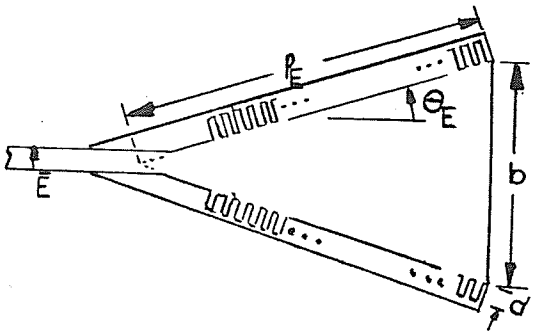

(a)

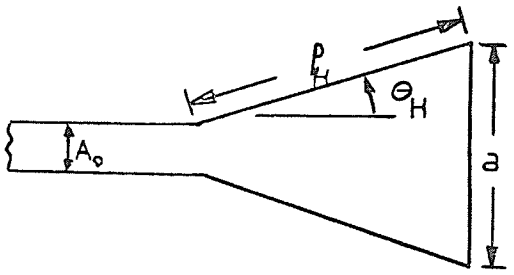

(b)

Fig. II.2. Terminology used for GTD analysis of pyramidal corrugated horns.

(a) Side view of the corrugated horn.

(b) Top view of the corrugated horn.

2.3.2 Horn with E-plane Magnetic Conducting Walls

A first approximation of the pyramidal corrugated horn shown in Figure (II.2) would be one with electrically conducting H-plane walls and magnetically conducting E-plane walls. This model, however, would fail to take into account the mixed boundary conditions resulting from the finiteness and the external walls of the horn which will be considered in the next section. For the magnetic conducting wall case, we need to consider the dual of (2.16) and (2.19a and b) with appropriate consideration to the fact that the E-plane edges now occupy different positions in space. Equations (2.19a and b) become

$$E_\theta^E = \eta\, H_\phi^E = \frac{-jk}{4\pi}\,\frac{e^{-jkR}}{R}\,\cos\phi\,(I_3+I_4) \tag{2.20a}$$

$$E_\phi^E = -\eta\, H_\theta^E = \frac{-jk}{4\pi}\,\frac{e^{-jkR}}{R}\,\sin\phi\,\cos\theta\,(I_3+I_4) \tag{2.20b}$$

where I_3 and I_4 are integrals involving the $\hat{y}$-directed equivalent currents on the H-plane edges at $x = \pm b/2$, and will be found in Appendix A. The use of (2.19) and (2.20) will give the far out side and backlobes for this approximate version of the pyramidal horn. Of course, the edge contributions will be included only for those regions of space at which the edge is visible.

2.3.3 Horn with E-plane Corrugated Walls

The model outlined in the preceding section would fail for radiation in the back direction since the finite depth of the corrugations require the walls to be rather thick. An approximate wedge model (Figure II.3) is used, therefore, to represent the E-plane walls with zero surface impedance on the end and on one side, and infinite capacitive reactance on the side of the resonant corrugations. The diffracted field of this model is found to be [34]

$$E_1^d = 1.55\ [K(\alpha)\ E_s(\alpha) + 2E_s(270^o) \cdot v_B(\alpha-90,\ d,\ 3/2)\ e^{jkd\ \sin\alpha}]\ \frac{e^{-jkr}}{r} \tag{2.21}$$

where $E_s(\alpha)$ is the slope diffracted field from the model in Figure (II.3b), and D_s is the slope diffraction coefficient. Expressions for $K(\alpha)$, $E_s(\alpha)$ and the function v_B are given in Appendix A.

The finite length of the E-plane horn edges may be taken into account by equivalent currents as previously formulated for the H-plane edges. In the E-plane ($\phi = 0$), the diffrated field from the E-plane edges will be [34]

$$E_\theta^E = \frac{-jk}{4\pi}\ \frac{e^{-jkR}}{R}\ (I_{3a}(\theta) + I_{4a}(\theta) + I_5(\theta) + I_6(\theta)) \tag{2.22}$$

where I_{3a} and I_{4a} are given by $3.1\ I_3$ and $3.1\ I_4$ while expressions for I_5 and I_6 will be found in Appendix A.

2.4 Special Techniques and Investigations

2.4.1 The Choked Waveguide Feed [39]

The structure of the choked waveguide feed is shown in Figure II.4. It is excited by the dominant TE_{11} mode in a smooth wall circular waveguide and possesses a finite number of short circuited annular slots in a perfectly conducting flange. This structure will be equivalent, therefore, to a corrugated conical horn of 90° flare semi-angle. If the flange is assumed to be infinite in extent then the total magnetic field at a point $\bar{r}$ in space can be written in terms of the electric field over the entire aperture plane as

$$\bar{H}(\bar{r}) = \frac{j}{2\pi\omega\mu_0}(k^2 + \nabla\nabla\cdot)(\hat{a}_z \times \int\int \bar{E}_A(\bar{r}')\Phi(\bar{r}|\bar{r}')\, ds') \sum \text{Apertures} \qquad (2.23)$$

$\bar{E}_A(\bar{r}')$ is the electric field over the aperture plane at source point $\bar{r}'$ and $\Phi(\bar{r}|\bar{r}')$ is the free space Green's function relating $\bar{r}$ to $\bar{r}'$. In practical cases, the slot depths range from $\lambda/4$ to $\lambda/2$ giving rise to a capacitive surface. Under these circumstances, the fields decay rapidly over the surface and it is of little consequence, therefore, whether the infinite flange is present or not.

The electric field $\bar{E}_A(\bar{r}')$ is zero everywhere except over the waveguide apertures. It can be expanded in terms of the normal modes in each waveguide region. The modal expansions

$$\bar{E}_A = \sum_i \sum_n B_n^{(i)} \bar{E}_n^{(i)} \quad \text{and} \quad \bar{H}_A = \sum_i \sum_n C_n^{(i)} \bar{H}_n^{(i)} \qquad (2.24)$$

are then employed in (2.23) to yield a system of simultaneous equations. Index i represents the summation over the number of apertures while n represents the summation over the number of modes. This set of equations can be solved by knowledge of the relationship of $B_n^{(i)}$ and $C_n^{(i)}$ to the complex reflection coefficient $R_n^{(i)}$ of the n'th mode in the i'th waveguide region. Once these coefficients are evaluated, equation (2.23) is then used again to compute the radiated field in the space $z \geq 0$. The result is:

$$E_\theta = j2\pi k \frac{e^{-jkr}}{r} \{I_x(\theta,\phi) \cos\phi + I_y(\theta,\phi) \sin\phi\} \tag{2.25}$$

$$E_\phi = j2\pi k \frac{e^{-jkr}}{r} \{- I_x(\theta,\phi) \sin\phi + I_y(\theta,\phi) \cos\phi\} \cos\theta \tag{2.26}$$

where

$$\bar{I}(\theta,\phi) = \frac{1}{(2\pi)^2} \sum_i \sum_n B_n^{(i)} \int_{\text{aperture } i} \int \bar{E}_n^{(i)}(x',y') \cdot e^{jk(x'\sin\theta \cos\phi + y'\sin\theta \sin\phi)} \, dx' \, dy' \tag{2.27}$$

$I_x(\theta,\phi)$ and $I_y(\theta,\phi)$ are the x and y components of $\bar{I}(\theta,\phi)$. In the case of a finite flange, the assumption is made that the field at the edge is given by (2.25) and (2.27) with $\theta = 90^\circ$. Standard GTD edge diffraction expressions are used with this incident field to predict the edge diffracted field. The total field is then given by the sum of the fields due to the aperture integrations and the edge diffractions.

2.4.2 Study of the Properties of Corrugated Surfaces for Corrugated Horn Design

In order to study the effects of varying the geometrical parameters of the corrugations, Mentzer and Peters [35, 36] used an integral equation of the magnetic type to find the scattered field and the surface currents associated with a groundplane-corrugated surface model as shown in Figure (II.5). This model was chosen for its similarity to one wall of a sectoral corrugated horn. In the horn, the illumination of the corrugations is by a cylindrical wave due to the diffraction at the horn-waveguide junction. In the model used, two magnetic line sources provide a similar cylindrical wave, while at the same time place a null in the far field in the direction of the adjacent edge of the groundplane. Since energy is forced off the corrugations, the fields over the corrugated surface need be matched only over those corrugations which have significant surface currents flowing on the walls. Thus the surface model used need not be closed, and the integral equation for the current J on the scatterer will be

$$J = - \left[H_z^i + \hat{a}_z \cdot \nabla \times \int J \, G \, d\bar{\ell}' \right]_{c^+} \tag{2.28}$$

where H_z^i is the incident magnetic field, $\hat{a}_z$ is a unit vector in the z direction, G is the two-dimensional Green's function and the integration is performed along the contour c^+ (just outside the contour c where the surface current J flows).

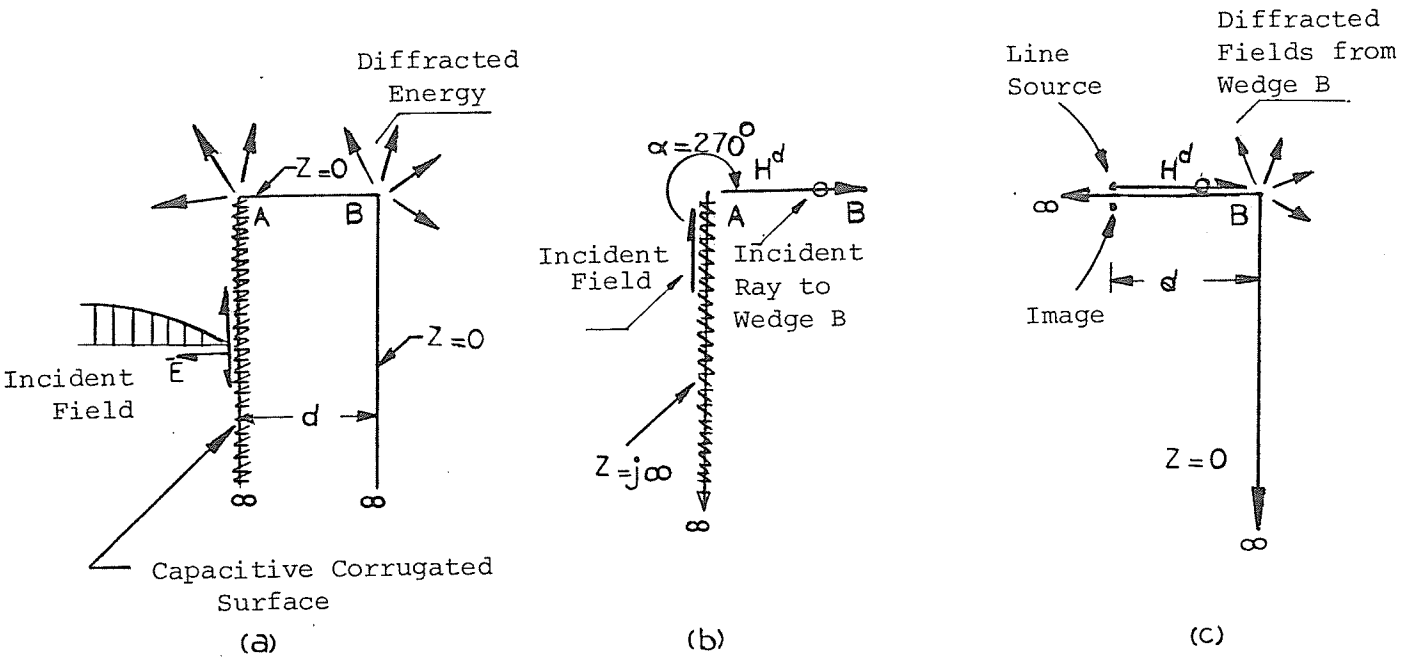

Fig. II.3. Thick Edge Model of Corrugated Horn E-Plane Wall.

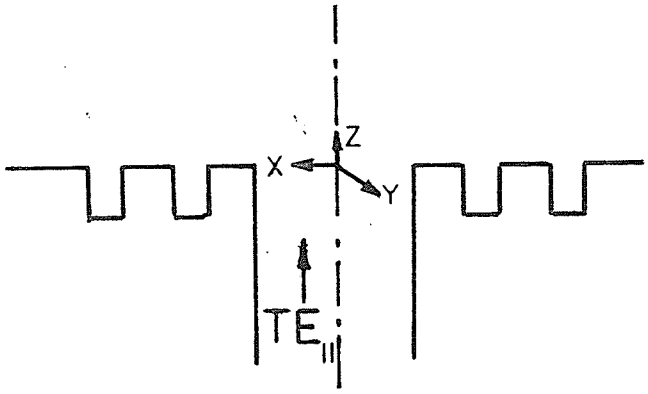

Fig. II.4. Choked Waveguide Feed.

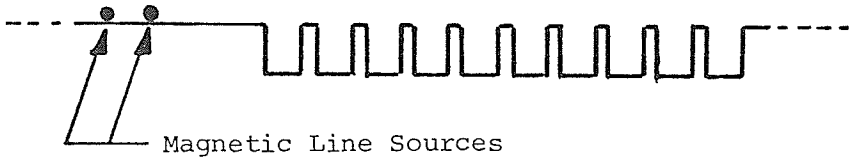

Fig. II.5. Scattering Model for Corrugated Horn Wall.

Equation (2.28) can be solved numerically using the moment method [23] . Once J is determined, the scattered field, power loss, etc. can all be evaluated using known formulae.

2.5 Conclusion

It becomes clear from the presentation of the preceding sections that previous analytical studies related to corrugated horns assume some simplifying approximations with respect to wall lengths or groove depths. This restricted the validity of these approaches to particular cases only. At the same time, numerical investigations made no attempt to reduce computer requirements in time and storage, and hence the possibility of their application to the problem of horn design was very limited.

In the next chapter we extend these investigations by studying the effectiveness of representing the corrugations by impedance surfaces to obtain the induced currents and the scattered fields. If this substitution is successful, numerical methods can then be applied to horns of practical sizes and would constitute a useful tool for corrugated horn design. Details of this study are presented in the following pages.

CHAPTER III

THE IMPEDANCE REPRESENTATION OF CORRUGATED SURFACES

3.1 Introduction

Ever-increasing needs for improved feed systems to be used in large radio astronomy and satellite tracking dishes have stimulated interest in the properties of corrugated horns which will reduce spill-over and cross-polarization losses and increase efficiency from the area of 50-60 percent to the level of 75-80 percent.

Previous analysis of such horns, however, have assumed approximations to the propagating modes in the axial region, wall length, slot depth and others, which greatly restricted the generality of the analysis, and accordingly, their usefulness for design purposes was limited.

The modal analysis as presented by Clarricoats and Saha [53], Jansen et al [54] and others, usually takes the form of a balanced hybrid mode that is valid when the corrugations are $\lambda/4$ in depth, or when the surface impedance is infinite, corresponding to a perfect magnetic conductor. This was the only possibility for the analysis to be consistent with the "separable-variable" assumption usually adopted in the analysis. In an attempt to generalize the solution for slot depths ranging from $\lambda/4$ to $\lambda/2$, Narasimhan [55] used a far field approximation in computing the aperture field after modifying the geometry of the corrugated boundary to coincide with a separable coordinate system.

Elliot and Hockam [56] used a Green's function technique applicable only to a 90° semiflare angle corrugated horn, which they represented as an open-ended waveguide with an annular slotted flange of infinite extent. On the other hand, the Geometrical Theory of Diffraction (GTD) form of analysis as carried by Mentzer et al [57] tends to give a physical insight into the process that prevents the uniform aperture distribution and makes it possible to evaluate the magnitude of the far out side and backlobes. This analysis, like the modal analysis, has assumed the surface impedance to be infinite.

It might appear therefore, that because of the restricted validity of the previous solutions, a numerical method could offer considerable advantages over the analytical procedures reported above. While this is true for many classes of problems, the numerical route offers no panacea. In principle, of course, one may employ the numerical procedure of Mentzer and Peters [58, 59] for solving the problem of an arbitrarily corrugated horn. Hence an integral equation for the currents on the horn walls can be formulated and solved using the moment method. However, the storage requirements on the computer, the execution time of the program and the numerical error in the solution tend to become excessive and even prohibitive for horns of moderate size when treated in such a manner. It can be easily realized, meanwhile that the obstacle in the numerical solution of the integral equation stems from the fact that the length of the contour tangent to the horn walls becomes excessively long when corrugations are considered. Two observations from the previous studies on this kind of radiator, however, deserve attention. First, many investigators

[54, 55] changed deliberately the shape of the corrugations in their theoretical analysis to make them coincide with separable coordinates. They also reported good agreement between their theoretical predictions and experimental results obtained using horns with corrugations cut perpendicularly, either to the horn wall or to the horn axis. Second, a careful study of the curves by Mentzer and Peters [58, 59] reveals that the scattering properties of the corrugated surface used for horns are not much dependent on the corrugation type. Hence, the scattered field by a corrugated surface model of the horn walls and the decay of the induced current on its surface, were almost unchanged when the resonant square-cut corrugations were substituted by resonant corrugations of the V-type (Figure III.1d) . Close similarity was also noticed for other values of slot depths. In addition, Mentzer and Peters came to the conclusion that the pattern of the V-corrugated horn will be "comparable" to the pattern of the square-corrugated one, provided the depth of the V-corrugations will now range from 0.3125λ to 0.625λ, in lieu of 0.25λ to 0.5λ in the case of the square-corrugations, for the respective surfaces to represent a capacitive reactance. If this is so, one can easily conclude that different corrugation types could be interchanged with the only precaution that they must present the same "conditions" to the electromagnetic field above the corrugated surface. Equivalently, any form of corrugations can be substituted with a proper "impedance surface". In this case, a square corrugated horn wall, for example with length L and N1 corrugations per wavelength, each of depth d, will be represented by an impedance surface of length L . When this is compared to the real

contour length around the corrugation namely (2xdxN1+1)xL, with typical values for d, N1 and L ranging from 0.25λ to 0.5λ, 4λ to 8λ and 2λ to 3λ respectively for a moderate size horn, the difference is indeed not trivial, ranging from 2λ to 8λ . A proper impedance surface will represent the corrugations in an integral equation formulation with a greatly reduced integration contour and without excessive requirements in computer time and storage. It is the purpose of the present chapter, therefore, to investigate the effectiveness of representing the corrugations by an impedance surface in the numerical solution of an electromagnetic scattering problem from a partially corrugated conducting prism (Figure III.1a) . The corrugated portion of the scatterer is represented by an impedance surface and the behaviour of the surface currents and the scattered fields are examined. The results will also be compared with available data on a similar problem [115].

3.2 The Scattering Surface

To apply the impedance boundary concept to study the corrugated surface properties used in electromagnetic horn design, the problem of scattering from a two-dimensional corrugated surface is considered. The geometry is a conducting rectangular prism, partially corrugated as shown in Figure (III.1a). The corrugations are then substituted with an impedance surface and the scatterer becomes as in Figure (III.1b). Mentzer and Peters studied a similar problem [58] where they have considered a conducting planar surface with corrugations only

on the right hand side of the plane along the positive x-axis and have solved the problem numerically (Figure III.1c) . For the excitation they have assumed two magnetic line sources, phased for a null in the back direction and located on the conducting plane along the negative x-axis. By utilizing the fact that the energy is usually forced off the corrugations, they have considered an open surface model and have formulated a matrix equation using the magnetic type integral equation [60] . This model was chosen for its similarity to one wall of a sectoral corrugated horn, where the corrugations are illuminated by a cylindrical wave due to the diffraction from the horn-waveguide junction. In the present investigation, the excitation is due to the same source configuration and hence we can compare our results with [58] . However, by representing the corrugations with an impedance surface, the geometry considered by Mentzer and Peters will shrink to an infinitely thin scatterer. In this case, the H-type integral equation which is used in the formulation of Mentzer and Peters become inappropriate, since it is known that this equation tends to lose its usefulness as the object becomes very thin. It is for this reason that a conducting rectangular prism with a partially corrugated surface as described above, is considered. Due to the finiteness of this geometry, it is expected that the calculated surface currents might demonstrate a standing wave character and yield non-zero radiation fields in the lower half-plane.

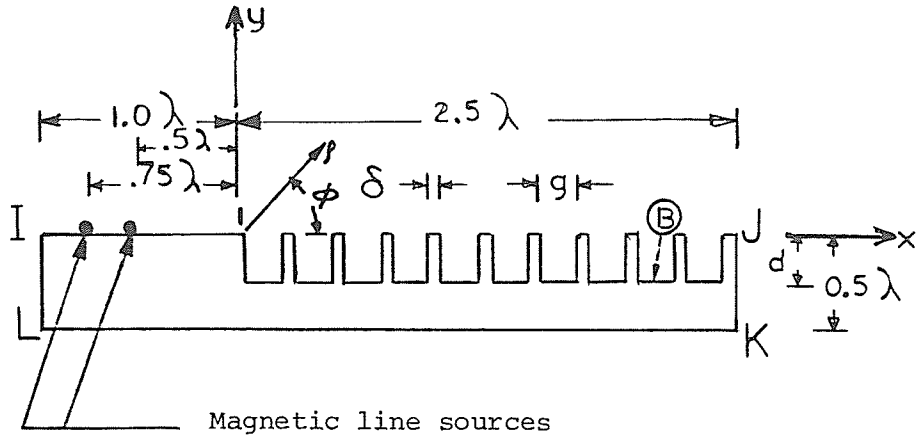

(a) Rectangular prism with corrugations.

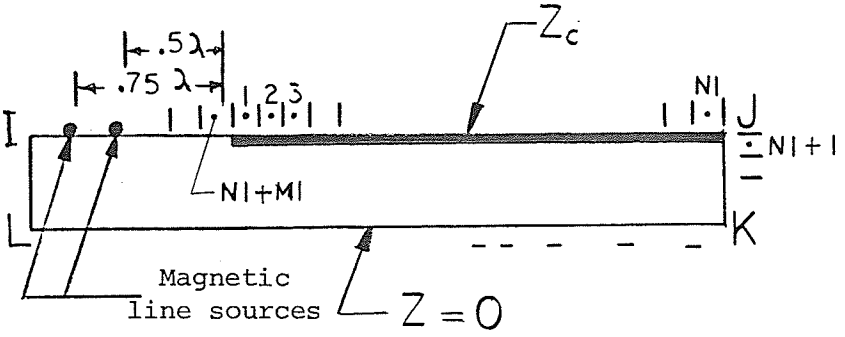

(b) Rectangular prism with corrugations replaced by an impedance surface.

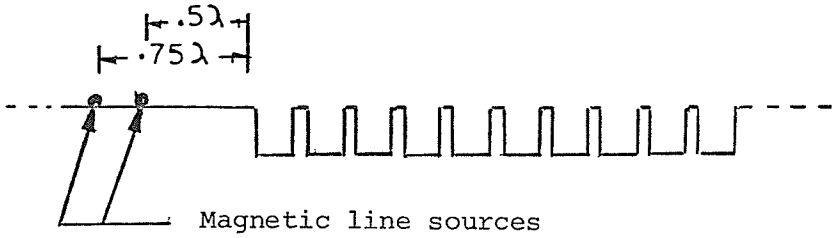

(c) Wall model with rectangular corrugations considered by Mentzer and Peters [35].

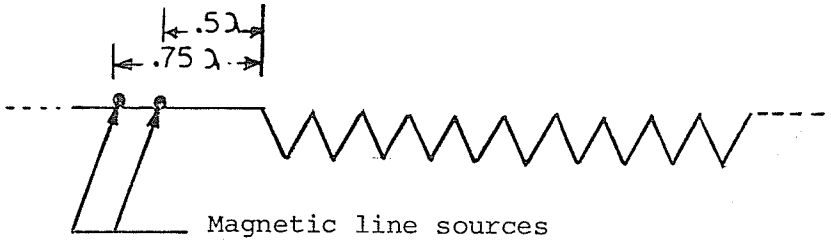

(d) Wall model with V-corrugations considered by Mentzer and Peters [36] .

Fig. III.1.

3.3 The Surface Current Integral Equation

When an electromagnetic wave with time variation $\exp(j\omega t)$ is normally incident on a scattering body with constant cross-section s along the z-direction (Figure III.2), both the total electric and magnetic fields are functions of the transverse coordinates only. For this case, the magnetic field integral equation (MFIE) [60] becomes completely uncoupled from the equation for the electric field. After some manipulations it takes the form:

$$\bar{H}(\bar{\rho}) = T\,\bar{H}^{inc}(\bar{\rho}) + T\,\frac{jk}{4}\oint_c \{\bar{H}(\bar{\rho}')H_1^{(2)}(k|\bar{\rho}-\bar{\rho}'|)\cos(\hat{n}',\bar{\rho}-\bar{\rho}') + (\frac{\partial \bar{H}}{\partial n'} - \hat{n}'\,\nabla_t'\cdot H_t)\,H_0^{(2)}(k|\bar{\rho}-\bar{\rho}'|)\}\,dc \qquad (3.1)$$

where $\bar{\rho}$ and $\bar{\rho}'$ represent the position vectors of the field and source points in the transverse plane, respectively, and $\hat{n}'$ is the unit outward normal to the scatterer. In general, primes will be used to indicate vector operations in source coordinates. Also a prime will be used to indicate a normal defined at a source point. $\bar{H}^{inc}$ is the incident magnetic field while $H_0^{(2)}$ and $H_1^{(2)}$ are the Hankel functions of the second kind of order zero and one respectively. $(\nabla_t'\cdot)$ is the divergence operator in a transverse plane and c is the linear integration contour around the cross-section s of the scatterer. k is the usual wave number while $\bar{H}_t$ and H_z denote the functional variation of the magnetic field in the transverse plane and the axial direction z, respectively. T is a constant with value 1 for $\bar{\rho}$ not on the surface, and assumes the value of

2 for $\bar{\rho}$ on a smooth portion of the surface. Also $\cos(\hat{n}', \bar{\rho}-\bar{\rho}')$ is the cosine of the angle between the normal and the vector connecting the observation and the source points in the transverse plane.

In our problem, the excitation is due to two magnetic line sources in the z-direction, and therefore we have only one component for $\bar{H}$, namely H_z. Accordingly $\nabla_t' \cdot \bar{H}_t = 0$ and $\frac{\partial H}{\partial n'} = \frac{\partial H_z}{\partial n'} \hat{a}_z$; $\hat{a}_z$ being a unit vector in the direction of increasing z. The presence of the normal derivative of H_z, however, is not desirable in the numerical solution of integral equations, since the approximation of a differential operator normally introduces excessive numerical errors [61]. Therefore we substitute $\frac{\partial H_z}{\partial n'}$, at the surface of the scatterer, in terms of the transverse component of the electric field E_c, tangent to the contour c (Appendix B), obtaining in this way

$$\frac{\partial H_z}{\partial n'} = j \frac{k}{\eta} E_c \qquad (3.2)$$

η being the free space wave impedance and is equal to 120π ohms. E_c is zero over the smooth parts of the scatterer but assumes non-vanishing values at places where it is transverse to the corrugations. Unlike the original equation (3.1), however, the final equation includes both the unknown electric and magnetic fields over the scatterer which are related to each other by the surface impedance. This impedance can be defined as

$$E_c = Z_c J_c \qquad (3.3)$$

where Z_c is the impedance value representing the corrugations on the smooth part of the prism, and J_c is the transverse current density at the surface of the scatterer. Substituting $J_c = H_z$ and making use of (3.3), equation (3.1) finally takes the form

$$H_z^{inc}(\bar{\rho}) = \frac{1}{2} J_c(\bar{\rho}) - \frac{j}{4} \oint_c J_c(\bar{\rho}') H_1^{(2)}(k|\bar{\rho}-\bar{\rho}'|) \cos(\hat{n}', \bar{\rho}-\bar{\rho}') \, dkc'$$

$$+ \frac{1}{4\eta} \oint_c Z_c(\bar{\rho}') J_c(\bar{\rho}') H_0^{(2)}(k|\bar{\rho}-\bar{\rho}'|) \, dkc' \qquad (3.4)$$

which is an integral equation of the second kind for the surface current J_c. It will be noted that because of the cosine term in the first integral, equation (3.4) becomes useless when the contour c degenerates into a straight line, and hence our choice of a prism instead of a plane surface model, with impedance boundaries, now becomes clearer.

3.4 The Impedance Representation

The geometrical parameters defining the corrugated surface are shown in Figure (III.1a). g and d denote respectively the slot width and depth, while the thickness of the teeth is given by δ. The impedance Z_c defined in (3.3) is the ratio E_c/H_z, and hence represents the wave impedance as seen looking into the corrugations. Within the slots of the corrugations, the parallel-plate transmission line mode exists and for air filled slots, the input impedance over their teeth is given

THE UNIVERSITY OF MANITOBA LIBRARIES

by $j\eta \tan kd$ [62] . Over the interval δ , however, the impedance is zero, and Z_c is then given by their average value

$$Z_c = j \frac{g}{g+\delta} \eta \tan (kd) \tag{3.5}$$

From a "transverse-resonance" consideration [63], the impedance looking into the corrugations should be equal to the negative of the wave impedance for the fields existing in the space above the corrugated surface. This can be checked by comparing (3.5) with the approximate value of the wave impedance given by Clarricoats and Saha [53] for corrugated circular horns.

3.5 Solution of the Integral Equation for the Surface Current

Upon substitution for the surface impedance Z_c from (3.5), the integral equation for the surface current J_c , can be solved numerically using the moment method [64] . The simplest procedure is to subdivide the contour c into small segments and use pulse function for basis. Subdivisions are numbered such that the leftmost segment on the impedance part will assume the number 1, and subsequent subdivisions are taken going clockwise around the scatterer. N1 and M1 are the total number of segments on the impedance and smooth parts of the contour, respectively. When the value of Z_c is not large, one can solve (3.4) directly for the current J_c . However, in the immediate vicinity of slot resonances, d is approximately $\lambda/4$ and Z_c approaches in-

finity, hence destroying the usefulness of the integral equation. In these cases, since E_c is finite over the corrugations, it may be more convenient to solve for J_c over the smooth part of the prism and the product $E_c = Z_c J_c$ over the impedance part. In this way, one can avoid possible numerical instability during the process of matrix inversion. When a point matching technique is finally adopted, one obtains the system of linear algebraic equations,

$$[C_{mn}]\ [U_n] \ = \ [D_m] \tag{3.6}$$

where $[C_{mn}]$ is a square coefficient matrix with elements C_{mn} given by:

$$C_{mn} = \begin{cases} 0.5\ Y_n & ; \quad \ldots\ m = n \le N1 \\ 0.5 & ; \quad \ldots\ m = n > N1 \\ Y_n \left\{ \frac{j}{4} H_1^{(2)}(k|\bar{\rho}_m - \bar{\rho}_n|)\ \cos\nu_{mn} + \frac{1}{4\eta} (Z_c)_n\ H_0^{(2)}(k|\bar{\rho}_m - \bar{\rho}_n|)\ (\Delta kc)_n \right\} ; & \\ & \ldots\ n \le N1, \text{ all } m\text{'s} \\ \frac{j}{4} H_1^{(2)}(k|\bar{\rho}_m - \bar{\rho}_n|)\ \cos\nu_{mn}\ (\Delta kc)_n \ ; \quad n > N1, \text{ all } m\text{'s} & \end{cases} \tag{3.7}$$

and with $\cos\nu_{mn} = \cos(\hat{n}', |\bar{\rho}_m - \bar{\rho}_n|)$.

$(Z_c)_n$ is the value of the surface impedance at the nth segment. Y_n=1 when solving for J_c over all the scatterer and equals $(Z_c)_n^{-1}$ when solving for J_c over the smooth portion and for E_c over the impedance

part. Also $(\Delta kc)_n$ is the length of the n'^{th} segment and subscripts m and n refer to the observation and source points respectively. The vector of unknowns $[U_n]$ is given by

$$[U_n] = \begin{bmatrix} (J_c)_1 \\ (J_c)_2 \\ \vdots \\ (J_c)_{N1} \\ (J_c)_{N1+1} \\ \vdots \\ (J_c)_{N1+M1} \end{bmatrix} \quad ; \text{ when } Y_n = 1 \qquad (3.8a)$$

and

$$[U_n] = \begin{bmatrix} (E_c)_1 \\ (E_c)_2 \\ (E_c)_{N1} \\ (J_c)_{N1+1} \\ (J_c)_{N1+2} \\ (J_c)_{N1+M1} \end{bmatrix} \quad ; \text{ when } Y_n = (Z_c)^{-1}_n \qquad (3.8b)$$

in which the subscript n in $(J_c)_n$ or $(E_c)_n$ refers to the n'th segment. The vector of constants in (3.6) is the incident magnetic field given by

$$D_m = (H_z^{inc})_m \tag{3.9}$$

and is calculated at the center of segment m. For the present problem, H_z^{inc} is due to the superposition of the fields from two magnetic line sources with values K_1 and K_2, and directed parallel to the z-axis at $\bar{\rho}_1'$ and $\bar{\rho}_2'$. The electric vector potential at a point $\bar{\rho}$ in the transverse plane due to this configuration is

$$F_z(\bar{\rho}) = \frac{K_1}{4j} H_0^{(2)}(k|\bar{\rho}-\bar{\rho}_1'|) + \frac{K_2}{4j} H_0^{(2)}(k|\bar{\rho}-\bar{\rho}_2'|) \tag{3.10}$$

Since there is no variation in the z-direction, H_z will then be given by

$$H_z(\bar{\rho}) = -j\omega\varepsilon F_z(\bar{\rho}) \tag{3.11}$$

Accordingly, the incident magnetic field will be

$$H_z^{inc}(\bar{\rho}) = \frac{-k}{4\eta}\{K_1 H_0^{(2)}(k|\bar{\rho}-\bar{\rho}_1'|) + K_2 H_0^{(2)}(k|\bar{\rho}-\bar{\rho}_2'|)\} \tag{3.12}$$

The two line sources are assigned the values $K_1 = 1e^{j0}$ and $K_2 = 1e^{j\pi/2}$, and are positioned on the negative x-axis at a distance of $\lambda/4$ apart.

A program from the "International Mathematical and Statistical Libraries (IMSL)", [65], is used to solve the matrix equation (3.6). The algorithm involved obtains the solution of the system of equations $CU = D$ by Crout's method [66] . Residuals are then evaluated and used in an iterative process to bring the solution accurate to machine precision. Double precision arithmetic is used to minimize round-off errors in the process of solving the matrix equation and hence, obtain an accurate estimate of the technique.

3.6 The Scattered Field

Since the scattered field $\bar{H}^{sc}$ at a point $\bar{\rho}$ is related to the incident field $\bar{H}^{inc}$ and the total field $\bar{H}$ at the same point through

$$\bar{H}^{sc}(\bar{\rho}) = \bar{H}(\bar{\rho}) - \bar{H}^{inc}(\bar{\rho}) \tag{3.13}$$

it is easily realized that the formula needed to compute the scattered field from the prism with impedance boundaries will be given by the right-hand-side of (3.1), after omitting the term with $\bar{H}^{inc}$ and making the substitution $T=1$. Considering the same arguments discussed above in deducing equation (3.4) from (3.1), one obtains the following expression for the scattered magnetic field at the point (ρ, ϕ) in the transverse plane

$$H_z^{sc}(\rho, \phi) = \frac{j}{4} \int_c J_c(\bar{\rho}') \cos\nu \, H_1^{(2)}(k|\bar{\rho}-\bar{\rho}'|) \, dkc'$$

$$- \frac{1}{4\eta} \int_c Z_c(\bar{\rho}') \, J_c(\bar{\rho}') \, H_0^{(2)}(k|\bar{\rho}-\bar{\rho}'|) \, dkc' \qquad (3.14)$$

We use ρ' and ϕ' to denote the cylindrical transverse coordinates for a point on the scatterer and the integration is carried around the contour c. $\cos\nu$ can be computed from

$$\cos\nu = \frac{(\bar{\rho}-\bar{\rho}') \cdot \hat{n}'}{|\bar{\rho}-\bar{\rho}'|} \qquad (3.15)$$

where, $\hat{n}'$ is the outward normal to the scatterer as mentioned before. In evaluating the scattered field at far distances using (3.14), we let ρ tend to infinity and substitute for the Hankel functions by their asymptotic forms, namely [67]

$$H_0^{(2)}(k|\bar{\rho}-\bar{\rho}'|) \xrightarrow[\rho \to \infty]{} \sqrt{\frac{2j}{\pi k\rho}} \, e^{-jk\rho} \, e^{jk\rho'\cos(\phi-\phi')} \qquad (3.16)$$

and

$$H_1^{(2)}(k|\bar{\rho}-\bar{\rho}'|) \xrightarrow[\rho \to \infty]{} \sqrt{\frac{2j}{\pi k\rho}} \, j \, e^{-jk\rho} \, e^{jk\rho'\cos(\phi-\phi')} \qquad (3.17)$$

Then using the solution for the current $J_c(\bar{\rho}')$ as obtained from the solution of (3.6) at the discrete points $\bar{\rho}_n$, one finally obtains for the scattered field

$$H_z^{sc}(\rho, \phi) =$$

$$\sqrt{\frac{j}{8\pi k\rho}}\, e^{-jk\rho} \left\{ \sum_{n=1}^{N1} \left[\frac{-1}{\eta} (Z_c)_n (J_c)_n + (J_c)_n \frac{(\bar{\rho}_n - \bar{\rho})\cdot\hat{n}'}{|\bar{\rho}_n - \bar{\rho}|} \right] \cdot \right.$$

$$\cdot\, e^{jk\rho_n \cos(\phi_n - \phi)}\, (\Delta kc)_n$$

$$\left. + \sum_{n=N1+1}^{N1+M1} \left[(J_c)_n \frac{(\bar{\rho}_n - \bar{\rho})\cdot\hat{n}}{|\bar{\rho}_n - \bar{\rho}|}\, e^{jk\rho_n \cos(\phi_n - \phi)}\, (\Delta kc)_n \right] \right\} \qquad (3.18)$$

Again, it is easy to show that when ρ tends to infinity, the term $\frac{(\bar{\rho}_n - \bar{\rho})\cdot\hat{n}'}{|\bar{\rho}_n - \bar{\rho}|}$ will assume the value $\sin\phi'$, $\cos\phi'$, $-\sin\phi'$ or $-\cos\phi'$ depending whether $\bar{\rho}_n$ lies on the sides IJ, JK, KL or LI, of the prism, respectively.

3.7 Numerical Results

The efficiency of using the integral equation formulation as derived above in the study of the corrugated surface properties used in corrugated horn design is investigated in this section by applying it to the scattering from a prism with impedance boundaries. First, Figures (III.3) to (III.5) compare our results for the currents with those of Mentzer and Peters [58] who considered an open surface model for the corrugated wall. Currents plotted are the ratio of the currents at the bottom of the corrugations (similar to point B in Figure (III.1a) to those at a point A located on the upper part of a non-corrugated prism and having the same x-coordinate as point B. Currents at B are obtained by

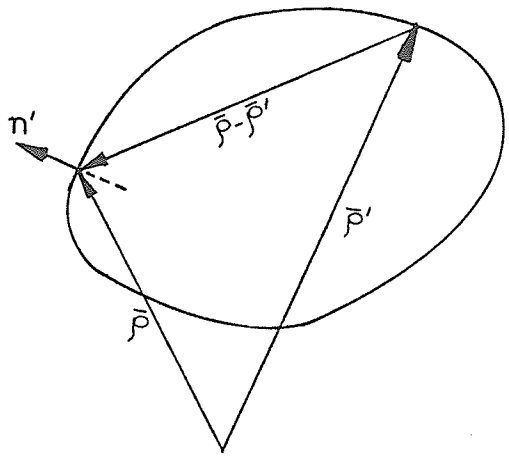

Fig. III.2. Cross-section of Scattering Cylinder.

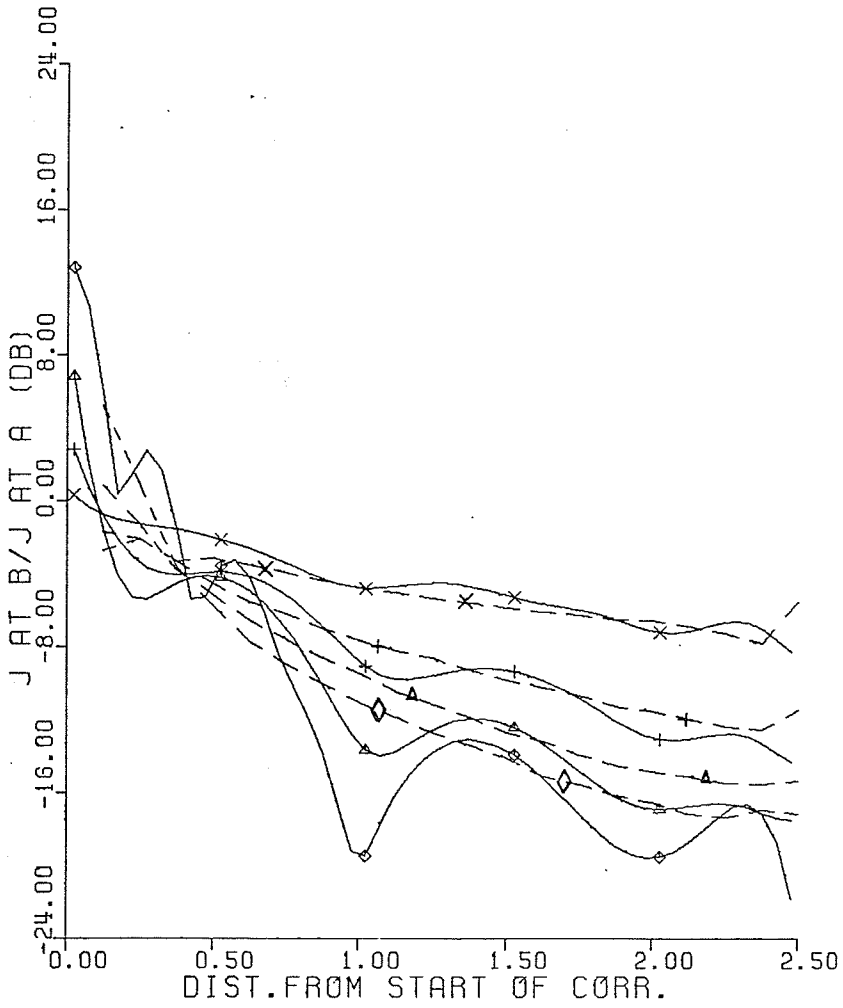

Fig. III.3. Current distribution over corrugated surface; $\frac{g}{g+\delta} = 0.9$.

x $d/\lambda = 0.4375$ Δ $d/\lambda = 0.3125$

\+ $= 0.315$ ----- Corresponding curves by Mentzer and Peters [58].

◊ $= 0.25$

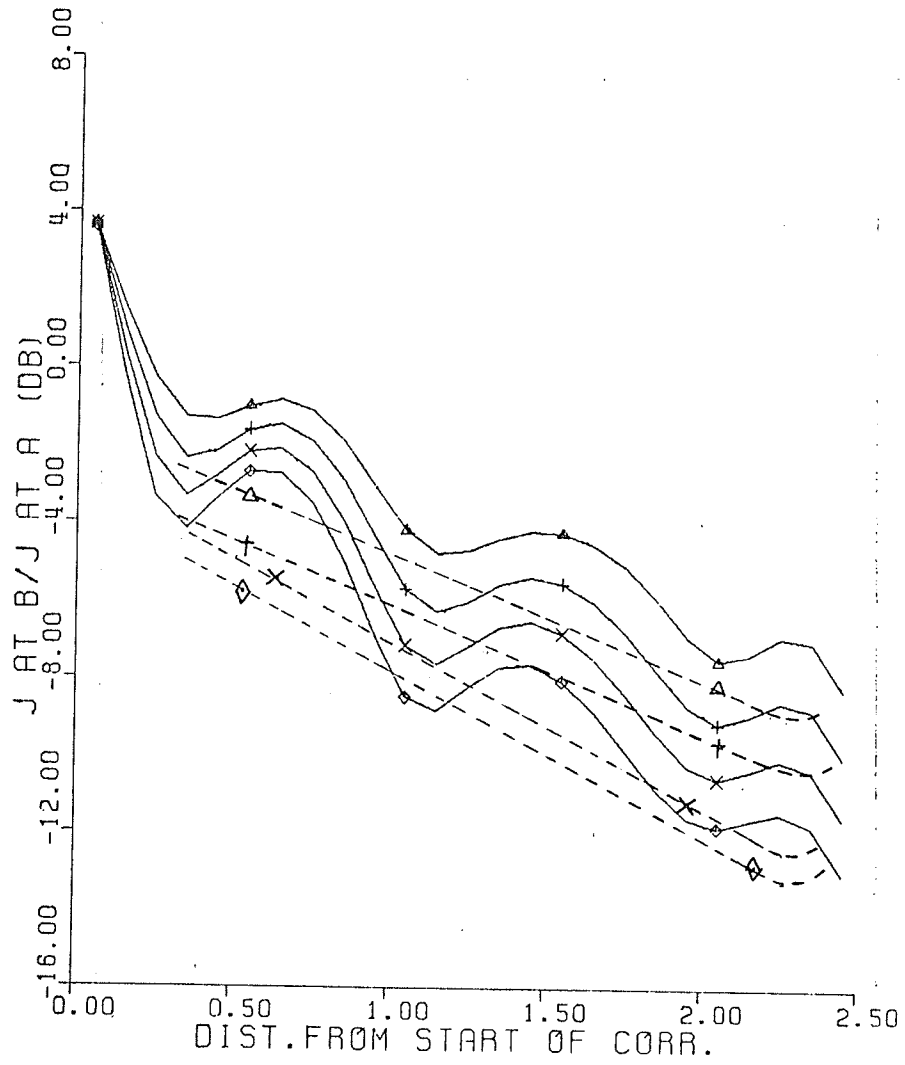

Fig. III.4. Current distribution over the corrugated surface ; $d/\lambda = 0.375$.
Δ $g/(g+\delta)$ = 0.5
\+ = 0.6
x = 0.7
◊ = 0.8
---- Corresponding curves by Mentzer and Peters [58].

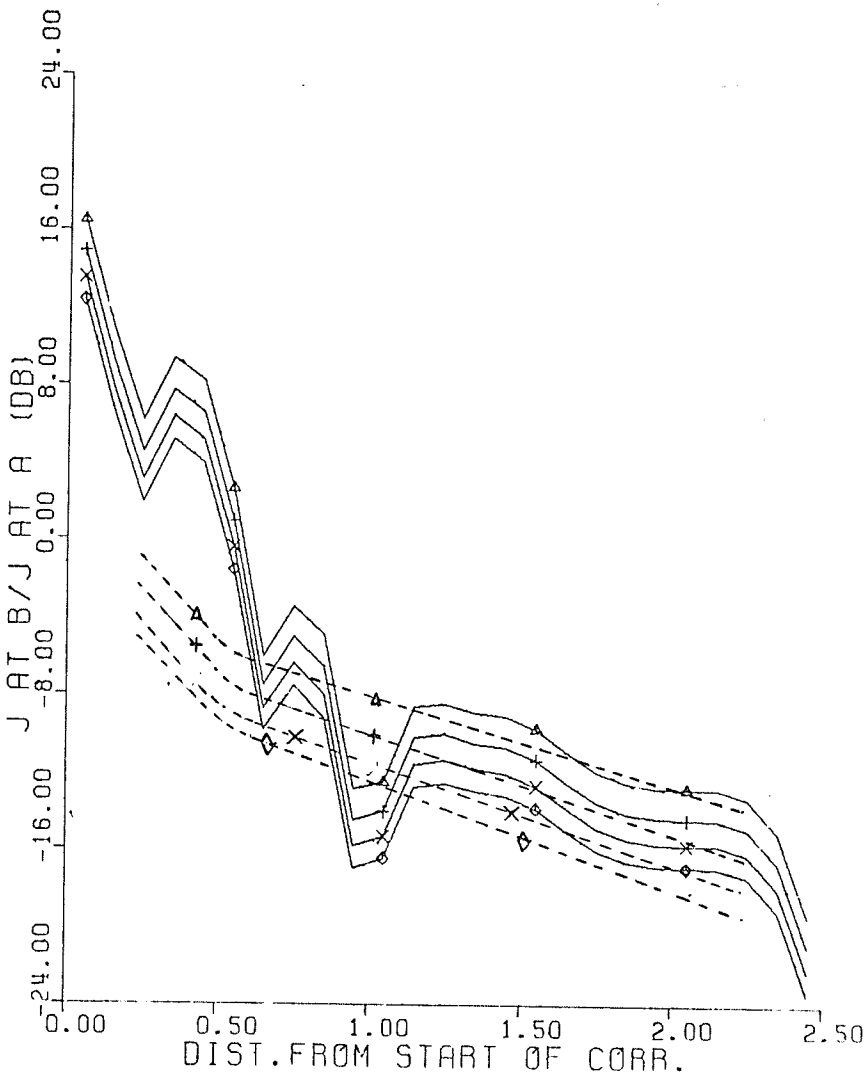

Fig. III.5. Current distribution over the corrugated surface ; $d/\lambda = 0.251$.
Δ $g/(g+\delta)$ = 0.5
\+ = 0.6
x = 0.7
◊ = 0.8

transferring the solution on the impedance part (J_c) to the bottom of the corrugation (with coordinate y) using the equation

$$|J_B| = |J_C| \; / \; \cos(kd) \tag{3.19}$$

Use of equation (3.19) is justified by the fact that only the TEM mode exists in the corrugation; higher order modes being negligible.

It is noticed that standing wave characters are more pronounced in our results due to the finite transverse dimensions of the prism. It is also noted that our calculated values for the currents are slightly higher, but this is attributed to the fact that the section of the prism covered with an impedance surface is much shorter than the corrugated part in [58] . The rate of decay of these currents, however, is approximately the same.

Radiation patterns are also compared in Figure (III.6), where we have included results from [58] and [59] only for the cases of resonant square-shaped and V-shaped corrugations. Except for a small tilt of 2°-3° in the main lobe towards the corrugated surface, Mentzer's scattering patterns were almost identical to ours. One should note in particular how the patterns for both resonant corrugation shapes agree well with our single calculations obtained by setting $Z_c = \infty$. The same kind of agreement was always noticed for other corrugations and the corresponding impedance surfaces. Considering the differences in the two models, one would expect some mismatch between the two solutions.

Any discrepancy, however, lies within acceptable limits, and satisfactory agreement, therefore, is believed to be reached through the use of the impedance boundaries in the representation of the corrugated surfaces.

Figure (III.7) shows an important aspect in the accuracy of the technique. Here the slot depths were assigned values of 0.251λ, 0.2501λ, 0.25001λ and 0.250001λ. For a real horn, of course, these changes in d/λ should not result in any change in performance. The value of Z_c as computed from (3.5) for these slot depths, however, change in the ratio of $1 : 10 : 100 : 1000$ because of the large slope of the tangent function at angles near $\pi/2$. On the other hand, the integral equation should be insensitive to such a variation for the results to be reliable. When the corresponding values of Z_c were used in (3.6), identical results were obtained. This agrees with the real situation and establishes at the same time the validity of the integral equation in this range of slot resonance. Furthermore, it became clear at this point that the separation of the solution into two cases, one for small and moderate values of Z_c, and the other for large values of Z_c was completely unnecessary, since both formulae given in (3.7) and (3.8), {with $Y_n=1$ and $Y_n=(Z_c)_n^{-1}$} gave exactly the same results up to the largest value of Z_c considered in the investigation.

Figure (III.6) also demonstrates the capability of the impedance surfaces in launching the electromagnetic energy into a well defined lobe away from the scattering boundaries. While the corrugations are more

effective for this purpose when they are nearer to slot resonance ($Z_c = \infty$), the case of zero impedance (smooth conductor) is clearly seen to be influenced by the fields diffracted at the edges of the prism. These fields add vectorially to the fields of the magnetic line sources and hence create an interference process resulting in a comparatively poor radiation pattern. The same results can also be deduced from Figure (III.8), where the impedance values have been increased in large steps by changing d/λ . Figure (III.9) shows the current decay over the impedance part for those values of slot depths. It can be realized that faster decay is associated with larger values of capacitive impedance which become therefore, reluctant to support any electromagnetic wave at grazing incidence, and consequently, eliminating the possibility of edge diffraction. Figures (III.10 and III.11) show the effect of changing the ratio $g/(g+\delta)$ at two different slot depths. For $d/\lambda = 0.375$, increasing this ratio will be accompanied by a corresponding increase in the surface impedance, and hence would drive the electromagnetic energy away from the metallic surface. The same increments, however, might not have any effect on the radiation characteristics when the corrugations are operated near slot resonance since the value of $\tan kd$ is almost infinity in this case.

Much useful information for corrugated horn design is readily available from the results just displayed above. First we note that since the corrugation density factor does not appear in the expression

for the surface impedance Z_c, then it is not expected that the electromagnetic performance of a horn employing corrugated walls will be dependent on the number of slots per wavelength as long as a reasonable density (4 to 8 slots per wavelength) is maintained. Furthermore, it was noticed that the most rapid current decay occurs for $Z_c = \infty$, and that, for any impedance value, the onset of the corrugations will carry high currents. Now, since the losses on a portion of a corrugated surface with resistivity R_s, contour length ℓ, and carrying a current J_c will be proportional to $\{R_s \int_0^{\ell} |J_c|^2 d\ell\}$, it is easy to conclude that most of the energy loss occurs at the start of the corrugations. Since J_c is hard to control, then either R_s or ℓ or both, should be modified to minimize the power loss in the first few corrugations. Special treatment of this area, such as silver coating, will reduce R_s, and consequently the power loss. Reducing ℓ, however, without changing the electromagnetic performance can be accomplished either by lowering the density of corrugations, or by using other corrugation shapes, which can offer the same impedance. Note also that if resonant corrugations are used, then accurate surface finishing after the first few corrugations is not necessary, since J_c is already negligible in this area.

The appreciable amount of electromagnetic radiation in the backward direction as noticed in Figure (III.8) deserves some comments. First we note that the shielding effectiveness of the corrugations was observed through the deviation of the main diffraction beam at an angle which is less than 90° from the corrugated surface. Furthermore, the ex-

citation was phased for a null at $\theta=180^{o}$. This leads to the conclusion that any backward radiation is due mainly to the sudden change of the impedance value at the onset of the corrugations. This of course will be more pronounced at slot resonance as Figures (III.6 and III.8) reveal. The large increase of the current (Figure III.9) at the start of the corrugations which is very clear for the case of $Z_c = \infty$, is also due to the same reason. Since the impedance of a horn is related to the magnitude of the wave reflected back toward the source, it is clear that introducing the corrugations on the horn walls will result in a poor VSWR, in particular if the corrugation slots were resonant. For a proper horn design, therefore, one should increase the wall impedance gradually from zero at the horn-waveguide junction, to the final value assumed near the horn aperture. This, of course, can be accomplished in more than one way. Hence, any corrugation shape with the desired impedance taper, can be cut near the throat of the horn. Simple shapes would be preferable for this purpose as this would be the most difficult part to handle during manufacturing. If, however, the shape of the corrugations is to be preserved all through, one could then change any of the geometrical factors to achieve the same goal. In the case of square corrugations for example, changing the ratio $g/(g+\delta)$ for the first few corrugations would be a possible solution. If the corrugated surface was designed, however, to work at its resonant mode, this method will be ineffective as discussed before in connection with Figure (III.7) . In this case, the corrugation depths should be used to control the impedance taper. Finally, the insertion of dielectrics with different permittivities will give the same

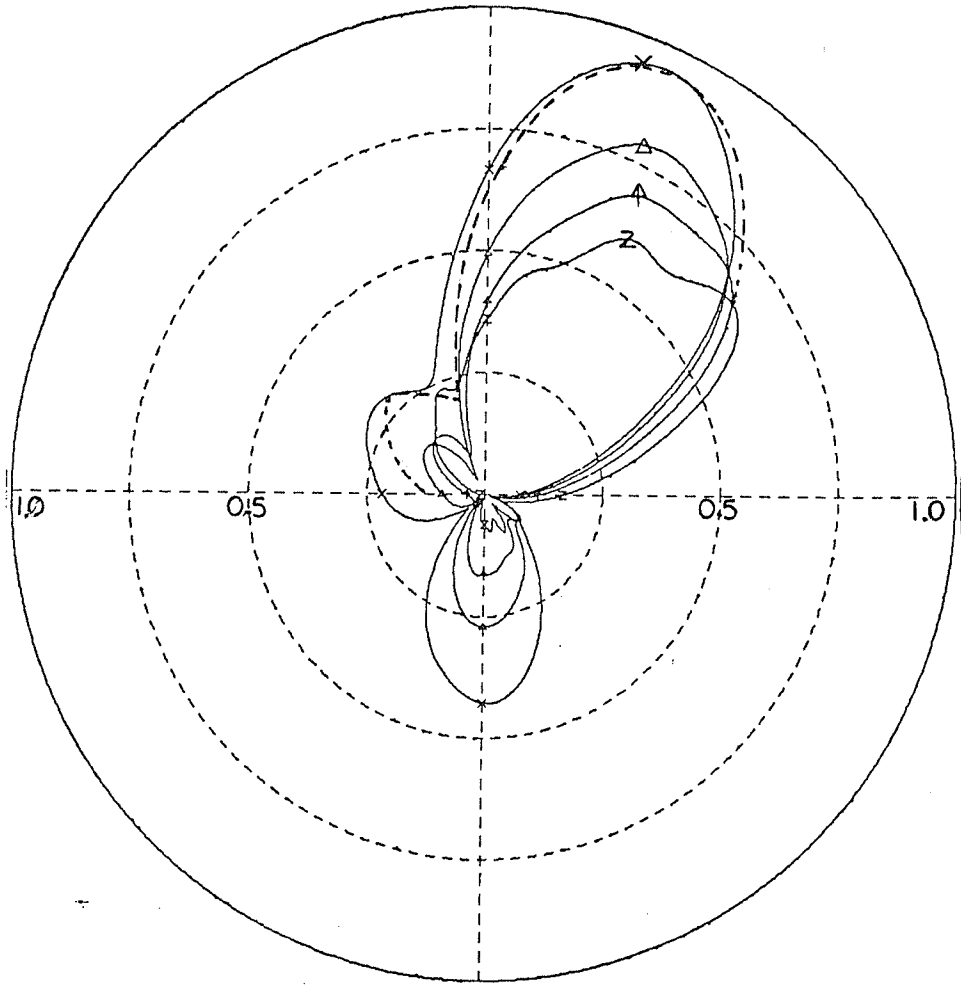

Fig. III.6. Total Radiation Pattern; $g/(g+\delta) = 0.9$.
x d/λ = 0.251
Δ = 0.3125
⇑ = 0.375
z = 0.4375
---- Mentzer and Peters, Resonant slots.

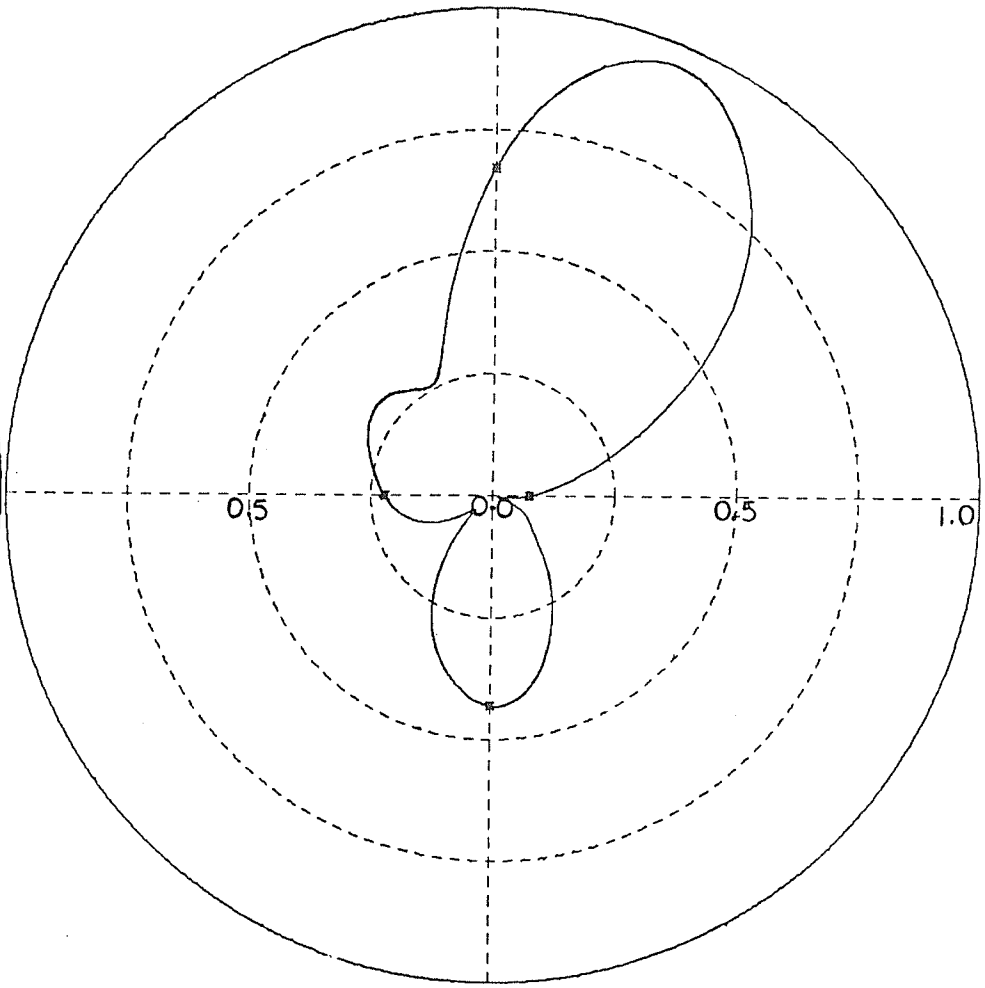

Fig. III.7. Total Radiation Pattern; $g/(g+\delta) = 0.9$.
d/λ = 0.251; 0.2501; 0.25001; 0.250001.

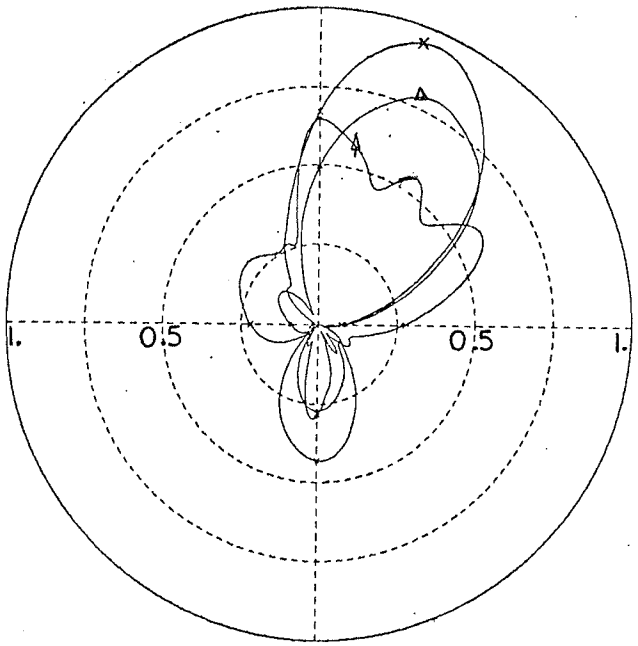

Fig. III.8. Total Radiation Pattern; $\frac{g}{g+\delta} = 0.85$.

x $d/\lambda = 0.251$
Δ $= 0.313$
4 $= 0.5$

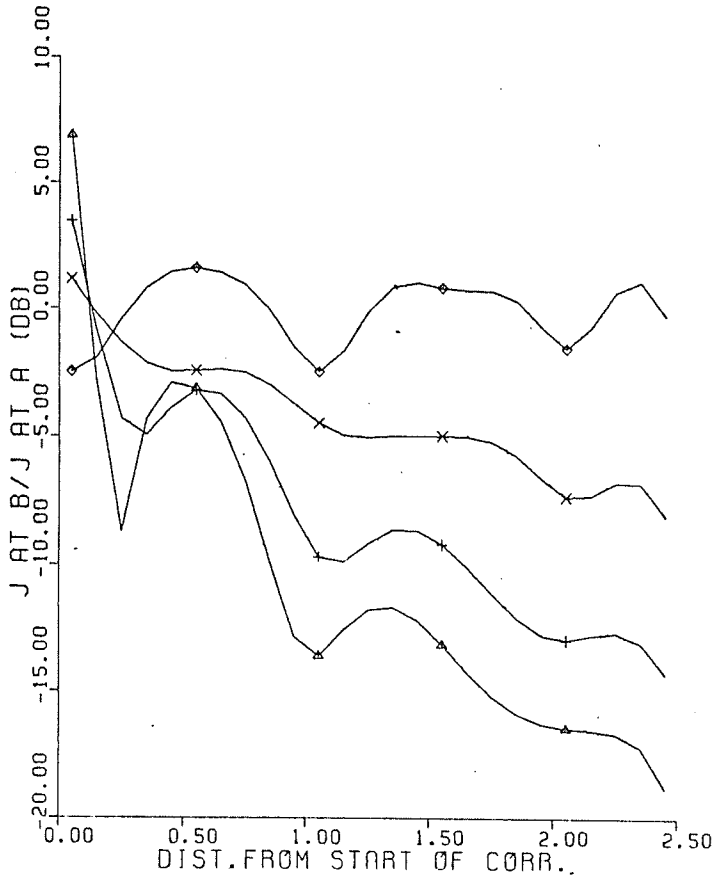

Fig. III.9. Current distribution over the corrugated surface, $\frac{g}{g+\delta} = 0.85$.

◊ $d/\lambda = 0.5$
x $= 0.437$
+ $= 0.375$
Δ $= 0.313$

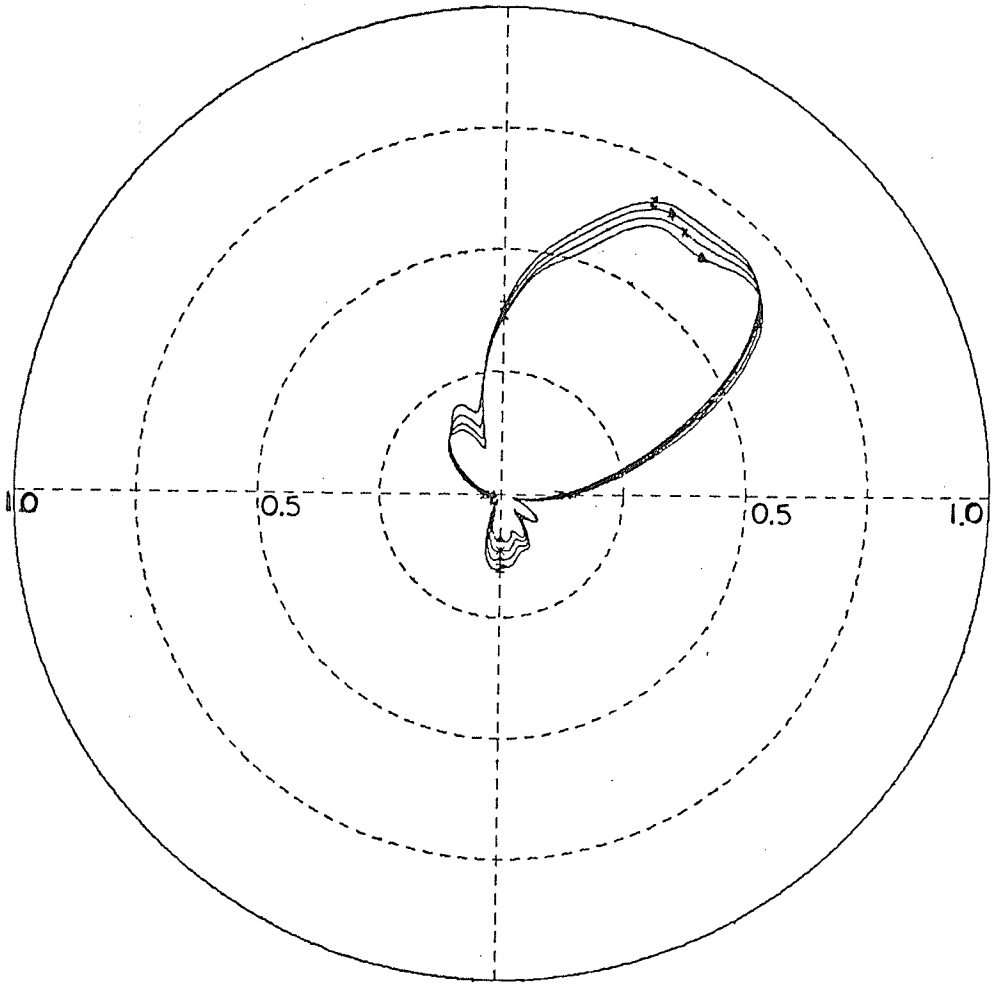

Fig. III.10. Total Radiation Pattern; $d/\lambda = 0.375$.
Δ $g/(g+\delta) = 0.5$
x $= 0.6$
◊ $= 0.7$
z $= 0.8$

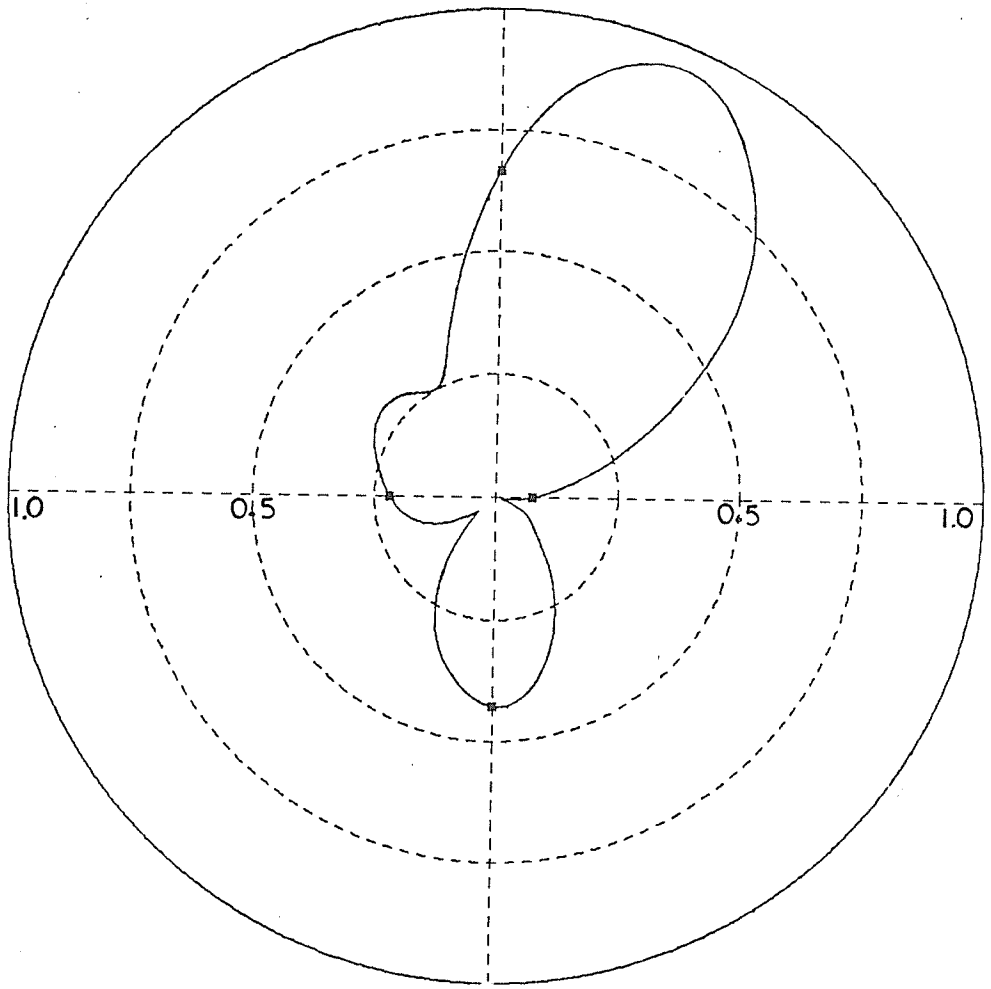

Fig. III.11. Total Radiation Pattern; $d/\lambda = 0.251$.

$\frac{g}{g+\delta} = 0.5$; 0.6 ; 0.7 ; 0.8.

result and might be applied in the use of uniform corrugations.

Now that the integral equation model using impedance boundary conditions has been demonstrated to produce valid design informations, other types of corrugated geometries could then be evaluated using the same technique with a reasonable degree of confidence. The extension of this study to apply to the case of an E-plane dihedral horn is carried next.

3.8 The E-plane Dihedral Horn [116]

The main problem usually faced with non-corrugated E-plane dihedral horns is the high level of undesirable radiation at the sides and the back of the horn. This is due to the strong illumination of the horn edges in the E-plane, which in turn results in high diffraction effects. Introducing proper corrugations parallel to the edges, however, will cause the fast decay of the electromagnetic fields propagating along the horn walls. When arriving at the aperture edges, these fields are too weak to produce any edge diffraction effects. The electromagnetic energy which has been diffracted away from the corrugated surface, however, propagates at an angle which is mainly dependent upon the impedance offered by the corrugations, and increases for large values of capacitive reactances (Figure III.6). It might happen therefore in some cases, that this wave will hit the opposite aperture edge, which is also illuminated by the rays diffracted at the horn-waveguide junction and those from the

onset of the corrugations. Hence, unless careful corrugation design is selected, along with a proper value of horn flare angle, the aperture edges might still be illuminated even stronger than the case of no corrugation, though by a different process, resulting in a radiation pattern which can be worse than that of a plain horn. As for the diffraction from the edge at the horn-waveguide junction, this can be minimized by using a proper curved transition. An adequate curvature for this purpose can be determined from the solution of the integral equation similar to the one discussed below.

The formulation of the preceding section for the scattering of electromagnetic energy from cylindrical bodies with anisotropic boundary conditions can be used for the determination of a proper combination of junction curvature, horn flare angle, and corrugation parameters and taper for the design of an E-plane dihedral horn with some desirable electromagnetic characteristics. Since the excitation of the horn in the E-plane can be represented by the field incident from a magnetic current filament parallel to the aperture edges and located on the axis of symmetry (Figure III-12), equation (3.4) therefore is directly applicable. The contour of integration c, however, will be as shown in Figure (III.12), which also shows the procedure for numbering the segments in preparation for a moment method of solution. The total number of subdivisions is 2xL1, which includes M1 segments over the corrugated part on each side of the horn. The appropriate matrix equation for the present case, when pulse functions are used in the expansion of the unknown surface currents,

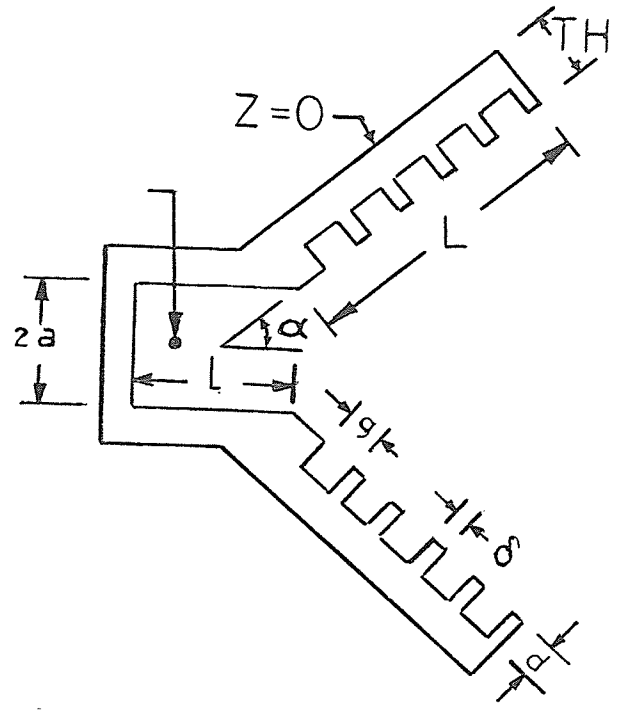

(a) The E-Plane Dihedral Horn.

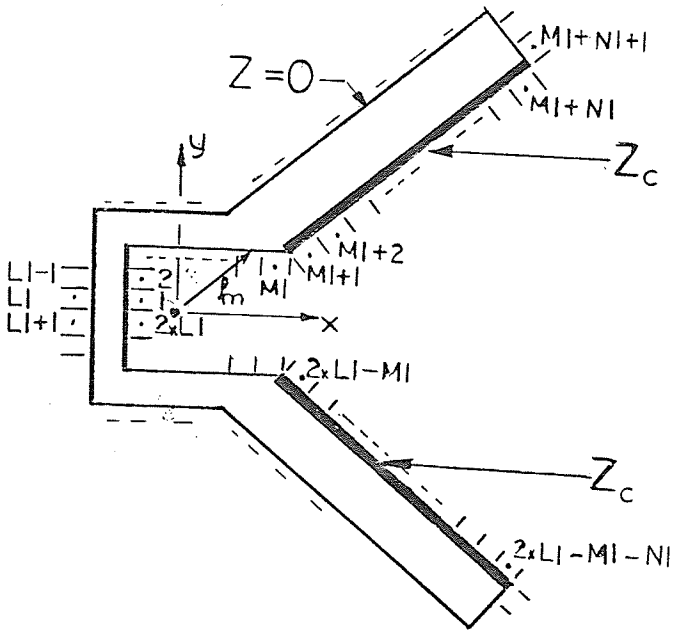

(b) Equivalent scatterer with surface impedance.

Fig. III.12.

and point matching procedure is applied for testing, will again be of the form,

$$[C_{mn}][U_n] = [D_m] \tag{3.20}$$

where D is a vector of length $2xL1$ representing the field incident from the magnetic line source of unit magnitude and zero phase. Assuming that the line source is located at the origin of the coordinates, then the m'th element of $[D_m]$ will be given by

$$D_m = \frac{-k}{4\eta} H_0^{(2)}(k\rho_m) \tag{3.21}$$

where ρ_m is the radial coordinate for the centre of segment m.

$[U_n]$ is the vector representing the unknown current coefficients, and

$[C_{mn}]$ is a $(2xL1) \times (2xL1)$ coefficient matrix with elements:

$$C_{mn} = \begin{cases} 0.5 & ; \quad \ldots \quad m=n \\ [\frac{j}{4} H_1^{(2)}(k|\bar{\rho}_m - \bar{\rho}_n|) \cos\nu_{mn} + \frac{1}{4\eta} (Z_c)_n H_0^{(2)}(k|\bar{\rho}_m - \bar{\rho}_n|)] (\Delta kc)_n & ; \\ \qquad \text{for } M1 + 1 \le n \le M1 + N1 & \\ \qquad \text{and } (2xL1) + 1 - (M1 + N1) \le n \le (2xL1) - M1 & \\ \frac{j}{4} H_1^{(2)}(k|\bar{\rho}_m - \bar{\rho}_n|) \cos\nu_{mn} & ; \quad \ldots \quad \text{otherwise} \end{cases} \tag{3.22}$$

where $\cos\nu_{mn}$ is given in (3.7), and $(Z_c)_n$ is that of (3.5). ρ, ρ', $\cos\nu$ have the same interpretations as before.

Equation (3.20) as it stands, might need more computer storage and CPU time for inversion than is really necessary. One can make use of the symmetry properties of the geometry and the excitation to reduce the computer requirements for core and time. Hence, from Figure (III.12), it is clear that two points on the contour c of the horn, symmetrically located with respect to the x-axis, will have exactly the same value for both the incident field and the surface current. Using the segment numbering shown in Figure (III.12b), it might be easily deduced that

$$D_i = D_{(2xL1)+1-i} \tag{3.23}$$

and

$$U_i = U_{(2xL1)+1-i} \tag{3.24}$$

Using (3.22) and (3.23) in (3.19), one obtains a new matrix equation, namely

$$[C'_{mn}][U'_n] = [D'_m] \tag{3.25}$$

where $[U'_n]$ and $[D'_m]$ are now vectors with L1 elements each, and $[C'_{mn}]$ is an L1xL1 square matrix. Solution for $[U_n]$ gives the surface current on one side of the horn. The matrix elements will now be given by

$$U'_m = U_m \quad ; \quad D'_m = D_m \quad ; \quad m = 1,2,3, \ldots L1 \tag{3.26}$$

and

$$C'_{mn} = C_{mn} + C_{m,(2xL1+1-n)} \quad ; \quad m=1,2,3, \ldots L1; \quad n=1,2,3, \ldots L1 \tag{3.27}$$

The new coefficient matrix $[C'_{mn}]$ now is stored in a space which is only 1/4 of that needed for the original matrix $[C_{mn}]$ of (3.20). In addition, since the number of columns and rows has been reduced to 1/2 each, the total inversion time is reduced to 1/8 of its original value [64]. The total radiated field at a point (ρ, ϕ) is obtained as the sum of the incident field plus the scattered field. Hence we have

$$H^{tot}(\rho,\phi) = \frac{-k}{4\eta} H_0^{(2)}(k\rho) + H^{sc}(\rho,\phi) \tag{3.28}$$

where $H^{sc}(\rho,\phi)$ is again given by (3.18). However the first summation in (3.18) is now applied for n=1 to M1, (M1+N1+1) to ((2xL1)-M1-N1) and from ((2xL1)-M1+1) to (2xL1). On the other hand, the second summation applies for n=(M1+1) to (M1+N1) and from ((2xL1)+1-(M1+N1)) to ((2xL1)-M1) .

Equation (3.25) was programmed on a digital computer and was solved for different horn designs. The horns radiation patterns were then evaluated using (3.28). Figure (III.13) shows how a matching combination of corrugation parameters (as for example in the case of $d/\lambda = 0.33$) and flare angle might result in an enhanced performance of the E-plane horn, with lower side and backlobes and higher gain in the forward direc-

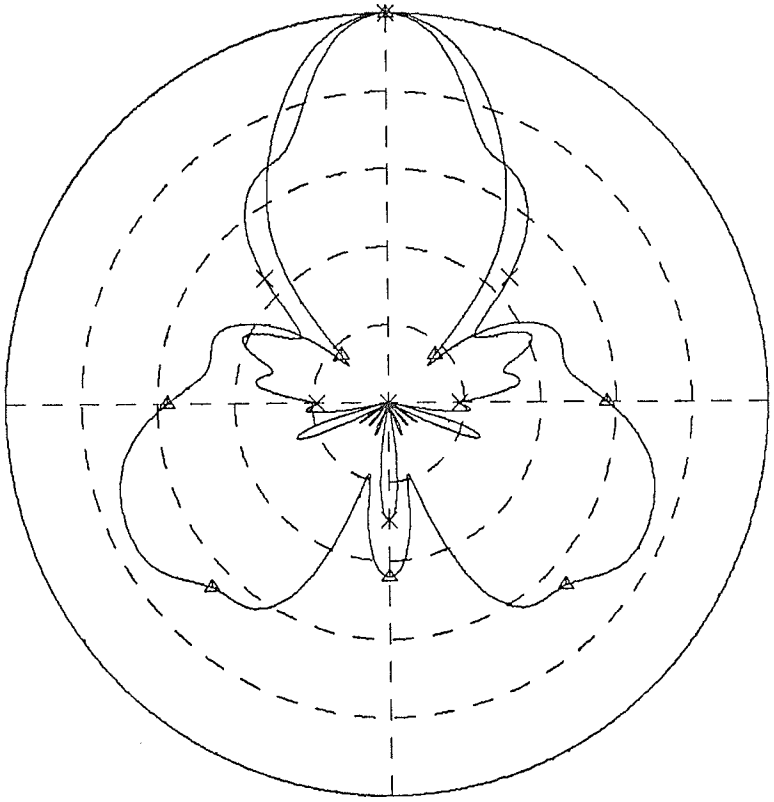

$x \frac{d}{\lambda} = 0.0$

$\Delta = 0.25$

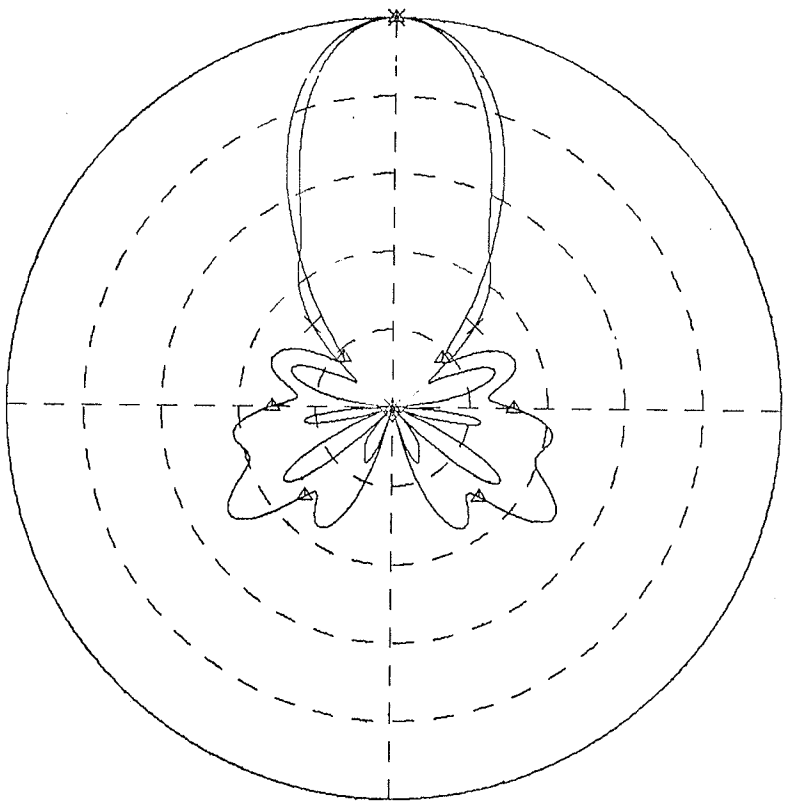

$x \frac{d}{\lambda} = 0.33$

$\Delta = 0.41$

Fig. III.13. Radiation Patterns of E-Plane Dihedral Horn.

$\alpha = 30^{\circ}$; $\ell = 2.15\lambda$; $L = 1.89\lambda$; $2a = 0.32\lambda$; 1 Division = 5dB .

tion. For the horns considered, it was found that resonant corrugations produce the worst results as shown in connection with the case of $d/\lambda = 0.25$. The radiation pattern for the corresponding plain horn is computed by assuming a zero value for the surface impedance and is shown in the same figure for comparison.

3.9 Conclusion

In conclusion, we have demonstrated that the properties of the corrugations, used in corrugated horn design, can be studied thoroughly if they are replaced by an impedance surface in an integral equation formulation of the problem. The currents over the impedance part and the field scattered from the impedance surface are the same as those obtained from a magnetic field integral equation (MFIE) solved along the extended contour of the corrugations with perfectly conducting boundaries. Once the currents are obtained from the numerical solution of this new integral equation, any other electromagnetic characteristic, as for example scattering patterns or power losses on the walls, can be easily evaluated in a straight forward manner.

The advantage of using impedance boundary conditions to represent the corrugated surface, is in the substantial savings in computer core and reduced time for matrix inversion needed in a direct solution of the MFIE as carried out by Mentzer and Peters [58, 59]. For the same reason, the study of the characteristics of E-plane dihedral horn

via an integral equation formulation is now made possible. The method has also its advantages over the mode matching technique adopted by other investigators, in which many approximations were introduced to obtain results in a close form. Hence the integral equation with impedance boundary conditions can be used in the solution of corrugated horns with moderate wall length and any flare angle with no restrictions on the corrugation slot depths, or tooth thickness.

The value of the impedance representing the rectangular corrugations is approximated by the ratio of the electric to the magnetic fields existing over the grooved parts of the corrugations, weighted by the factor $g/(g+\delta)$ which takes care of the smooth surface of the teeth. This ratio is determined by assuming that only the TEM mode can exist in the slot, and the approximation proved to be useful for design purposes. It was also found that the severe geometrical condition, $\delta \leq 0.1g$, usually required for the validity of the expression for rectangular corrugations, can be relaxed to a great extent in the numerical solution. In fact, this expression was used in (3.4) to represent the impedance of corrugated surfaces with $\delta = 0.5g$. The results for currents and scattered field obtained in this case were still in good agreement with those obtained by direct application of the MFIE to the corrugated surface (Figures III.4 and III.5). In the case where this approximation is not desirable, the impedance function of the corrugations can be assumed as a product of a continuous and pulse functions, with pulses located in place of the slots. Since the integral equation is applicable when the impedance is a varying function of position, this situation will not present any complication.

The integral equation formulation with impedance boundary conditions also allows the investigation of corrugated horns with dielectric filled slots with only the expression of Z_c having to be multiplied by the characteristic impedance of the TEM mode in the dielectric. Extension for the case of dielectric filled corrugations using Mentzer's integral equation, on the other hand, is not obvious.

It also becomes clear now, that as long as the corrugation parameters and the dielectric inside the corrugations are selected such that the surface impedance remains the same, the resulting surface currents and the radiation fields will also remain the same. Such an equivalence, which is valid within the validity range of the surface impedance, is not obvious without the use of the impedance representation. By studying the impedance curves for various corrugation shapes, one might be able to choose the type of corrugation which will result in a broader band performance. Hence, the smaller the rate of change of the impedance around a particular frequency, the larger the operating bandwidth.

Finally, it is not difficult to realize that the integral equation as formulated in this chapter cannot be directly applied to corrugated horns with rotational symmetry, as a formulation in three dimensions would then be required. Matrix formulation for circular corrugated horns will be treated therefore in the next chapter.

CHAPTER IV

SCATTERING FROM BODIES OF REVOLUTION WITH IMPEDANCE BOUNDARY CONDITIONS

4.1 Introduction

It became clear from the investigation presented in the previous chapter, that the scattering properties of the corrugated surfaces can well be determined from an integral equation formulation of the current induced on a geometrical counterpart, whereby the corrugations are replaced by a smooth impedance surface. The value of this impedance is given in terms of the wave impedance as seen by a TM wave propagating into the slots. The close agreement of the previously published data with the results obtained using the impedance model, plus the substantial saving in computer time and storage, encouraged us to utilize the impedance boundary concept to study corrugated horn problems. Of course, the case now is more complicated as we have to deal with three dimensional geometries. In the mean time, we note that practical corrugated horns are either pyramidal or conical in shape. In the first of these two types, corrugations are usually cut only in the E-plane walls. This is due to the fact that, in this particular plane, the radiation patterns of the smooth wall pyramidal horns possess high back and sidelobe levels, caused by the appreciable diffraction effects at the E-plane aperture edges. In such a case, the radiation properties in the H-plane are unaffected by the presence of the corrugations, and one may use the dihedral horn model considered in Chapter III to study the changes in the E-plane pattern resulting from the introduction of the corrugations.

As for the rotationally symmetric corrugated horn, the corrugations exist all around the inner surface of the flare, and no simple two-dimensional model can be assumed to lead to an examination of its properties through a simplified analysis. Fortunately, this horn exhibits a particular symmetry which could be exploited with the help of proper electromagnetic considerations, to reduce the amount of labour involved in the solution. It is the purpose of the present chapter, therefore, to formulate and solve the relevant equations for the special case of rotationally symmetric corrugated horns. The study proves to be useful for other applications as will be shown at a later stage of this work, where it will be used for the determination of the scattering properties of receiver horns in general.

4.2 Modelling, and the Solution Technique [117,118]

To study the problem numerically, the corrugated horn can be considered as a scatterer, rather than a radiator of electromagnetic energy. The excitation is provided by a current element placed in the waveguide region of the horn. Both the location and the polarization of this current element are chosen such as to allow for the dominant TE_{11} waveguide mode to be incident on the horn-waveguide junction (Figure IV.1). The corrugations on the inner wall are replaced by an anisotropic impedance surface. A valid formulation for the scattering properties of this configuration would then be based on one of the Stratton-Chu integral equations usually known as the electric and magnetic field integral equations

(EFIE and MFIE, respectively) [68] . The MFIE happened to be our choice for studying the characteristics of two dimensional corrugated surfaces in Chapter III. An alternative formulation based on the electric and magnetic, vector and scalar potentials, can also be used. Such an approach was considered by Andreasen [69] in the study of the electromagnetic scattering from bodies of revolution with perfectly conducting boundaries. It is also used in deriving the Pocklington's integral equation for perfectly conducting wire antennas [70] . In general, the Stratton-Chu integral equations provide a more elegant formulation, which is in a final form ready for applications. However, due to its final vectorial form, this type of formulation obscures certain simplified relationships among field components, based on the geometry and boundary conditions. The vector-scalar potential approach, on the other hand, needs basic manipulations in the course of which, possible simplifications to the problem can be incorporated. For this reason, vector and scalar potentials will be used in our derivation of the integral equation for the currents over the horn with impedance surface. It will also be found that this method turns out to be very advantageous in our case since it makes excellent use of existing solutions for a perfectly conducting counterpart (one which possesses the same geometry as the impedance model but with perfectly conducting boundaries). This utilization of the solution for perfectly conducting objects is carried out either directly or through the application of the principle of duality in electromagnetics, to construct different parts of the solution for the present problem.

Let us return now to the particular scattering body which we will consider throughout this chapter. As mentioned before, this is a corrugated rotationally symmetrical horn with corrugations replaced by a smooth impedance surface. Since the geometry is three-dimensional, it is expected that an integral equation obtained either from a Stratton-Chu or a vector and scalar potential formulation will include surface integrals of undetermined functions. This is usually referred to as the solid surface integral equation. One way of avoiding the double integrations in this equation is to use a wire grid model of the scatterer [71] . In this case, the original surface is substituted by a scattering mesh of wires. Integral equations for wire scattering are used and the formulation of the horn problem leads therefore to an integral equation involving line integrals only. This modelling technique is based on physical reasoning, namely, that the difference in the electromagnetic properties between a solid conducting object and its wire grid replica can be made arbitrarily small as the wire grid spacings are decreased in size. Solution of the resulting integral equation can then be obtained by dividing the wires into small segments and expanding the wire currents into a set of basis functions with unknown coefficients. These coefficients can be determined by applying the method of moments.

On the other hand, one may seek a direct solution of the solid surface integral equation using the moment method. For our particular problem, computational efforts in the solution are highly dependent on the choice of the basis function. One method of solution in this case would involve approximating the scattering surface with a patchwork of

planar segments. The unknown currents are then assumed constant over each patch area. This is equivalent to approximating the currents by a summation of pulse functions with unknown coefficients. When the integral equation is then applied at the centre of each patch, a system of linear equations is obtained. Solution of these equations gives the magnitude and phase of the current over each patch.

The impedance model of the corrugated horn, however, is rotationally symmetric both from the geometrical and physical (i.e., boundary conditions) point of view. This rotational symmetry allows the current variation in the direction on the surface orthogonal to the rotation axis (azimuthal direction) to be expanded in a Fourier series in the azimuthal angle. Due to the orthogonality of the basis function representation for the various modes in the series expansion, a solution for the modal current amplitudes as a function of surface position along the axial direction is possible on a mode-by-mode basis. The complete solution can then be obtained from the superposition of the solution for the individual modes. It will seem that the amount of work should increase in this case, but in reality this is not true. In particular, two important points should be observed: First, the separation of variables reduces any double integration appearing in the integral equation, to the product of two independent single variable integrals. One of these integrals includes the azimuthal variable only and involves known functions, and can be evaluated analytically. When this is done, the original integral equation reduces to one involving single integrals only and can

be solved along the generating curve similar to the case of a two-dimensional scatterer. The second point to note is that the formulation for all modes of excitation is exactly the same and accordingly, the equations for any mode can be obtained from a general formula by considering the proper mode number. If the moment method is used to obtain the solution, then for each mode, only one matrix inversion will be needed. Furthermore, due to the symmetric properties of the modes, it will become necessary to consider only the zero and the positive modes. This will reduce the number of matrix inversions to approximately one half (or exactly one half if the zero order mode is not excited).

A useful comparison of the above methods can be based on the number and size of the matrices obtained through the application of the moment method. First, it was found by experience [71] that more current samples are required for the wire grid model than for the patch method. As this leads to larger matrices, only the patch and the body of revolution method, therefore, need to be compared. Let N1 and K1 be the number of subdivisions along the generating curve and the azimuth direction, respectively. The surface patch method in this case will require one inversion of a matrix of size $(2xN1xK1)^2$. The factor of "2" reflects the two components of current on each patch. For the formulation based on the bodies of revolution, however, the matrix dimension depends only on N1 and is given by $(2xN1)^2$. On the other hand, one matrix inversion is needed for all existing modes which contribute significantly to the solution. Considering the fact that the computation time of each

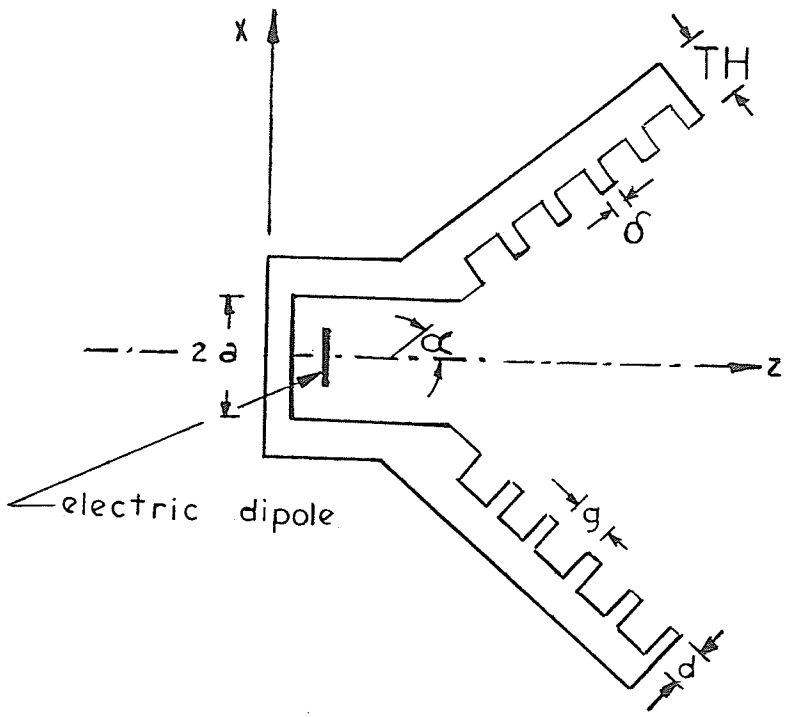

(a) Rotationally Symmetric Corrugated Horn with excitation for TE_{11} Circular Waveguide Mode.

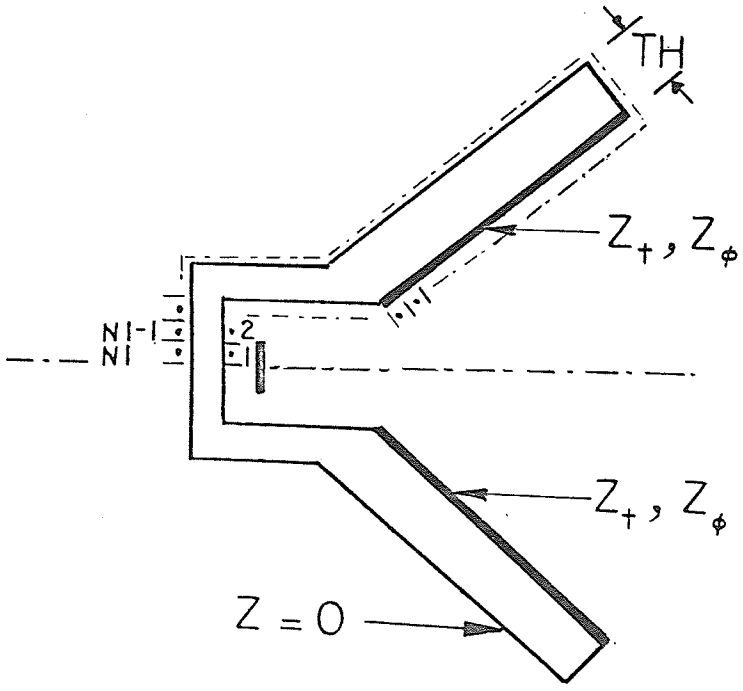

(b) Equivalent Scatterer with Impedance Surfaces.

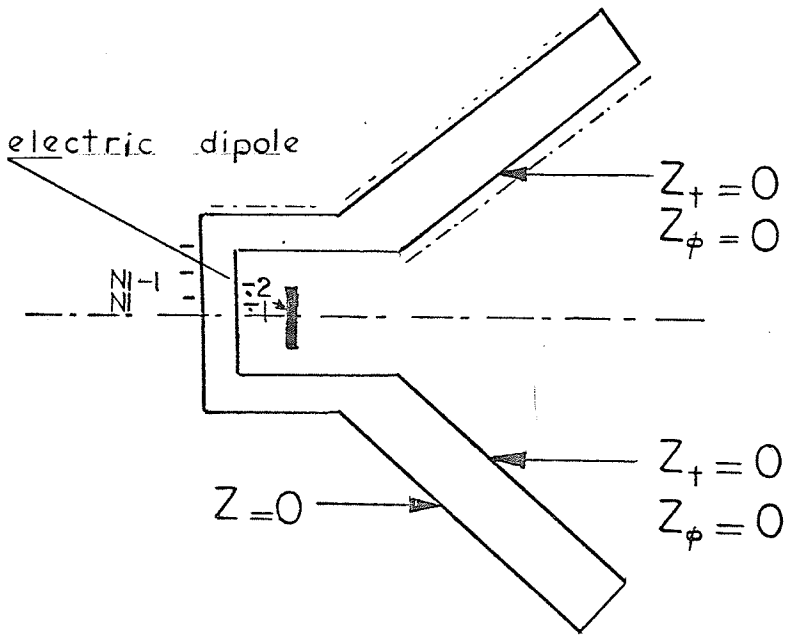

(c) Smooth Wall Counterpart.

Fig. IV.1 .

matrix inversion increases as the 3rd power of the matrix size [72], the ratio of the required computation time of the above two methods can be expressed as $(Kl)^3$. This relation shows that as long as the number of modes with significant contribution is smaller than $2x(Kl)^3$, the latter method is more economical. In addition, most horn antennas operate with single or double modes, and the computational savings of the second method become significant.

In the following sections, we will first present some useful vector relationships needed for later manipulations. We will then proceed to obtain the integral equation for the currents induced on a scattering body with general surface impedances. Following this, the derived equations will be modified according to the symmetric properties of bodies of revolution. These final results will then be used in Chapter V to study the radiation properties of rotationally symmetric corrugated horns and the scattering from conical horns in the receiving mode.

4.3 The Scattering Geometry

As mentioned before, we are particularly interested in the case of a rotationally symmetric scatterer whose geometry is defined by the rotation of an arbitrary "generating curve" about a fixed axis z. The generated structure is known as a "Body of Revolution".

Referring to Figure (IV.2), it is clear that we can define the location of any point on the surface of a Body of Revolution using two orthogonal coordinates t and ϕ. We define $\hat{u}_t$ and $\hat{u}_\phi$ as unit vectors in the direction of increasing t and ϕ, respectively. The outward normal to the surface of the structure is defined by the direction of the unit vector $\hat{n}$ given by

$$\hat{n} = \hat{u}_\phi \times \hat{u}_t \tag{4.1}$$

In the following sections, we will refer to a field point on the scatterer as (t,ϕ) or (ρ,ϕ,z) while (t',ϕ') or (ρ',ϕ',z') will denote a source point on it. The unit vectors tangential to the t and ϕ coordinates at these two points will be denoted $\hat{u}_t$, $\hat{u}_\phi$ and $\hat{u}_{t'}$, $\hat{u}_{\phi'}$, respectively.

Let ν be the angle between $\hat{u}_t$ and the z-axis. We will assume ν to be positive if $\hat{u}_t$ points away from the z-axis, and negative if $\hat{u}_t$ points toward the z-axis. Similarly, we may define ν' as the corresponding angle evaluated at (t', ϕ'). For future reference, we introduce the following relationships [73] which might be obtained by inspection of Figure (IV.2).

$$\hat{u}_t = \sin\nu\, \hat{u}_\rho + \cos\nu\, \hat{u}_z \tag{4.2a}$$

$$= \sin\nu\cos\phi\, \hat{a}_x + \sin\nu\sin\phi\, \hat{a}_y + \cos\nu\, \hat{a}_z \tag{4.2b}$$

$$\hat{u}_t' = \sin\nu' \, \hat{u}_\rho + \cos\nu' \, \hat{u}_z$$

$$= \sin\nu' \cos(\phi'-\phi) \, \hat{u}_\rho + \sin\nu' \sin(\phi'-\phi) \, \hat{u}_\phi + \cos\nu' \, \hat{u}_z \qquad (4.3)$$

$$\hat{u}_\phi' = -\sin(\phi'-\phi) \, \hat{u}_\rho + \cos(\phi'-\phi) \, \hat{u}_\phi \qquad (4.4)$$

where $\hat{a}_x$, $\hat{a}_y$ and $\hat{a}_z$ are unit vectors in the directions of the cartezian coordinates (x,y,z) and $\hat{u}_\rho$, $\hat{u}_\phi$ and $\hat{u}_z$ are the similar vectors along a cylindrical coordinate system (ρ, ϕ, z), with $\hat{a}_z = \hat{u}_z$. In addition, if the positional vectors of points (t,ϕ) and (t',ϕ') are $\bar{r}$ and $\bar{r}'$ respectively, then

$$\bar{r} = \rho \, \hat{u}_\rho + z \, \hat{u}_z \qquad (4.5)$$

and

$$\bar{r}' = \rho' \cos(\phi'-\phi) \, \hat{u}_\rho + \rho' \sin(\phi'-\phi) \, \hat{u}_\phi + z' \, \hat{u}_z \qquad (4.6)$$

where

$$|\bar{r}-\bar{r}| = \sqrt{(\rho-\rho')^2 + (z-z')^2 + 4\rho\rho' \sin^2\left(\frac{\phi-\phi'}{2}\right)} \qquad (4.7)$$

Also, by definition, the surface gradient of a scalar function Φ on the body of revolution is given by

$$\nabla_s \Phi = \hat{u}_t \frac{\partial\Phi}{\partial t} + \hat{u}_\phi \frac{\partial\Phi}{\rho\partial\phi} \qquad (4.8a)$$

and the surface divergence of a vector function $\bar{W}$ is defined as

$$\nabla_s \cdot \bar{W} = \frac{1}{\rho} \frac{\partial}{\partial t}(\rho \, \bar{W} \cdot \hat{u}_t) + \frac{1}{\rho} \frac{\partial}{\partial\phi}(\bar{W} \cdot \hat{u}_\phi) \qquad (4.8b)$$

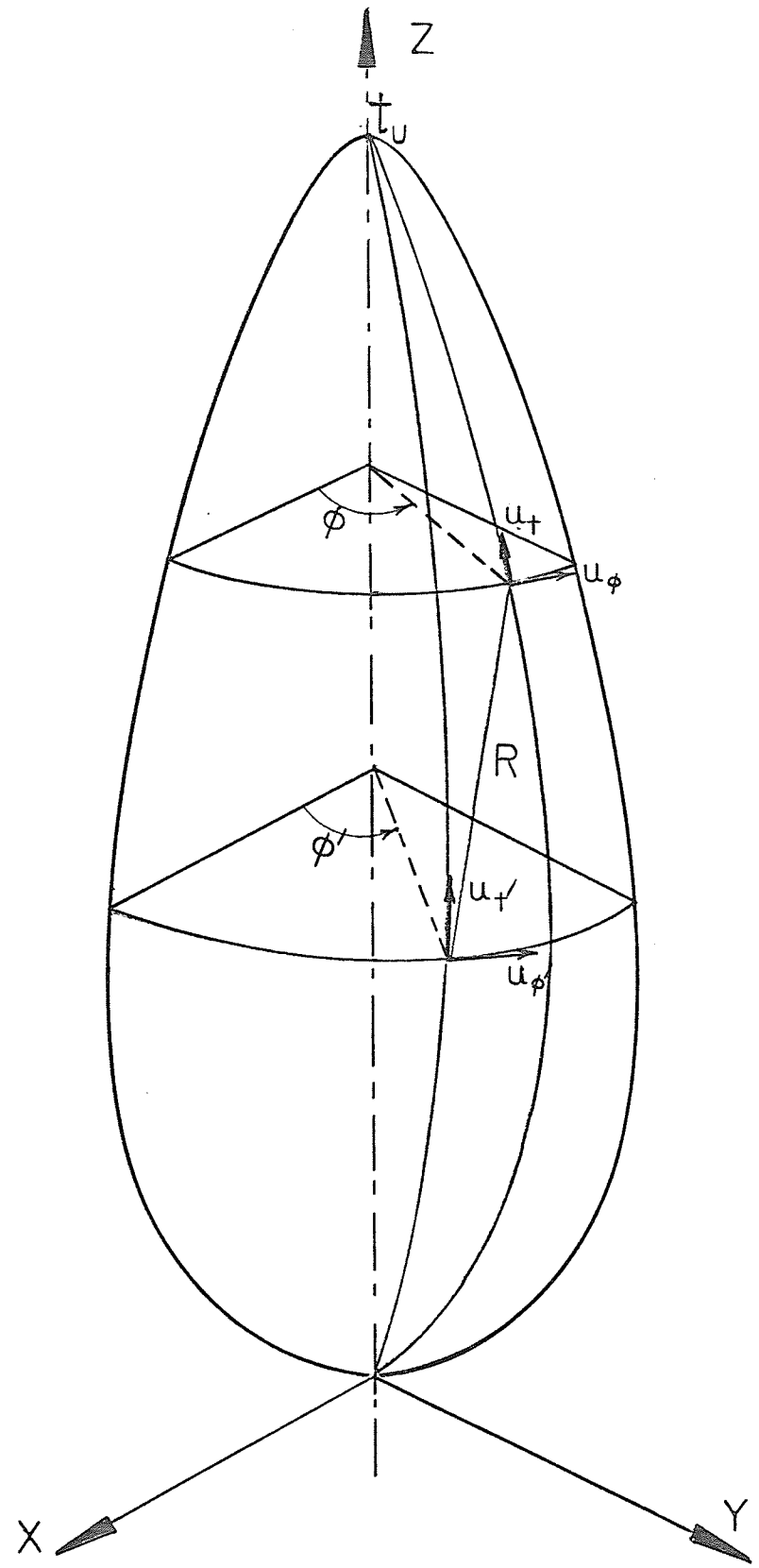

Fig. IV.2. Geometry of Body of Revolution.

4.4 The Integral Equation for the Electric Current Density on the Surface of a Scatterer with Impedance Boundary Conditions

Let $\bar{E}^{inc}$ be the field incident on a scatterer with impedance boundary conditions and $\bar{E}^{sc}$ the scattered field, defined as the difference between the incident field and the total field $\bar{E}$ when the obstacle is present. Hence, for any point $\bar{r}$ in space we can write

$$\bar{E}(\bar{r}) = \bar{E}^{inc}(\bar{r}) + \bar{E}^{sc}(\bar{r}) \tag{4.9}$$

Since the scattering body is not a perfect conductor, then both the magnetic and electric field components tangential to its surface are non-zero. It follows therefore that an electric current density $\bar{J}$ amp/m and a magnetic current density $\bar{M}$ volt/m , proportional to the tangential $\bar{H}$ and $\bar{E}$ vectors, will be induced on the scattering surface. These linear current densities are related to the total surface fields $\bar{H}$ and $\bar{E}$ by [68]

$$\bar{J} = \hat{n}x\bar{H} \tag{4.10}$$

and

$$\bar{M} = \bar{E}x\hat{n} \tag{4.11}$$

Both $\bar{J}$ and $\bar{M}$ constitute the sources of the scattered electric and magnetic fields $\bar{E}^{sc}$ and $\bar{H}^{sc}$, which must satisfy Maxwell's equations. In particular, $\bar{E}^{sc}$ can be obtained from [70]

$$\bar{E}^{sc} = -j\omega \bar{A} - \nabla V - \frac{1}{\epsilon} \nabla x\bar{F} \tag{4.13}$$

where $\bar{A}$ and $\bar{F}$ are the magnetic and the electric vector potentials defined as

$$\bar{A} = \mu \iint_S \bar{J}\, \Phi\, ds' \tag{4.14}$$

$$\bar{F} = \varepsilon \iint_S \bar{M}\, \Phi\, ds' \tag{4.15}$$

and V is the electric scalar potential given by

$$V = \iint_S \frac{1}{\varepsilon}\, \sigma\, \Phi\, ds' \tag{4.16}$$

In these equations Φ is the free space Green's function of the form

$$\Phi = \frac{e^{-jk|r-r'|}}{4\pi\,|r-r'|} \tag{4.17}$$

and the integration in equations (4.14) and (4.15) is performed over the scattering surface s'. Also, σ is the surface electric charge density, k is the usual wave number, and r and $\bar{r}'$ are the positional vectors of the observation and source points (x, y, z) and (x', y', z'), respectively. The time dependence $e^{j\omega t}$ is assumed and is suppressed throughout. The permeability μ and the permittivity ε are replaced by their respective free space values μ_0 and ε_0, since the currents $\bar{J}$ and $\bar{M}$ radiate in free space.

When the field point approaches the scattering surface from inside, the boundary condition $\bar{E} = 0$ is satisfied and for a field point on the surface, (4.9) together with (4.13 - 4.16) give

$$\bar{E}^{inc} = -\bar{E}^{sc} = j\omega \bar{A} + \nabla V + \frac{1}{\varepsilon} \nabla x \bar{F} \tag{4.18a}$$

$$= j\omega\mu \int\int_s \bar{J} \Phi \, ds' + \nabla \frac{1}{\varepsilon} \int\int_s \sigma \Phi \, ds' + \nabla x \int\int_s \bar{M} \Phi \, ds' \tag{4.18b}$$

Now the electric charge density σ can be substituted in terms of $\bar{J}$ by using the equation of continuity. Hence [73]

$$\sigma = -\frac{1}{j\omega} \nabla_s \cdot \bar{J}(\bar{r}) \tag{4.19}$$

Similarly, the magnetic current density $\bar{M}$ is related to $\bar{J}$ through the surface impedance and can be expressed as [74]

$$\begin{bmatrix} M_t \\ M_\phi \end{bmatrix} = \begin{bmatrix} Z^\phi & 0 \\ 0 & Z^t \end{bmatrix} \begin{bmatrix} J_\phi \\ -J_t \end{bmatrix} \tag{4.20}$$

J_t, M_t and J_ϕ, M_ϕ are the components of $\bar{J}$ and $\bar{M}$ in the directions t and ϕ, respectively. Z^t and Z^ϕ give the components of the anisotropic surface impedance [Z] in those directions.

Using (4.19) and (4.20) in (4.18), one directly obtains the integral equation for the current $\bar{J}$ on the surface of the scatterer with

impedance boundary conditions. The result is of the form

$$\bar{E}^{inc} = j\omega\mu \int\int_S \bar{J}\,\Phi\,ds' - \frac{1}{j\omega\varepsilon}\nabla \int\int_S (\nabla_s\cdot\bar{J})\,\Phi\,ds' + \nabla \times \int\int_S \bar{M}\,\Phi\,ds' \tag{4.21}$$

It will be noted here that the second and the third terms on the right hand side of this equation need the evaluation of the divergence and the curl of unknown functions. However, by utilizing known vectorial identities, these difficulties can be overcome and the above vectorial operators can be made to operate on known functions. In this case, the numerical approximation of the divergence and curl operators, which greatly affect the accuracy of the solution, will be avoided. Equations (4.18a and b) and (4.21) will be referred to alternatively in the course of the investigation.

4.5 Solution of the Integral Equation (4.21)

The unknown current densities $\bar{J}$ and $\bar{M}$ appearing in (4.18b), possess both components t and ϕ tangential to the scattering surface. Hence, for the case of a rotationally symmetric scatterer we can write:

$$\bar{J}(\bar{r}') = \hat{u}_{t'}\, J^{t}(t',\phi') + \hat{u}_{\phi'}\, J^{\phi}(t',\phi') \tag{4.22}$$

and

$$\bar{M}(\bar{r}') = \hat{u}_{t'} M^{t}(t',\phi') + \hat{u}_{\phi'} M^{\phi}(t',\phi') \tag{4.23}$$

For a numerical solution of (4.18 or 4.21) using the method of Moments [75], we may divide the generating curve of the body into Nl segments and write an expression for $\bar{J}$ in the form [73, 76]

$$\bar{J}(\bar{r}') = \sum_{m=-Ml}^{Ml} \sum_{n=1}^{Nl} I_{mn}^{t} J_{mn}^{t}(t',\phi') \hat{u}_{t'} + I_{mn}^{\phi} J_{mn}^{\phi}(t',\phi') \hat{u}_{\phi'} \tag{4.24}$$

where I_{mn}^{t} and I_{mn}^{ϕ} are coefficients to be determined while $\{J_{mn}^{t}\}$ and $\{J_{mn}^{\phi}\}$ are expansion functions with elements defined as

$$J_{mn}^{t}(t',\phi') = f_n(t') e^{jm\phi'} = J_{mn}^{\phi}(t',\phi') \tag{4.25}$$

The range -Ml to +Ml gives the total number of azimuthal modes with significant contribution to the current. The expansion function $f_n(t')$ defines the behaviour of the mode current along the generating curve of the scattering body. In practice, for the numerical solution using the moment method, a variety of forms for $f_n(t')$ are selected in the literature. To reduce the computational efforts, they are normally assumed to be spatially orthogonal. This means that a new function is defined for each segment along the generating curve. In the present work, we have selected $\rho f_n(t')$ to be a triangular function on each segment, with a unit peak at the centre of the segment. More details on these expansion functions will be given in Section 4.6.

Using equations (4.20) and (4.11) which relate $\bar{M}$ to $\bar{J}$ and to the tangential component of $\bar{E}$, we obtain through the help of (4.23)

$$\begin{aligned} M^t \hat{u}_t + M^\phi \hat{u}_\phi &= (E_t \hat{u}_t + E_\phi \hat{u}_\phi + E_n \hat{n}) \times \hat{n} \\ &= - E_\phi \hat{u}_t + E_t \hat{u}_\phi \\ &= Z^\phi J^\phi \hat{u}_t - Z^t J^t \hat{u}_\phi \end{aligned} \tag{4.26}$$

which is satisfied at any point on the scatterer. Hence

$$M^t = - E_\phi = Z^\phi J^\phi \tag{4.27a}$$

and

$$M^\phi = E_t = - Z^t J^t \tag{4.27b}$$

In addition, since the scatterer is assumed to be rotationally symmetric, then both Z^t and Z^ϕ can possess variation only along the t direction. Therefore, using (4.27a and b) and (4.24), we can write:

$$\begin{aligned} \bar{M}(\bar{r}') &= \hat{u}_{t'} Z^\phi(t') J^\phi(t',\phi') - \hat{u}_{\phi'} Z^t(t') J^t(t',\phi') \\ &= \sum_{n=-M1}^{M1} \sum_{n=1}^{N1} \{ I^\phi_{mn} Z^\phi_n J^\phi_{mn}(t',\phi') \hat{u}_{t'} \\ &\qquad - I^t_{mn} Z^t_n J^{t'}_{mn}(t',\phi') \hat{u}_{\phi'} \} \end{aligned} \tag{4.28}$$

where Z^t_n and Z^ϕ_n are the respective values of Z_t and Z_ϕ evaluated

on the nth segment of the generating curve. According to the moment method, we then define a set of testing functions $\{\bar{W}_{\ell i}\}$ as

$$\bar{W}^{t}_{\ell i} = \hat{u}_t \, f_i(t) \, e^{-j\ell\phi} \tag{4.29a}$$

and

$$\bar{W}^{\phi}_{\ell i} = \hat{u}_\phi \, f_i(t) \, e^{-j\ell\phi} \tag{4.29b}$$

and take their inner products with both sides of (4.18b), after having replaced $\bar{J}$ and $\bar{M}$ by their expansions from (4.24) and (4.28). By definition, the inner product of two vectors $\bar{P}$ and $\bar{Q}$, is given by the dot product of $\bar{P}$ and $\bar{Q}$ integrated over the surface of the scatterer, i.e.,

$$< \bar{P}, \bar{Q} > = \int\int_S \bar{P} \cdot \bar{Q} \, ds' \tag{4.30}$$

We note, however, that the functions $\{\bar{W}_{\ell i}\}$ and $\{J_{mn}\}$, as defined in (4.29a and b) and (4.25), are orthogonal over the period 0 to 2π in ϕ. Because of the linearity of the operators in (4.18b), $\{\bar{W}_{\ell i}\}$ is also orthogonal to $\{J_{mn}\}$. It follows therefore that all inner products involving different modes $\ell \neq m$ of $\bar{W}^{p}_{\ell i}$ and J^{p}_{mn} ($p = t$ or ϕ) are zero, with the result that each mode can be treated independently. This is the major simplification introduced by the rotational symmetry of the body. Accordingly, we obtain for each mode m a matrix equation of the form

$$\begin{bmatrix} [Z_m^{tt}] & [Z_m^{t\phi}] \\ [Z_m^{\phi t}] & [Z_m^{\phi\phi}] \end{bmatrix} \begin{bmatrix} [I_m^t] \\ [I_m^\phi] \end{bmatrix} = \begin{bmatrix} [V_m^t] \\ [V_m^\phi] \end{bmatrix} \tag{4.31}$$

where

$$(V_m^t)_i = < \bar{W}_{mi}^t , \bar{E}^{inc} > \tag{4.32a}$$

$$(V_m^\phi)_i = < \bar{W}_{mi}^\phi , \bar{E}^{inc} > \tag{4.32b}$$

$[I_m^t]$ and $[I_m^\phi]$ are the unknown coefficients in the expansion of the current for mode m. They are in the form

$$[I_m^t] = \begin{bmatrix} I_{m1}^t \\ I_{m2}^t \\ \vdots \\ I_{m,N1}^t \end{bmatrix} \quad \text{and} \quad [I_m^\phi] = \begin{bmatrix} I_{m1}^\phi \\ I_{m2}^\phi \\ \vdots \\ I_{m,N1}^\phi \end{bmatrix} \tag{4.33}$$

The sub-matrices $[Z_m^{tt}]$ and $[Z_m^{t\phi}]$ are the coefficients of $[I_m^t]$ and $[I_m^\phi]$ obtained by taking the inner product of $\{\bar{W}_m^t\}$ with the right hand side of (4.18b). Similarly $[Z_m^{\phi t}]$ and $[Z_m^{\phi\phi}]$ result when the inner products are taken between $\{\bar{W}_m^\phi\}$ and the right hand side of (4.18b). These four sub-matrices form what is known as the"impedance matrix" $[Z_m]$, for mode m. Because of the complexity of the analysis, contribution from the electric vector and scalar potentials to the matrix $[Z_m]$ will be evaluated first in the next section, while the contribution from the

magnetic vector potential will be treated separately. It will be found in particular, that these contributions can be determined from a careful study of the solutions available for a body of revolution with perfectly conducting boundaries. When the coefficient matrix $[Z_m]$ and the column vectors $[V_m^t]$ and $[V_m^\phi]$ are computed for each mode m, equation (4.31) can then be solved for the coefficients of the currents for that mode. Finally, superposing the solutions resulting from the different modes of excitation, the total scatterer currents can be determined by the summation of all contributing modes.

4.5.1 Contributions of the Terms $j\omega \bar{A}$ and ∇V to the Impedance Matrix

Since the potentials $\bar{A}$ and V are due to the electric current over the scattering surface, then the first and the second terms in the right hand side of (4.18a) can be denoted $(-\bar{E}^{sc}_{\bar{J}})$, which stands for the scattered field due to the electric current $\bar{J}$. Hence we have

$$-\bar{E}^{sc}_{\bar{J}} = j\omega \bar{A}(\bar{J}) + \nabla V(\bar{J}) \tag{4.34}$$

Taking the inner product of each function in the set $\{\bar{W}_{mi}\}$ with both sides of (4.34) we obtain a set of matrix equations of the form [72]

$$[Z_m^{tt,\bar{J}}][I_m^t] + [Z_m^{t\phi,J}][I_m^\phi] = [\Psi_m^t] \tag{4.35a}$$

and

$$[Z_m^{\phi t,\bar{J}}][I_m^t] + [Z_m^{\phi\phi,\bar{J}}][I_m^\phi] = [\Psi_m^\phi] \tag{4.35b}$$

with $m = 0, \pm 1, \pm 2, \ldots$ and $[I_m^t]$ and $[I_m^\phi]$ are defined in (4.23). In general, the elements of the above impedance matrix can be defined as $(Z_m^{pq,\bar{J}})$ given by

$$(Z_m^{pq,\bar{J}})_{ij} = \int\int_s \bar{W}_{mi}^p \cdot [j\omega \bar{A}(J_{mj}^q) + \nabla V(J_{mj}^q)] \, ds' \tag{4.36}$$

where p and q are permutations of t and ϕ and the superscript $\bar{J}$ again refers to the contributions of the electric current $\bar{J}$ to the impedance matrix. Also, the ith element in the columns of the right hand side of (4.35a or b) is given by

$$(\psi_{mi}^p) = \int\int_s \bar{W}_{mi}^p \cdot (-\bar{E}_{\bar{J}}^{sc}) \, ds' \tag{4.37}$$

V is given in terms of $\bar{J}$ which is still undetermined and the presence of the term ∇V in (4.36) is therefore undesirable. However, we can transfer the differential operator from V to $\bar{W}$ with the help of the vector identities (Appendix C). If this is done, the impedance elements of (4.37) then become:

$$(Z_m^{pq,\bar{J}})_{ij} = j\omega \int\int_s [\bar{W}_{mi}^p \cdot \bar{A}(J_{mj}^q) + v_{mi}^p V(J_{mj}^q)] \, ds' \tag{4.38}$$

where

$$v_{mi}^p = \frac{-1}{j\omega} \nabla_s \cdot \bar{W}_{mi}^p \tag{4.39}$$

Using (4.8), together with (4.29) and (4.39) we can write

$$v^{t}_{mi} = \frac{-1}{j\omega\rho} \frac{\partial}{\partial t} (\rho f_i(t))\, e^{-jm\phi} \tag{4.40a}$$

and

$$v^{\phi}_{mi} = \frac{\pm m}{\omega\rho} f_i(t)\, e^{-jm\phi} \tag{4.40b}$$

Hence, if $\bar{A}$ and V are substituted in terms of $\bar{J}$ (equations (4.14 and (4.16)), and expressions (4.24), (4.29) and (4.40) for the components of $\bar{J}_{mi}$, $\bar{W}_{mi}$ and v^{p}_{mi} are used, then one can show (Appendix D) by the aid of the vector relationships of Section 4.3 that the contributions of the electric potentials to the impedance matrix for mode m will be given by [73]

$$(Z^{tt,\bar{J}}_{m})_{ij} = j \int dt \int dt' \{k^2 \rho f_i(t)\, \rho' f_j(t') \cdot [G_1 \sin\nu \sin\nu' + G_2 \cos\nu \cos\nu'] - \frac{\partial}{\partial t} (\rho f_i(t)) \frac{\partial}{\partial t'} (\rho' f_j(t))\, G_2\}$$

$$(Z^{\phi t,\bar{J}}_{m})_{ij} = -\int dt\, \rho\, f_i(t) \int dt' \left[k^2 \rho' f_j(t')\, G_3 \sin\nu' + \frac{m}{\rho} \frac{\partial}{\partial t'} (\rho' f_j(t')) G_3\right]$$

$$(Z^{t\phi,\bar{J}}_{m})_{ij} = \int dt \int dt'\, \rho' f_j(t') \left[k^2 \rho f_i(t)\, G_3 \sin\nu + \frac{m}{\rho'} \frac{\partial}{\partial t} (\rho f_i(t))\, G_2\right]$$

$$(Z^{\phi\phi,\bar{J}}_{m})_{ij} = j \int dt\, \rho f_i(t) \int dt'\, \rho' f_j(t') \left(k^2 G_1 - \frac{m^2}{\rho\rho'} G_2\right) \tag{4.41}$$

where $$G_1 = \int_0^{\pi} \frac{e^{-jkR}}{kR} \cos\phi' \cos(m\phi')\, d\phi' \tag{4.42}$$

$$G_2 = \int_0^{\pi} \frac{e^{-jkR}}{kR} \cos(m\phi')\, d\phi' \tag{4.43}$$

$$G_3 = \int_0^{\pi} \frac{e^{-jkR}}{kR} \sin\phi' \sin(m\phi')\, d\phi' \tag{4.44}$$

and

$$R = \sqrt{(\rho-\rho')^2 + (z-z')^2 + 4\rho\rho' \sin^2(\frac{\phi'}{2})} \tag{4.45}$$

4.5.2 Contribution of the Term $\nabla x\bar{F}$ to the Impedance Matrix

Consider first the case of a perfectly conducting scatterer. The magnetic field on its surface will be related to the induced electric current density by [73]

$$\hat{n} \times \bar{H}^{sc} = \frac{1}{\mu} \hat{n} \times \nabla \times \bar{A}$$

$$= \lim_{\Delta \to 0} \hat{n} \times \nabla \times \int\int_s \bar{J}(r')\, \Phi\, ds' \tag{4.46}$$

where Δ is the distance between the field point $\bar{r}$ and the surface s and $\bar{r}'$ is the positional vector of the source point on s. Taking the limit in (4.46) we obtain [73, 77] (Appendix E)

$$\hat{n} \times \bar{H}^{sc} = \frac{-\bar{J}(\bar{r})}{2} + \int\int_s \hat{n} \times \nabla \times (\bar{J}(\bar{r}')\, \Phi)\, ds' \tag{4.47}$$

If the principle of duality in electromagnetics is used, then one needs to

change $(\bar{H}^{sc} \rightleftharpoons -\bar{E}^{sc})$, $(\bar{A}/\mu \rightleftharpoons \bar{F}/\varepsilon)$ and $(\bar{J} \rightleftharpoons \bar{M})$ [78] , and the dual form of (4.46) and (4.47) for a magnetic vector potential becomes

$$-\hat{n} \times \bar{E}^{sc} = \frac{1}{\varepsilon} \hat{n} \times \nabla \times \bar{F}$$

$$= -\frac{\bar{M}(\bar{r})}{2} + \int\int_{s} \hat{n} \times \nabla \times (\bar{M}(\bar{r}') \Phi) \, ds' \qquad (4.48)$$

Consequently, (4.48) will be the equation to be satisfied by the magnetic current $\bar{M}$ on the surface of a scatterer with perfectly conducting magnetic walls.

Using the identity of [70]

$$\nabla \times (\Phi \bar{M}) = (\nabla \Phi) \times \bar{M} + \Phi (\nabla \times \bar{M}) \qquad (4.49)$$

and since $\nabla \times \bar{M} = 0$, due to the fact that $\bar{M}$ is only a function of the source coordinates (x',y',z'), (4.48) becomes

$$-\hat{n} \times \bar{E}^{sc} = -\frac{\bar{M}(\bar{r})}{2} + \int\int_{s} \hat{n} \times (\nabla \Phi \times \bar{M}) \, ds' \qquad (4.50)$$

Now using the expression (4.17) for Φ and the relation

$$\nabla \left(\frac{e^{-jk|\bar{r}-\bar{r}'|}}{|\bar{r}-\bar{r}'|}\right) = -\left(\frac{1+jk|\bar{r}-\bar{r}'|}{|\bar{r}-\bar{r}'|^3}\right) e^{-jk|\bar{r}-\bar{r}'|} \qquad (4.51)$$

equation (4.17) reduces to

$$\frac{\bar{M}(\bar{r})}{2} + \frac{1}{4\pi} \int\int_S \left(\frac{1+jk|\bar{r}-\bar{r}'|}{|\bar{r}-\bar{r}'|^3}\right) e^{-jk|\bar{r}-\bar{r}'|}\, \hat{n} \times [(\bar{r}-\bar{r}') \times \bar{M}(r')]\, ds' = \hat{n} \times \bar{E}^{sc} \tag{4.52}$$

Finally, expressing $\bar{M}$ in terms of its components M^t and M^ϕ from (4.23), this equation reduces to (Appendix F)

$$\begin{aligned}
&\hat{u}_t \Big\{\frac{M^t(t,\phi)}{2} + \frac{k^3}{4\pi} \int \rho' dt' \int_0^{2\pi} d\phi'\, G'\, M^t(t',\phi'+\phi)\, [((\rho'-\rho)\cos\nu' - (z'-z)\sin\nu')\cos\phi' \\
&\quad - 2\rho\cos\nu' \sin^2\left(\frac{\phi'}{2}\right)] + \frac{k^3}{4\pi} \int \rho'\, dt' \int_0^{2\pi} d\phi'\, G'\, M^\phi(t',\phi'+\phi)\, (z'-z)\sin\phi' \Big\} \\
&+ \hat{u}_\phi \Big\{\frac{M^\phi(t,\phi)}{2} + \frac{k^3}{4\pi} \int \rho'\, dt' \int_0^{2\pi} d\phi\, G'\, M^t(t',\phi'+\phi)\, (\rho'\sin\nu\cos\nu' - \rho\sin\nu'\cos\nu \\
&\quad - (z'-z)\sin\nu\sin\nu')\sin\phi' + \frac{k^3}{4\pi} \int \rho'\, dt' \int_0^{2\pi} d\phi'\, G'\, M^\phi(t',\phi'+\phi) \\
&\quad [((\rho'-\rho)\cos\nu - (z'-z)\sin\nu)\cos\phi' + 2\rho'\cos\nu \sin^2\left(\frac{\phi'}{2}\right)]\Big\} = \hat{n} \times \bar{E}^{sc}
\end{aligned} \tag{4.53}$$

where

$$G' = \frac{1+jkR}{k^3R^3} e^{-jkR} \tag{4.54}$$

and R is as given in (4.45).

For a moment method of solution, we choose to expand M^t and M^ϕ as in (4.24) in terms of basis functions of the form

$$M^t(\bar{r}') = \sum_{m=-Ml}^{Ml} \sum_{n=1}^{Nl} b_{mn}^t\, M_{mn}^t(t',\phi') \tag{4.55a}$$

and

$$M^{\phi}(\bar{r}') = \sum_{m=-Ml}^{Ml} \sum_{n=1}^{Nl} b_{mn}^{\phi} \; M_{mn}^{\phi}(t',\phi') \tag{4.55b}$$

where $M_{mn}^{t}(t',\phi')$ and $M_{mn}^{\phi}(t',\phi')$ are expansion functions given by

$$M_{mn}^{t}(t',\phi') = f_n(t')\, e^{jm\phi'} = M_{mn}^{\phi}(t',\phi') \tag{4.56}$$

and b_{mn}^{t}, b_{mn}^{ϕ} are constants to be determined.

We now replace M^{t} and M^{ϕ} by their expansions from (4.55), and use the set of testing functions $\{\bar{W}_{\ell i}\}$ defined in (4.29) to evaluate the inner products with both sides of (4.53). In this case we obtain a matrix equation for each mode m in the form

$$\begin{bmatrix} [\tilde{Z}_m^{tt,\bar{F}}] & [\tilde{Z}_m^{t\phi,\bar{F}}] \\ [\tilde{Z}_m^{\phi t,\bar{F}}] & [\tilde{Z}_m^{\phi\phi,\bar{F}}] \end{bmatrix} \begin{bmatrix} [b_m^{t}] \\ [b_m^{\phi}] \end{bmatrix} = \begin{bmatrix} [\Theta_m^{t}] \\ [\Theta_m^{\phi}] \end{bmatrix} \tag{4.57}$$

where we have defined the elements of the right hand column matrices of (4.57) as

$$(\Theta_m^{t})_i = < \bar{W}_{mi}^{t} , \hat{n} \times \bar{E}^{sc} > \tag{4.58a}$$

and

$$(\Theta_m^{\phi})_i = < \bar{W}_{mi}^{\phi} , \hat{n} \times \bar{E}^{sc} > \tag{4.58b}$$

The superscript $\bar{F}$ appearing in (4.57) refers to the magnetic vector potential $\bar{F}$ and p and q again will be used as permutations for

t and ϕ . The column vectors $[b_m^t]$ and $[b_m^\phi]$ are formed by the coefficients of the magnetic currents (4.55), and the elements of the $[\tilde{Z}_m^{pq,\bar{F}}]$ sub-matrices are given by

$$(\tilde{Z}_m^{pq,\bar{F}})_{ij} = \frac{1}{\varepsilon} \int\int_s \bar{W}_{mi}^p \cdot (\hat{n} \times \nabla \times \bar{F}(\bar{M}_{mj}^q)) \, ds' \tag{4.59}$$

For a scatterer with rotational symmetry, the last equation reduces to:

$$(\tilde{Z}_m^{tt,\bar{F}})_{ij} = \pi \int dt\, \rho f_i(t) f_j(t) + k^3 \int dt\, \rho f_i(t) \int dt'\, \rho' f_j(t') \{[(\rho'-\rho)\cos\nu' - (z'-z)\sin\nu'] G_5 - G_4 \rho \cos\nu'\}$$

$$(\tilde{Z}_m^{\phi t,\bar{F}})_{ij} = jk^3 \int dt\, \rho f_i(t) \int dt'\, \rho' f_j(t') [\rho' \sin\nu \cos\nu' - \rho\nu' \cos\nu - (z'-z)\sin\nu \sin\nu'] G_6$$

$$(\tilde{Z}_m^{t\phi,\bar{F}}) = jk^3 \int dt\, \rho f_i(t) \int dt'\, \rho' f_j(t') (z'-z) G_6$$

$$(\tilde{Z}_m^{\phi\phi,\bar{F}})_{ij} = \pi \int dt\, \rho f_i(t) f_j(t) + k^3 \int dt\, \rho f_i(t) \int dt'\, \rho' f_j(t') \{[(\rho'-\rho)\cos\nu - (z'-z)\sin\nu] G_5 + G_4 \rho' \cos\nu\} \tag{4.60}$$

where

$$G_4 = 2 \int_0^\pi G' \sin^2\left(\frac{\phi'}{2}\right) \cos(m\phi') \, d\phi' \tag{4.61}$$

$$G_5 = \int_0^{\pi} G' \cos\phi' \cos(m\phi')\, d\phi' \tag{4.62}$$

$$G_6 = \int_0^{\pi} G' \sin\phi' \sin(m\phi')\, d\phi' \tag{4.63}$$

Now we return to our original problem of a body of revolution with impedance surfaces and try to evaluate the contribution of $< \bar{W}^p_{mi}, \nabla \times \bar{F} >$, $(p=t \text{ or } \phi)$, to the impedance matrix $[Z_m]$ of (4.31). Since the portion of the scattered field which is due to the magnetic vector potential $\bar{F}$ can be denoted by $\bar{E}^{sc}_{\bar{F}}$, then using (4.13) we can write

$$\begin{aligned} -\bar{E}^{sc}_{\bar{F}} &= \frac{1}{\varepsilon} \nabla \times \bar{F} \\ &= \lim_{\Delta \to 0} \nabla \times \int\int_s \bar{M}\, \Phi\, ds' \end{aligned} \tag{4.64}$$

If $\bar{M}$ is substituted in terms of $\bar{J}$ and the surface impedance Z^t and Z^{ϕ}, (equation (4.20)), and the moment method is applied, the above equation for the mth mode takes the form

$$\begin{bmatrix} [Z_m^{tt,\bar{F}}] & [Z_m^{t\phi,\bar{F}}] \\ [Z_m^{\phi t,\bar{F}}] & [Z_m^{\phi\phi,\bar{F}}] \end{bmatrix} \begin{bmatrix} [I_m^t] \\ [I_m^{\phi}] \end{bmatrix} = \begin{bmatrix} [\tau_m^t] \\ [\tau_m^{\phi}] \end{bmatrix} \tag{4.65}$$

where

$$(\tau_m^p)_i = < \bar{W}_{mi}, -\bar{E}^{sc}_{\bar{F}} > \quad ; \; p = t \text{ or } \phi \tag{4.66}$$

$[I_m^t]$ and $[I_m^{\phi}]$ are given by (4.33) and

$$(Z^{pq,\bar{F}})_{ij} \; (I_m^q)_j = \frac{1}{\varepsilon} \int\int_s \bar{W}_{mi}^p \cdot \nabla \times \bar{F}(J_{mj}^q) \, ds \tag{4.67}$$

An examination of (4.67) and (4.59) shows that the impedance coefficients in (4.65) can be obtained from (4.60) by a multiplication and a reordering. This can be done in two steps. The first will be to eliminate the effect of the additional cross-product appearing in (4.59), and the second is to use equation (4.27) relating $\bar{M}$ to $\bar{J}$, (Appendix G). When this is done we obtain:

$$\begin{aligned}
(Z_m^{tt,\bar{F}})_{ij} &= -Z_j^t \, (\tilde{Z}_m^{\phi\phi,\bar{F}})_{ij} \\
(Z_m^{\phi t,\bar{F}})_{ij} &= Z_j^t \, (\tilde{Z}_m^{t\phi,\bar{F}})_{ij} \\
(Z_m^{t\phi,\bar{F}})_{ij} &= Z_j^\phi \, (\tilde{Z}_m^{\phi t,\bar{F}})_{ij} \\
(Z_m^{\phi\phi,\bar{F}})_{ij} &= -Z_j^\phi \, (\tilde{Z}_m^{tt,\bar{F}})_{ij}
\end{aligned} \tag{4.68}$$

4.5.3 The Impedance Matrix for the mth Mode on a Body of Revolution with Impedance Boundary Conditions

The elements of the impedance matrix $[Z_m]$ appearing in (4.31) can now be obtained by adding the contribution of $\nabla \times \bar{A}$, ∇V and $\nabla \times \bar{F}$ as obtained in (4.41) and (4.68). The result is

$$\begin{aligned}
[Z_m^{tt}] &= [Z_m^{tt,\bar{J}}] + [Z_m^{tt,\bar{F}}] \\
[Z_m^{t\phi}] &= [Z_m^{t\phi,\bar{J}}] + [Z_m^{t\phi,\bar{F}}]
\end{aligned}$$

$$[Z_m^{\phi t}] = [Z_m^{\phi t,\bar{J}}] + [Z_m^{\phi t,\bar{F}}]$$

$$[Z_m^{\phi\phi}] = [Z_m^{\phi\phi,\bar{J}}] + [Z_m^{\phi\phi,\bar{F}}] \qquad (4.69)$$

4.6 Numerical Evaluation of the Impedance Matrix $[Z_m]$

To compute the elements in (4.69), the functions $f_i(t)$ should now be considered in more detail. We define $\rho f_i(t)$ as in [73] to be a four impulse approximation to a triangle function of unit peak and base equal to the width of segment i. Although the formulae for this representation are available in [73], it was found necessary to report them here for the interpretation of the final expression of the impedance elements as given at the end of this section. We define an odd number greater than 5 of consecutive points $\bar{t}_i$ on the generating line, where

$$\bar{t}_i \equiv (\bar{\rho}_i, \bar{z}_i) \; ; \; i = 1,2, \ldots, L1 \qquad (4.70a)$$

and

$$L1 = (2 \times N1) + 3 \qquad (4.70b)$$

$(\bar{\rho}_1, \bar{z}_1)$ and $(\bar{\rho}_{L1}, \bar{z}_{L1})$ coincide with the poles of the generating curve. The points $\bar{t}_i$ are such that $\hat{u}_t$ points from $\bar{t}_i$ to $\bar{t}_{i+1}$. The generating curve is then approximated by drawing straight lines between the points $(\bar{\rho}_i, \bar{z}_i)$, $i = 1,2, \ldots, L1$, and we define the points

$$t_i = (\rho_i, z_i) = \left(\frac{\bar{\rho}_i + \bar{\rho}_{i+1}}{2}, \frac{\bar{z}_i + \bar{z}_{i+1}}{2}\right) \qquad (4.71)$$

on the piecewise approximation of the generating curve. The length h_i of the interval centered about t_i is then

$$h_i = \sqrt{(\bar{\rho}_{i+1} - \bar{\rho}_i)^2 + (\bar{z}_{i+1} - \bar{z}_i)^2} \tag{4.72}$$

We now replace $\rho f_i(t)$ by the impulse approximation of a triangular function with proper weighting factors. Hence

$$\rho f_i(t) = \frac{1}{k} \sum_{p=1}^{4} T_{p+4i-4} \, \delta(t - t_{p+2i-2}) \tag{4.73}$$

where $\delta(t-t_j)$ is a unit impulse function at $t = t_j$ and the weighting factors T_{p+4i-4}/k with $p = 1, .., 4$ are given in terms of area subdivisions of the triangle as shown in Figure (IV.3a). These are

$$\begin{aligned}
T_{4i-3} &= \frac{k\, h_{2i-1}^2}{2(h_{2i-1} + h_{2i})} \\
T_{4i-2} &= \frac{k(h_{2i-1} + 0.5h_{2i})\, h_{2i}}{h_{2i-1} + h_{2i}} \\
T_{4i-1} &= \frac{k(h_{2i+2} + 0.5h_{2i+1})\, h_{2i+1}}{h_{2i+1} + h_{2i+2}} \\
T_{4i} &= \frac{k\, h_{2i+2}^2}{2(h_{2i+1} + h_{2i+2})}
\end{aligned} \tag{4.74}$$

In the evaluation of the elements of $[Z_m^{pq,\bar{F}}]$, the derivative of $\rho f_i(t)$ with respect to the coordinate t is also needed. Figure (IV.3b) shows the derivative of the triangle function and will be used to approximate

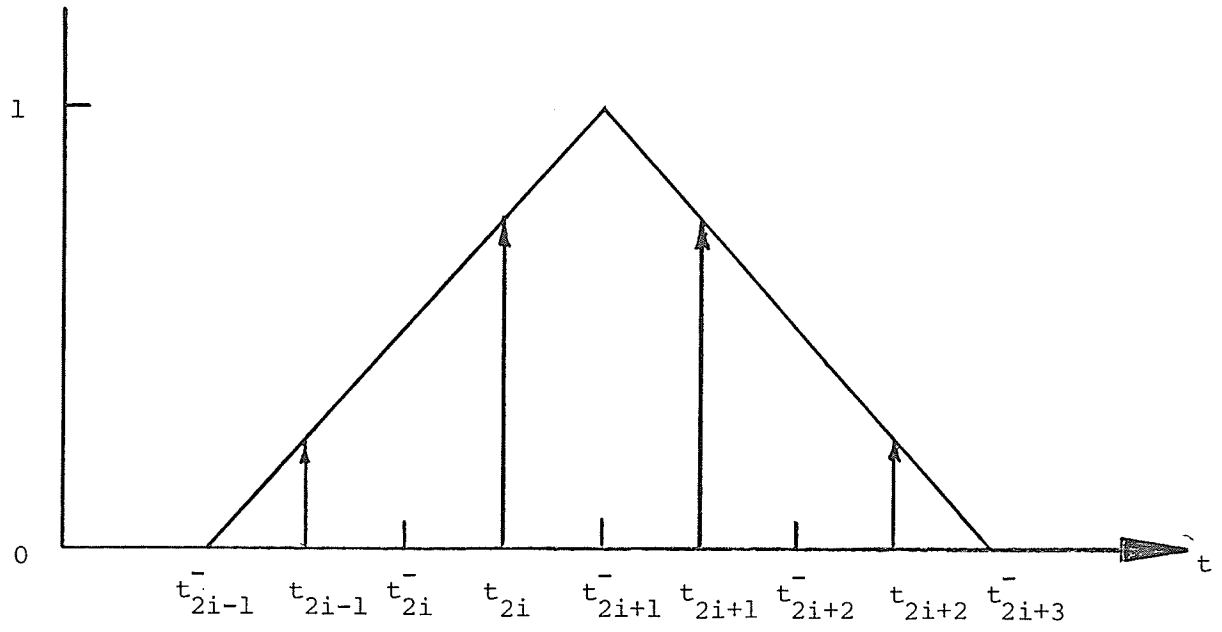

(a). Triangle Function (solid) and Four Impulse Approximation (arrows).

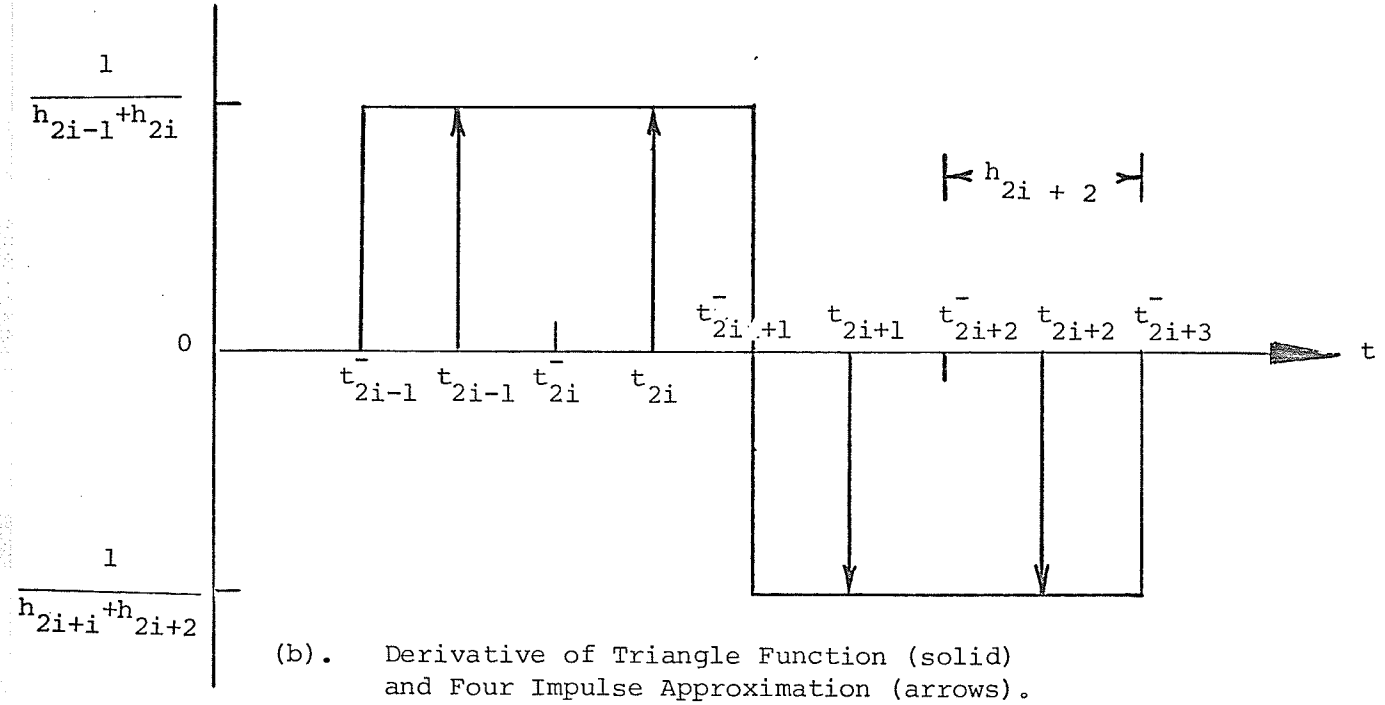

(b). Derivative of Triangle Function (solid) and Four Impulse Approximation (arrows).

Fig. IV.3 .

$\frac{\partial}{\partial t}(\rho f_i(t))$, again in terms of four impulses with proper weighting functions. Hence we write

$$\frac{\partial}{\partial t}(\rho f_i(t)) = \sum_{p=1}^{4} T'_{p+4i-4}\ \delta(t-t_{p+2i-2}) \tag{4.75}$$

where T'_{p+4i-4} with $p = 1, .., 4$ will now be given by the area subdivisions shown in Figure (IV.3b). They are

$$T'_{4i-3} = \frac{h_{2i-1}}{h_{2i-1} + h_{2i}}$$

$$T'_{4i-2} = \frac{h_{2i}}{h_{2i-1} + h_{2i}}$$

$$T'_{4i-1} = \frac{-h_{2i+1}}{h_{2i+1} + h_{2i+2}}$$

$$T'_{4i} = \frac{-h_{2i+2}}{h_{2i+1} + h_{2i+2}} \tag{4.76}$$

Substituting from (4.73) and (4.75) in (4.69) and evaluating the integrals in t, we finally obtain

$$(Z_m^{tt})_{ij} = j \sum_{p=1}^{4} \sum_{p=1}^{4} \{T_p, T_q, [G_1 \sin\nu_i, \sin\nu_j, + G_2 \cos\nu_i, \cos\nu_j,] - T'_p, T'_q, G_2$$

$$- \sum_{q=1}^{4} Z_j^t, \sum_{p=1}^{4} \{T_p, T_q, [k((\rho_j,-\rho_i,) \cos\nu_i, - (z_j,-z_i,) \sin\nu_i') G_5$$

$$+ k\rho_j, G_4 \cos\nu_i,]\}$$

$$.... i' \neq j'$$

or

$$= j \sum_{p=1}^{4} \sum_{q=1}^{4} \{T_p, T_q, [G_1 \sin\nu_i, \sin\nu_j, + G_2 \cos\nu_i, \cos\nu_j,] - T'_p, T'_q, G_2\}$$

$$- \sum_{q=1}^{4} Z_j^t, \sum_{p=1}^{4} \{T_p, T_q, [\frac{\pi}{k^2 h_i, \rho_i,} + k\rho_i, G_4 \cos\nu_i,]\}$$

..... $i' = j'$

$$(Z_m^{\phi t})_{ij} = - \sum_{p=1}^{4} \sum_{q=1}^{4} \{T_p, T_q, G_3 \sin\nu_j, + \frac{m}{k\rho_i,} T_p, T'_q, G_2\}$$

$$+ jk \sum_{q=1}^{4} Z_j^t, \sum_{p=1}^{4} \{T_p, T_q, (z_j, -z_i,) G_6\}$$

$$(Z_m^{t\phi})_{ij} = \sum_{p=1}^{4} \sum_{q=1}^{4} \{T_p, T_q, G_3 \sin\nu_i, + \frac{m}{k\rho_j,} T'_p, T_q, G_2\}$$

$$+ jk \sum_{q=1}^{4} Z_j^{\phi}, \sum_{p=1}^{4} \{T_p, T_q, [\rho_j, \sin\nu_i, \cos\nu_j, - \rho_i, \sin\nu_j, \cos\nu_i,$$

$$- (z_j, -z_i,) \sin\nu_i, \sin\nu_j,] G_6$$

$$(Z_m^{\phi\phi})_{ij} = j \sum_{p=1}^{4} \sum_{q=1}^{4} T_p, T_q, (G_1 - \frac{m^2}{k^2 \rho_i, \rho_j,} G_2)$$

$$- \sum_{q=1}^{4} Z_j^{\phi}, \sum_{p=1}^{4} \{T_p, T_q, [k ((\rho_j, -\rho_i,) \cos\nu_j, - (z_j, -z_i,) \sin\nu_j,) G_5$$

$$- k\rho_i, G_4 \cos\nu_j,]\}$$

..... $i' \neq j'$

or

$$= j \sum_{p=1}^{4} \sum_{q=1}^{4} T_{p'} T_{q'} \left(G_1 - \frac{m^2}{k^2 \rho_{i'} \rho_{j'}} G_2\right)$$

$$- \sum_{q=1}^{4} Z_{j'}^{\phi} \sum_{p=1}^{4} \{T_{p'} T_{q'} \left(\frac{\pi}{k^2 h_{i'} \rho_{i'}} - k\rho_{i'} G_4 \cos\nu_{i'}\right)\}$$

$$\ldots\ldots \quad i' = j' \tag{4.77}$$

where

$$p' = p + 4i - 4$$

$$q' = q + 4j - 4 \tag{4.78}$$

$$i' = p + 2i - 2$$

$$j' = q + 2j - 2 \tag{4.79}$$

Also, it is understood that the letter j appearing outside of the summation stands for $\sqrt{-1}$.

The functions G_1, G_2, G_3, G_4, G_5 and G_6 are given by (4.42 to 4.44) and (4.61 to 4.63) in which R is evaluated between the points $(\rho,z) \equiv (\rho_{i'},z_{i'})$ and $(\rho',z') \equiv (\rho_{j'},z_{j'})$. None of these functions, however, converges when $i' = j'$, since for this case

$$R \xrightarrow{i' = j'} 2\rho_{i'} \sin\left(\frac{\phi'}{2}\right) \tag{4.80}$$

which introduces a singularity of the third order in (4.54) when $\phi' = 0$.

To overcome this difficulty, the field point is usually displaced a small distance from its original position. Mautz and Harrington gave an estimate for R in this case as [75]

$$R\Big|_{i'=j'} \simeq \sqrt{(\frac{h_{i'}}{4})^2 + 4\rho_{i'}^2 \sin^2(\frac{\phi'}{2})} \tag{4.81}$$

Furthermore, due to the impulse approximation of (4.73), the first term in the right hand side in each of the first and last equations of (4.60) result in two coincident impulse functions when $i' = j'$. To evaluate the integrals in this case, one of the impulse functions is replaced by an equivalent pulse over the interval $h_{i'}$. This substitution results in the terms $T_{p'}$, $T_{q'}$, $\frac{\pi}{k^2 h_{i'}\rho_{i'}}$ appearing in the expressions for $(Z_m^{tt})_{ij}$ and $(Z_m^{\phi\phi})_{ij}$ when $i' = j'$.

4.7 The Excitation Matrix

We assume that the field incident on the body of revolution with impedance boundaries is due to an x-directed current element whose centre is located at point $(x',y',z') \equiv (0,0,z_d)$. z_d is made small such that the dipole is located near the inner wall of the waveguide termination. We also choose the waveguide radius "a" such that

$$1.841 < ka < 2.405$$

This ensures that only the dominant TE_{11} circular waveguide mode will be

incident on the waveguide-horn junction. In this way, the radiation characteristics of corrugated horns can be studied for this particular mode of excitation. When z_d is made very large, the incident field on the horn is that of a plane wave. This provides the excitation necessary for studying the scattering properties of horns.

To calculate the excitation matrix (4.32) for mode m, namely $[V_m^p]$, with $p = t$ or ϕ, we note first that the incident electric field from a current element is given by [79]

$$\bar{E}^{inc} = - j\omega \bar{A}_d - \nabla \Phi_d \tag{4.82}$$

where

$$\bar{A}_d = \frac{-jk\mu}{4\pi} \overline{I\,\ell}\, h_0^{(2)}(k|\bar{r}-\bar{r}'|) \tag{4.83}$$

and

$$\Phi_d = \frac{\eta}{4\pi} \overline{I\,\ell} \cdot \nabla h_0^{(2)}(k|\bar{r}-\bar{r}'|) \tag{4.84}$$

$h_0^{(2)}$ is the spherical Hankel function of the second kind and order zero and $\overline{I\,\ell}$ is the product of the element current by its length. It is a vector parallel to the x-direction. When the inner product is evaluated between $\bar{W}_{mi}$ and $\bar{E}^{inc}$, as given in (4.29) and (4.82), the elements of $[V_m^p]$ become,

$$(V_m^t)_i = \int\int_S \bar{W}_{mi}^t \cdot \bar{E}^{inc}\, ds$$

$$= \frac{\eta}{4\pi}\left[-k^2 \int_0^{t_u} dt\, \rho f_i(t) \int_0^{2\pi} d\phi\, (\overline{I\,\ell} \cdot \hat{u}_t)\, h_0^{(2)}\, e^{-jm\phi}\right.$$

$$\left. + \int_0^{t_u} dt\, \frac{\partial}{\partial t}(\rho f_i(t)) \int_0^{2\pi} d\phi\, (\overline{I\,\ell} \cdot \nabla h_0^{(2)})\, e^{-jm\phi}\right] \qquad (4.85a)$$

and

$$(V_m^\phi)_i = \int\int_S \bar{W}_{mi}^\phi \cdot \bar{E}^{inc}\, ds$$

$$= \frac{\eta}{4\pi}\left[-k^2 \int_0^{t_u} dt\, \rho f_i(t) \int_0^{2\pi} d\phi\, (\overline{I\,\ell} \cdot \hat{u}_\phi)\, h_0^{(2)}\, e^{-jm\phi}\right.$$

$$\left. - jm \int_0^{t_u} dt\, f_i(t) \int_0^{2\pi} d\phi\, (\overline{I\,\ell} \cdot \nabla h_0^{(2)})\, e^{-jm\phi}\right] \qquad (4.85b)$$

where t_u is the t coordinate of the upper end of the generating curve, and the argument of $h_0^{(2)}$ is understood to be $(k|\bar{r}-\bar{r}'|)$.

The dot products in (4.85) are given by:

$$\overline{I\,\ell} \cdot \hat{u}_t = (|\overline{I\,\ell}|\, \hat{a}_x) \cdot (\sin\nu\cos\phi\, \hat{a}_x + \sin\nu\sin\phi\, \hat{a}_y + \cos\nu\, \hat{a}_z)$$

$$= |\overline{I\,\ell}|\, \sin\nu\cos\phi \qquad (4.86a)$$

$$\overline{I\,\ell} \cdot \hat{u}_\phi = (|\overline{I\,\ell}|\,\hat{a}_x) \cdot (-\sin\phi\,\hat{a}_x + \cos\phi\,\hat{a}_y)$$

$$= -|\overline{I\,\ell}|\sin\phi \tag{4.86b}$$

Now, since

$$h_0^{(2)}(k|r-r'|) = j\,\frac{e^{-jk|r-r'|}}{k|\bar{r}-\bar{r}'|} \tag{4.87}$$

Then using (4.51) and (4.87) we obtain, in general

$$\overline{I\,\ell} \cdot \nabla h_0^{(2)} = j(|\overline{I\,\ell}|\,\hat{a}_x) \cdot \{(\frac{1}{R_d} + jk)(\frac{e^{-jkR_d}}{kR_d})(\frac{x_d-x}{R_d}\hat{a}_x + \frac{y_d-y}{R_d}\hat{a}_y + \frac{z_d-z}{R_d}\hat{a}_z)\}$$

$$= -j|\overline{I\,\ell}|\,(\frac{1}{R_d} + jk)(\frac{e^{-jkR_d}}{kR_d})\,\frac{\rho\cos\phi}{R_d} \tag{4.88}$$

where x_d, y_d and z_d are the cartezian coordinates at the middle of the current element. For our case $x_d = 0 = y_d$ and R_d is the distance between this source and a field point (ρ,ϕ,z), given by

$$R_d = \sqrt{\rho^2 + (z-z_d)^2} \tag{4.89}$$

Substituting from (4.86 to 4.88) in (4.85a and b), and using (4.73) and (4.75) for the impulse approximations of the expansion functions and their derivatives, we obtain:

$$(V_m^t)_i \begin{cases} = \left(\frac{-j\eta\,|\overline{I\,\ell}|}{4}\right) \sum_{p=1}^{4} \left[\frac{e^{-jkR_d}}{kR_d}\right]_{i'} \left\{(T_{p'}\, k^2 \sin\nu_{i'}) + \left[\frac{\rho}{R_d}\left(\frac{1}{R_d} + jk\right)\right]_{i'} T'_{p'}\right\} & \cdots\cdots m = \pm 1 \\ = 0 & \cdots\cdots \text{otherwise} \end{cases}$$

and

$$(V_m^\phi)_i \begin{cases} = \mp \left(\frac{\eta\,|\overline{I\,\ell}|}{4}\right) \sum_{p=1}^{4} \left\{\left(\frac{e^{-jkR_d}}{kR_d}\right)_{i'} \left[-k^2 + \left(\frac{1}{R_d} + jk\right)\frac{1}{R_d}\right]_{i'} T_{p'}\right\} & \cdots\cdots m = \pm 1 \\ = 0 & \cdots\cdots \text{otherwise} \end{cases}$$

(4.90)

where p' and i' have the same meaning as in (4.78) and (4.79) and R_d is evaluated at $\rho_{i'}$ and $z_{i'}$. In the mean time, we note that only modes with azimuthal variations $e^{+j\phi}$ and $e^{-j\phi}$ are excited.

4.8 The Measurement Coefficients

Since the induced currents $\bar{J}$ and $\bar{M}$ on the impedance surface of the rotationally symmetric body are of the electric and magnetic type, then the scattered field components E_θ^{sc} and E_ϕ^{sc} in the θ and ϕ directions at a far field point (r_0, θ_0, ϕ_0) can be written as [80]

$$E_\theta^{sc} = \frac{-j\omega\mu}{4\pi r_0} e^{-jkr_0} F_1(\theta_0,\phi_0) \tag{4.91a}$$

and

$$E_\phi^{sc} = \frac{-j\omega\mu}{4\pi r_0} e^{-jkr_0} F_2(\theta_0,\phi_0) \tag{4.91b}$$

with

$$F_1(\theta_0,\phi_0) = \iint_s (\bar{J} \cdot \hat{i}_\theta + \frac{1}{\eta} \bar{M} \cdot \hat{i}_\phi) e^{jk\hat{r}_0 \cdot \bar{r}'} ds' \tag{4.92a}$$

and

$$F_2(\theta_0,\phi_0) = \iint_s (\bar{J} \cdot \hat{i}_\phi - \frac{1}{\eta} \bar{M} \cdot \hat{i}_\theta) e^{jk\hat{r}_0 \cdot \bar{r}'} ds' \tag{4.92b}$$

where the integrations are carried over the surface of the scatterer. $\hat{r}_0$ is a unit vector in the direction from the origin of coordinates to the field point and $\bar{r}'$ is the positional vector of a source point (x',y',z') on the scatterer. $\hat{i}_\theta$ and $\hat{i}_\phi$ are unit vectors in the direction of increasing θ and ϕ respectively. Referring to the field point, these vectors can be written as:

$$\hat{i}_\theta = \cos\theta_0 \cos\phi_0 \hat{a}_x + \cos\theta_0 \sin\phi_0 \hat{a}_y - \sin\theta_0 \hat{a}_z \tag{4.93a}$$

$$\hat{i}_\phi = -\sin\phi_0 \hat{a}_x + \cos\phi_0 \hat{a}_z \tag{4.93b}$$

and the dot product in the exponential term of (4.92) can be shown to be

$$\bar{r}_0 \cdot \bar{r}' = (x'\cos\phi_0 + y'\sin\phi_0)\sin\theta_0 + z'\cos\theta_0$$

$$= \rho' \cos(\phi'-\phi_0)\sin\theta_0 + z'\cos\theta_0 \qquad (4.94)$$

where ρ', ϕ' and z' are the cylindrical coordinates of the point (x', y', z'). If now we substitute for $\bar{J}(\bar{r}')$ and $\bar{M}(\bar{r}')$ from (4.24) and (4.28) in (4.92), and use the relationships of Section 4.3 and equation (4.93) to evaluate the dot products $(\hat{u}_{t'} \cdot \hat{i}_\theta)$, $(\hat{u}_{t'} \cdot \hat{i}_\phi)$, $(\hat{u}_{\phi'} \cdot \hat{i}_\theta)$ and $(\hat{u}_{\phi'} \cdot \hat{i}_\phi)$, then $F_1(\theta_0,\phi_0)$ and $F_2(\theta_0,\phi_0)$ take the form:

$$F_1(\theta_0,\phi_0) = \int_0^{t_u}\int_0^{2\pi} \sum_{m=-Ml}^{Ml} \sum_{j=1}^{Nl} f_j(t')\, e^{jm\phi'}\, e^{jk[\rho' \cos(\phi'-\phi_0)\sin\theta_0 + z'\cos\theta_0]}$$

$$\cdot \{ I_{mj}^{t} [\sin\nu' \cos\theta_0 \cos(\phi'-\phi_0) - \cos\nu' \sin\theta_0]$$

$$- I_{mj}^{\phi} \cos\theta_0 \sin(\phi'-\phi_0)$$

$$- \frac{1}{\eta} Z^{t}(t')\, I_{mj}^{t} \cos(\phi'-\phi_0)$$

$$+ \frac{1}{\eta} Z^{\phi}(t')\, I_{mj}^{\phi} \sin\nu' \sin(\phi'-\phi_0)\} \rho'\, dt'\, d\phi'$$

and

$$F_2(\theta_0,\phi_0) = \int_0^{t_u}\int_0^{2\pi} \sum_{n=-Ml}^{Ml} \sum_{j=1}^{Nl} f_j(t')\, e^{jm\phi'}\, e^{jk[\rho' \cos(\phi'-\phi_0)\, \sin\theta_0 + z'\cos\theta_0]}$$

$$\cdot \{ \; I^t_{mj} \sin\nu' \sin(\phi'-\phi_0)$$

$$+ I^{\phi}_{mj} \cos(\phi'-\phi_0)$$

$$- \frac{1}{\eta} Z^t(t')\, I^t_{mj} \cos\theta_0 \sin(\phi'-\phi_0)$$

$$+ Z^{\phi}(t')\, I^{\phi}_{mj} [\sin\nu' \cos\theta_0 \cos(\phi'-\phi_0) - \cos\nu' \sin\theta_0]\} \tag{4.95}$$

where we have also used the relationship

$$\hat{u}_{\phi'} = -\sin\phi' \hat{a}_x + \cos\phi' \hat{a}_y \tag{4.96}$$

and the expansions (4.25) for J^t_{mj} and J^{ϕ}_{mj}.

Using the integral representation of the Bessel function of the first kind, namely [81]

$$J_n(\rho) = \frac{j^n}{2\pi} \int_0^{2\pi} e^{-j\rho\cos\alpha}\, e^{-jn\alpha}\, d\alpha \tag{4.97}$$

the integrations in (4.95) involving the azimuthal coordinate ϕ' can be evaluated as

$$\int_{\phi'=0}^{2\pi} e^{jm\phi'} \; e^{jk\rho' \cos(\phi'-\phi_0) \sin\theta_0} \, d\phi' = 2\pi j^m e^{jm\phi_m} J_m(k\rho' \sin\theta_0) \tag{4.98a}$$

$$\int_{\phi'=0}^{2\pi} e^{jm\phi'} \; e^{jk\rho'(\cos\phi'-\phi_0) \sin\theta_0} \left\{ \begin{matrix} \cos(\phi'-\phi_0) \\ \sin(\phi'-\phi_0) \end{matrix} \right\} d\phi' =$$

$$= \pi j^m e^{jm\phi_0} \left\{ \begin{matrix} j\,[J_{m+1}(k\rho' \sin\theta_0) - J_{m-1}(k\rho' \sin\theta_0)] \\ [J_{m+1}(k\rho' \sin\theta_0) + J_{m-1}(k\rho' \sin\theta_0)] \end{matrix} \right\} \tag{4.98b}$$

Similarly using the impulse approximation for $\rho' f_j(t')$ as given in (4.73) to evaluate the integrals in t', we finally arrive at:

$$F_1(\theta_0,\phi_0) = \sum_{m=-M1}^{M1} \sum_{j=1}^{N1} [(R_m^{t\theta})_j I_{mj}^t + (R_m^{\phi\theta})_j I_{mj}^{\phi}] \tag{4.99a}$$

and

$$F_2(\theta_0,\phi_0) = \sum_{m=-M1}^{M1} \sum_{j=1}^{N1} [(R_m^{t\phi})_j I_{mj}^t + (R_m^{\phi\phi})_j I_{mj}^{\phi}] \tag{4.99b}$$

where

$$(R_m^{t\theta})_j = \sum_{q=1}^{4} C(m,q',z',\phi_0,\theta_0) \; [j(J_{m+1} - J_{m-1})(\sin\nu_{j'} \cos\theta_0 - \frac{1}{\eta} Z_{j'}^t) - 2 \cos\nu_{j'} \sin\theta_0 J_m]$$

$$(R_m^{\phi\theta})_j = \sum_{q=1}^{4} C(m,q',z',\phi_0,\theta_0) \cdot (J_{m+1} + J_{m-1})(-\cos\theta_0 + \frac{1}{\eta} Z_{j'}^{\phi}, \sin\nu_{j'})$$

$$(R_m^{t\phi})_j = \sum_{q=1}^{4} C(m,q',z',\phi_0,\theta_0) \cdot (J_{m+1} + J_{m-1})(\sin\nu_{j'}, -\frac{1}{\eta} Z_{j'}^{t}, \cos\theta_0)$$

$$(R_m^{\phi\phi})_j = \sum_{q=1}^{4} C(m,q',z',\phi_0,\theta_0) \cdot [j(J_{m+1} - J_{m-1})(1 - \frac{1}{\eta} Z_{j'}^{\phi}, \sin\nu_{j'}, \cos\theta_0) + \frac{2}{\eta} Z_{j'}^{\phi}, \cos\nu_{j'}, \sin\theta_0 J_m] \qquad (4.100)$$

and

$$C(m,q',z',\phi_0,\theta_0) = \pi j^m e^{jm\phi_0} e^{jkz' \cos\theta_0} T_{q'} \qquad (4.101)$$

q' and j' have the same meaning as in (4.78) and (4.79). The coefficients $(R_m^{t\theta})_j$, $(R_m^{\phi\theta})_j$, $(R_m^{t\phi})_j$ and $(R_m^{\phi\phi})_j$ are generally termed as the "Measurement coefficients" [73].

4.9 Symmetric Properties of $[Z_m]$

By now it should be clear that for each mode of excitation m, a matrix $[Z_m]$, (equation 4.31), must be evaluated and inverted. Since a considerable fraction of the computer time is required for the evaluation of the elements of $[Z_m]$ and its inversion, much saving on the computational cost can therefore result from a careful study of the symmetry properties of this matrix.

First we note that, since the expansion of $\bar{J}$ includes 2xN1 unknowns, I^{t}_{mn} and I^{ϕ}_{mn} ; n=1 to N1, then we need to perform 2xN1 inner products with each side of (4.18b) which results in a (2xN1) x (2xN1) impedance matrix $[Z_m]$. We note also from (4.69) and (4.68) that $[Z_m]$ can be written in the form

$$[Z_m] = \begin{bmatrix} [Z_m^{tt,\bar{J}}] & [Z_m^{t\phi,\bar{J}}] \\ [Z_m^{\phi t,\bar{J}}] & [Z_m^{\phi\phi,\bar{J}}] \end{bmatrix} + [B] \cdot \begin{bmatrix} [\tilde{Z}_m^{\phi\phi,\bar{F}}] & [\tilde{Z}_m^{\phi t,\bar{F}}] \\ [\tilde{Z}_m^{t\phi,\bar{F}}] & [\tilde{Z}_m^{tt,\bar{F}}] \end{bmatrix} \tag{4.102}$$

where [B] is a (2xN1) x (2xN1) matrix formed by the values of the surface impedances Z^t and Z^{ϕ} at the segments 1 to N1 of the generating curve. The elements of [B] can be determined from an inspection of (4.68) and are given in Appendix H .

Now, the entries of the first matrix in the right hand side of (4.102) are given in (4.41). Of course, a replacement of (i,j,p,q) by (j,i,q,p) in this matrix, implies the replacement of (i',j',p',q') by (j',i',q',p'), and since G_1, G_2 and G_3 are symmetric in i' and j', then we have

$$\begin{aligned} (Z_m^{tt,\bar{J}})_{ij} &= (Z_m^{tt,\bar{J}})_{ji} \\ (Z_m^{\phi t,\bar{J}})_{ij} &= -(Z_m^{t\phi,\bar{J}})_{ji} \\ (Z_m^{\phi\phi,\bar{J}})_{ij} &= (Z_m^{\phi\phi,\bar{J}})_{ji} \end{aligned} \tag{4.103}$$

The elements of the third matrix in the right hand side of (4.102), on the other hand, are given by (4.60). Except for the term $\pi \int dt\ \rho f_i(t)\ f_j(t)$ appearing in the first and last of these equations, it will be noted that a replacement of (i,j,p,q) by (j,i,q,p) results in

$$
\begin{aligned}
(\tilde{Z}_m^{tt,\bar{F}})_{ij} &= -(\tilde{Z}_m^{\phi\phi,\bar{F}})_{ji} \\
(\tilde{Z}_m^{\phi t,\bar{F}})_{ij} &= -(\tilde{Z}_m^{\phi t,\bar{F}})_{ji} \\
(\tilde{Z}_m^{t\phi,\bar{F}})_{ij} &= -(\tilde{Z}_m^{t\phi,\bar{F}})_{ji}
\end{aligned}
\tag{4.104}
$$

4.10 Mode Dependence of $[Z_m]$

Symmetric properties of the impedance matrix $[Z_m]$ with respect to the mode number m can be obtained from an examination of (4.77) and the expressions for G_1, G_2, G_3, G_4, G_5 and G_6 as given in (4.42 to 4.44) and (4.61 to 4.63). These equations show that as long as the surface impedances Z^t and Z^ϕ are not dependent on the mode number m, then

$$
\begin{bmatrix} [Z_{-m}^{tt}] & [Z_{-m}^{t\phi}] \\ [Z_{-m}^{\phi t}] & [Z_{-m}^{\phi\phi}] \end{bmatrix} = \begin{bmatrix} [Z_m^{tt}] & -[Z_m^{t\phi}] \\ -[Z_m^{\phi t}] & [Z_m^{\phi\phi}] \end{bmatrix} \tag{4.105}
$$

This is another useful property of $[Z_m]$ which can be used in the minimiza-

tion of the computer time needed for the evaluation of the solution for symmetrical modes.

4.11 Mode Dependence of the Measurement Coefficients R_m^{pq}

Similar to $[Z_m]$, the measurement coefficients R_m^{pq} ($p \equiv t$ or ϕ, $q = \theta$ or ϕ) for negative mode numbers $(-m)$ can be obtained from their corresponding values evaluated when m is positive. Hence, examination of (4.100) shows that if the coefficients R_{mj}^{pq} for m positive, are written in the form

$$
\begin{aligned}
R_{mj}^{t\theta} &= \tilde{R}_{mj}^{t\theta} \; e^{jm\phi_0} \\
R_{mj}^{\phi\theta} &= \tilde{R}_{mj}^{\phi\theta} \; e^{jm\phi_0} \\
R_{mj}^{t\phi} &= \tilde{R}_{mj}^{t\phi} \; e^{jm\phi_0} \\
R_{mj}^{\phi\phi} &= \tilde{R}_{mj}^{\phi\phi} \; e^{jm\phi_0}
\end{aligned}
\qquad (4.106)
$$

in which $\tilde{R}_{mj}^{pq}$ are independent of ϕ_0, then using the relation

$$
J_{-n}(z) = (-)^n J_n(z) \qquad (4.107)
$$

for the Bessel functions, we can directly deduce the coefficients for m negative as

$$
\begin{aligned}
R^{t\theta}_{-m,j} &= \tilde{R}^{t\theta}_{mj}\, e^{-jm\phi_0} \\
R^{\phi\theta}_{-m,j} &= -\tilde{R}^{\phi\theta}_{mj}\, e^{-jm\phi_0} \\
R^{t\phi}_{-m,j} &= -\tilde{R}^{t\phi}_{mj}\, e^{-jm\phi_0} \\
R^{\phi\phi}_{-m,j} &= \tilde{R}^{\phi\phi}_{mj}\, e^{-jm\phi_0}
\end{aligned}
\qquad (4.108)
$$

4.12 Evaluation of the Total Surface Current and the Total Scattered Field

Due to the mode symmetry of the matrix $[Z_m]$, (equation (4.105)), and the excitation matrix $[V^p_m]$, (p = t or ϕ) as shown in equation (4.90), it is clear that the solution for the expansion coefficients of the current $\bar{J}$ for positive and negative values of m are related through:

$$
I^t_{-m,j} = I^t_{m,j} \quad \text{and} \quad I^{\phi}_{-m,j} = -I^{\phi}_{m,j} \qquad (4.109)
$$

Since the only non-vanishing modes resulting from our excitation are those with m = +1 and -1, then the use of (4.109) in (4.24) gives

$$
\begin{aligned}
\bar{J}(\bar{r}') &= \sum_{\ell=1}^{N1} [I^t_{1\ell}\, f_\ell(t')\, e^{j\phi'}\, \hat{u}_{t'} + I^{\phi}_{1\ell}\, f_\ell(t')\, e^{j\phi'}\, \hat{u}_{\phi'} \\
&\qquad + I^t_{1\ell}\, f_\ell(t')\, e^{-j\phi'}\, \hat{u}_{t'} - I^{\phi}_{1\ell}\, f_\ell(t')\, e^{-j\phi'}\, \hat{u}_{\phi'}] \\
&= \sum_{\ell=1}^{N1} [2\, I^t_{1\ell}\, f_\ell(t')\, \cos\phi'\, \hat{u}_{t'} + 2j\, \sin\phi'\, I^{\phi}_{1\ell}\, f_\ell(t')\, \hat{u}_{\phi'}]
\end{aligned}
\qquad (4.110)
$$

Also, using (4.106), (4.108) and (4.109), the scattering patterns $F_1(\theta_0,\phi_0)$ and $F_2(\theta_0,\phi_0)$ given in (4.99) can then be written as

$$F_1(\theta_0,\phi_0) = \sum_{\ell=1}^{Nl} [I_{1\ell}^{t} \tilde{R}_{1\ell}^{t\phi} (e^{j\phi_0} + e^{-j\phi_0}) + I_{1\ell}^{\phi} \tilde{R}_{1\ell}^{\phi\theta} (e^{j\phi_0} + e^{-j\phi_0})]$$

$$= 2 \cos\phi_0 \sum_{\ell=1}^{Nl} [I_{1\ell}^{t} \tilde{R}_{1\ell}^{t\theta} + I_{1\ell}^{\phi} \tilde{R}_{1\ell}^{\phi\theta}]$$

and

$$F_2(\theta_0,\phi_0) = \sum_{\ell=1}^{Nl} [I_{1\ell}^{t} \tilde{R}_{1\ell}^{t\phi} (e^{j\phi_0} - e^{-j\phi_0}) + I_{1\ell}^{\phi} \tilde{R}_{1\ell}^{\phi\phi} (e^{j\phi_0} - e^{-j\phi_0})]$$

$$= 2j \sin\phi_0 \sum_{\ell=1}^{Nl} [I_{1\ell}^{t} \tilde{R}_{1\ell}^{t\phi} + I_{1\ell}^{\phi} \tilde{R}_{1\ell}^{\phi\phi}] \qquad (4.111)$$

where, again, we have assumed the modes $m = +1$ and -1 only.

Equations (4.110) and (4.111) show that both the induced surface current and the scattered field can be obtained from the solution of positive azimuthal modes only. Accordingly only one matrix $[Z_m]$ with $m=1$ needs to be evaluated and inverted for our particular configuration of source and scatterer.

4.13 Conclusion and General Remarks on the Computer Program

A computer program based on the theory of the previous sections was developed and tested on the IBM 370/168 computer of the University of

Manitoba. The program can handle the general case of a body of revolution with anisotropic impedance surface varying along the coordinate t of the body but independent of the mode number m. As mentioned before, the excitation was provided by an x-directed current element located on the z-axis. When the z coordinate of this exciting source is very large, the incident field at the origin is that of a plane wave propagating in the negative z-direction. For such a case, the scattering properties of electromagnetic waves by bodies of revolution can be studied. This particular method of excitation was seen to excite azimuthal modes with $m = +1$ and -1 only (Section 4.7), and because of the symmetric properties of $[Z_m]$ and R_m^{pq}, only mode $m=1$ needed to be considered. Expressions for G_1, G_2, G_3, G_4, G_5 and G_6 were evaluated using a Gaussian quadrature formula with 20 intervals. The separation of the impedance matrix $[Z_m]$ into three matrices, $[Z_m]^{\bar{J}}$, $[B]$ and $[\tilde{Z}_m]^{\bar{F}}$ with the first and last being dependent only on the geometry of the body of revolution, proved to be very advantageous when studying the effect of different surface impedances. In such cases, only the matrix $[B]$ need to be evaluated and the same matrices $[Z_m]^{\bar{J}}$ and $[\tilde{Z}_m]^{\bar{F}}$ can be used as long as the geometry remains unchanged.

It was also noticed that for reliable results, the scatterer should be assigned a non-zero thickness. This is due to the fact that part of the solution was obtained from a dual form of the MFIE for a perfectly conducting scatterer ; the latter is known to give inaccurate results for problems involving thin scatterers.

The particulars of applying the computer program to study the radiation and scattering properties of rotationally symmetric corrugated and smooth wall horns is reported in the next chapter.

CHAPTER V

RADIATION AND SCATTERING FROM ROTATIONALLY SYMMETRIC ELECTROMAGNETIC HORNS

5.1 Introduction

In the previous chapter we have analyzed the problem of electromagnetic scattering by bodies of revolution with impedance boundary conditions. It remains now to show how this analysis would apply to some problems of engineering interest. In particular, we will study the radiation characteristics and the scattering properties of rotationally symmetric corrugated or smooth wall horns, using the previous derivations.

A computer program, ROTM, has been developed for these purposes and is available for users as a University of Manitoba report [82]. In this chapter we will discuss some particular aspects of computations using this program. We will focus our attention on the precise modelling of the horn, the representation of the corrugations and the termination which would represent proper matching effects. The arithmetic precision needed for computations is also discussed. Meanwhile we show how the density of matching points used in the moment method of solution will affect the numerical output of the program and also point out some anomalous behaviour of the solution for particular geometrical dimensions.

5.2 The Numerical Solution

As mentioned earlier, the numerical solution is obtained by dividing the generating curve of the body of revolution into short linear segments, and the surface currents are approximated by triangular expansion functions. On the subsection n, the solution for the mth mode currents in the t and ϕ directions were given by I^{t}_{mn} and I^{ϕ}_{mn}. They can be evaluated by programming equation (4.31). The elements of the coefficient matrix in the left hand side of the equation are given in (4.77) while the excitation terms in the right hand side are given by (4.90). The scattered field is obtained from (4.99) with the measurement coefficients being calculated using (4.100). Symmetry properties discussed in Section 4.9 were used to reduce the computational efforts. The expressions for G_1 to G_6 were evaluated using Gauss numerical integration with 20 intervals. Solution of the matrix equation was obtained using the same technique adopted in Chapter III.

Both the co-polar and cross-polar radiation patterns from corrugated circular horns have been evaluated for particular horn parameters. The equations for cross-polarization patterns are given in the next section.

5.3 Co-polar and Cross-polar Radiation from Rotationally Symmetric Corrugated Horns

The co-polar radiation in both the E- and H- planes of the corrugated horns is obtained by evaluating the sum of the incident field from

the current element placed inside the waveguide, plus the scattered field due to the induced currents on the scatterer as obtained from (4.111). The E- and H-plane radiation patterns are calculated from the previously mentioned equations by substituting for ϕ by 0° and 90° respectively.

Inspection of equation (4.3) for the scattered field and also Appendix I for the field of a current element in free space, show that the total field radiated from the horn can be written in the form

$$\bar{E}_{tot} = E_{\theta}^{tot}(\theta)\Big|_{\phi=0} \cos\phi\ \hat{i}_{\theta} + E_{\phi}^{tot}(\theta)\Big|_{\phi=\pi/2} \sin\phi\ \hat{i}_{\phi} \qquad (5.1)$$

where $E_{\theta}^{tot}(\theta)\Big|_{\phi=0}$ and $E_{\phi}^{tot}(\theta)\Big|_{\phi=\pi/2}$ are the total electric field in the θ and ϕ direction in the planes $\phi=0$ and $\phi=\pi/2$, respectively. The special representation of equation (5.1) is a result of the fact that only modes with azimuthal indices $m = \pm 1$ are excited.

To calculate the cross-polarization, we use Ludwig's third definition to express the unit vector, $\hat{i}_{cross}$, in the cross-polar direction [83]. Hence

$$\hat{i}_{cross} = \sin\phi\ \hat{i}_{\theta} - \cos\phi\ \hat{i}_{\phi} \qquad (5.2)$$

The cross-polar field, $E_{cross}(\theta,\phi)$ radiated from the horn can now be obtained by forming the dot product of $\bar{E}^{tot}$ and $\hat{i}_{cross}$ as given in (5.1) and (5.2). Hence

$$E_{cross}(\theta,\phi) = \bar{E}^{tot} \cdot \hat{i}_{cross} = \sin\phi \cos\phi \left[E_{\theta}^{tot}(\theta)\Big|_{\phi=0} - E_{\phi}^{tot}(\theta)\Big|_{\phi=\pi/2} \right] \quad (5.3)$$

It is clear from (5.3) that the maximum cross-polarized radiation occurs in the plane $\phi = 45^{o}$. The co-polarization component is given by :

$$E_{co}(\theta,\phi) = E^{tot}(\theta)\Big|_{\phi=0} \cos^2(\phi) + E^{tot}(\theta)\Big|_{\phi=\pi/2} \sin^2(\phi) \quad (5.4)$$

We note, meanwhile, that for no cross-polarization, $E_{\theta}^{tot}\Big|_{\phi=0}$ and $E_{\phi}^{tot}\Big|_{\phi=\pi/2}$ must be equal. Corrugated horns usually satisfy this condition and it is precisely for this reason that they are of primary interest in many antenna applications. Cross-polarization patterns reported later are computed in the $\phi = 45°$ plane and are normalized relative to the co-polarization field in the same plane.

5.4 The Impedance Representation for the Rotationally Symmetric Corrugated Horn

The value of the surface impedance representing the corrugations is obtained as the ratio of electric to magnetic fields for the propagating mode in the slots. Such fields were studied by Clarricoats, Jansen, and others. This ratio is given by Jansen [84] as

$$\frac{E_r}{H_{\phi}} = -j\eta \tan(kr\theta_1) \quad (5.5)$$

where $r\theta_1$ is the depth of the groove as measured in the direction of increase of the angle θ (Figure II.1c). E_r and H_ϕ are components of the electric and magnetic field in the r and ϕ directions, respectively. In the practical case, the teeth are perpendicular either to the walls or to the horn axis. One can use equation (5.5) therefore after substituting for $r\theta_1$ by d, the depth of the groove along one of those two directions. Such an approximation is valid as it was mentioned before with the analysis of Chapter III. The shape of the corrugations is in effect immaterial in the performance of the horn, as long as these corrugations present the same impedance value to the wave propagating inside the groove. As it was the case in two dimensions, the weighting factor $g/g+\delta$ is multiplied to the right hand side of (5.5) to take care of the zero impedance over the teeth. The resulting expression for the average impedance representing the corrugations is therefore, given by

$$Z_c \cong -j \frac{g}{g+\delta} \eta \tan (kd) \tag{5.6}$$

Expression (5.6) gives the required surface impedance Z_t representing the corrugations. Of course, since $E_\phi = 0$ over the corrugations then $Z_\phi = 0$.

5.5 The Precise Modelling of the Rotationally Symmetric Corrugated Horn

The modelling of the horn as a scatterer with an impedance surface having rotational symmetry was already introduced in Chapter IV and the contour of the generating curve was given in Figure (IV.1). This modelling, with any possible approximation, should be tested, first, in conjunction with the moment method. Numerical outputs, therefore, were compared with experimental results obtained from a radiating horn which consists of a section of circular waveguide of radius $a = 0.31\lambda$ loaded with rings. This is in effect a corrugated horn with $\alpha = 90^{o}$, $L = 1.55\lambda$, $g = 0.11\lambda$ and $\delta = 0.021\lambda$. The waveguide was excited by the TE_{11} circular mode. The horn was designed at the Communications Research Centre (CRC) [85] to provide a high performance feed for low cost earth terminals. Its dimensions as given before were determined empirically to obtain a rotationally symmetric pattern.

At first an open model (Figure V.1a) was assumed to represent the horn. Numerical results, however, were not satisfactory, showing high backlobes and differences in E- and H-plane patterns. The results also did not improve when longer portions of the outer wall were considered (Figure V.1b, c). Finally it was realized that the term $\nabla \times \int\int_{S} \bar{M}\, \Phi\, ds'$ in equation (4.18) has a similar mathematical form as the term $\nabla \times \int\int_{S} \bar{J}\, \Phi\, ds'$ in the magnetic field integral equation (equation (4.46)). That term is known to cause much numerical instability when the MFIE is applied to thin objects. A closed contour was therefore assumed and calcu-

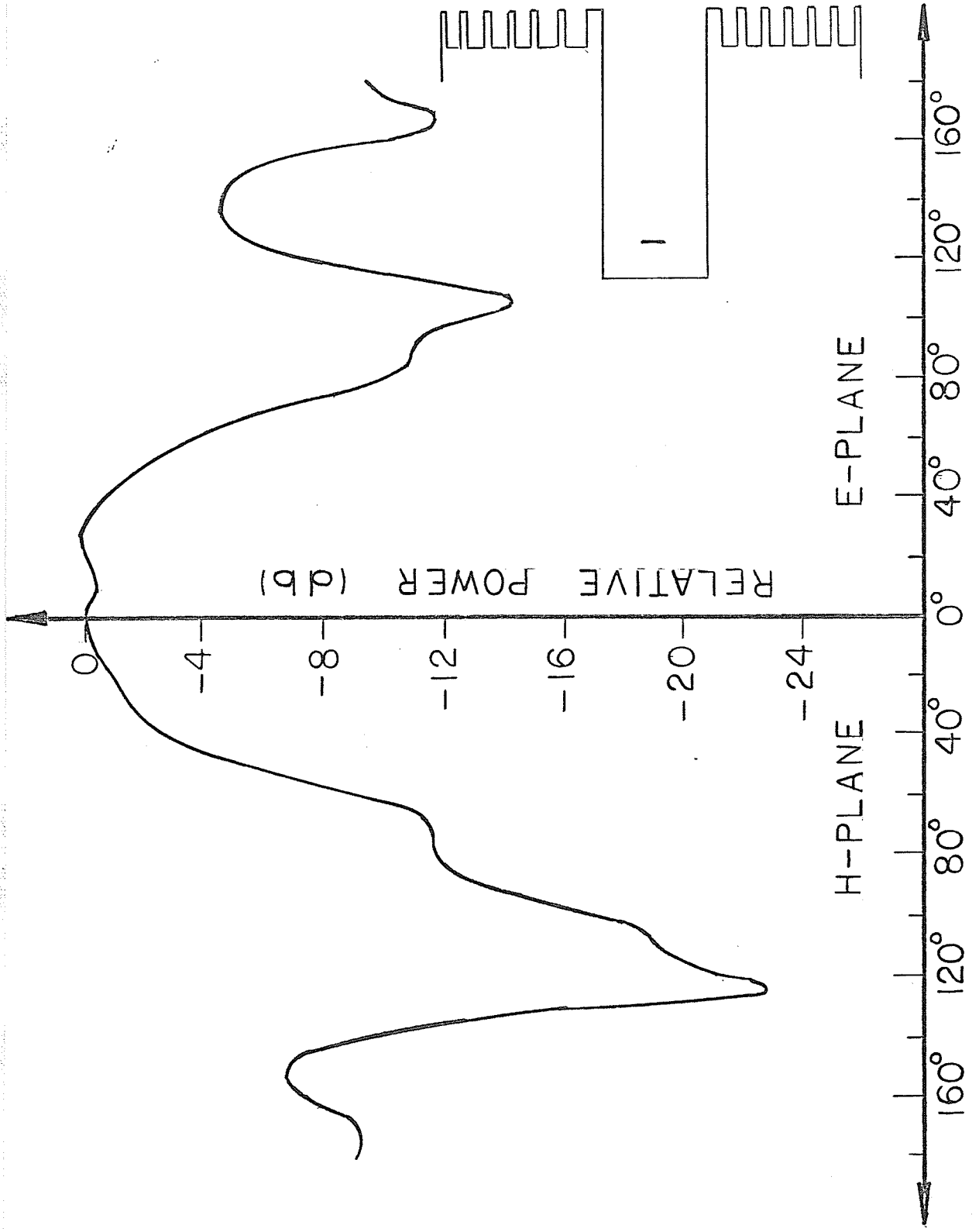

Fig. V.1(a). Unsuccessful Modelling of Corrugated Horn.

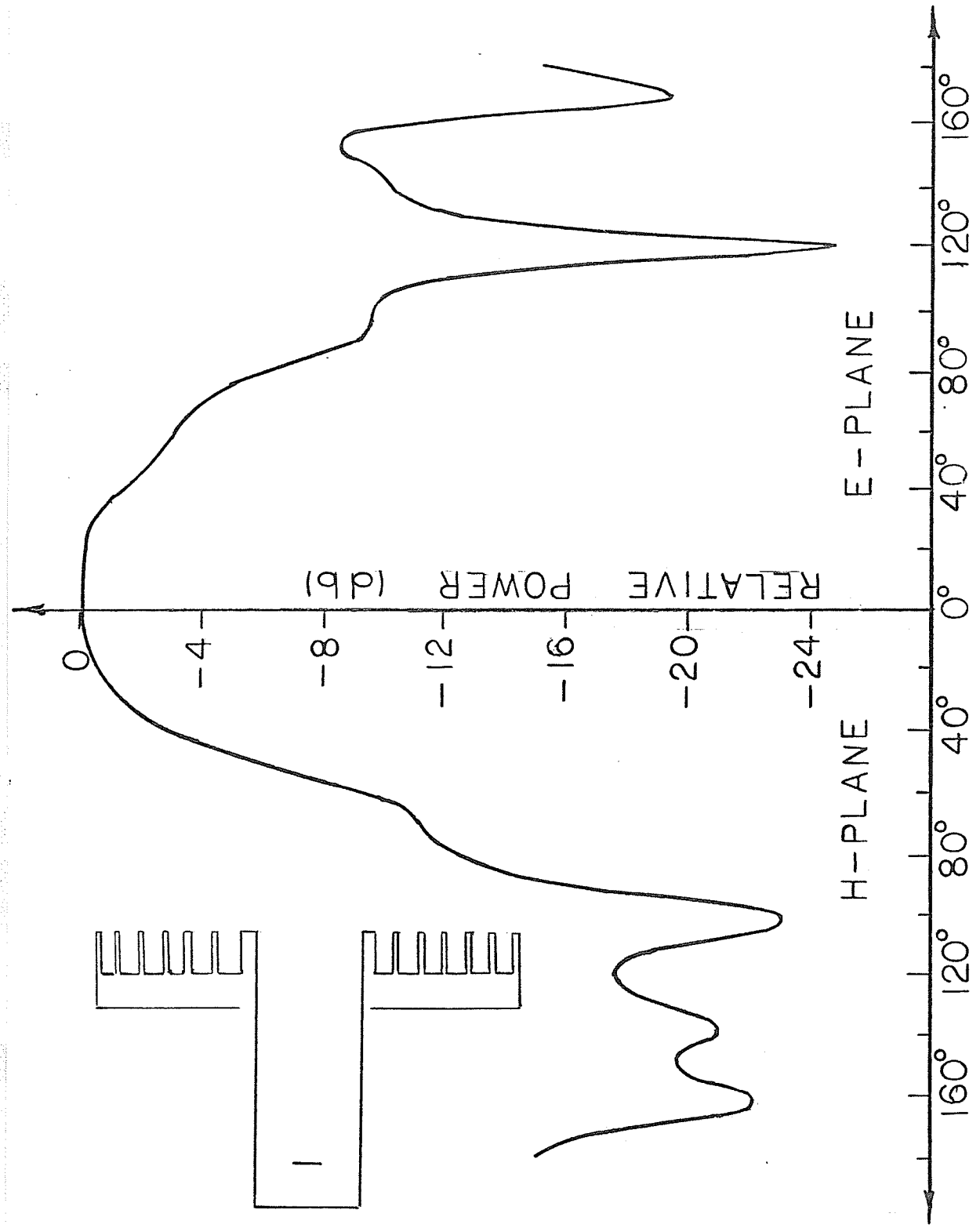

Fig. V.1(b). Unsuccessful Modelling of Corrugated Horn.

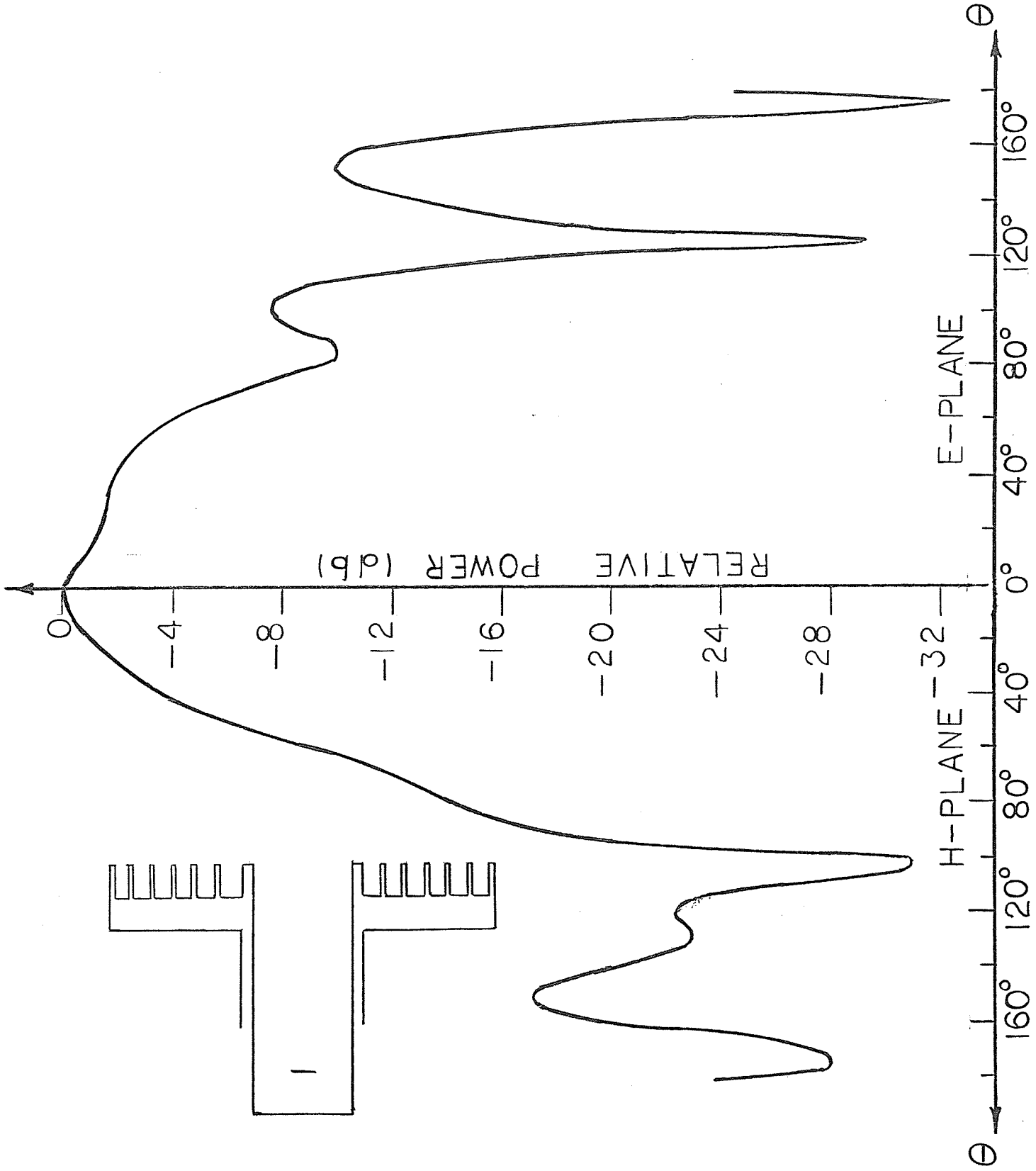

Fig. V.1(c). Unsuccessful Modelling of Corrugated Horn.

lations for this case agreed very satisfactorily with the experimental results (Figure V.2). It was concluded accordingly that all sections of the horn model should be assigned a finite thickness in order to obtain a reliable numerical solution of the integral equation.

The computer program was also tested with single and double precision modes on an IBM 370 computer model. No appreciable difference was observed in the co-polar patterns when the arithmetic precision was doubled (Figure V.3a). As for the cross-polar patterns, a small shift in the values of the maximum and minimum was observed (Figure V.3b). The maximum difference between the two curves is around 4dB at a level of -40dB of cross-polarization. This means a deviation of 10% between values obtained by single and double precision calculations. Considering the fact that, for horns with rotationally symmetric patterns, the cross-polarization is the difference between two quantities, almost identical, (see equation 5.4), then the deviation in the results obtained through single precision arithmetic is therefore acceptable for most investigation purposes.

The density of matching points needed for a converging solution was investigated for two particular waveguide dimensions. In the first case, the waveguide radius a/λ was chosen midway between its respective cutoff values for the dominant and first higher order mode. In the second case, the waveguide was operated near the cutoff of the dominant mode. Figures (V.4a and b) show the co-polar and cross-polar radiation

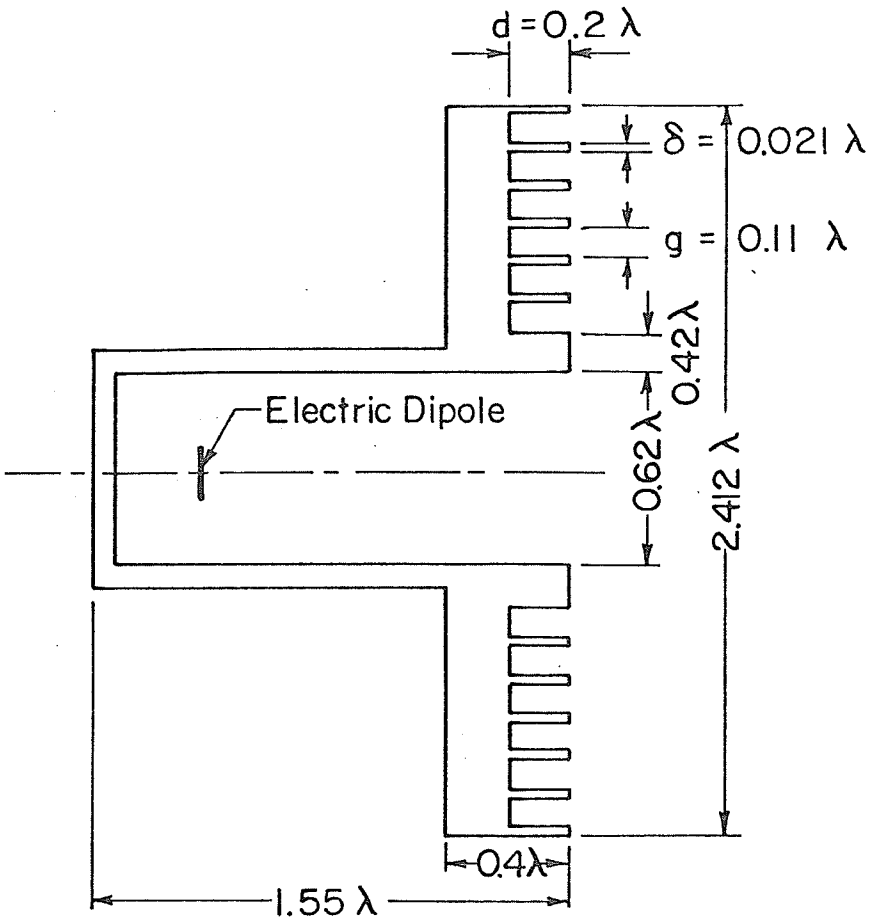

Fig. V.2(a). Thick wall modelling of corrugated horn. (Horn geometry).

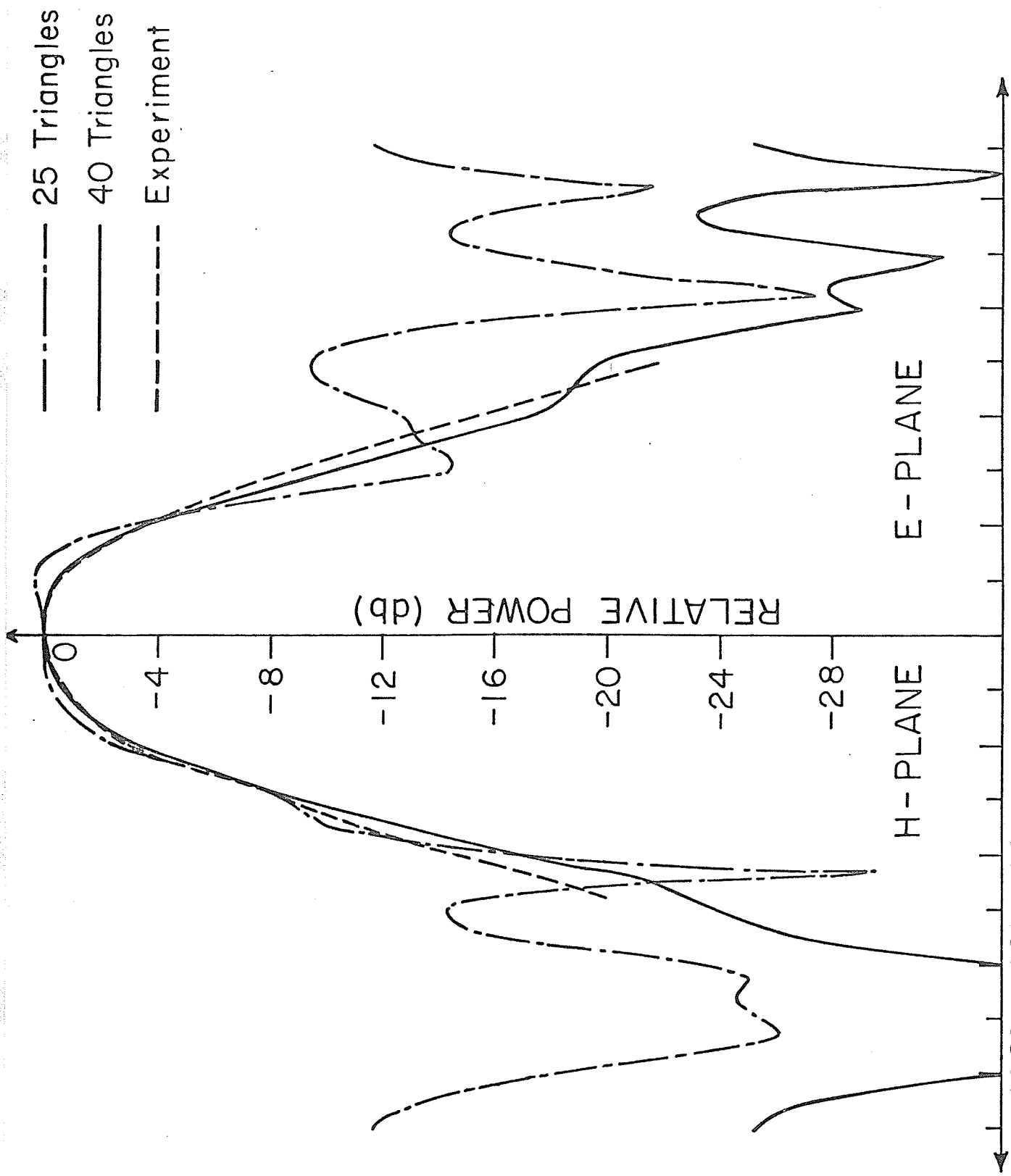

Fig. V.2(b). Thick Wall Modelling of Corrugated Horn. (Radiation Patterns).

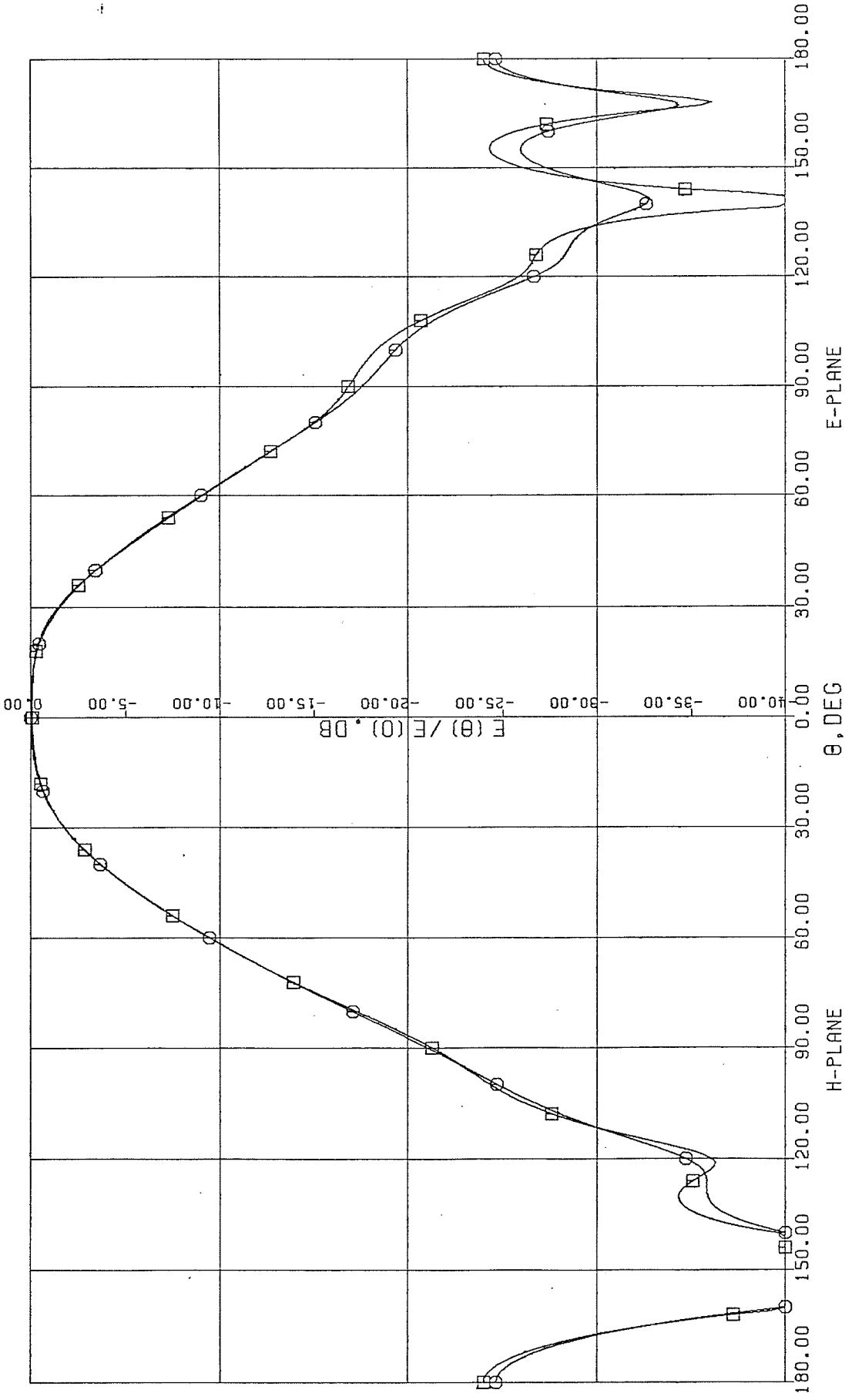

Fig. V.3(a). Co-polar radiation pattern for corrugated horn with $a/\lambda = 0.32$; $d/\lambda = 0.15$; $\alpha = 30^{o}$; NP = 60 .

□ Single precision ; ○ Double precision.

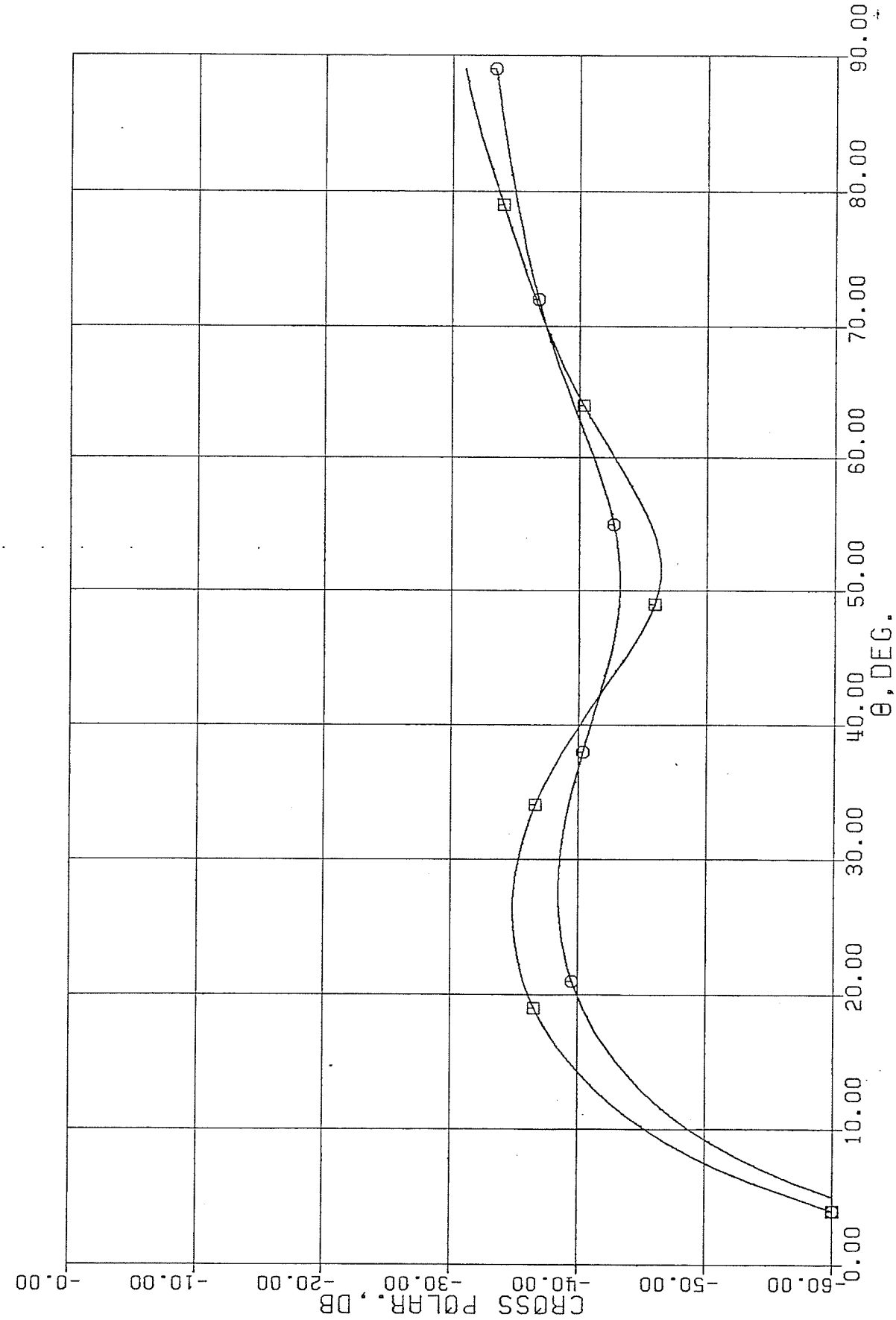

Fig. V.3(b). Cross-Polar radiation pattern for corrugated horn.

$a/\lambda = 0.32$; $d/\lambda = 0.15$; $\alpha = 90^{\circ}$; NP = 60

□ Single precision ; ○ Double precision.

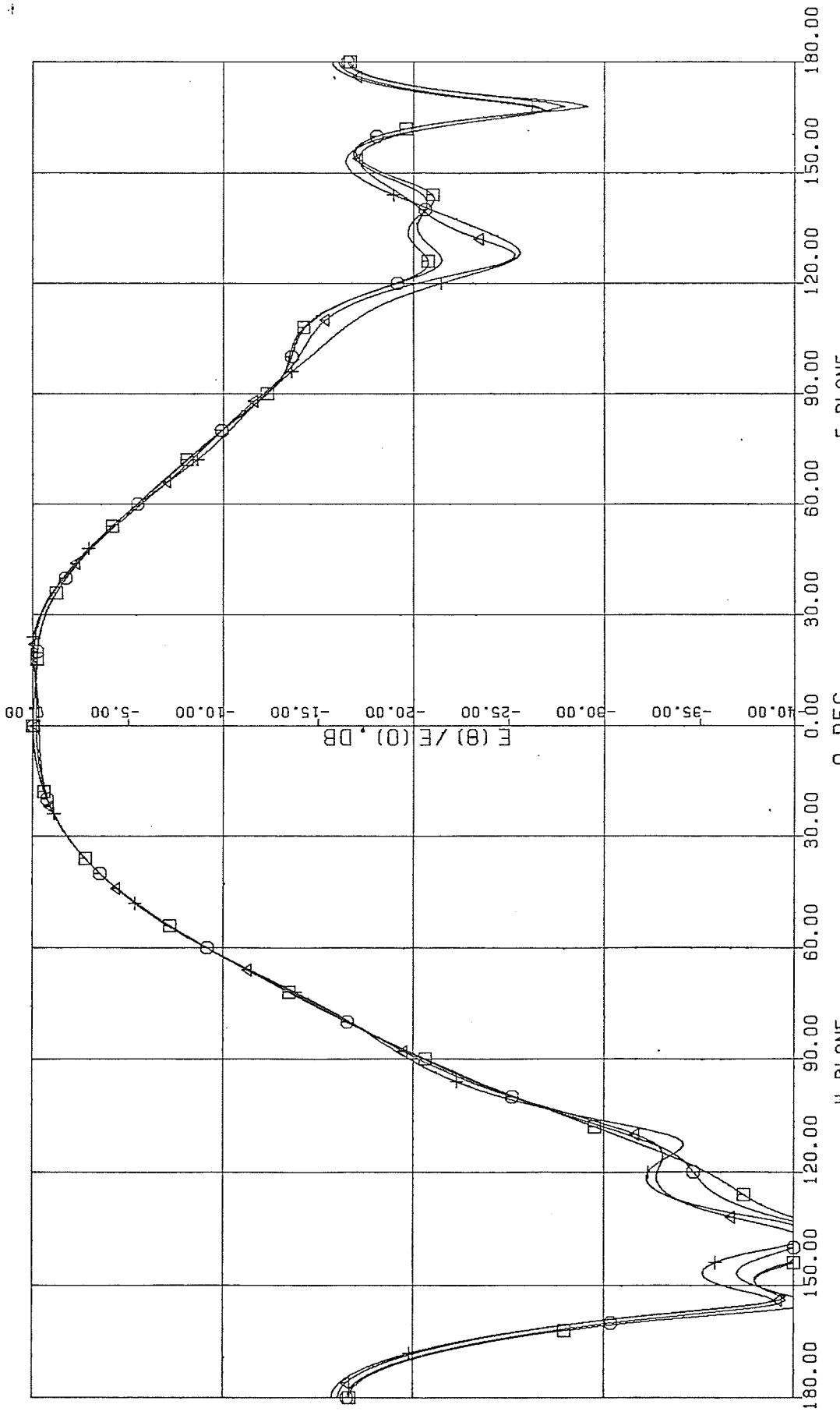

Fig. V.4(a). Co-polar radiation patterns for smooth wall horn ($d/\lambda = 0.0$) with $a/\lambda = 0.36$; $\alpha = 90^{o}$.

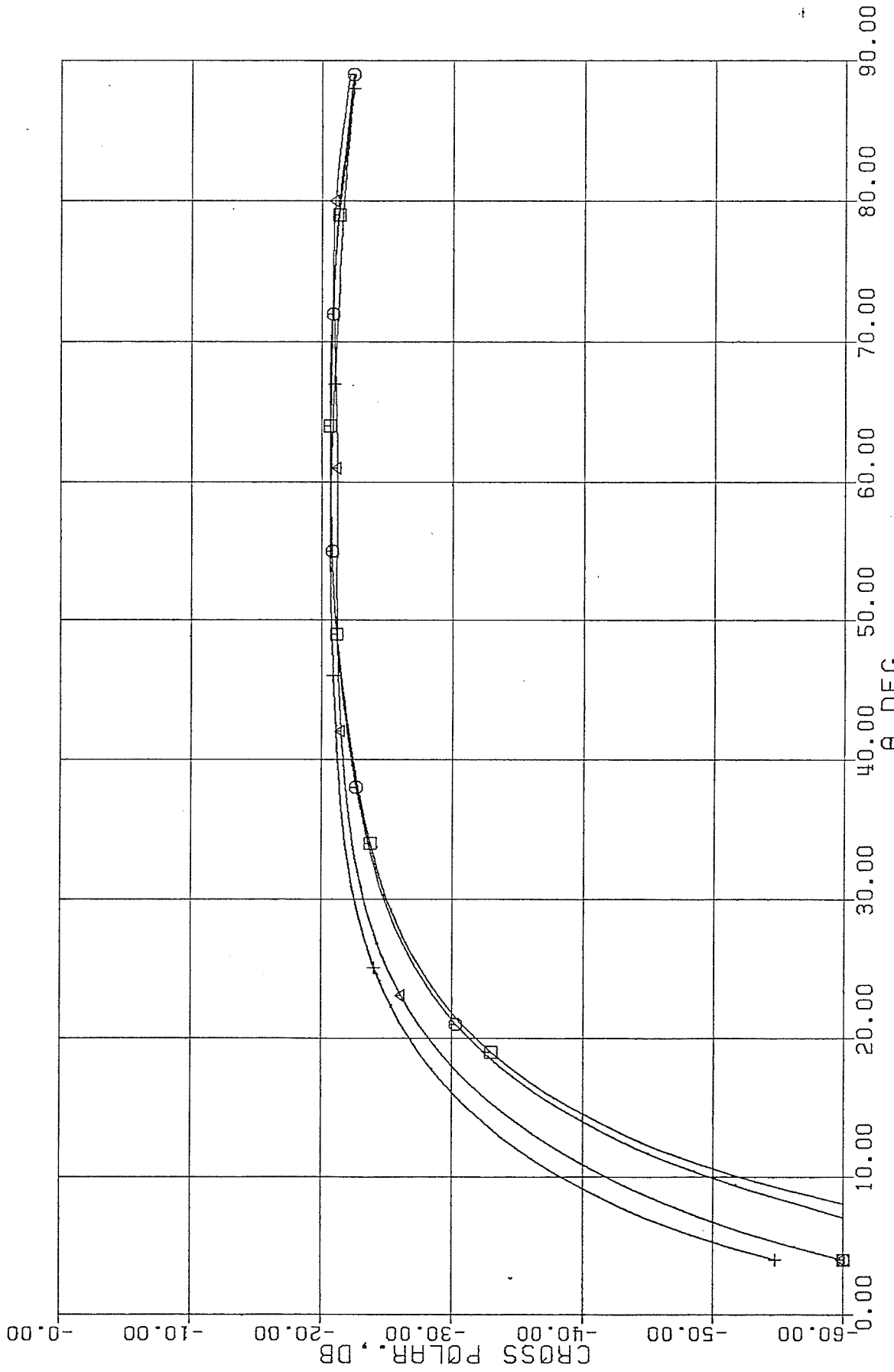

Fig. V.4(b). Cross-Polar radiation pattern for smooth wall horn ($d/\lambda = 0$) with $a/\lambda = 0.36$; $\alpha = 90^{o}$.

+ NP = 30
Δ = 35
□ NP = 50
○ = 60

patterns for the first case.when the total number of matching points was changed from NP = 30 to 35, 50 and 60 points. The H-plane co-polar pattern was practically unchanged, while the E-plane showed differences of few decibels only in a relatively small angular range, and at low levels of radiation. Cross-polarization patterns computed using 50 and 60 matching points were in very good agreement. Low densities of matching points resulted in a slightly higher value of cross-polarization. The maximum value obtained using 30, 35, 50 and 60 points, however, was the same.

For the waveguide operated near cutoff, the results converged when the total number of matching points was approximately 60 points, (Figure V.5a) resulting in matrices of the order of 120 x 120. Lower densities of matching points would usually display high levels of side and backlobes and narrower main beam. They also would result in a higher level of maximum cross-polarization than the value obtained at convergence (Figure V.5b).

It was concluded therefore that an average density of 7 to 8 matching points per wavelength, and the use of single precision mode would constitute an optimum choice. This will result in a convergent solution with minimum computational time, provided operation is not too close to the cutoff of the dominant mode. Discrepancies are more likely to appear in the backlobe region of the E-plane co-polar radiation pattern, where true levels are presumably lower. Cross-polarization patterns might not be exact in the whole angular range but their main features will be usually

displayed. In other words, the maxima of these cross-polarization patterns will be reliable with respect to both values and locations.

From here, several horns with different design parameters were investigated to study the radiation characteristics of rotationally symmetric corrugated horns. The effect of different impedance values was investigated on two groups, with parameters given in connection with Figures (V.6) and (V.7). The horn flare angles were chosen as 90° and 30° for the first and second group, respectively. The effects of the corrugations were investigated by varying the depth d/λ in each case. At first, it was assumed that the $\lambda/4$ slots should give the most desirable patterns. Hence d/λ was assigned a value of 0.251, but the results were disappointing, showing in general high backlobes and sidelobes, and high cross-polarization levels. When d/λ was slightly changed to 0.249, sidelobes and backlobes were still high, and in addition, a null appeared at $\theta=0^{o}$ for the horn with 90° flare angles. At this point, these poor results were thought as due to probable numerical instability in the computer program when large values for the impedance are considered. Hence we turned to the range of $0.25 < d/\lambda < 0.5$ which provides a non-resonant capacitive impedance surface. Since capacitive walls cannot support surface waves, this range of d/λ was expected to minimize diffraction at the horn aperture. Still however, high backlobe levels were observed in both the E- and H-planes, with very wide main radiation beam. Finally, when d/λ was assigned values in the range between 0.0 and 0.25, results were extremely impressive. For corruga-

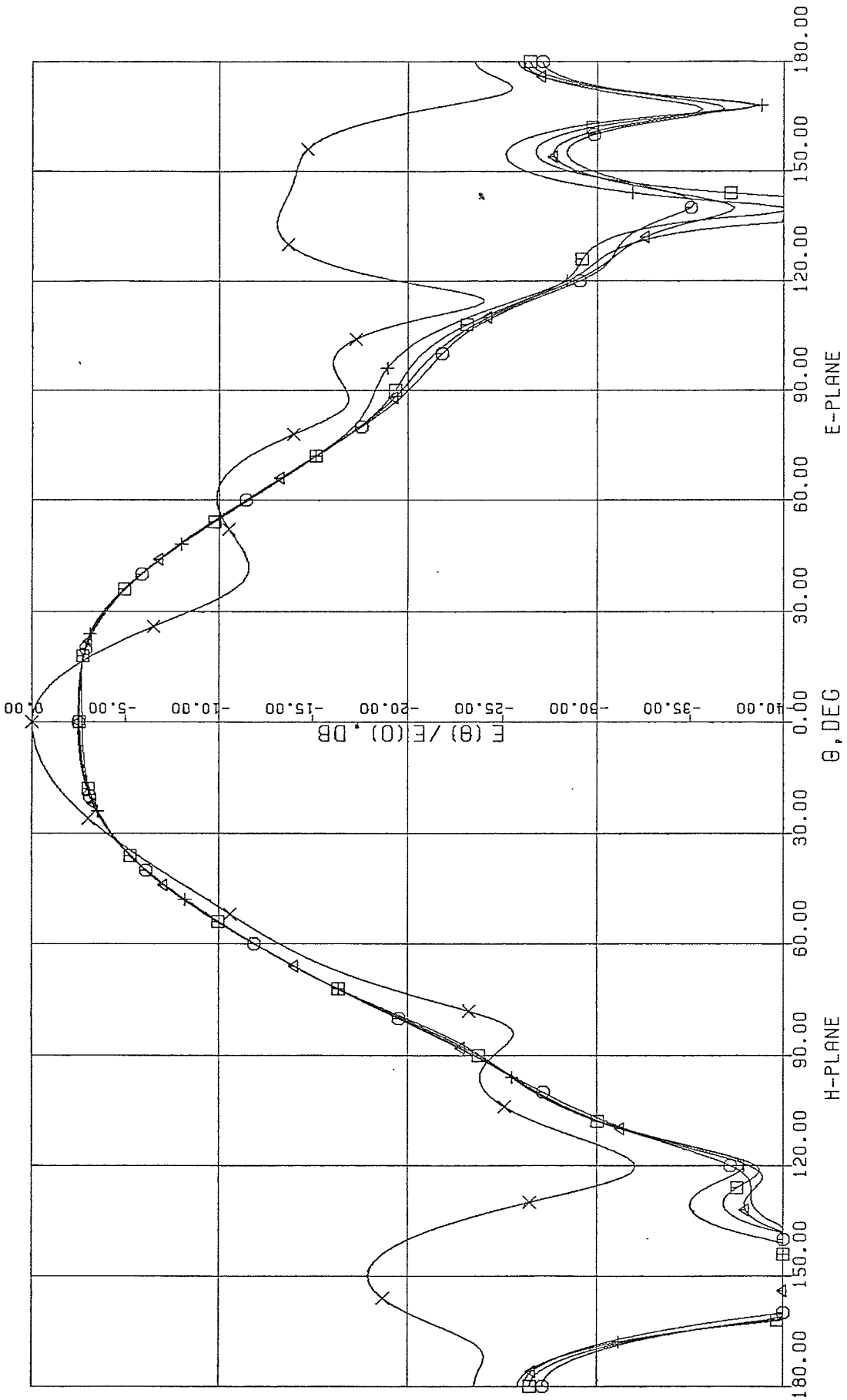

Fig. V.5(a). Co-polar Radiation Pattern for Corrugated Horn with
a/λ = 0.32 d/λ = 0.15 α = 90°
x NP = 30 Δ NP = 50
+ = 35
□ = 40 ○ = 60

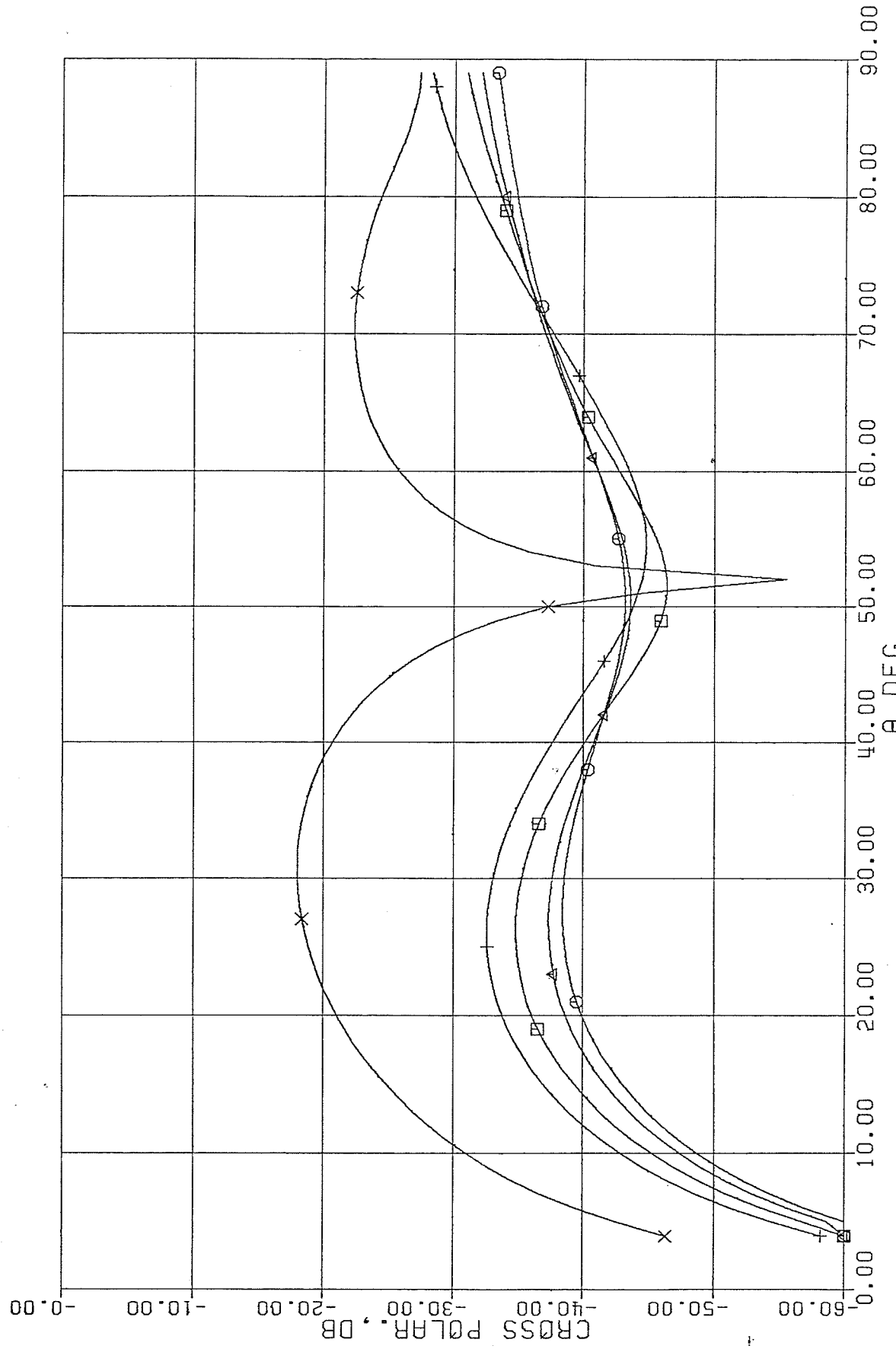

Fig/ V.5(b). Cross-polar Radiation Pattern for Corrugated Horn with
a/λ = 0.32 d/λ = 0.15 α = 30°
x NP = 30 Δ NP = 50
+ = 35
□ = 40 ○ = 60

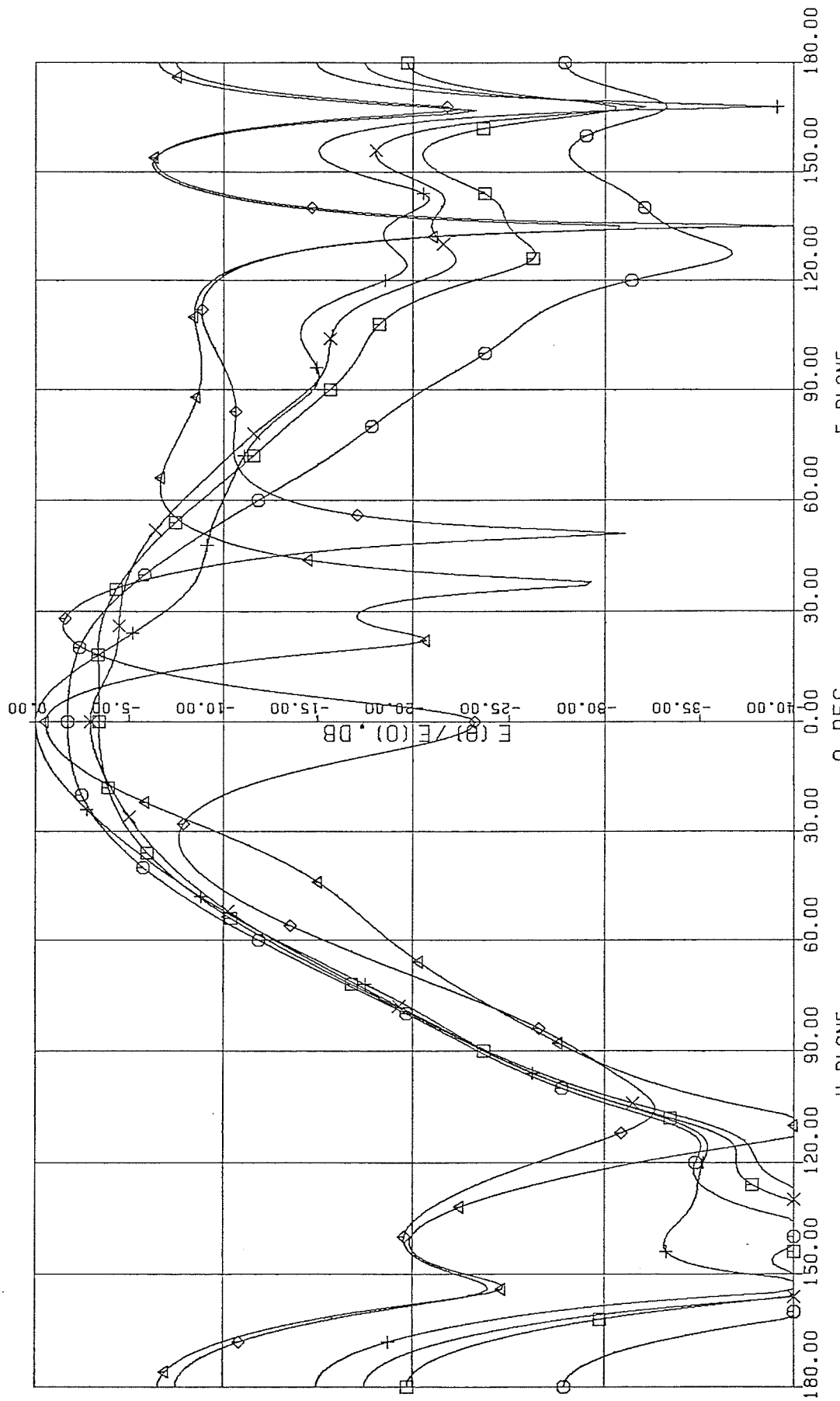

Fig. V.6(a). Co-polar Radiation Pattern for Corrugated Horn with $a/\lambda = 0.36$ $\alpha = 90^{o}$

□ $d/\lambda = 0.0$ Δ $d/\lambda = 0.251$

○ $= 0.15$ + $= 0.35$

◇ $= 0.249$ x $= 0.45$

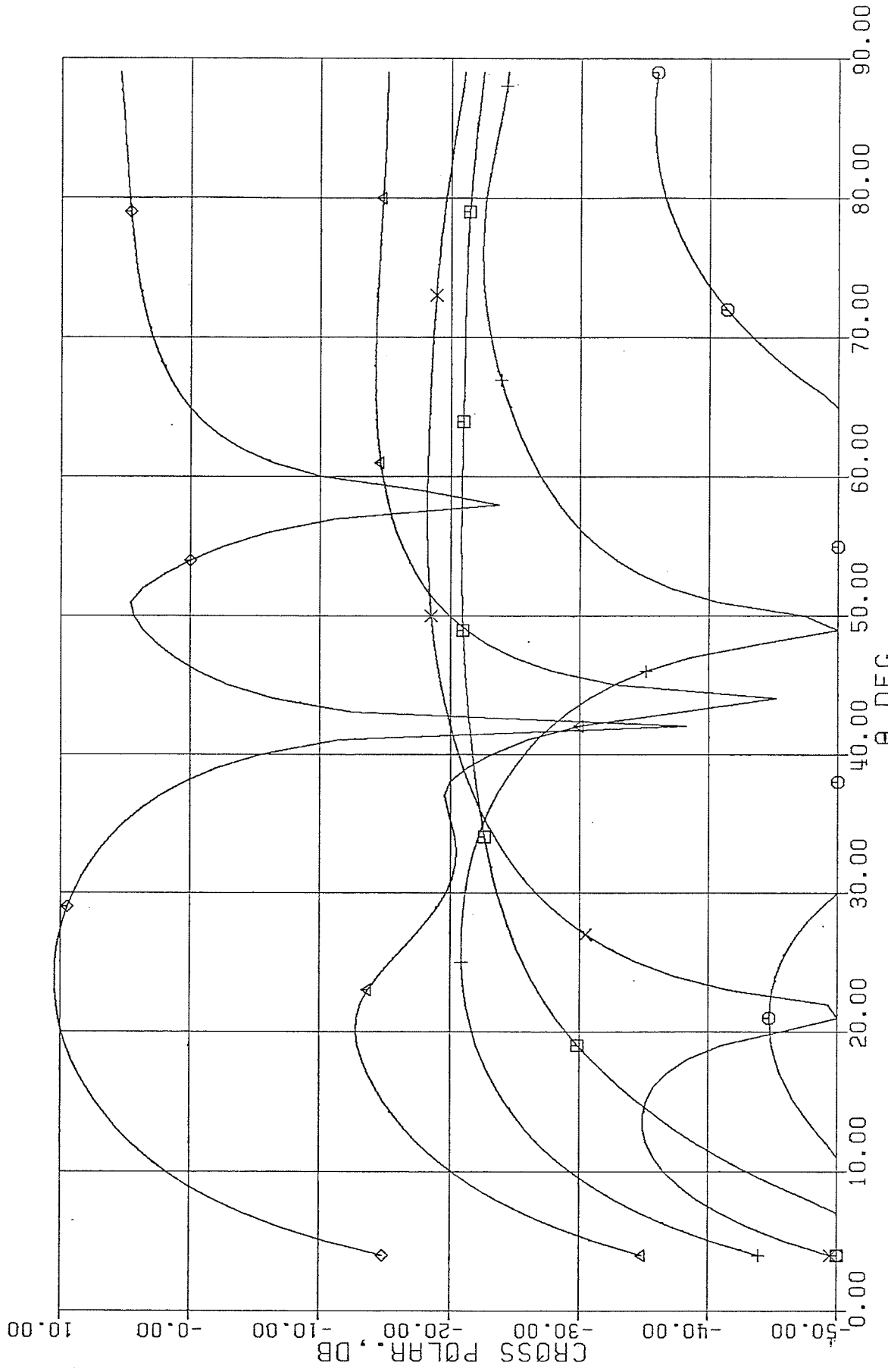

Fig. V.6(b). Cross-polar Radiation Pattern for Corrugated Horn with $a/\lambda = 0.36$ $\alpha = 90^{\circ}$

□ $d/\lambda = 0.0$ + $d/\lambda = 0.35$

○ $= 0.15$ x $= 0.45$

△ $= 0.251$

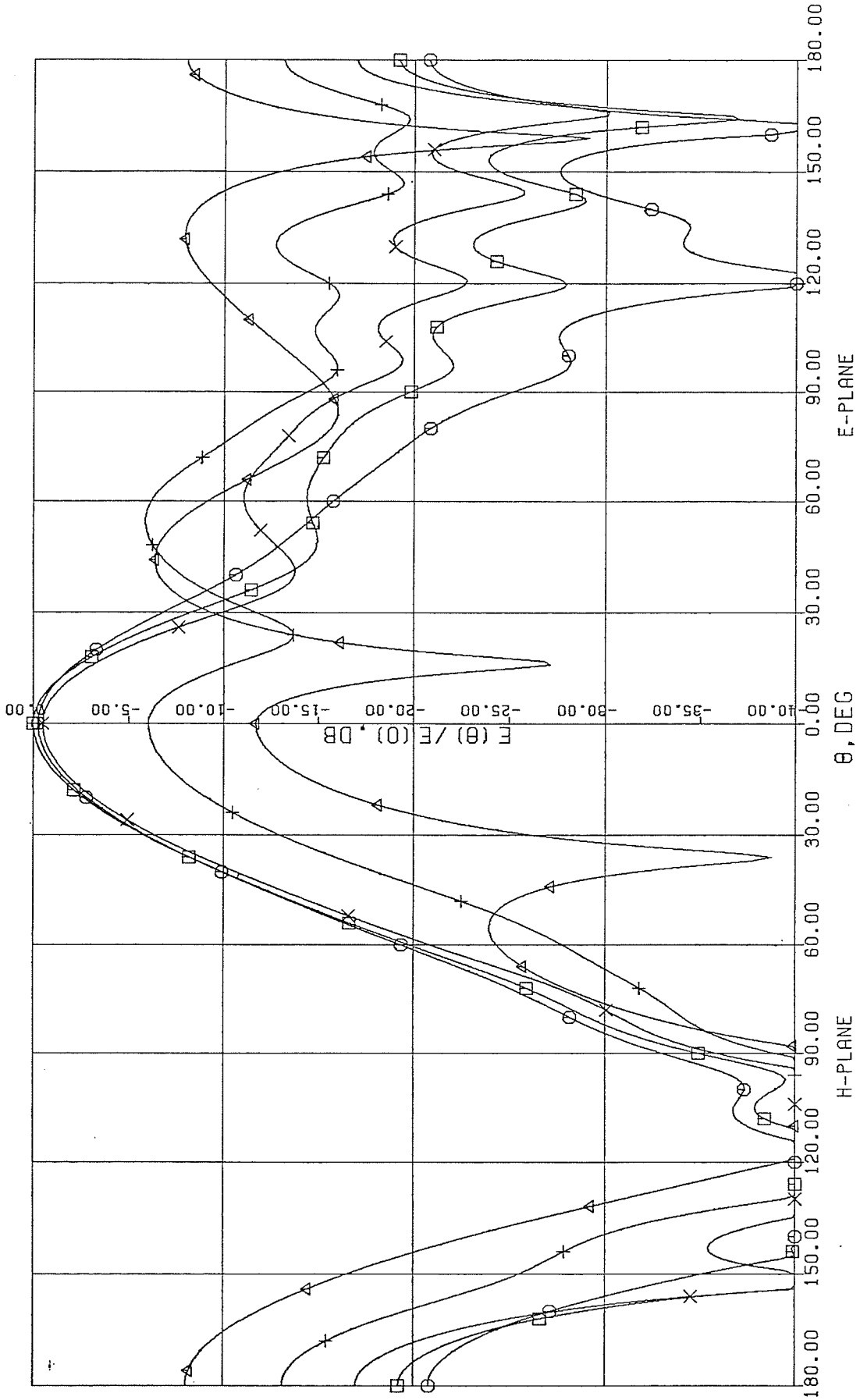

Fig. V.7(a). Co-polar Radiation Pattern for Corrugated Horn with
$a/\lambda = 0.36$ $\alpha = 30^{o}$
□ $d/\lambda = 0.0$ + $d/\lambda = 0.35$
○ $= 0.15$
△ $= 0.251$ x $= 0.45$

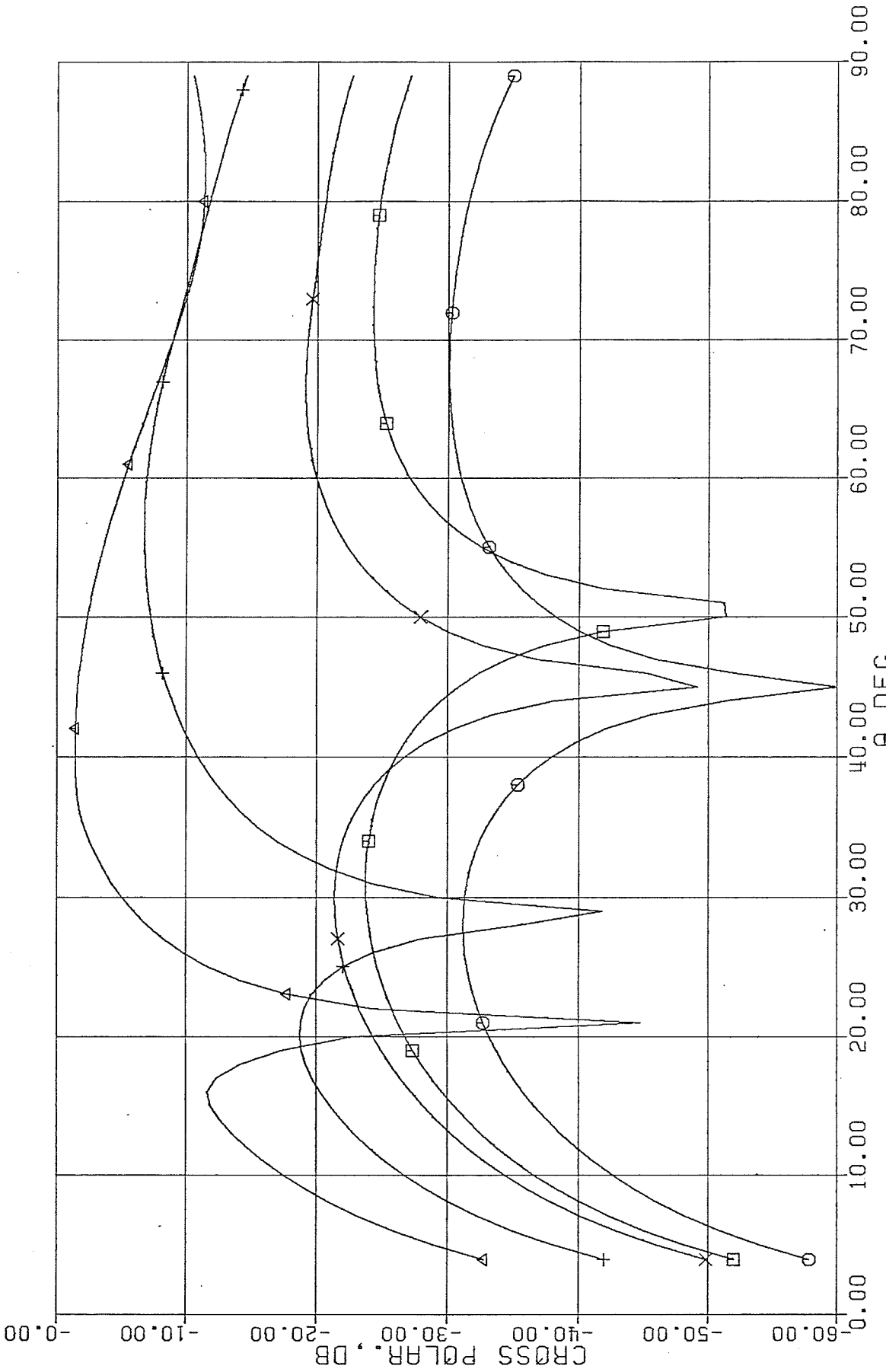

Fig. V.7(b). Cross-polar Radiation Pattern for Corrugated Horn with
$a/\lambda = 0.36$ $\alpha = 30^{o}$
□ $d/\lambda = 0.0$ + $d/\lambda = 0.35$
○ $= 0.15$ x $= 0.45$
△ $= 0.251$

tions with $d/\lambda = 0.15$ and $g/(g+\delta) = 0,84$, the E- and H-plane patterns were almost identical, with higher directivity than in the case of smooth conducting walls. Sidelobe and backlobe levels were also very low. Maxima of cross-polarization patterns occurred at a lower level. Although these desirable features were not expected when d/λ is such that the corrugations present an inductive surface impedance, nevertheless, the same behaviour was obtained from experiment [85] . In fact as was reported before, the experimental results obtained using the horn dimensions mentioned in Section 5.5 agreed satisfactorily with the numerical computation (Figure V.2), hence giving much confidence to our work.

The optimum impedance value for a horn with $a/\lambda = 0.32$ and $\alpha = 90^{o}$ was also obtained by testing several cases as shown in Figures (V.8a and b). The different curves are obtained by changing d/λ from 0.13 to 0.17 in steps of 0.01. Variations were noticed in the E-plane pattern, showing that for optimum performance, d/λ is 0.17 . For this value, the 3dB and 10dB beam widths in both the E- and H-planes are equal 37.5^{o} and 61° respectively. The peak cross-polarization in this case is -48.6dB at an angle $\theta = 50^{o}$ from the axial direction.

5.6 Scattering from Electromagnetic Horns

It is known that a receiving antenna scatters some electromagnetic energy in its process of absorbing power from an incident wave. In

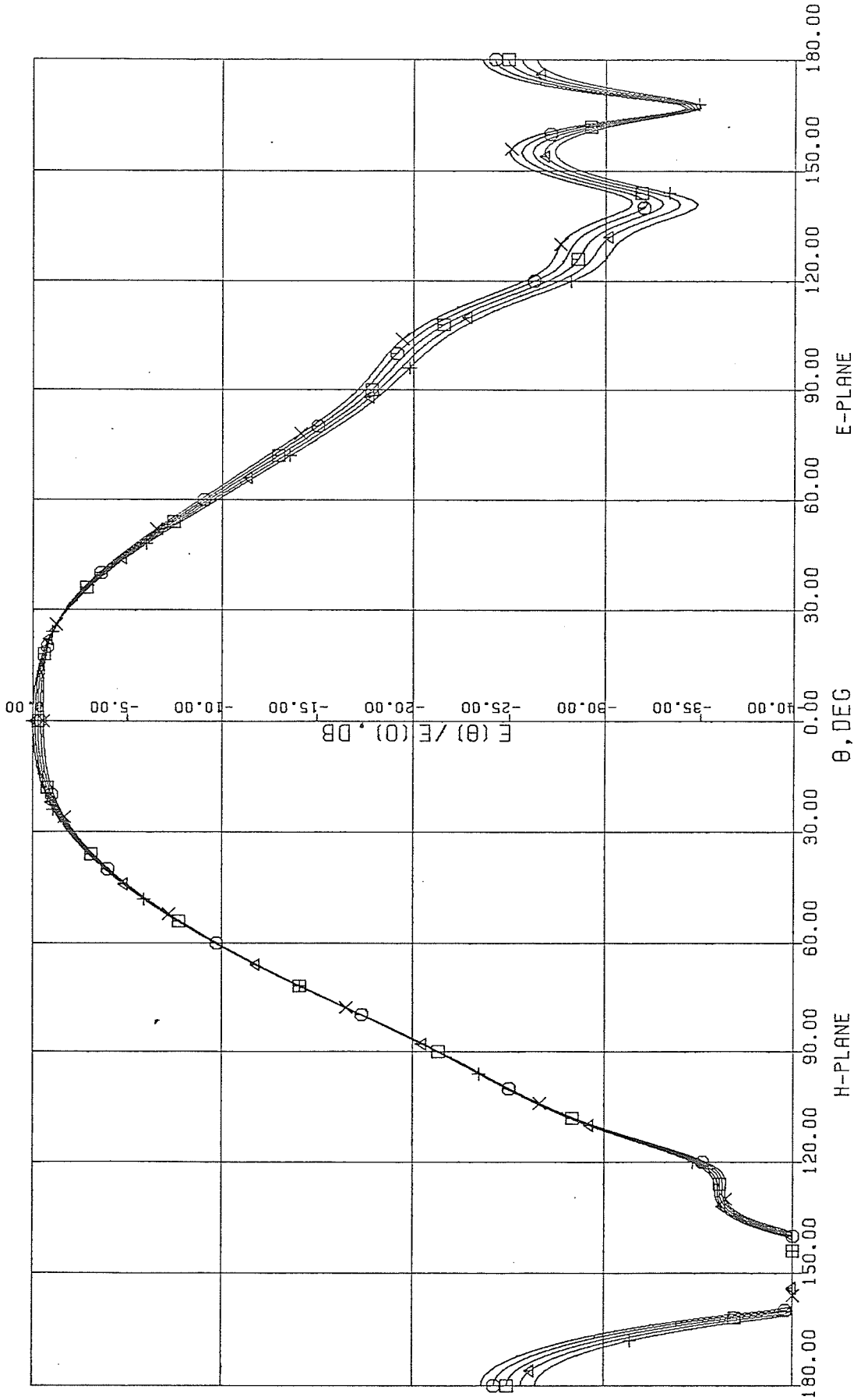

Fig. V.8(a). Co-polar radiation patterns for optimum corrugated horn with $a/\lambda = 0.32$; $\alpha = 90^{o}$; $g/g+\delta = 0.84$.

x $d/\lambda = 0.13$ Δ $d/\lambda = 0.16$

○ $= 0.14$ + $= 0.17$

□ $= 0.15$

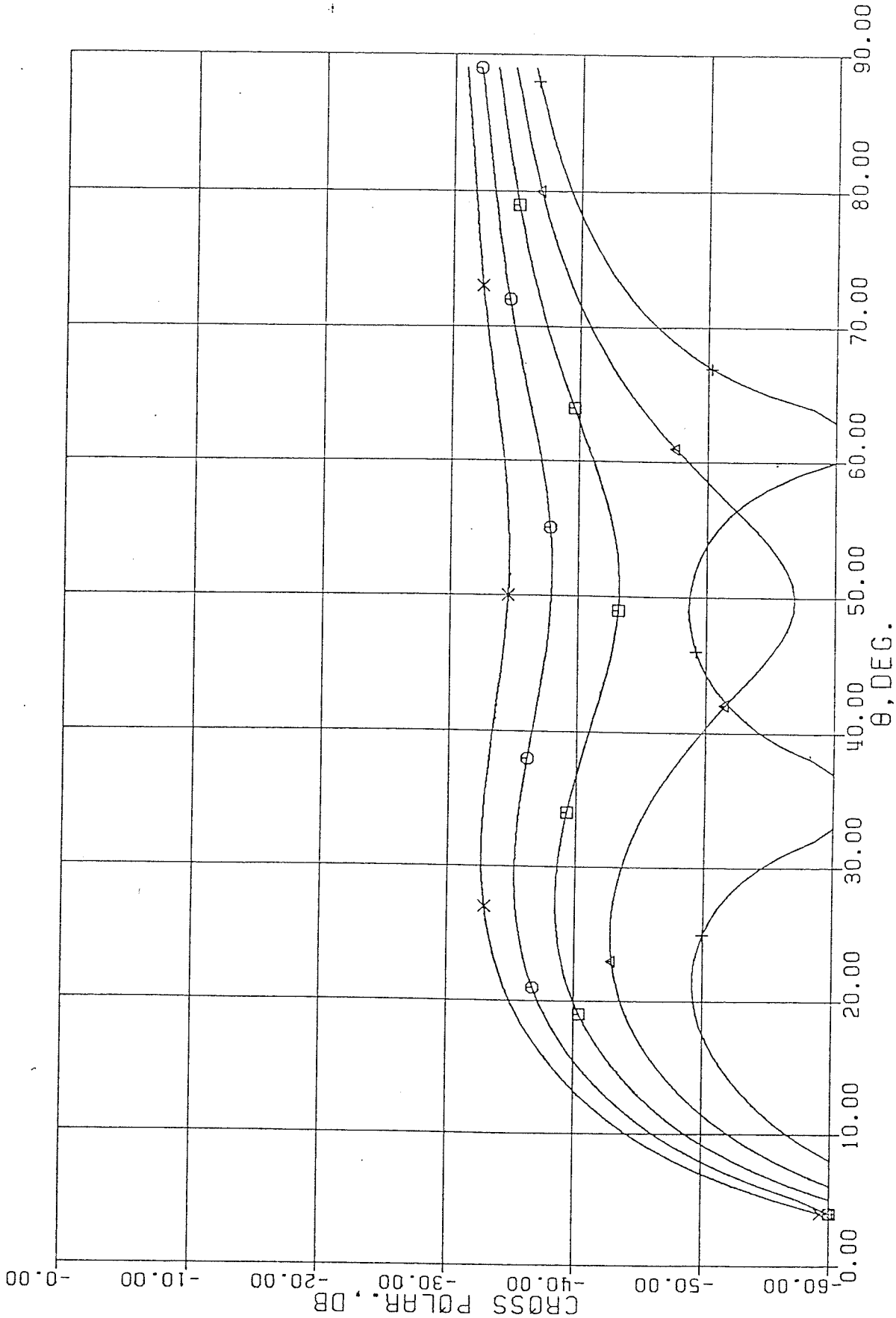

Fig. V.8(b). Cross-Polar radiation patterns for optimum corrugated horn with $a/\lambda = 0.32$; $\alpha = 90^{\circ}$.

x d/λ = 0.13 Δ d/λ = 0.16
○ = 0.14
□ = 0.15 + = 0.17

fact, the reception mechanism may be viewed as one of destructive interference where the antenna scatters a field that cancels certain components of the incident field. In general, the scattering and radiation patterns of the antenna are different. However, if this antenna is to be made invisible, it must scatter a field of structure identical with that which it radiates [86] .

Accordingly, the determination of the scattered field from an antenna becomes important for any proper design. Scattered field determination is also of great interest in problems of spherical near field measurements (SNF) as well as in paraboloidal reflection antenna systems. The SNF technique is based on a theory which does not take into account the multiple scattering between the test antenna and the measuring probe. It is important to study the scattering properties in this case since reflections from the probe could introduce errors to the measurements. On the other hand, a study of the scattering properties of the primary feed in reflector antennas could be used to study the effect of aperture blockage on the radiation pattern.

Detailed studies of the scattering by small dipoles and loops have been carried out by Harrington [87] . Scattering by loaded cylindrical antennas from a boundary value point of view is described by King [88], Chen and Lepa [89] and Chen [90] . Studies on the scattering properties of electromagnetic horns, however, seem very limited. The only work that we are aware of, in this subject, is that of Frandsen [91], which became

available at the time of our present investigation. Frandsen's starting equation to calculate the scattered field from an antenna with arbitrary load impedance, namely $\bar{E}^{sc}(\Gamma_L,\theta,\phi)$ is given by [86]

$$\bar{E}^{sc}(\Gamma_L,\theta,\phi) = \frac{\Gamma_L}{1-S_{00}\Gamma_L}\,\bar{E}_0^s(\theta,\phi) + \bar{E}_d^s(\theta,\phi) \tag{5.7}$$

where Γ_L and S_{00} are the load and the antenna reflection coefficients, respectively (Figure V.9). θ and ϕ are the usual spherical coordinates. The first term on the right hand side of (5.7) is the re-radiated field, i.e., the field received by the antenna, reflected from the load and transmitted according to the radiation properties of this antenna. The pattern of $\bar{E}_0^s$ is therefore the radiation pattern of the antenna. $\bar{E}_d^s$ is of course equal to $\bar{E}^{sc}$ when $\Gamma_L = 0$; i.e., the total scattered field when the load is matched.

To determine the three unknowns S_{00}, $\bar{E}_0^s$ and $\bar{E}_d^s$, Frandsen calculated $\bar{E}^{sc}(\Gamma_L,\theta,\phi)$ for three values of Γ_L. He used a computer program developed for the determination of the scattered field from perfectly conducting bodies of revolution, and the three values of Γ_L were obtained by changing the position of the short circuit termination at the inner side of the waveguide section. As a check on the accuracy of the calculations, the scattered field $\bar{E}^{sc}$ was calculated for 4 different positions of the short. In this way one can solve 4 x (3 equations in three unknowns) and obtains 4 independent solutions for the same variable. The difference in the calculated values for the same variable is a measure of the accuracy of this solution.

With the availability of the computer program, ROTM, based on the theory of Chapter IV, the scattered field $\bar{E}^{sc}(\Gamma_L,\theta,\phi)$ can now be computed for any complex value of Γ_L without changing the position of the termination. This is one of the advantages of our treatment as compared to that of Frandsen, since obtaining $\bar{E}^{sc}$ by considering the scattered field from three structures, different in geometry, might not be desirable.

To determine the scattered field $\bar{E}^{sc}(\Gamma_L,\theta,\phi)$ for any value of the reflection coefficient Γ_L, the inner wall of the waveguide termination must be substituted by a proper surface impedance. Hence when $\Gamma_L = 0$, both Z_ϕ and Z_t at the bottom of the waveguide should match the wave impedance of the propagating mode inside the waveguide. Since the dimensions of the feed are usually chosen to allow only for the dominant mode to propagate, the required matching impedance value must therefore be equal to the characteristic impedance of the TE_{11} mode in the circular waveguide. This is given by $(Z_0)^{TE_{11}}$. Hence we have

$$Z_\phi = Z_t = (Z_0)^{TE_{11}} = 120\pi \Big/ \sqrt{1 - \left(\frac{1.841}{2\pi a/\lambda}\right)^2} \tag{5.8}$$

"a" being the radius of the waveguide. It is also understood that both Z_ϕ and Z_t are zero over any section of the scatterer, away from section $a_1\ a_2$ of the guide (Figure V.10).

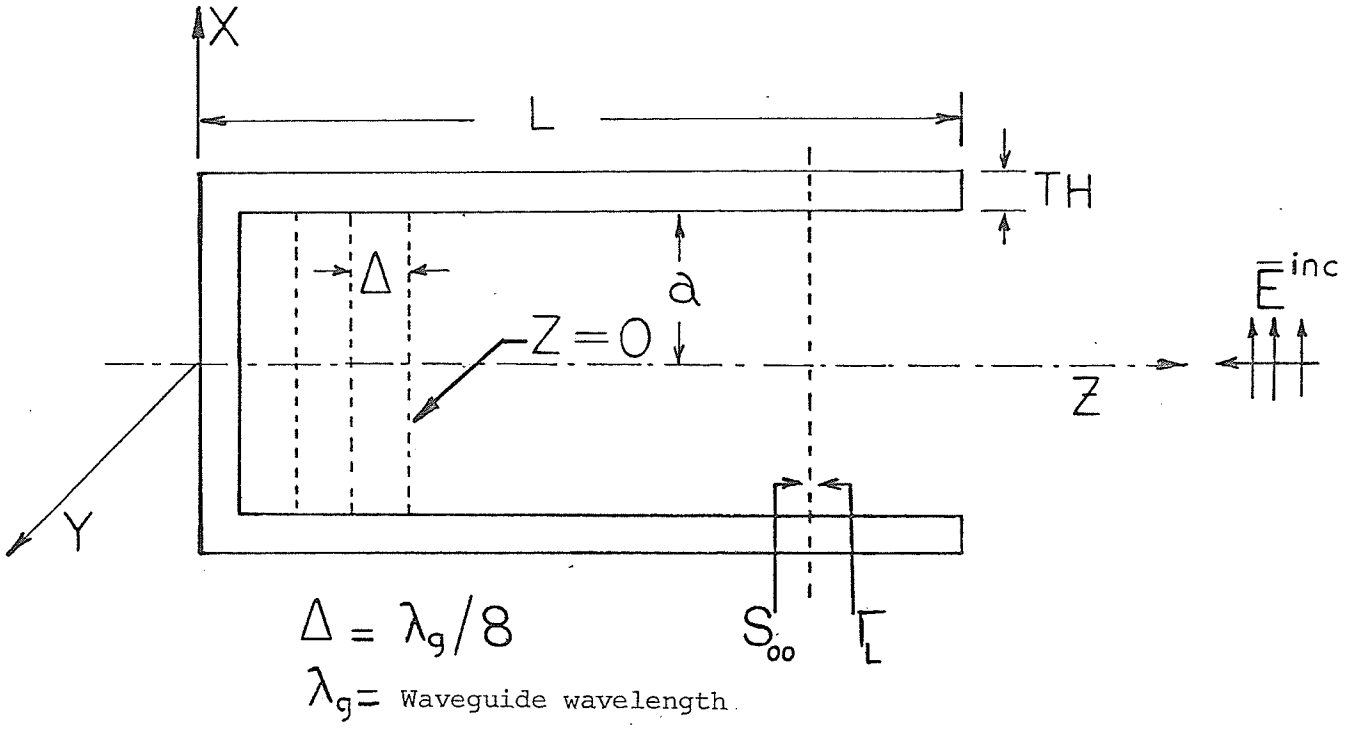

Fig. V.9. Scattering model of receiver horn used by Frandsen [91].

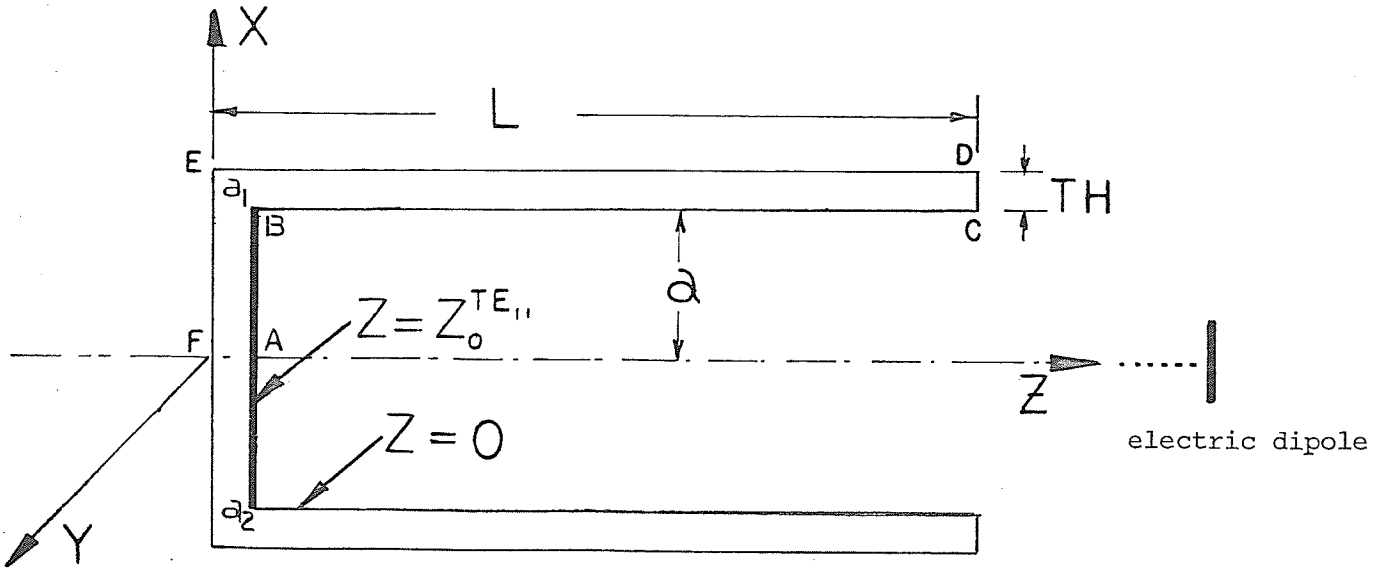

Fig. V.10. Scattering Model using impedance boundaries.

5.7 The Numerical Output

The program ROTM was used to determine the scattering properties of rotationally symmetric horns. The scattering pattern for horns with matching termination was determined by assuming an impedance value as given in (5.8) for the section a_1 a_2 of the generating curve of the horn (Figure V.10). Only open ended waveguides were tested. Plane wave incidence from the axial direction was obtained by placing an electric dipole at a large distance along the z-axis.

Two criteria were used to check the accuracy of the solution. The first was based on the idea that if the correct solution is reached, then increasing the number of matching points along the waveguide should not result in any change in the numerical results. Another accuracy check became available when the guide was terminated by a matching impedance. In this case, the solutions for the tangential currents I_t and I_ϕ must show a travelling wave behaviour along the inner wall of the guide.

Figures (V.11a and b) show the effect of doubling the number of triangle functions expansion used for a waveguide with particular dimensions and a short circuit termination, on the tangential currents I_t and I_ϕ. Figures (V.12a and b) show the results for a matched termination. The corresponding effect on the scattering patterns is shown in Figures (V.11c) and (V.12c). The lower density of matching points was found sufficient for a converging solution when the waveguide is short-

circuited. When it is terminated with a matching impedance, a higher density of matching points is necessary to obtain the traveling wave behaviour in the waveguide. It was also found by experience that the termination should be covered by a high density of points.

On the other hand, the scattered field for both cases of $Z = 0$ and $Z = Z_0^{TE_{11}}$, did not show any appreciable change when the number of matching points was increased appreciably. This of course is a result of the stationary properties of the field.

Figures (V.13a,b and c) show the currents and fields when different values of terminating impedances are considered. It is clear that neither the outer, nor the inner currents can be neglected because of their appreciable relative magnitude. It was also noticed that the currents on the outer walls of the guide were not largely dependent on the value of the termination. When Γ_L is not equal to zero, the currents I_t and I_ϕ are found to oscillate around those obtained in the case of a matching surface impedance.

For some particular waveguide dimensions with matched termination, it was noticed that ripples in the currents along the inner walls still appear with high densities of triangle functions. When the thickness of the walls was changed, these ripples were reduced (Figures V.14 and V.15 (a and b)). It was concluded therefore that the excessive ripples in the former case are due to possible internal resonance of the structure.

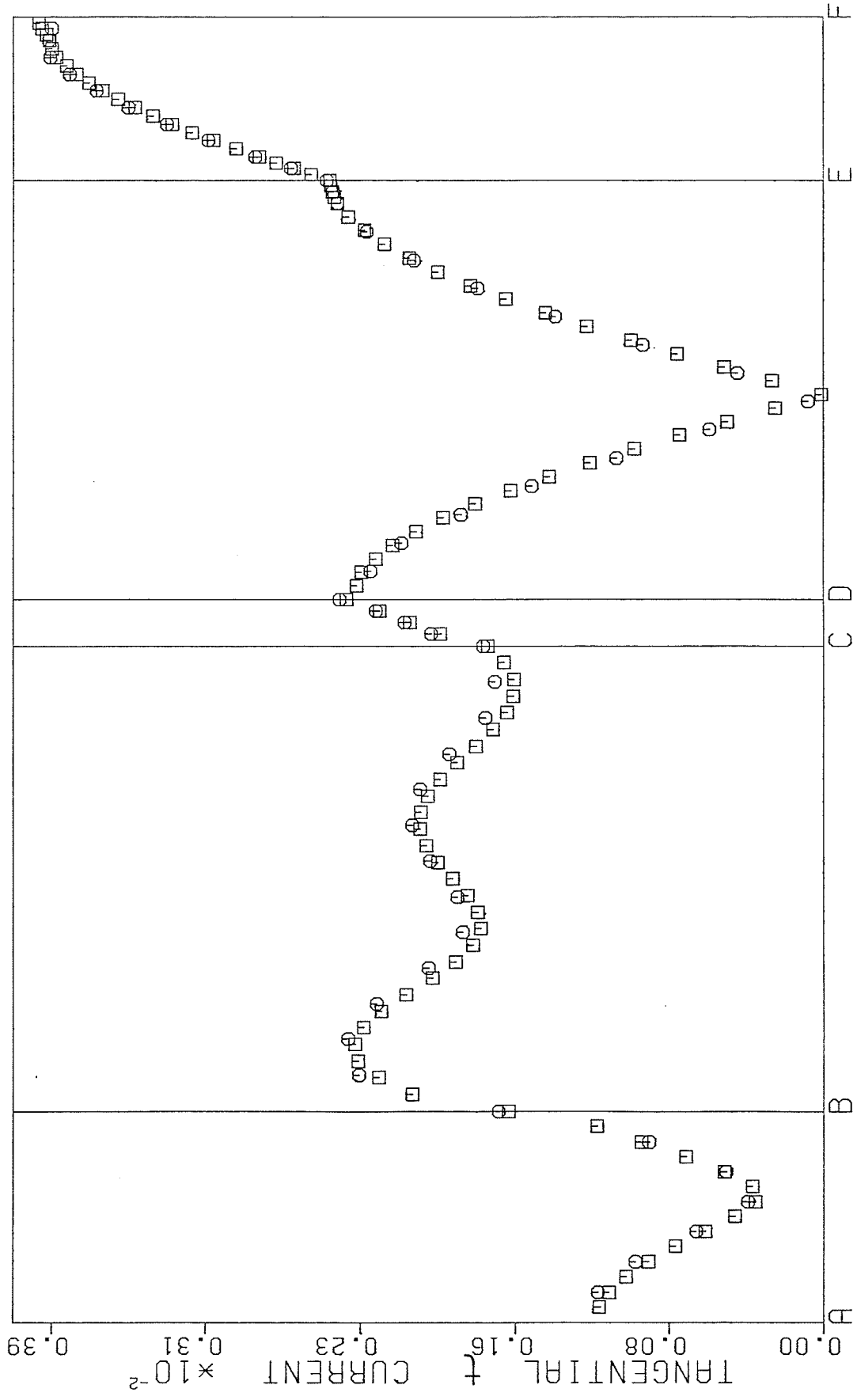

Fig. V.11(a). Induced Current I_t on a Waveguide Section with $Z_t = Z_\phi = 0.0$

L/λ = 1.0 a/λ = 0.35 TH/λ = 0.1

NP = 50

= 100

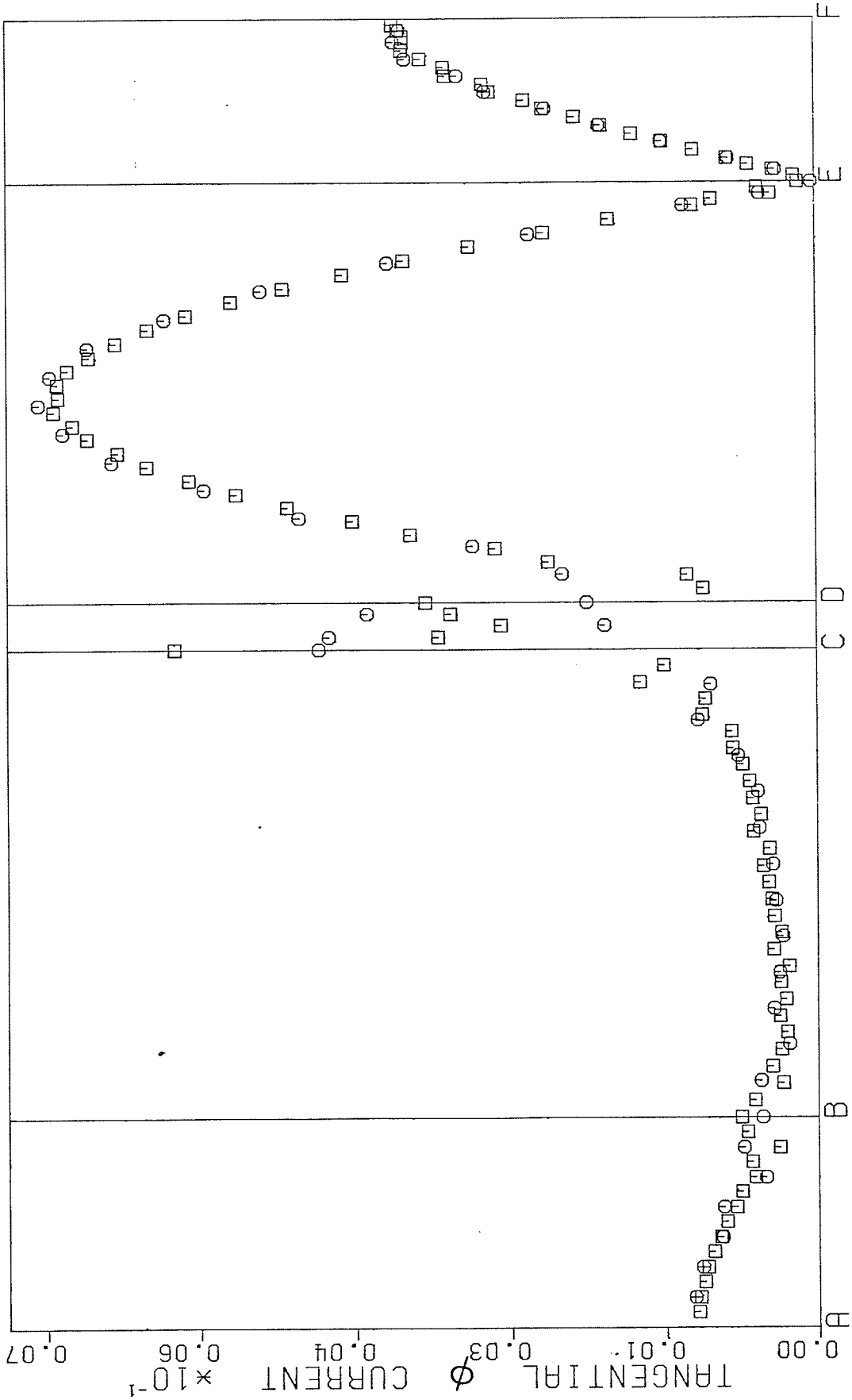

Fig. V.11(b). Induced Current I_ϕ on a Waveguide Section with

$L/\lambda = 1.0$; $a/\lambda = 0.35$; $TH/\lambda = 0.1$; $Z_t = Z_\phi = 0.0$; ○ NP = 50 ; □ NP = 100

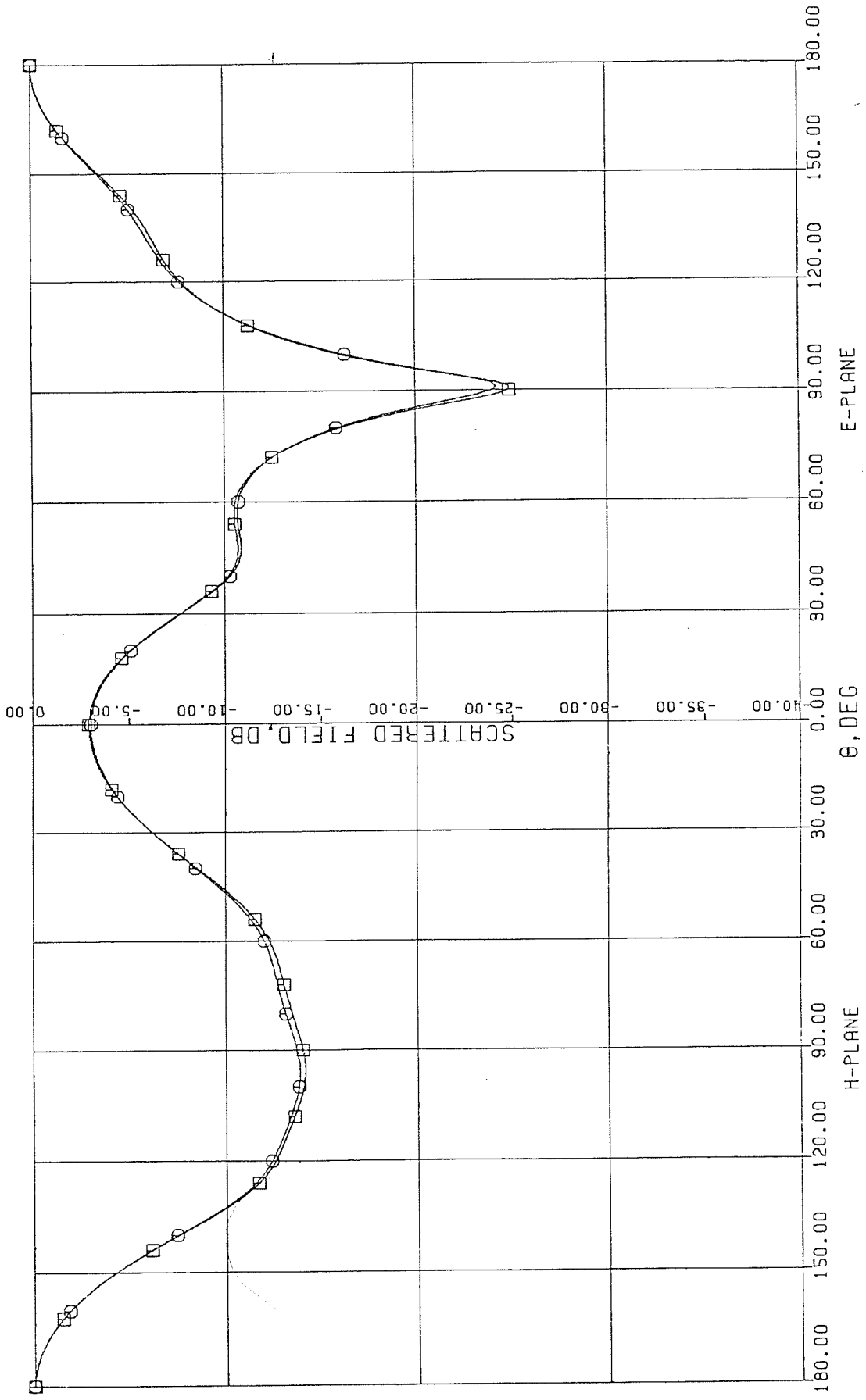

Fig. V.11(c). Scattering Patterns from a Waveguide Section with $L/\lambda = 1.0$ $a/\lambda = 0.35$ $Z_t = Z_\phi = 0.0$

○ NP = 50 □ NP = 100

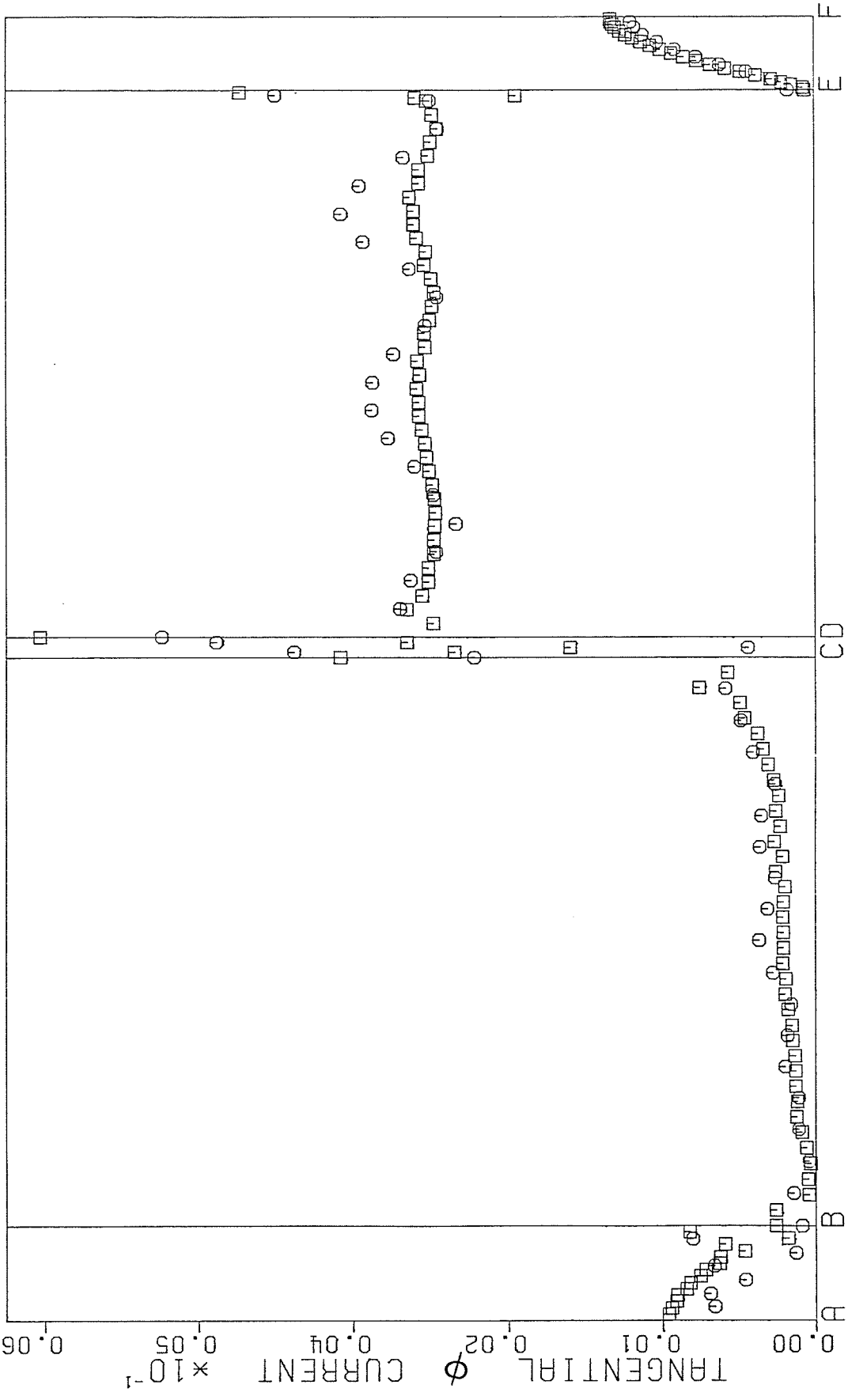

Fig. V.12(a). Induced Current I_t on a Waveguide Section with TE_{11}

$L/\lambda = 2.7$ $a/\lambda = 0.35$ $TH/\lambda = 0.1$ $Z_t = Z_\phi = Z_0$

○ NP = 60 □ NP = 120

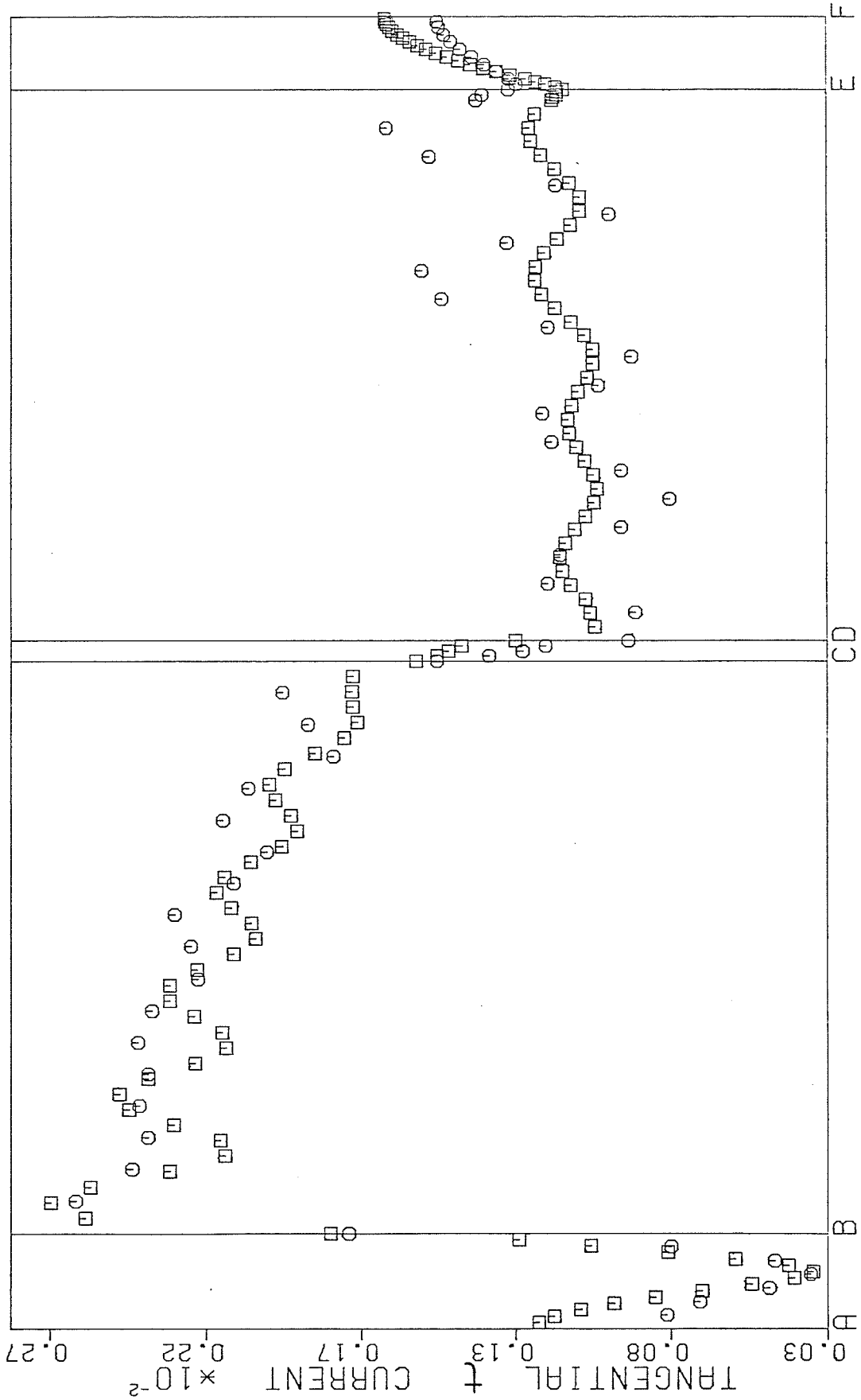

Fig. V.12(b). Induced Current I_ϕ on a Waveguide Section with TE_{11}

$L/\lambda = 2.7$ $a/\lambda = 0.35$ $TH/\lambda = 0.1$ $Z_t = Z_\phi = Z_0$

○ NP = 60 □ NP = 120

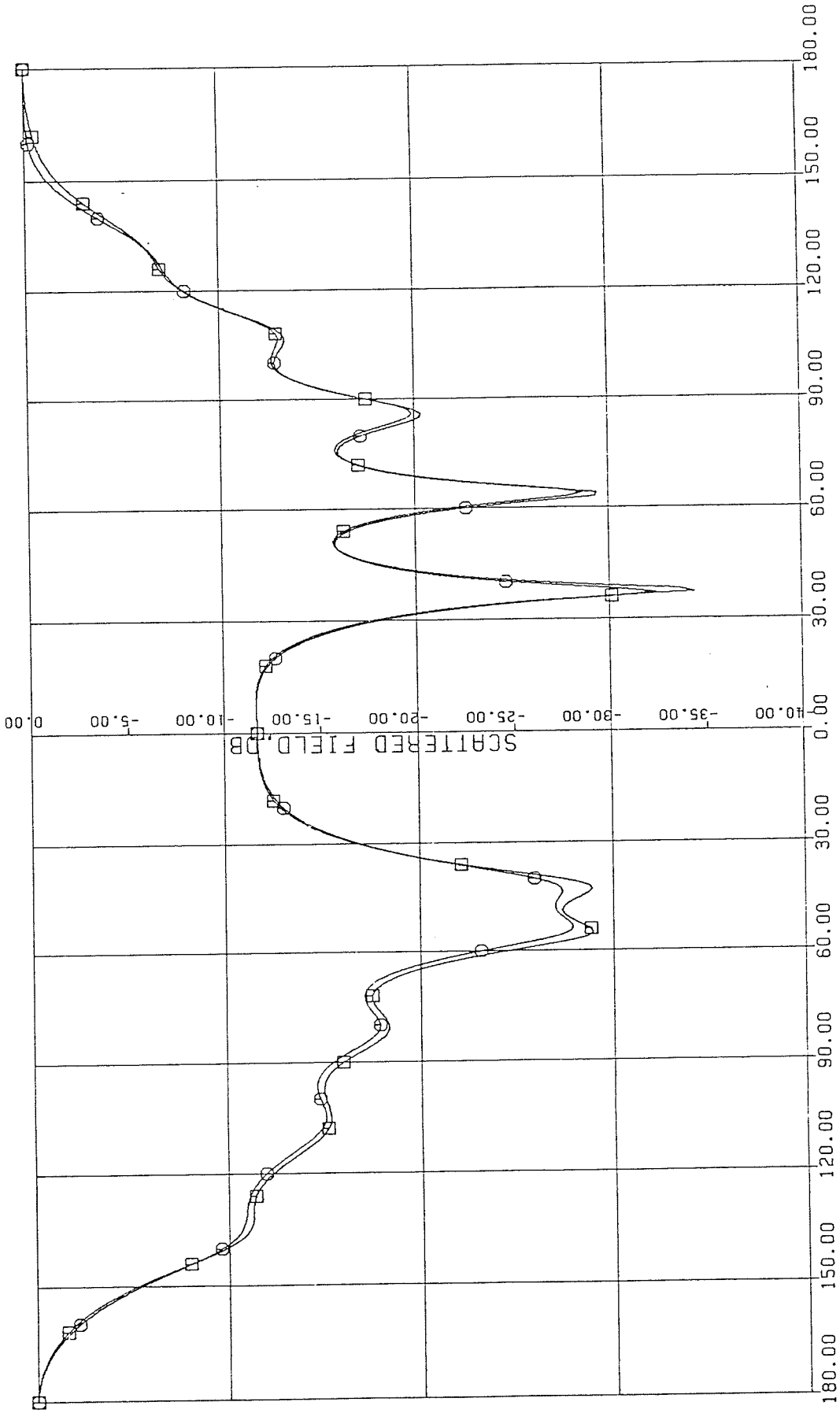

Fig. V.12(c). Scattering Patterns from a Waveguide Section with TE_{11}
$L/\lambda = 2.25$ $a/\lambda = 0.35$ $TH/\lambda = 0.1$ $Z_t = Z_\phi = Z_0$
○ NP = 60 □ NP = 120

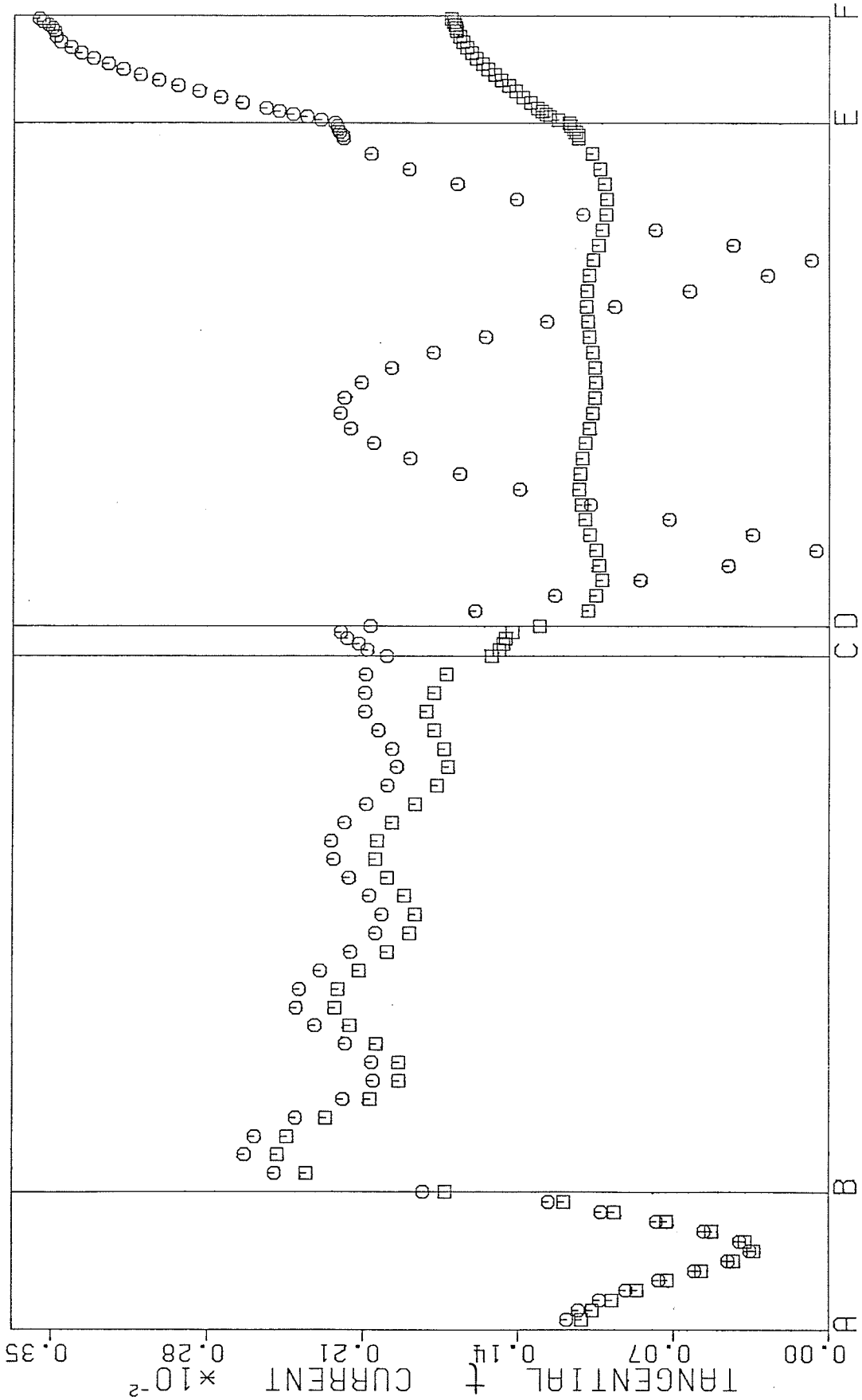

Fig. V.13(a). Induced current I_t on a waveguide section with
$L/\lambda = 1.75$; $a/\lambda = 0.35$; $TH/\lambda = 0.1$;
○ $Z_t = Z_\phi = 0.0$; □ $Z_t = Z_\phi = Z_0^{TE_{11}}$.

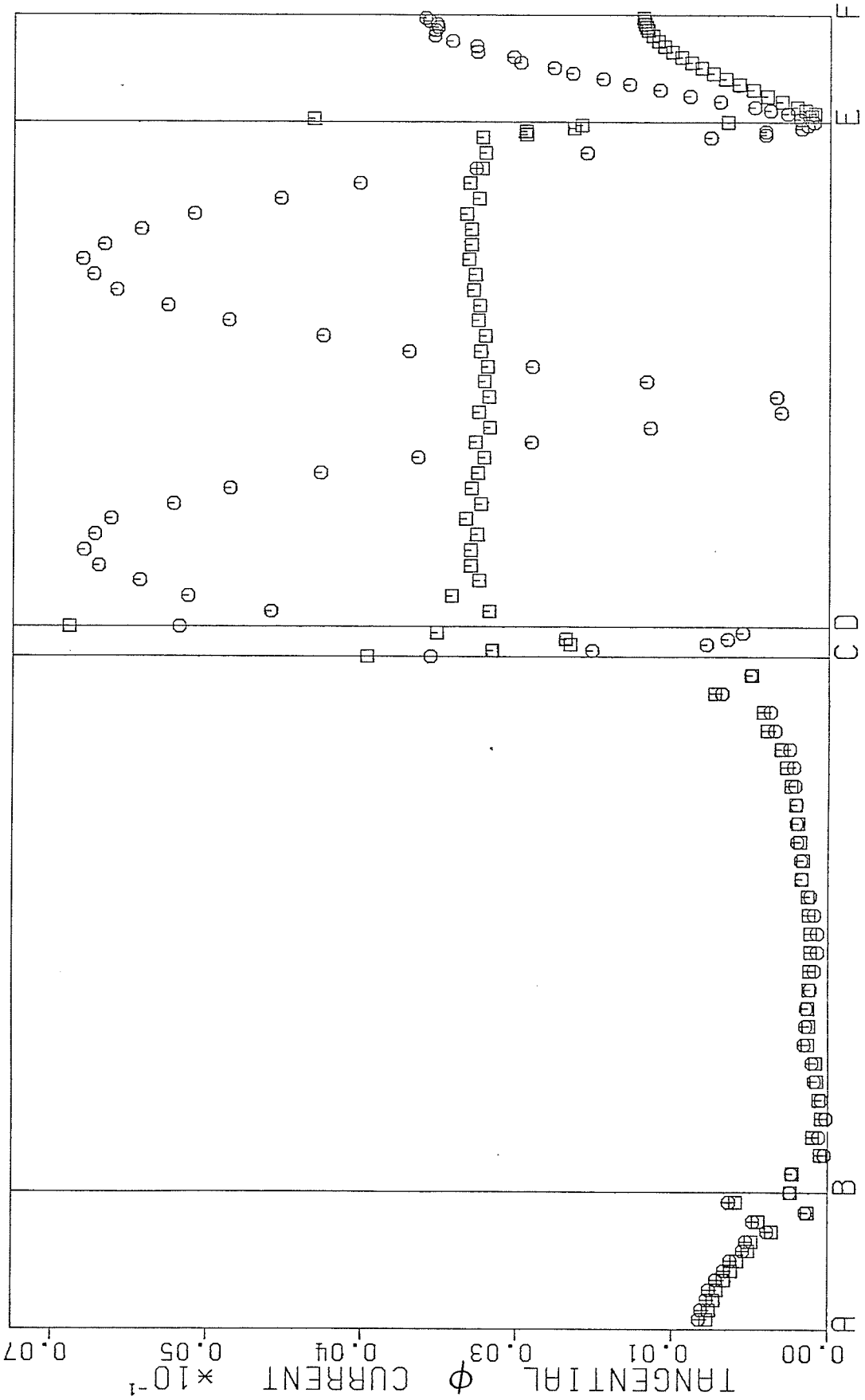

Fig. V.13(b). Induced Current I_ϕ on a Waveguide Section with
$L/\lambda = 1.75$; $a/\lambda = 0.35$; $TH/\lambda = 0.1$;
$\square$ $Z_t = Z_\phi = 0.0$; $\square$ $Z_t = Z_\phi = Z_0^{TE_{11}}$.

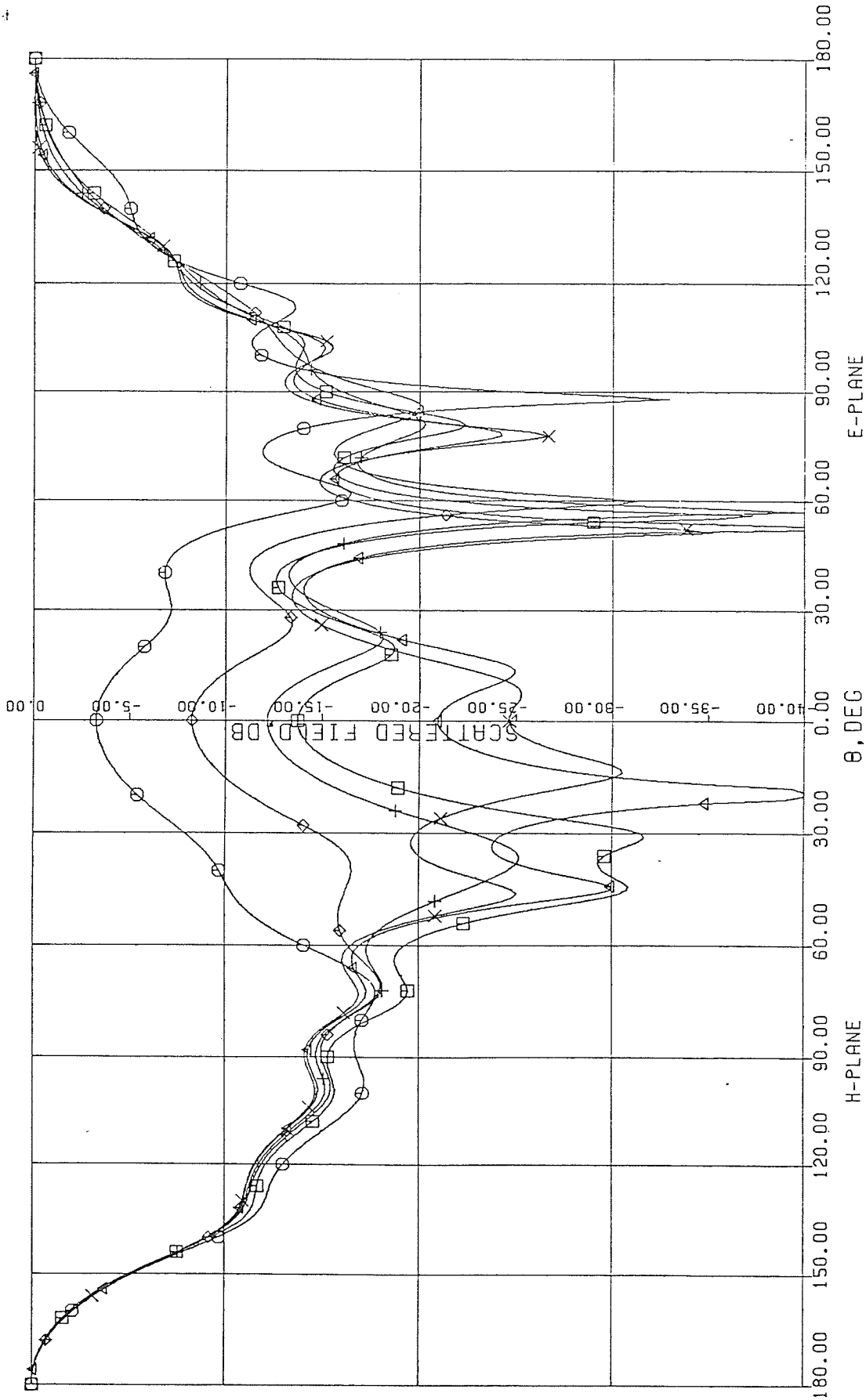

Fig. V.13(c). Scattering Patterns from a Waveguide Section with TE_{11}
$L/\lambda = 2.0$ $a/\lambda = 0.35$ $TH/\lambda = 0.1$ $Z_t = Z_\phi = pZ_0$
○ p = 0.0 □ p = 1.0
◇ = 0.4 △ = 1.3
\+ = 0.7 x = 1.6

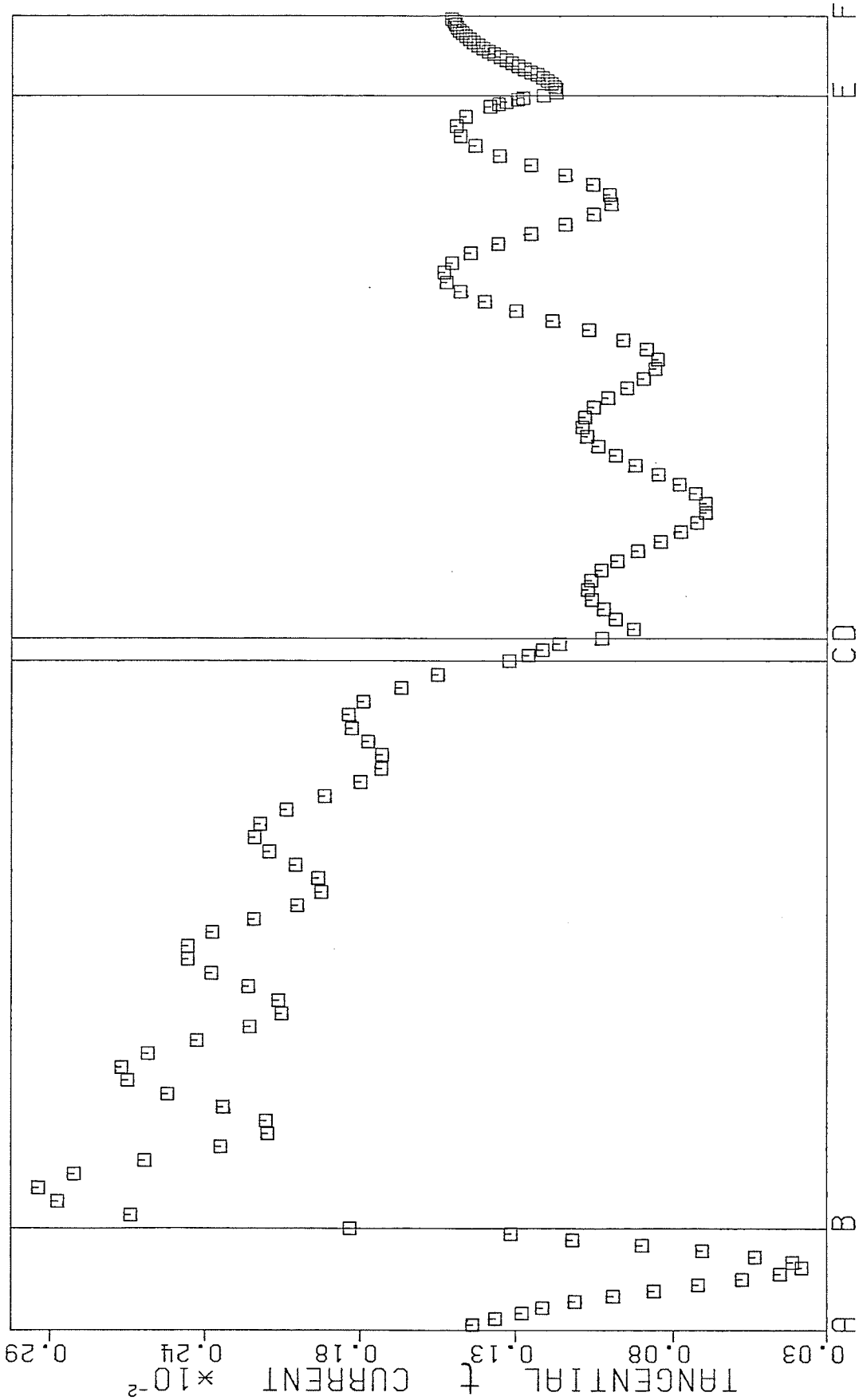

Fig. V.14(a). Induced Current I_t on a Waveguide Section with TE_{11}

$L/\lambda = 2.5$ $a/\lambda = 0.35$ $TH/\lambda = 0.1$ NP = 150 $Z_t = Z_\phi = Z_0$

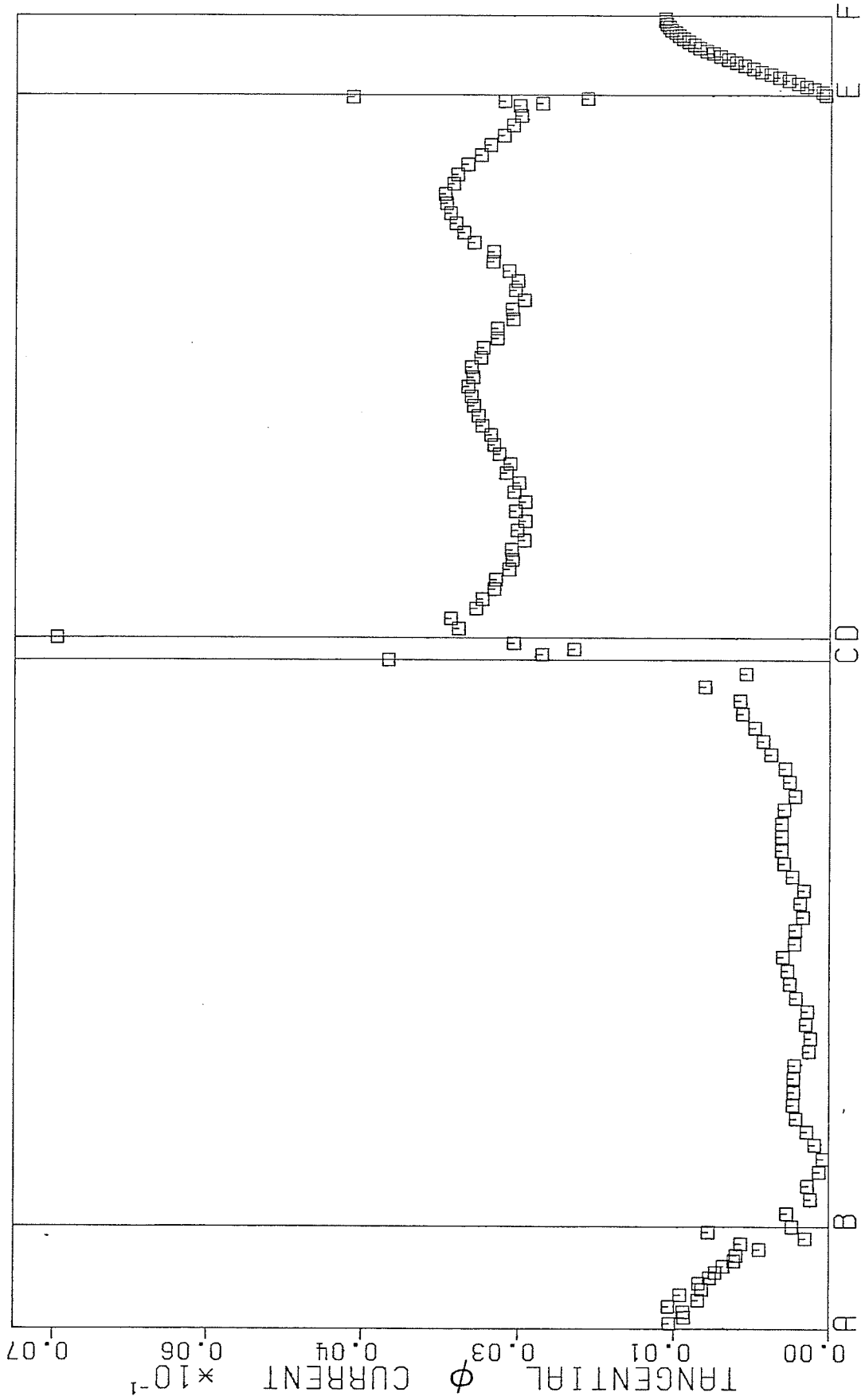

Fig. V.14(b). Induced Current I_ϕ on a waveguide section with $L/\lambda = 2.5$; $a/\lambda = 0.35$; $TH/\lambda = 0.1$; NP = 150 ; $Z_t = Z_\phi = Z_0^{TE_{11}}$.

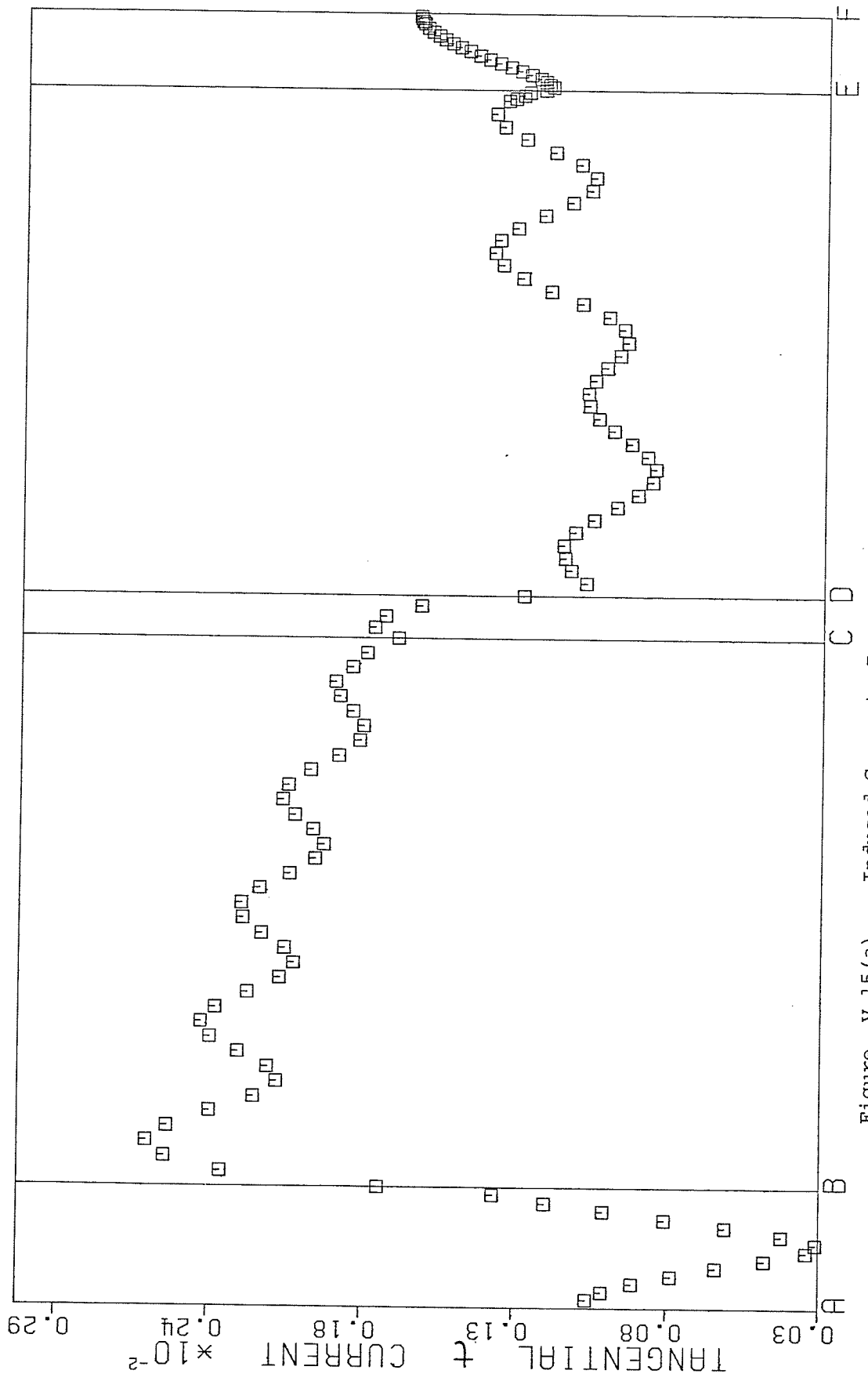

Figure V.15(a). Induced Current I_t on a Waveguide Section with $L/\lambda = 2.5$ $a/\lambda = 0.35$ $TH/\lambda = 0.2$ NP = 120 $Z_t = Z_\phi = Z_o^{TE_{11}}$

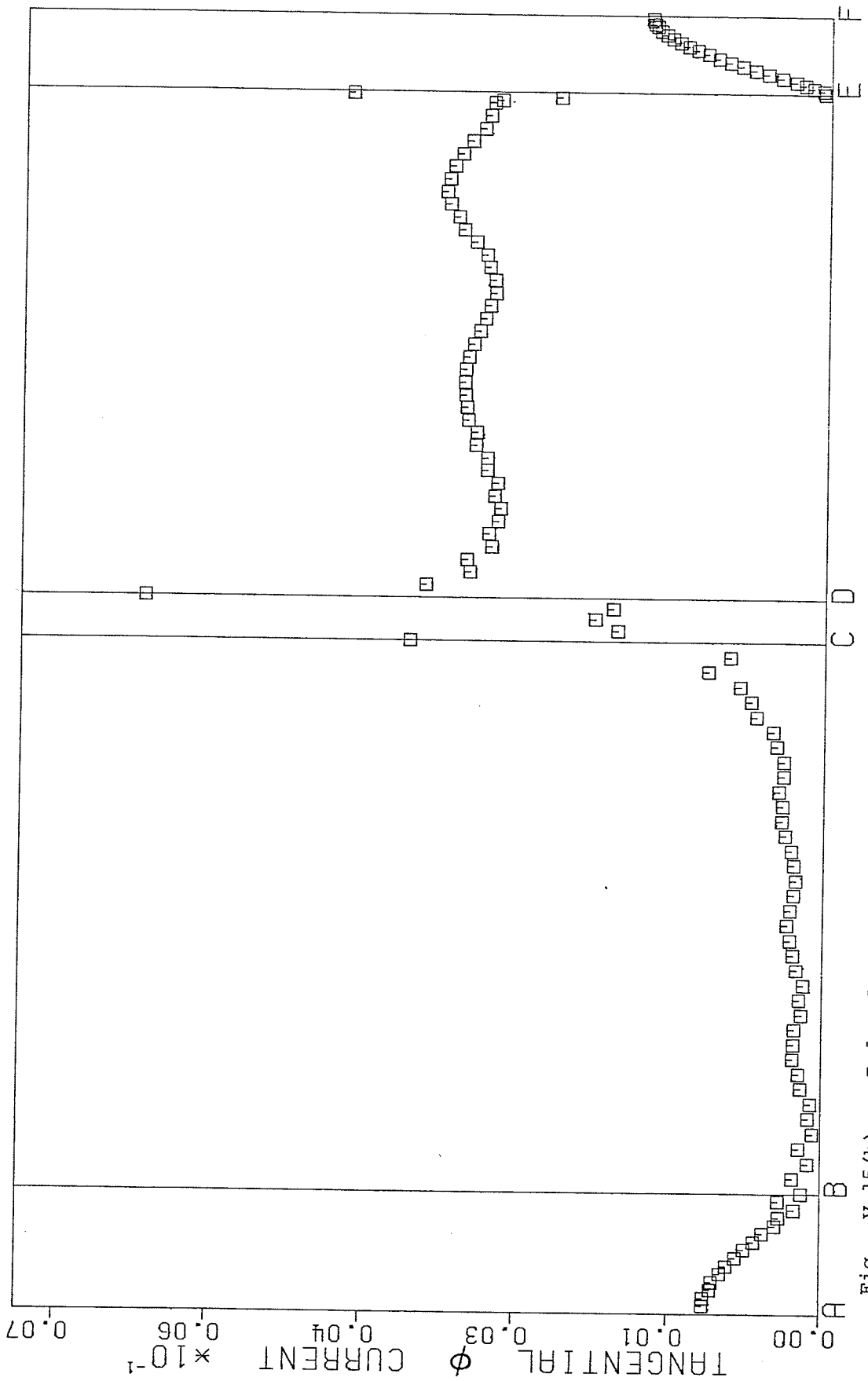

Fig. V.15(b). Induced Current I_ϕ on a waveguide section with $L/\lambda = 2.5$; $a/\lambda = 0.35$; $TH/\lambda = 0.2$; NP = 120 ; $Z_t = Z_\phi = Z_0^{TE_{11}}$.

In such circumstances, the numerical solution of the integral equation could be unstable and the ripples can be mistaken as standing waves. It was found necessary therefore to check the effect of wall thickness on the final solution whenever high densities of triangle functions still result in such ripples in the final solution.

Finally, Figure (V.16) compares our solution with that of Frandsen for a waveguide with $\Gamma_L = 0$. Good agreement can be clearly noticed for NP $\geq$ 40 .

5.8 Conclusion

In this chapter, we have studied the practical problems of radiation from rotationally symmetric corrugated horns and that of electromagnetic scattering from receiving horns. The investigation was based on the integral equation formulation for the currents induced on a scatterer with impedance boundary conditions, illuminated by a nearby current element for the first case, or an incident plane wave in the second. The application of the moment method for the solution of this integral equation required that the horn model be assigned a finite thickness. The proper values of surface impedance representing the corrugations and the matched termination were determined from existing modal analysis. For the corrugated surface, this impedance is given in terms of the ratio of electric to magnetic fields at the boundary between the grooves and the axial region

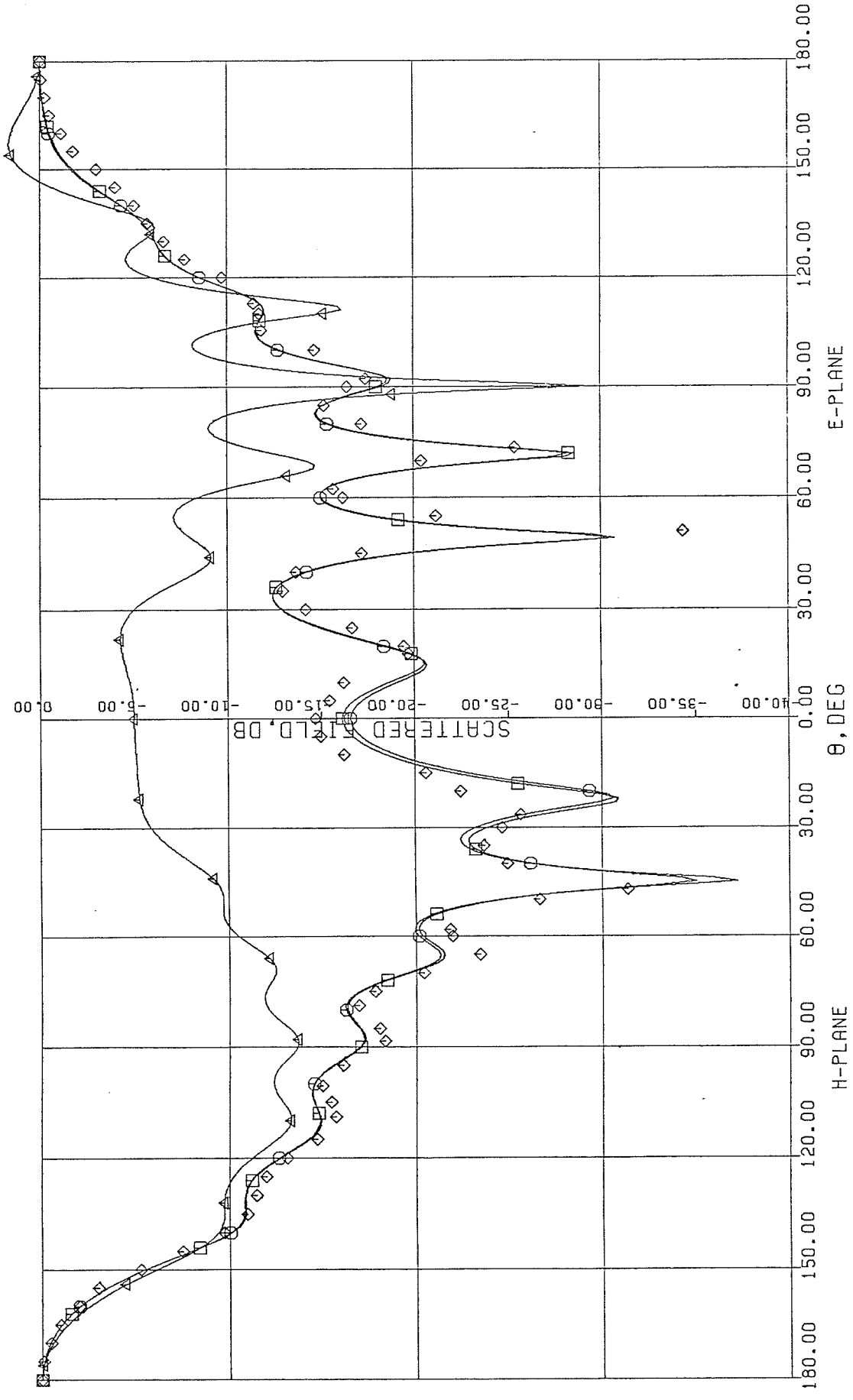

Fig. V.16. Scattering patterns from a waveguide section with $L/\lambda = 2.5$; $a/\lambda = 0.35$; $TH/\lambda = 0.1$.

◇ Frandsen's Solution [91] .

△ Present Solution with NP = 40 .

□ Present Solution with NP = 60 .

○ Present Solution with NP = 120 .

of the horn. The matched termination is the same as the characteristic impedance of the dominant mode in the circular waveguide.

The numerical aspects of the computer program developed to handle both cases were also studied. For models with a generating curve of approximately 6λ, it was found that an average density of 8 matching points per wavelength would give converging results. This requires inversion of matrices of the order of 100×100. Single precision arithmetic on the IBM 370 computer was found quite adequate for our calculations. When the frequency is too close to the cutoff value corresponding to the dominant mode in the waveguide section, higher densities of matching points are required for the solution. The numerical results were compared either to experimental data available or with the solution obtained using another technique. Satisfactory agreement was obtained in both cases.

It is worthwhile noting that the technique applies satisfactorily to short horns. This is due to the fact that no assumption was made regarding the length of the horn walls as it is the case in the modal analysis of Clarricoats, Jansen, and others. It is mainly for this reason that our solution agreed with experimental results obtained with horns having corrugation depths in the range $0 < d < \lambda/4$. According to previously developed theories for the corrugated horns, this range of d/λ was thought to give undesirable performance, contrary to the experimental results obtained by Shafai [85].

The integral equation also proved to be useful in the investigation of the scattering properties of circular horns. Excellent agreement was obtained by comparing our results with those obtained from a different approach due to Frandsen [91] . The present solution, however, is obtained through only one process of matrix inversion, rather than three inversions of matrices of comparable sizes. Accordingly, the remaining electromagnetic characteristics of the horn can be adequately determined without excessive computer requirements.

An interesting extension to the present work will be the study of the scattering properties of corrugated horns. This is a problem which has not been tackled by investigators until now. The use of our computer program [82] for such an investigation is straight forward.

At this point, however, one might still be interested in obtaining numerical solutions for corrugated horns with much larger sizes. These horns are used efficiently with beam waveguides in Cassegrain antenna systems for earth station terminals. Although our technique is still applicable, the problem of computer storage and time becomes again a major limitation. As no other simplification to reduce the effective contour length of the generating curve seems available, the question rises on the possibility of modifying the conventional procedure used with the moment method of solution to reduce the resulting matrix size. Modifications also are needed which eliminate internal resonance effects which might be present in the solution. One possible way of accomplishing these two goals

appears in the use of different Green's functions in the integral equation formulation of the problem. Since the field of a multi-element source can be made to decrease with distance at a higher rate than that of an elementary source (whether it is a line source or a point source, as used in two-dimensional and three-dimensional problems, respectively), then the development of new integral equations using the field of these multi-element sources in their kernels might lead to a better solution. In particular, a moment method applied to these new integral equations should result in matrices which are predominantly diagonal. If this is the case, then some simplifying approximations can be introduced to reduce the labour during matrix inversion. Details of such an investigation is the subject of our next chapter.

CHAPTER VI

FORMULATION OF THE INTEGRAL EQUATIONS USING NEW GREEN'S FUNCTIONS

6.1 Introduction

So far, we have been mainly interested in developing matrix equations for surfaces with impedance boundary conditions to study corrugated horn problems. Based on some electromagnetic considerations, we were able to reduce the true surface area of a corrugated horn to a much smaller effective one, characterized by a reactive value of the surface impedance, and which would simplify the process of numerical solution. This is a result of the fact that as the scatterer surface area becomes smaller, less matching points are needed in a method of moments solution, and accordingly smaller matrices need be inverted. The size of these matrices are now dependent only on the dimensions of a geometrical counterpart in which the corrugations are replaced by a smooth surface. For practical horns of moderate size as those considered in Chapter V, matrices of the order of 120 x 120 were sometimes considered. Although matrices of that size can be handled on a modern computer, the inversion process however, might involve some numerical errors. Hence, even when high precision arithmetic with 16 byte/word is used, round off errors and possible internal resonance of the structure might cause inaccurate evaluation of the currents, fields, directivity, .. etc .. . When horns with larger overall dimensions are studied, the size of the associated matrices become an obstacle in the process of the numerical solution, and the question of

numerical accuracy becomes more serious. These problems, however, are general when large and/or resonant scatterers are considered, and many investigators attempted to deal with such difficulties through different processes. Normally, two types of investigations can be related to this topic. The first group includes the attempts to formulate the problem in terms of smaller matrices. The second belongs to those investigations dealing with the numerical aspects of the problem, near or at internal resonance.

The first possible method of reducing the size of the matrix to be inverted would be to make use of any symmetry of the structure. For symmetric bodies, the matrix possesses a known periodicity which allows the filling of the entire matrix from a subset of its elements. The symmetry can be further exploited when the source has symmetry in common with that of the structure since the number of unknowns can also be reduced. Mirror or plane symmetry, has been considered by Mitzner [92], Tsai et al [93], and Wu and Cheng [94] . Symmetry exhibited by a body whose surface is formed by rotating a curved line about some axis have also been studied by Andreasen [95] and Mautz and Harrington [96] . Of course simplifications in the coefficient matrix due to symmetry do not include any approximation in the numerical values of its elements. Other approaches involve the combination of the moment method with some other asymptotic techniques. Hence Tew and Tsai [97] used physical optics to improve convergence of the moment method solution. Azarbar and Shafai [98] studied some reflector properties using a pseudo physical optics approximation which employs the

standard physical optics current for the illuminated portion of the reflector, and an integral equation to find the current in the shadow region as explained in [99] . Geometrical optics has also been included with the moment method to study diffraction from wedges [Burnside et al, 100] and scattering from corner reflectors [101] . Other approximate numerical approaches include Kinzel's method [102] for large reflector pattern calculations, where the surface of the scatterer is divided into several segments and only three adjacent ones are considered at a time. The moment method is then applied to the integral equation for this set of subsections and only the current on the middle section is retained. This method, essentially assumes that the current on one section is significantly affected only by those on the adjoining sections. For a smooth and large reflector this method is justified since the physical optics approximation holds. For a scatterer of arbitrary shape and size, however, such an approximation is generally not valid, and the induced field on the illuminated portion of the object is necessary to partially cancel the incident field on the shadow side. Shafai [103] extended Kinzel's sectioning method by including, progressively, the effect of computed surface current distribution. His method utilizes the shielding property of conductors together with the reduction in mutual interaction among the surface field distribution as a function of the electrical distance, to reduce the matrix dimensions.

Other investigators were interested in studying the numerical aspects of the solution when the method of moments is used. Hence Klein and Mittra [104, 105] showed that either the condition number or the pivot

ratio of the coefficient matrix can detect situations such as resonances which cause ill-conditioned results. They also discussed the methods of filtering, regularization and extending the boundary conditions, for the derivation of accurate results in the presence of ill-conditioning. Bolomey and Tabbara [106] investigated the consequences of non-uniqueness for integral equations used in the numerical resolution of electromagnetic scattering problems. They have shown how to test for the non-uniqueness of the solution and how to avoid possible errors by using the notion of an equivalent problem. One of the tests they have described consists of satisfying the boundary conditions inside the closed conducting objects. If the computed field vanishes at points inside the scatterer, then the solution is correct. The other method checks the energy conservation at infinity using the calculated scattered field. Obtaining the correct solution of the integral equation when internal resonance occurs is based on the idea of formulating a fictitious problem equivalent to the physical one in the external region of the scatterer, but which does not possess any resonant frequency for real values of the wave number k. This is accomplished by representing the diffracted field as a suitable linear combination of single and double layer retarded potentials. Another technique, due to Waterman [107], uses the "generalized boundary conditions" to ensure that the field vanishes on the entire inner region of the scatterer, provided that its contour is not discontinuous. Unique solutions at frequencies corresponding to interior resonances of a conducting surface can also be obtained from a combination of an H-field and E-field integral equations as applied by Mautz and Harrington [108] for conducting bodies of revolution.

As mentioned before, these studies are divided into two groups. The first group seeks solution of large scatterers by investigating different approximations leading to smaller matrices. The second investigates possible methods of solutions when ill-conditioned matrices result in the analysis because of particular dimensions of the scatterer. It would be advantageous, however, to extend these studies to new methods that will avoid the unstable conditions of internal resonance, and at the same time reduce the labour in the process of matrix inversion associated with any formulation involving the moment method. Such an investigation, when completely explored, would be quite useful in our study of horn radiators considered in the present work. The reason, of course, lies in the fact that we are still interested in reducing the size of the coefficient matrices obtained in our formulations of Chapters III and IV. In addition, we prefer to obtain accurate estimates of all electromagnetic quantities at frequencies when internal resonance of the closed horn structure might occur.

In this chapter, we will study the properties of the coefficient matrix obtained by the application of the moment method to integral equations formulated in terms of new Green's functions. These new functions are defined as the field of two or more elementary sources and are considered for the determination of unique solutions at frequencies of internal resonance. The possibility of using these new Green's functions to obtain sparse coefficient matrices for large scatterers will also be discussed. For simplicity, only two dimensional problems will be considered and results for both TM and TE plane wave excitations will be

presented. In particular, we will apply the new integral equation to the problem of electromagnetic scattering by cylindrical conducting bodies of circular cross-section for which an exact analytical solution is known [109] .

6.2 E-Field and H-Field Integral Equations in Two-Dimensions

Consider a two-dimensional scattering cylinder generated by moving a straight line parallel to the z-axis, around a closed contour "c" . The total electromagnetic wave at any point described by the radius vector $\bar{\rho}'$ is the sum of the incident and scattered fields, and can be evaluated from a knowledge of the axial component of either the electric (E_z) or the magnetic (H_z) field only [109] . Using Green's theorem and the conditions that the electromagnetic field must satisfy at the boundaries of a perfect conductor, one can show that

$$E_z^{inc}(\bar{\rho}') = E_z(\bar{\rho}') + \int_c \{jk\eta\, J_z(\bar{\rho})\}\, G(\rho,\bar{\rho}')\, dc \qquad (6.1)$$

and

$$H_z^{inc}(\bar{\rho}') = H_z(\bar{\rho}') + \int_c J_c(\bar{\rho})\, \frac{\partial\, G(\rho,\bar{\rho}')}{\partial n}\, dc \qquad (6.2)$$

where the superscript "inc" refers to the incident field. The line integral in (6.1 and 6.2) extends around the contour c of the cylinder cross-section and $\frac{\partial}{\partial n}$ means differentiation with respect to the normal to c at the

point with radius vector $\bar{\rho}$. G is the two-dimensional free space Green's function defined by

$$G = -\frac{j}{4} H_0^{(2)}(k|\bar{\rho}-\bar{\rho}'|) \tag{6.3}$$

with $H_0^{(2)}$ being the Hankel function of second kind and order zero. The time dependence $\exp(j\omega t)$ is suppressed throughout. J_z and J_c are the surface currents along, and normal to the z-direction, respectively.

When a TM polarized wave is incident on the scatterer, then

$$H_z^{inc} = 0 = H_z = J_c \qquad \text{(for TM polarization)} \tag{6.4}$$

and equation (6.1) must be used to formulate the problem.

Similarly, for a TE polarized wave, we have

$$E_z^{inc} = 0 = E_z = J_z \qquad \text{(for TE polarization)} \tag{6.5}$$

and hence equation (6.2) must be used.

Suppose now that we seek a solution of equations (6.1) and (6.2) using the moment method as explained in Chapter III. Dividing the contour c into Nl segments with lengths Δc_n and using pulse functions for basis, we can write

$$jk\eta J_z(\rho) = \sum_{n=1}^{Nl} \alpha_n f_n(\rho) \tag{6.6}$$

and

$$J_c(\rho) = \sum_{n=1}^{N1} \beta_n f_n(\rho) \tag{6.7}$$

where

$$f_n = \begin{cases} 1 & \text{on } \Delta c_n \\ 0 & \text{on all other } \Delta c_m \end{cases} \tag{6.8}$$

and α_n and β_n are unknown constants to be determined. For testing, we use Dirac delta functions defined at the middle of the segments Δc_n. Taking the inner products of those testing functions with both sides of equation (6.1) we obtain,

$$[\ell_{mn}][\alpha_n] = [(E_z^{inc})_m] \tag{6.9}$$

while inner products with (6.2) lead to

$$[C_{mn}][\beta_n] = [(H_z^{inc})_m] \tag{6.10}$$

$(E_z^{inc})_m$ and $(H_z^{inc})_m$ are the values of the z-directed electric and magnetic fields, respectively, at the centre of cell m., and $[\ell_{mn}]$ and $[C_{mn}]$ are square matrices of order N1 with elements given by [110] :

$$\ell_{mn} = \frac{-j}{4} \int_{\Delta c_n} H_0^{(2)}(k|\rho-\rho_m|)\, dc \;\tilde{=}\; \begin{cases} -\frac{j}{4}\Delta c_n\, H_0^{(2)}(k|\bar{\rho}_n-\bar{\rho}_m|) & ; \ldots m \neq n \quad (6.11a) \\ -\frac{j}{4}\Delta c_n \left[1 - j\frac{2}{\pi}\log\left(\frac{\gamma k\, \Delta c_n}{4e}\right)\right] & ; \ldots m = n \quad (6.11b) \end{cases}$$

and

$$C_{mn} = \frac{-j}{4} \int_{\Delta c_n} \frac{\partial}{\partial n}\left[H_0^{(2)}(k|\rho-\rho_m|)\right] dc \;\tilde{=}\; \begin{cases} \frac{j}{4} k\, \Delta c_n\, H_1^{(2)}(k|\bar{\rho}_n-\rho_m|)\cos(\hat{n}', \bar{\rho}_n-\bar{\rho}_m) & ; \ldots m \neq n \quad (6.12a) \\ 0.5 & ; \ldots m = n \quad (6.12b) \end{cases}$$

where $H_1^{(2)}$ is Hankel function of second kind and order 1, while $e = 2.718$ and $\gamma = 0.5772$ is Euler's constant. $\cos(\hat{n}', \bar{\rho}_n - \bar{\rho}_m)$ denotes the cosine of the angle between the vector $(\bar{\rho}_n - \bar{\rho}_m)$ and the outward normal at point $\bar{\rho}_n$ on the contour.

6.3 The Modified Electric Field Integral Equation [119]

6.3.1 The Dipole Source

The coefficient matrices $[\ell_{mn}]$ or $[C_{mn}]$ given in (6.11a and b) and (6.12a and b) are usually dense since all entries are of the same order of magnitude. Any attempt to neglect or approximate even the smallest elements by zeros, usually leads to some errors in the computed results. In an attempt to let those coefficient matrices diagonally dominant, we

consider first equation (6.1) for a TM wave incidence. Taking the derivative with respect to the normal to the contour c when the equation is applied at a point on or below the surface ($E_z = 0$), gives

$$\frac{\partial E_z^{inc}(\bar{\rho}')}{\partial n'} = \int_c jk\eta J_z(\bar{\rho}) \frac{\partial G(\bar{\rho},\bar{\rho}')}{\partial n'} dc \tag{6.13}$$

n' denotes a displacement along the normal to c at the field point and $\partial/\partial n'$ means differentiation along the normal at the same point. Of course $\frac{\partial J_z}{\partial n'} = 0$ since J_z is a function of the source coordinates only. Now we choose a point "a" (on or directly below the surface of the scatterer) and a point "b", displaced from "a" a small distance "d" along the normal n' and inside the scatterer, (Figure VI.2). Equation (6.13) can then be used to give

$$(E_{z,a}^{inc} - E_{z,b}^{inc}) = \int_c jk\eta J_z(\bar{\rho}) (\Delta G)_{ab} dc \tag{6.14}$$

for the difference in the incident electric field at points "a" and "b". ΔG_{ab} is given by

$$(\Delta G)_{ab} = \frac{\partial G}{\partial n'} \Delta n'$$

$$= \frac{-j}{4} kd H_1^{(2)}(k|\bar{\rho}-\bar{\rho}_a|) \cos(\hat{n}', \bar{\rho}-\bar{\rho}_a) \tag{6.15}$$

where use has been made of equation (6.3). Alternatively, one can write

$$(\Delta G)_{ab} = G(\bar{\rho},\bar{\rho}_a) - G(\bar{\rho},\bar{\rho}_b)$$

$$= \frac{-j}{4}\left[H_0^{(2)}(k|\bar{\rho}-\bar{\rho}_a|) - H_0^{(2)}(k|\bar{\rho}-\bar{\rho}_b|)\right] \qquad (6.16)$$

If equation (6.14) is solved using the moment method, one obtains with the help of (6.16), the following matrix equation:

$$[\ell'_{mn}][\alpha_n] = [(E^{inc}_{z,ab})_m] \qquad (6.17)$$

where

$(E^{inc}_{z,ab})_m$ is the difference in the incident field at the points "a" and "b" corresponding to subsection m, while the elements of the coefficient matrix are now given by

$$\ell'_{mn} = \int_{\Delta c_n} (\Delta G)_{ab}\, dc \qquad (6.18)$$

In (6.18), $(\Delta G)_{ab}$ may be substituted from either (6.15) or (6.16) and the integration of the left hand side can be approximated by $\{(\Delta G)_{ab} \cdot \Delta c_n\}$ for non-diagonal elements. If (6.16) is used to evaluate $(\Delta G)_{ab}$, then we have

$$\ell'_{mn} = (\ell_{mn})\Big|_{\bar{\rho}_m=\bar{\rho}_a} - (\ell_{mn})\Big|_{\bar{\rho}_m=\bar{\rho}_b} \qquad (6.19)$$

where $(\ell_{mn})_{\bar{\rho}_m=\bar{\rho}_a}$ and $(\ell_{mn})_{\bar{\rho}_m=\bar{\rho}_b}$ are obtained from the right hand side of

(6.11) with $\bar{\rho}_m = \bar{\rho}_a$ and $\bar{\rho}_b$ respectively. If however, (6.15) is used, then we have

$$\ell'_{mn} = -jd\, C_{mn}\Big|_{\bar{\rho}_m=\bar{\rho}_a} \tag{6.20}$$

where $C_{mn}\Big|_{\bar{\rho}_m=\bar{\rho}_a}$ is obtained from (6.12) with $\bar{\rho}_m=\bar{\rho}_a$.

When (6.16) is used for the off-diagonal elements ℓ'_{mn} , then for $m = n$,, we use (6.111b) to obtain

$$\ell'_{nn} = \frac{-j}{4}\Delta c_n \left[1 - j\frac{2}{\pi}\log\left(\frac{\gamma k\,\Delta c_n}{4e}\right)\right] + \frac{j}{4}\int_{\Delta c_n} H_0^{(2)}\left(k\left|\bar{\rho}-\bar{\rho}_b\right|\right)\, dc \tag{6.21}$$

while, with (6.15), the diagonal elements would be

$$\ell'_{nn} = \int_{\Delta c_n} \frac{-j}{4}\, kd\, H_1^{(2)}\left(k\left|\bar{\rho}-\bar{\rho}_a\right|\right)\cos\left(\hat{n}', \bar{\rho}-\bar{\rho}_a\right)\, dc \tag{6.22}$$

and the integrations in both (6.21) and (6.22) can be performed numerically for any shape of the contour c . On the other hand, all elements ℓ'_{mn} , could be obtained by numerical integration for better accuracy. If, however, point "a" is on the surface of the scatterer, the integrand for $\bar{\rho} \equiv \bar{\rho}_a$ in (6.22) becomes singular. In this case, point "a" is displaced a small distance below the surface and the integration is carried on.

An interpretation of equation (6.14) is that it is an integral equation obtained by considering a Green's function which represents the field of two parallel, z-directed line sources located along the normal to the contour "c" below the surface of the scatterer. The two line sources are of unit magnitude and opposite signs and are separated by a distance "d" . These two lines constitute a dipole line source. Since the far field of a dipole decays faster than that of a single line source, it is expected that the elements of the coefficient matrix $[\ell'_{mn}]$ should decrease faster with distance than those of $[\ell_{mn}]$. In this case, the current on each segment of the contour c will be affected mostly by the neighbouring segments and the coefficient matrix will be dense only around its diagonal and the corner elements.

6.3.2 The Quadrupole Source

According to the previous interpretation, one should expect that Green's functions which represent the field of multipole sources, will result in faster decay in the magnitude of the mutual elements of the coefficient matrix. This, of course, is built on the fact that the far field of multipole sources decay much faster when the order of multiplicity is increased. Hence for a quadrupole source, we consider the second derivative of (6.1) with respect to n', i.e.,

$$\frac{\partial^2 E_z^{inc}}{\partial n'^2} = \int_c jk\eta\, J_z(\bar{\rho}) \frac{\partial^2 G(\bar{\rho},\bar{\rho}')}{\partial n'^2}\, dc \qquad (6.23)$$

and we make the approximations (Figure (VI.3)) .

$$(E^{inc}_{z,a})'' = \frac{\partial^2}{\partial n'^2}(E^{inc}_z)_a \simeq \frac{(E^{inc}_z)_a - 2(E^{inc}_z)_b + (E^{inc}_z)_e}{d^2} \tag{6.24}$$

When the moment method is applied to (6.23), then using (6.6) we obtain

$$[\ell''_{mn}][\alpha_n] = [(E^{inc}_{z,a})'']_m \tag{6.25}$$

where $(E^{inc}_{z,a})''_m$ is determined from (6.24) by considering the three points a, b, and e corresponding to segment m of the contour and the elements ℓ''_{mn} are given by

$$\ell''_{mn} = \int_{\Delta c_n} \frac{\partial^2 G}{\partial n'^2}\, dc \tag{6.26a}$$

$$\simeq \frac{\partial^2 G}{\partial n'^2}\Delta c_n \tag{6.26b}$$

One, therefore, can differentiate expression (6.3) to obtain $\frac{\partial^2 G}{\partial n'^2}$. When substituting in (6.26) we can evaluate the mutual elements (i.e., $m \neq n$), ℓ''_{mn}. The diagonal elements, however, are preferably obtained through numerical integration by considering point "a" to be just below the surface. For a better approximation, we let

$$\frac{\partial^2 G}{\partial n'^2} \simeq \frac{G(\bar{\rho},\bar{\rho}_a) - 2G(\bar{\rho},\bar{\rho}_b) + G(\bar{\rho},\bar{\rho}_e)}{d^2} \tag{6.27}$$

and in this case

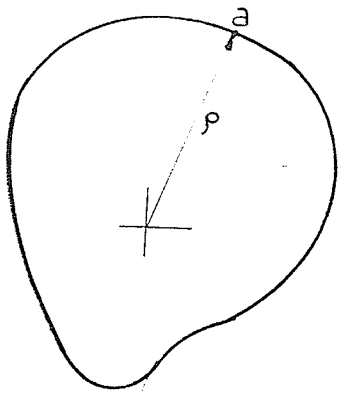

Fig. VI.1. Scatterer Cross-Section. Green's Function is the field of a point source located at "a" .

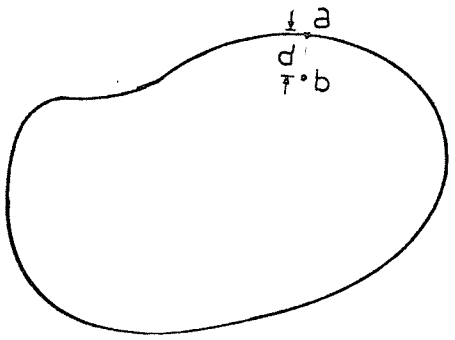

Fig. VI.2. Scatterer Cross-Section. Green's Function is the field of a dipole source "ab" .

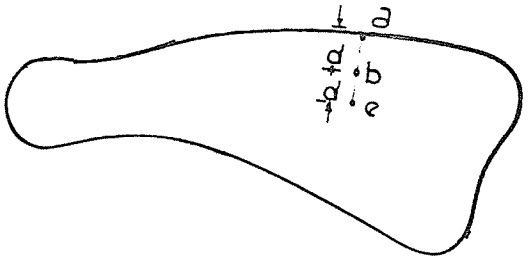

Fig. VI.3. Scatterer Cross-Section. Green's Function is the field of a quadrupole source "abe" .

$$\ell''_{mn} = (\ell_{mn})\Big|_{\bar{\rho}_m=\bar{\rho}_a} - 2(\ell_{mn})\Big|_{\bar{\rho}_m=\bar{\rho}_b} + (\ell_{mn})\Big|_{\bar{\rho}_m=\bar{\rho}_e} \tag{6.28}$$

and either the approximations of (6.11) or, again, numerical integrations can be used to evaluate the right hand side of (6.28).

6.4 The Modified Magnetic Field Integral Equation [119]

Consider now equation (6.2).. When applied at a point below the surface of the scatterer, then $H_z(\bar{\rho}') = 0$. Denoting $\frac{\partial G(\bar{\rho},\bar{\rho}')}{\partial n'}$ by G', and applying the equation at both points "a" and "b" of Figure (VI.2) (with point "a" being slightly displaced to the inside of the scatterer), we obtain

$$H^{inc}_{z,a} - H^{inc}_{z,b} = \int_c J_c(\bar{\rho})\ [G'_a - G'_b]\ dc \tag{6.29}$$

where

$$G'_a = \frac{\partial\ G(\rho,\rho')}{\partial n'}\Big|_{\rho'=\rho_a} \tag{6.30}$$

and similarly for G'_b .

As before, we use (6.7) to expand J_c in terms of pulse functions, and by choosing point matching procedure for testing we obtain the matrix equation

$$[C'_{mn}][\beta_n] = [(H^{inc}_{z,ab})_m] \tag{6.31}$$

where $(H^{inc}_{z,ab})_m$ is the difference between the incident field evaluated at the points "a" and "b" corresponding to segment m. The elements of the coefficient matrix $[C'_{mn}]$ are given by

$$C'_{mn} = C_{mn,a} - C_{mn,b} \tag{6.32}$$

where $C_{mn,a}$ is given by (6.12) with $\bar{\rho}_m \equiv \bar{\rho}_a$ and similarly for $C_{mn,b}$. Equation (6.29), of course, is the one which would be obtained by differentiating (6.2) with respect to n', and therefore, the kernel $(G'_a - G'_b)$ corresponds to the consideration of the dipole source discussed before.

Higher order derivatives for the original H-field equation, can also be obtained in a straight forward manner as dealt with in the case of the E-field equation. The corresponding formulae for second order derivatives of equation (6.2) are not reported, however, since they did not lead to accurate results.

6.5 Numerical Results

The modified electric and magnetic field integral equations obtained by single or double differentiation of equations (VI.1) and (VI.2) were studied by their application to the problem of TM and TE plane wave scattering from a two-dimensional circular cylinder. For

simplicity we have assumed normal incidence, and hence the incident field were of the form

$$E_z^{inc} = E_0 e^{-jkx} \qquad \text{for TM polarization} \tag{6.33}$$

and

$$H_z^{inc} = H_0 e^{-jkx} \qquad \text{for TE polarization} \tag{6.34}$$

for waves propagating in the positive x-direction.

The circular contour of the scatterer cross-section is divided into 40 subsections. Symmetry in the problem was not exploited so as to end up with conclusions which are general for any cross-sectional shape.

Figures (VI.4a, b and c) show the relative magnitude of the elements in the first row of the coefficient matrix when the standard E-field equation, its first and second derivatives are considered. The curves represent ℓ_{1m}/ℓ_{11}, ℓ'_{1m}/ℓ'_{11} or ℓ''_{1m}/ℓ''_{11} depending upon the case under investigation. Because of the symmetry in the problem, only half of the 40 elements in the first row need be displayed. For the same reason, the relative decay of the entries in all other rows relative to the diagonal element in that row, will be exactly the same and are not shown in the figure.

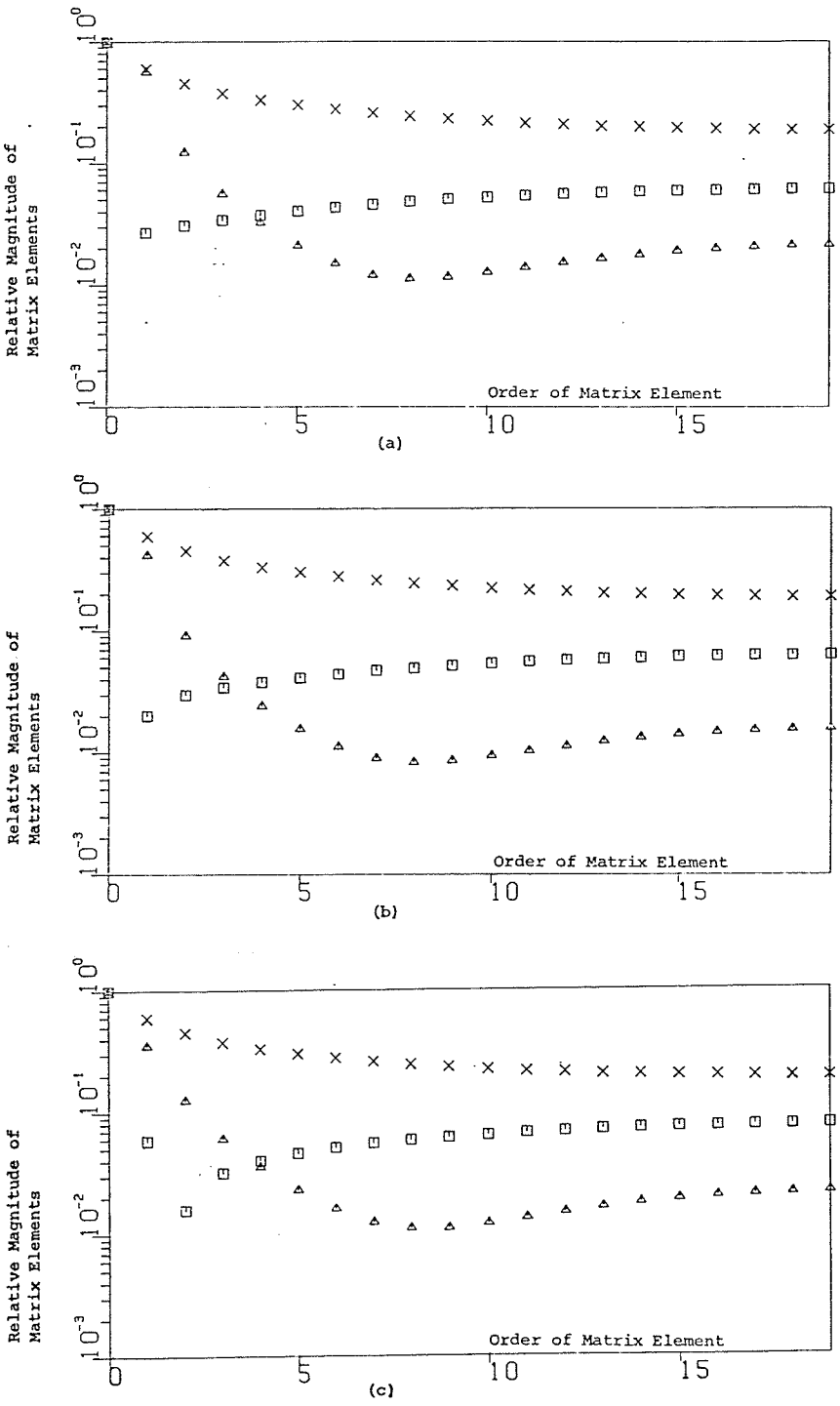

Fig. VI.4. Relative decay of Matrix Elements in the EFIE and its Modified Forms (ka = 1.5).
x Standard Case ; □ Dipole Source ; Δ Quadrupole Source.
(a) kd = 0.001 ; (b) kd = 0.01 ; (c) kd = 0.1 .

The corresponding solution for the induced surface currents compared to the exact solution is given in Tables VI.Ia, b and c for different values of kd . The first column in Table VI.1a gives the subsection number at which the current is calculated. Columns 2 and 3 give the magnitude and phase of the current obtained from the analytical solution. Column 4 is the ratio of magnitude between the original E-field integral equation and the analytical solution and column 5 shows their difference in phase. Columns 6, 7 and 8, 9 give the corresponding ratios of magnitudes and differences in phases for the dipole and quadrupole cases as compared to the analytical solutions. Tables VI.1b and c give the corresponding solution for other values of kd while the solution obtained from the original moment method is omitted.

It is clearly seen from the three tables that the solution for the dipole case agrees quite satisfactorily with the analytical solution for the three values of kd considered. The 180° difference is uniform all through in the phase column of each table and is therefore irrelevant in any computation. The quadrupole case, on the other hand showed that best agreement would occur at an optimum value of kd near 0.01. Inspection of Figures (VI.4a,b and c) also shows that the mutual elements in the coefficient matrix obtained from the consideration of a Green's function representing the field of two line sources, decay much faster than the corresponding elements resulting from the original E-field integral equation. A sudden drop in the values of these elements occur near the diagonal of the matrix. Usually, these values rise by a small

amount after the second or third terms, depending on kd, and then asymptotically approach a constant value. For the quadrupole case, the original decay from the diagonal element is generally smoother, and the entries are normally smaller than both cases of single and double line sources. It is also clear from the figures that the wide variation in the value of kd did not have much effect on the values of the coefficients.

The modified E-field integral equation, therefore, results in coefficient matrices which are less dense than the corresponding matrix obtained from the application of the moment method to the original E-field equation. Obviously then, one would try to neglect the smaller elements (i.e., assigning them zero values) and observe the effect on the accuracy of the solution. This is done in Table VI.2a and b which gives a comparison between an exact solution and data obtained from the modified integral equation for the dipole case and some of its approximations. The value of ka was chosen as 2.405 which corresponds to the cutoff value of the first TM mode inside the circular cylinder. The first column in the table gives the angular positions of seventeen points equally spaced on one side of the cylinder. The second column gives the exact value of the current at those points as obtained from the solution of the scalar wave equation by the method of separation of variables. In column 3, the solution of the currents is given as obtained from the original E-field integral equation (6.1). The fourth column shows the solution when the new integral equation (6.14) is considered. The coefficient

TABLE VI.1(a)

INDUCED CURRENT (J_z) ON CYLINDER. TM CASE

Comparison between Analytical and Moment Method Solutions of the EFIE and its Modified Forms

ka = 1.5 ; kd = 0.001 ; N1 = 40

I	Analytical Solution		Ratio P.S.		Ratio Dip.		Ratio Quad.	
	Magnitude	Phase(Deg.)	Magnitude	Phase(Deg.)	Magnitude	Phase(Deg.)	Magnitude	Phase(Deg.)
1	.4581865D-03	-82.77337	1.005436	179.9249	1.004629	179.5187	36.73882	32.45166
2	.4398399D-03	-75.85792	1.005361	179.9137	1.004580	179.5251	36.56981	24.39768
3	.4137031D-03	-53.83760	1.004928	179.8860	1.004519	179.5469	33.90903	-1.428477
4	.4568284D-03	-20.06034	1.004036	179.8785	1.004684	179.5764	24.53346	-42.98040
5	.6126773D-03	11.70320	1.003488	179.8984	1.004898	179.5960	13.78108	-88.66859
6	.8464826D-03	36.89578	1.003288	179.9098	1.004920	179.6146	7.738654	-134.2459
7	.1119665D-02	58.87139	1.003102	179.9113	1.004808	179.6398	4.992013	-175.5460
8	.1417678D-02	80.01139	1.002843	179.9106	1.004620	179.6718	3.282778	154.8134
9	.1742955D-02	101.0711	1.002537	179.9129	1.004386	179.7093	1.816239	145.7124
10	.2104025D-02	121.9392	1.002248	179.9200	1.004116	179.7506	1.288739	-177.6525
11	.2505809D-02	142.1897	1.002026	179.9306	1.003813	179.7937	2.135997	-161.2053
12	.2944501D-02	161.3983	1.001889	179.9422	1.003473	179.8374	2.954015	-170.9293
13	.3407872D-02	179.2520	1.001824	179.9529	1.003098	179.8805	3.345416	173.5084
14	.3878488D-02	-164.4672	1.001807	179.9615	1.002697	179.9223	3.304282	155.9972
15	.4336977D-02	-149.9312	1.001817	179.9681	1.002288	179.9618	2.941784	136.7185
16	.4764123D-02	-137.2969	1.001838	179.9728	1.001891	179.9980	2.431309	114.2540
17	.5141959D-02	-126.7143	1.001862	179.9761	1.001529	-179.9704	1.990537	86.60070
18	.5454434D-02	-118.3218	1.001883	179.9782	1.001223	-179.9444	1.818768	55.76634
19	.5688050D-02	-112.2371	1.001898	179.9795	1.000990	-179.9251	1.915968	30.67384
20	.5832529D-02	-108.5492	1.001908	179.9803	1.000844	-179.9131	2.084517	16.33861
21	.5881421D-02	-107.3137	1.001911	179.9805	1.000795	-179.9091	2.158643	11.85317

I = Segment number

Ratio P.S. = Ratio of Moment Solution for the EFIE (Point Source) to analytical solution.

Ratio Dip = Ratio of Moment Solution for modified EFIE (Dipole) to analytical solution.

Ratio Quad = Ratio of Moment Solution for modified EFIE (Quadrupole) to analytical solution.

TABLE VI.1(b)

INDUCED CURRENT (J_z) ON CYLINDER . TM CASE

Comparison between Analytical and Moment Method Solutions of the Modified EFIE

ka = 1.5 ; kd = 0.01 ; N1 = 40

I	Analytical Solution		Ratio Dip.		Ratio Quad.	
	Magnitude	Phase(Deg.)	Magnitude	Phase(Deg.)	Magnitude	Phase(Deg.)
1	.4581865D-03	-82.77337	1.012097	-179.8952	1.669385	170.7777
2	.4398399D-03	-75.85792	1.012599	-179.9600	1.646751	167.6429
3	.4137031D-03	-53.83760	1.012612	179.8144	1.488534	158.6438
4	.4568284D-03	-20.06034	1.008456	179.5764	1.086059	153.2325
5	.6126773D-03	11.70320	1.003476	179.5961	.8269200	167.1720
6	.8464826D-03	36.89578	1.001128	179.7061	.8695689	-178.8829
7	.1119665D-02	58.87139	1.000246	179.7947	.9750715	-174.7575
8	.1417678D-02	80.01139	.9999448	179.8562	1.056990	-175.3484
9	.1742955D-02	101.0711	.9999063	179.8982	1.099672	-177.6454
10	.2104025D-02	121.9392	.9999961	179.9255	1.105986	179.8613
11	.2505809D-02	142.1897	1.000128	179.9411	1.087538	178.0319
12	.2944501D-02	161.3983	1.000243	179.9482	1.059509	177.2208
13	.3407872D-02	179.2520	1.000311	179.9501	1.034623	177.3371
14	.3878488D-02	-164.4672	1.000327	179.9496	1.019626	178.0114
15	.4336977D-02	-149.9312	1.000304	179.9485	1.015364	178.8283
16	.4764123D-02	-137.2969	1.000257	179.9477	1.019047	179.5011
17	.5141959D-02	-126.7143	1.000203	179.9477	1.026802	179.9208
18	.5454434D-02	-118.3218	1.000153	179.9481	1.035318	-179.8897
19	.5688050D-02	-112.2371	1.000115	179.9487	1.042428	-179.8468
20	.5832529D-02	-108.5492	1.000091	179.9492	1.046999	-179.8624
21	.5881421D-02	-107.3137	1.000083	179.9494	1.048562	-179.8749

I = Segment number

Ratio Dip = Ratio of Moment Solution for modified EFIE (Dipole) to analytical solution.

Ratio Quad = Ratio of Moment Solution for modified EFIE (Quadrupole) to analytical solution.

TABLE VI.1(c)

INDUCED CURRENT (J_z) ON CYLINDER. TM CASE

Comparison between Analytical and Moment Method Solutions of the Modified EFIE

ka = 1.5 ; kd = 0.1 ; N1 = 40

I	Analytical Solution		Ratio Dip.		Ratio Quad.	
	Magnitude	Phase(Deg.)	Magnitude	Phase(Deg.)	Magnitude	Phase(Deg.)
1	.4581865D-03	-82.77337	1.009251	179.9176	.4803335	166.7081
2	.4398399D-03	-75.85792	1.009561	179.8788	.4602430	173.9690
3	.4137031D-03	-53.83760	1.009577	179.7428	.5238596	-164.6765
4	.4568284D-03	-20.06034	1.007029	179.5992	.8018247	-160.6587
5	.6126773D-03	11.70320	1.003930	179.6148	.9668644	-170.3103
6	.8464826D-03	36.89578	1.002409	179.6882	.9883691	-177.6484
7	.1119665D-02	58.87139	1.001764	179.7510	.9569694	178.7159
8	.1417678D-02	80.01139	1.001463	179.7996	.9164085	177.9568
9	.1742955D-02	101.0711	1.001318	179.8383	.8893477	179.2339
10	.2104025D-02	121.9392	1.001254	179.8694	.8867752	-178.6622
11	.2505809D-02	142.1897	1.001221	179.8940	.9059572	-176.9884
12	.2944501D-02	161.3983	1.001179	179.9133	.9351744	-176.3573
13	.3407872D-02	179.2520	1.001104	179.9289	.9629350	-176.6846
14	.3878488D-02	-164.4672	1.000995	179.9424	.9827900	-177.5924
15	.4336977D-02	-149.9312	1.000860	179.9545	.9931668	-178.7108
16	.4764123D-02	-137.2969	1.000715	179.9658	.9955026	-179.7819
17	.5141959D-02	-126.7143	1.000576	179.9760	.9925255	179.3349
18	.5454434D-02	-118.3218	1.000455	179.9847	.9871019	178.6883
19	.5688050D-02	-112.2371	1.000362	179.9914	.9816069	178.2682
20	.5832529D-02	-108.5492	1.000304	179.9956	.9776917	178.0389
21	.5881421D-02	-107.3137	1.000284	179.9970	.9762879	177.9669

I = Segment number

Ratio Dip = Ratio of Moment Solution for modified EFIE (Dipole) to analytical solution.

Ratio Quad = Ratio of Moment Solution for modified EFIE (Quadrupole) to analytical solution.

TABLE VI.2(a)

INDUCED CURRENT MAGNITUDE (J_z) ON CYLINDER. TM CASE.

COMPARISON BETWEEN ANALYTICAL AND MOMENT METHOD SOLUTIONS

OF THE EFIE AND ITS MODIFIED FORMS

Angle (Degrees)	Analytical Solution	MM Solution of EFIE	MM Solution of Modified EFIE (Dipole Source with $kd = 0.145 \times 10^{-2}$		
			Sparsity = 0%	Sparsity = 6.25%	Sparsity = 12.5%
.0	.2387D-03	.1413D-02	.2561D-03	.5763D-03	.8800D-03
11.25	.2059D-03	.1335D-02	.2222D-03	.5229D-03	.8132D-03
22.50	.2246D-03	.1162D-02	.2308D-03	.3882D-03	.6188D-03
33.75	.3953D-03	.1098D-02	.3941D-03	.2833D-03	.3258D-03
45.00	.6104D-03	.1379D-02	.6106D-03	.4308D-03	.2493D-03
56.25	.8526D-03	.1929D-02	.8576D-03	.7614D-03	.6666D-03
67.50	.1168D-02	.2521D-02	.1177D-02	.1145D-02	.1107D-02
78.75	.1583D-02	.2966D-02	.1589D-02	.1525D-02	.1466D-02
90.00	.2082D-02	.3144D-02	.2082D-02	.1909D-02	.1769D-02
101.2	.2642D-02	.3050D-02	.2637D-02	.2364D-02	.2159D-02
112.5	.3240D-02	.2835D-02	.3232D-02	.2940D-02	.2742D-02
123.7	.3843D-02	.2773D-02	.3839D-02	.3598D-02	.3457D-02

TABLE VI.2(a) (cont'd)

Angle (Degrees)	Analytical Solution	MM Solution of EFIE	MM Solution of Modified EFIE (Dipole Source with kd = 0.145 x 10^{-2})		
			Sparsity = 0%	Sparsity = 6.25%	Sparsity = 12.5%
135.0	.4413D-02	.3054D-02	.4415D-02	.4245D-02	.4159D-02
146.2	.4908D-02	.3576D-02	.4915D-02	.4796D-02	.4736D-02
157.5	.5290D-02	.4110D-02	.5301D-02	.5202D-02	.5139D-02
168.7	.5532D-02	.4487D-02	.5544D-02	.5446D-02	.5370D-02
180.0	.5614D-02	.4621D-02	.5627D-02	.5527D-02	.5444D-02
	Error	.4057	.2836D-02	.6585D-01	.1173
		NZ	0	64	128

MM = Moment Method.

NZ = Number of entries set to zero in coefficient matrix.

TABLE VI.2(b)

SCATTERED FIELD MAGNITUDE (E_z) FROM CYLINDER. TM CASE.

COMPARISON BETWEEN ANALYTICAL AND MOMENT METHOD SOLUTIONS OF THE EFIE

AND ITS MODIFIED FORMS. (ka = 2.405)

Angle (Degrees)	Analytical Solution	MM Solution of EFIE	MM Solution of Modified EFIE (Dipole Source with kd = 0.145×10^{-2})		
			Sparsity = 0%	Sparsity = 6.25%	Sparsity = 12.5%
.0	.10428	.10449	.10420	.96883D-01	.91291D-01
11.25	.98360D-01	.98523D-01	.98282D-01	.91556D-01	.86520D-01
22.50	.82620D-01	.82673D-01	.82558D-01	.77551D-01	.74144D-01
33.75	.62607D-01	.62587D-01	.62602D-01	.60259D-01	.59340D-01
45.00	.46103D-01	.46179D-01	.46220D-01	.46777D-01	.48279D-01
56.25	.39513D-01	.39833D-01	.39745D-01	.41509D-01	.43594D-01
67.50	.40665D-01	.41113D-01	.40886D-01	.41445D-01	.42079D-01
78.75	.42862D-01	.43274D-01	.42985D-01	.41522D-01	.40109D-01
90.00	.43557D-01	.43860D-01	.43568D-01	.40446D-01	.37493D-01
101.3	.43330D-01	.43519D-01	.43270D-01	.39504D-01	.36225D-01
112.5	.43206D-01	.43302D-01	.43146D-01	.40008D-01	.37748D-01
123.7	.43532D-01	.43553D-01	.43536D-01	.41983D-01	.41442D-01

TABLE VI.2(b) (cont'd)

Angle (Degrees)	Analytical Solution	MM Solution of EFIE	MM Solution of Modified EFIE (Dipole Source with kd = 0.145 x 10^{-2})		
			Sparsity = 0%	Sparsity = 6.25%	Sparsity = 12.5%
135.0	.44098D-01	.44059D-01	.44198D-01	.44571D-01	.45740D-01
146.2	.44624D-01	.44537D-01	.44821D-01	.46969D-01	.49511D-01
157.5	.44984D-01	.44862D-01	.45257D-01	.48765D-01	.52269D-01
168.7	.45176D-01	.45033D-01	.45497D-01	.49840D-01	.53905D-01
180.0	.45235D-01	.45085D-01	.45571D-01	.50195D-01	.54444D-01
	Error	.3120D-02	.2490D-02	.5937D-01	.1087
		NZ	0	64	128

MM = Moment Method.

NZ = Number of entries set to zero in coefficient matrix.

Each solution corresponds to current on same column in Table VI.2(a).

matrix obtained through the application of the moment method to this new equation is then approximated and used for the determination of the currents in columns 5 and 6 of the table. Hence elements of this matrix which are equal to or less than 4% and 4.5% of the largest entry are replaced by zeros to obtain the solution in the fifth and sixth columns, respectively. The number of elements replaced by zeros in each case is also shown right below the solution vectors. The ratio of the number of elements set to zero relative to the total number of entries in the coefficient matrix is defined as the "sparsity" and is shown for each case. The row marked "error" gives an estimate of the overall accuracy of the solution. This is determined from the expression $\|\delta X\| / \|X\|$ where $\|X\|$ is the unit norm of the exact solution vector given in column 2 of the table. It is defined as [111]

$$\|X\| = \sum_{i=1}^{N1} |X_i| \tag{6.35}$$

$\|\delta X\|$ is the unit norm of the difference vector obtained by subtracting the elements of a particular solution from the corresponding values of the exact solution.

It is clear from this table that the solution of the new integral equation is in better agreement with the exact analytical results, when compared with the solution of the original E-field equation. This is manifested by a closer agreement of the current at each point and a lower value of $\|\delta X\| / \|X\|$. It is also interesting to note that even the

solutions obtained by approximating the coefficient matrix of the new formulation gave results very close to the exact values of the currents. The corresponding solution for the scattered field, on the other hand, was less accurate when the smallest elements in the coefficient matrix are approximated to zero (Table VI.2b) . It is concluded therefore that the phases of the currents in the modified method of solution become less accurate when the small elements are neglected.

The modified H-field integral equations were also applied to the problem of scattering from a conducting cylinder with $ka = 1.5$. It was noticed for these cases (Figures VI.5a, b and c) that, as kd becomes smaller, the relative magnitude of the elements in the coefficient matrices decreases much faster for the dipole and quadrupole cases than their corresponding values for the standard case. The agreement between the modified solutions and the exact ones, however, was better for larger kd (Tables VI.3a and b). This is in contrast with the behaviour shown by the modified E-field integral equation. When ka was changed to 4.5, a larger decay for the elements of the coefficient matrices in both the dipole and quadrupole cases was noticed even with large values of kd (Figure VI.6 a and b). Convergence in this case started to occur near $kd = 0.8$ (Table VI.4a and b). In general, convergence of the solution for the modified H-field integral equation was more difficult to obtain.

As a result, it might be concluded that there exists an optimum value of kd/ka . For this optimum, the maximum decay in the value of the matrix elements corresponding to the dipole and quadrupole cases can be

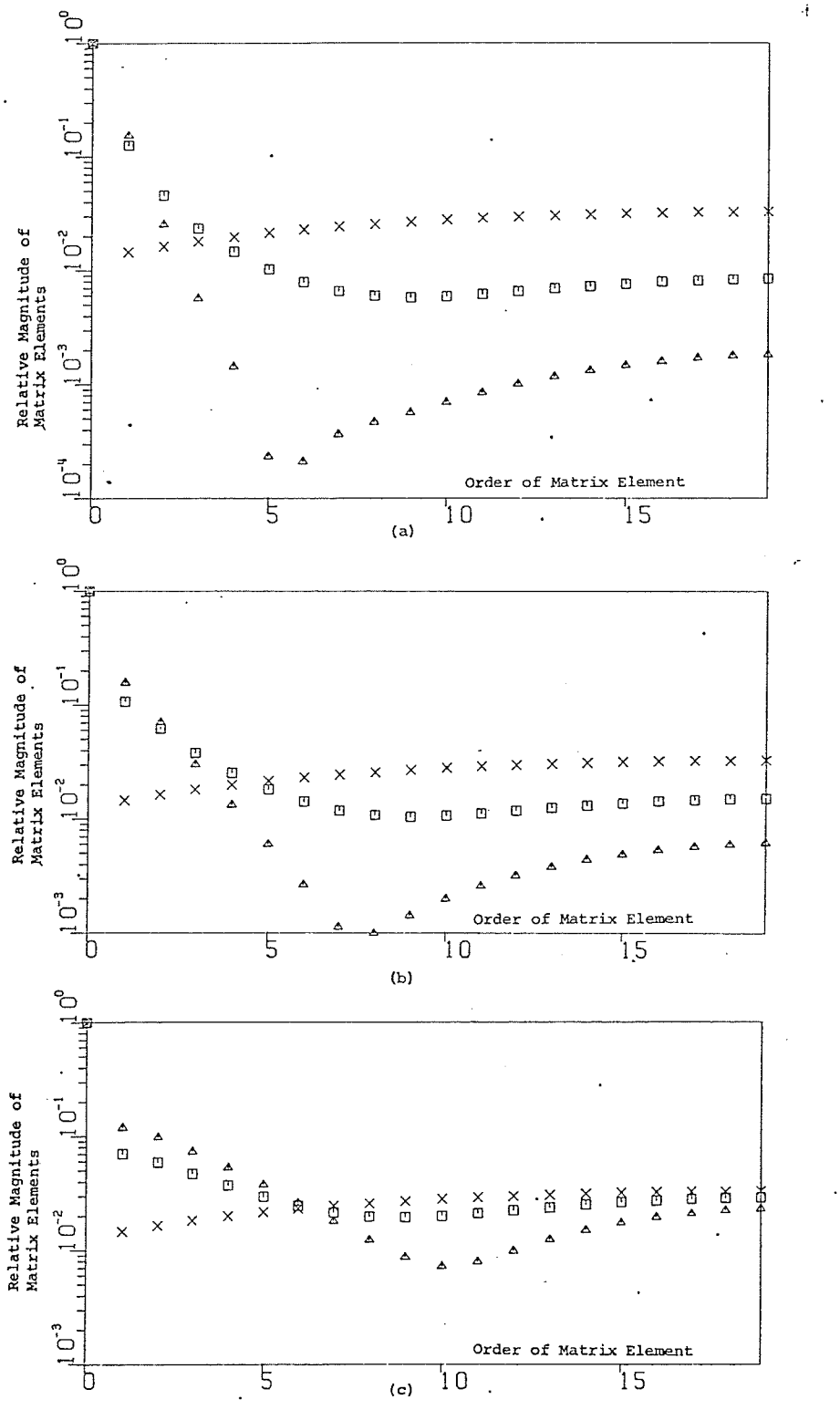

Fig. VI.5. Relative decay of Matrix Elements in the MFIE and its Modified Forms. (ka = 1.5).
x Standard Case ; □ Dipole Source ; Δ Quadrupole Source.
(a) kd = 0.2 ; (b) kd = 0.4 ; (c) kd = 0.8 .

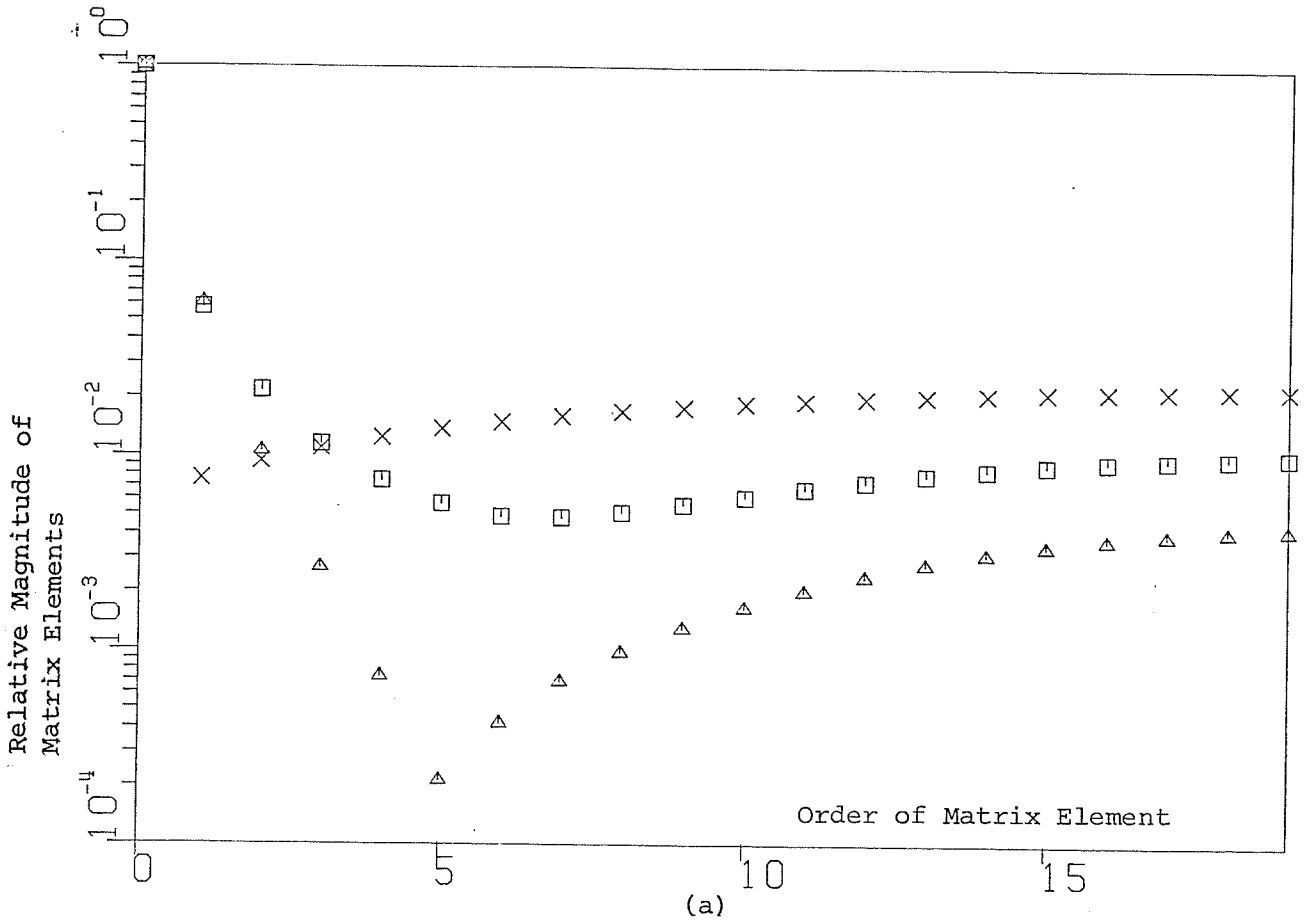

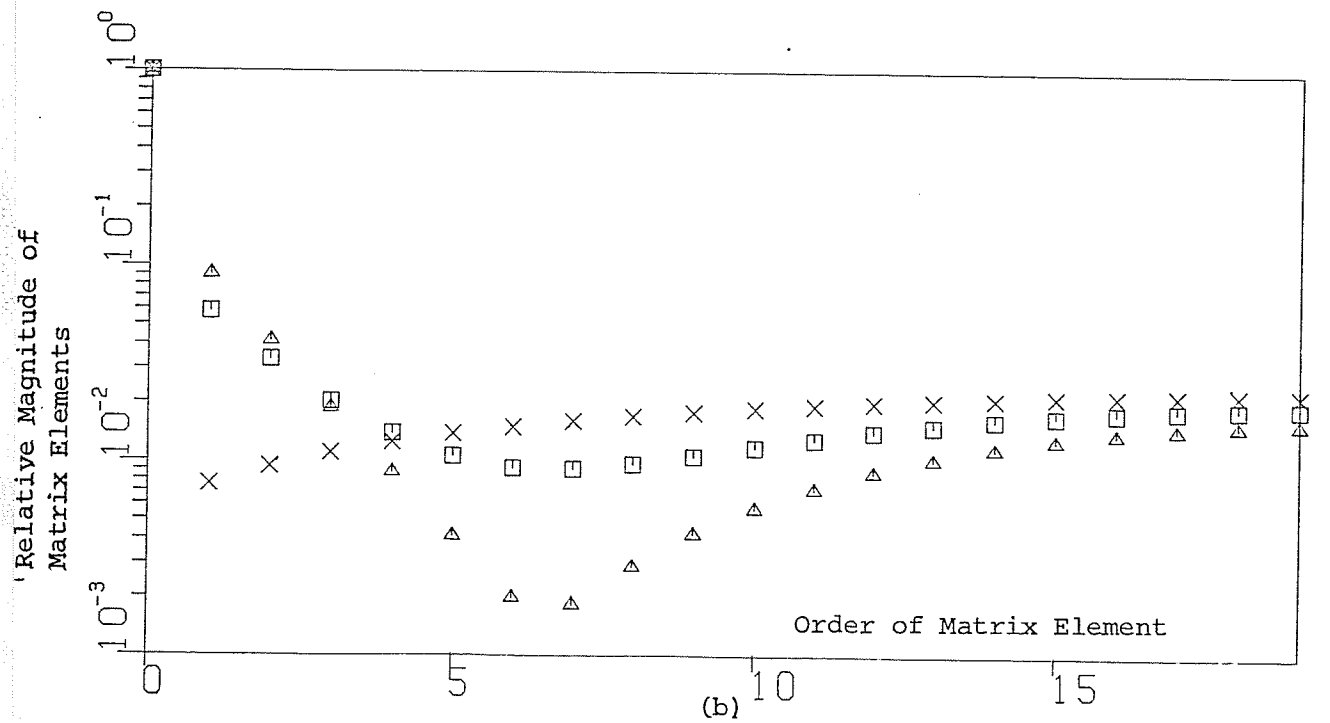

Fig. VI.6. Relative decay of Matrix Elements in the MFIE and its Modified Forms. (ka = 4.5).
x Standard Case ; □ Dipole Source ; Δ Quadrupole Source.
(a) kd = 0.4 ; (b) kd = 0.8 .

TABLE VI.3(a)

INDUCED CURRENT (J_c) ON CYLINDER, TE CASE

Comparison between Analytical and Moment Method Solutions of the MFIE and its Modified Forms

ka = 1.5 ; kd = 0.2 ; N1 = 40

I	Analytical Solution		Ratio P.S.		Ratio Dip.		Ratio Quad.	
	Magnitude	Phase (Deg.)	Magnitude	Phase (Deg.)	Magnitude	Phase (Deg.)	Magnitude	Phase (Deg.)
1	.8076084	-165.1969	.9732560	26.10513	1.331042	-38.37510	.3365644	-88.14035
2	.7768069	-162.6604	.9880874	26.55362	1.359470	-40.62961	.3418955	-89.98435
3	.6934726	-154.2756	1.041501	27.56677	1.442610	-48.25491	.3569076	-96.32386
4	.5889848	-137.5560	1.156755	27.42221	1.547572	-64.02754	.3723325	-109.7455
5	.5266805	-109.9958	1.312493	22.37604	1.510441	-91.05767	.3487173	-132.9343
6	.5760225	-77.67295	1.358994	13.49691	1.150347	-124.4452	.2500035	-160.0956
7	.7277064	-51.75452	1.295259	7.672546	.7281730	-155.2606	.1430850	179.5006
8	.9184469	-32.93708	1.234216	5.310745	.4658766	173.8484	.7382837D-01	165.8724
9	1.101508	-17.84303	1.200947	4.343423	.3639451	139.7917	.3489431D-01	154.7183
10	1.253546	-4.261941	1.187839	3.676996	.3709078	110.4918	.1467742D-01	144.4959
11	1.367259	8.890891	1.185905	2.880604	.4267000	90.85182	.6451688D-02	153.5967
12	1.446438	22.06157	1.188051	1.807558	.4963446	77.84310	.9668688D-02	-174.6570
13	1.501526	35.28916	1.188611	.4679596	.5647394	68.33414	.2152773D-01	-175.0604
14	1.544723	48.31158	1.183662	-1.011915	.6239593	60.74466	.3914058D-01	178.5859
15	1.585497	60.66766	1.171910	-2.439439	.6694730	54.46658	.6049166D-01	172.4486
16	1.628034	71.83593	1.154919	-3.636014	.7001255	49.34082	.8311360D-01	167.2314
17	1.671415	81.36892	1.135993	-4.507556	.7178863	45.33773	.1045884	163.0469
18	1.711690	88.96254	1.118511	-5.060026	.7264581	42.40526	.1229789	159.8980
19	1.744234	94.45027	1.104869	-5.363775	.7296570	40.44079	.1369387	157.7310
20	1.765287	97.75891	1.096347	-5.503729	.7304179	39.32450	.1456218	156.4714
21	1.772556	98.86353	1.093464	-5.542823	.7304825	38.96386	.1485655	156.0591

I = Segment number

Ratio P.S. = Ratio of Moment Solution for the MFIE (Point Source) to analytical solution.

Ratio Dip = Ratio of Moment Solution for modified MFIE (Dipole) to analytical solution.

Ratio Quad = Ratio of Moment Solution for modified MFIE (Quadrupole) to analytical solution.

Comparison between Analytical and Moment Method Solutions of the Modified MFIE

ka = 1.5 ; kd = 0.8 ; N1 = 40

I	Analytical Solution		Ratio Dip.		Ratio Quad.	
	Magnitude	Phase(Deg.)	Magnitude	Phase(Deg.)	Magnitude	Phase(Deg.)
1	.8076084	-165.1969	.9556455	-39.98469	12.35177	-29.58006
2	.7768069	-162.6604	.9423261	-42.37561	12.65667	-32.08353
3	.6934726	-154.2756	.8878128	-50.60934	13.56250	-40.38960
4	.5889848	-137.5560	.7338660	-68.66707	14.78632	-57.05126
5	.5266805	-109.9958	.3868477	-108.8097	14.74564	-84.70600
6	.5760225	-77.67295	.2577731	117.4857	11.47900	-117.5205
7	.7277064	-51.75452	.5842284	67.83674	7.275830	-144.8123
8	.9184469	-32.93708	.7917262	50.00093	4.221627	-167.0179
9	1.101508	-17.84303	.9235826	40.22744	2.227492	168.9625
10	1.253546	-4.261941	1.021016	33.78913	1.013131	124.8497
11	1.367259	8.890891	1.101097	28.81105	.9597229	43.09921
12	1.446438	22.06157	1.168584	24.41415	1.648829	2.329605
13	1.501526	35.28916	1.222164	20.21757	2.357916	-20.17175
14	1.544723	48.31158	1.258539	16.16128	2.982490	-37.90505
15	1.585497	60.66766	1.276025	12.38731	3.501919	-53.37251
16	1.628034	71.83593	1.276713	9.105262	3.911907	-66.90457
17	1.671415	81.36892	1.266032	6.470618	4.220068	-78.32128
18	1.711690	88.96254	1.250518	4.529591	4.440783	-87.38822
19	1.744234	94.45027	1.235764	3.237041	4.588428	-93.94229
20	1.765287	97.75891	1.225557	2.509566	4.673321	-97.89777
21	1.772556	98.86353	1.221945	2.276112	4.701053	-99.21923

I = Segment number

Ratio Dip = Ratio of Moment Solution for modified MFIE (Dipole) to analytical solution.

Ratio Quad = Ratio of Moment Solution for modified MFIE (Quadrupole) to analytical solution.

TABLE VI.4(a)

INDUCED CURRENT (J_c) ON CYLINDER. TE CASE

Comparison between Analytical and Moment Method Solutions of the MFIE and its Modified Forms

ka = 4.5 ; kd = 0.2 ; N1 = 40

I	Analytical Solution		Ratio P.S.		Ratio Dip.'		Ratio Quad.	
	Magnitude	Phase(Deg.)	Magnitude	Phase(Deg.)	Magnitude	Phase(Deg.)	Magnitude	Phase(Deg.)
1	.5110052	-98.13316	2.448656	-146.7221	1.044674	109.7025	.2060146	31.87800
2	.3661598	-86.73700	3.589328	-157.1381	1.431880	101.3854	.2804343	23.48844
3	.2039254	-.4222667	7.190858	120.4306	2.435033	24.32397	.4667028	-53.87759
4	.4957064	57.99626	3.256222	70.58939	.9150935	-18.63240	.1684478	-97.62130
5	.6622802	86.16645	2.506676	57.53828	.6053953	-25.19553	.1039526	-105.7642
6	.6367917	126.5108	2.481516	41.30702	.5419533	-38.33053	.8268331D-01	-121.2873
7	.7000521	-176.3136	2.123366	19.49615	.4130309	-64.21955	.5206007D-01	-149.6223
8	.9345248	-127.9275	1.667715	13.77497	.2446092	-79.58527	.2323010D-01	-166.1427
9	1.102650	-86.66710	1.619601	13.10265	.1414631	-88.44823	.8953922D-02	-173.7538
10	1.180744	-42.19797	1.675104	5.253483	.6024566D-01	-106.0990	.1900252D-02	175.1890
11	1.307588	4.662199	1.538681	-5.722773	.2090861D-01	116.3975	.2384280D-03	-42.73871
12	1.486466	47.65228	1.286011	-10.58740	.6990556D-01	80.08172	.1819678D-02	-178.8303
13	1.616243	86.69846	1.115211	-8.245252	.1057684	75.67626	.6427514D-02	171.4796
14	1.688319	123.9968	1.068464	-3.678945	.1362881	75.81996	.1298053D-01	167.8976
15	1.757199	159.0381	1.091953	-1.372143	.1648710	76.68303	.2056592D-01	165.3261
16	1.834281	-170.2161	1.124341	-1.598237	.1915687	77.51733	.2826546D-01	164.0147
17	1.892304	-144.6839	1.144726	-3.052649	.2165446	78.06693	.3576164D-01	163.7519
18	1.920583	-124.3083	1.152047	-4.973663	.2387652	78.05215	.4274886D-01	163.7043
19	1.930815	-109.1918	1.148595	-6.851311	.2559326	77.56274	.4850886D-01	163.4479
20	1.935048	-99.80467	1.140741	-8.196040	.2663730	77.01064	.5226117D-01	163.1089
21	1.936554	-96.61560	1.136836	-8.678675	.2698049	76.77952	.5355279D-01	162.9576

I = Segment number

Ratio P.S. = Ratio of Moment Solution for the MFIE (Point Source) to analytical solution.

Ratio Dip = Ratio of Moment Solution for modified MFIE (Dipole) to analytical solution.

Ratio Quad = Ratio of Moment Solution for modified MFIE (Quadrupole) to analytical solution.

TABLE VI.4(b)

INDUCED CURRENT (J_c) ON CYLINDER. TE CASE

Comparison between Analytical and Moment Method Solutions of the Modified MFIE

ka = 4.5 ; kd = 0.8 ; N1 = 40

I	Analytical Solution		Ratio Dip.		Ratio Quad.	
	Magnitude	Phase(Deg.)	Magnitude	Phase(Deg.)	Magnitude	Phase(Deg.)
1	.5110052	-98.13316	3.818649	109.6697	4.117270	56.08621
2	.3661598	-86.73700	5.179429	101.2364	5.575957	46.80027
3	.2039254	-.4222667	8.535511	24.00870	9.134374	-33.18161
4	.4957064	57.99626	3.052079	-18.56079	3.208759	-81.06100
5	.6622802	86.16645	1.915658	-23.24742	1.906839	-94.63325
6	.6367917	126.5108	1.688302	-33.01028	1.449895	-116.9424
7	.7000521	-176.3136	1.354651	-57.10085	.8686200	-154.5694
8	.9345248	-127.9275	.8669569	-76.06954	.3622986	172.7136
9	1.102650	-86.66710	.5202841	-96.14915	.1313544	122.8451
10	1.180744	-42.19797	.2334878	-147.0056	.1075837	24.68980
11	1.307588	4.662199	.2677251	108.8758	.1308752	-41.04467
12	1.486466	47.65228	.4435176	71.86628	.1419144	-107.7927
13	1.616243	86.69846	.5341758	56.67259	.2289881	-163.2466
14	1.688319	123.9968	.5627675	50.86089	.3729274	164.3669
15	1.757199	159.0381	.5781580	52.29872	.5146034	143.3590
16	1.834281	-170.2161	.6305128	56.96938	.6225865	129.6405
17	1.892304	-144.6839	.7215971	59.88804	.7011575	121.3700
18	1.920583	-124.3083	.8208333	60.04918	.7625386	116.5984
19	1.930815	-109.1918	.9015550	58.72394	.8099699	113.8371
20	1.935048	-99.80467	.9509938	57.32397	.8404689	112.3409
21	1.936554	-96.61560	.9672110	56.75788	.8509737	111.8589

I = Segment number

Ratio Dip = Ratio of moment solution for modified MFIE (Dipole) to analytical solution.

Ratio Quad = Ratio of Moment Solution for modified MFIE (Quadrupole) to analytical solution.

obtained while still maintaining the solutions for the currents within acceptable limits. Furthermore, if the rate of decay of the matrix elements is large enough at this optimum value of kd/ka, then the smallest elements in the matrices can be approximated to zero without affecting appreciably the value of the solution.

The effect of internal resonance of the structure on the stability of the solution was investigated in connection with the E-field integral equation and its modified forms only. This was accomplished by determining both the condition number and pivot ratio for the coefficient matrix to detect any ill-conditioned situation. The latter is characterized by a relatively high value of both condition number and pivot ratio. The condition number of an Nl x Nl matrix [A] is defined as [111]

$$\text{Cond}(A) = \|A\|_{\infty} \cdot \|A^{-1}\|_{\infty} \tag{6.36}$$

where $\|A\|$ in the infinite norm of the matrix [A] as is given by

$$\|A\|_{\infty} = \max_{1 \le i \le Nl} \sum_{j=1}^{Nl} |a_{ij}| \tag{6.37}$$

while $[A]^{-1}$ is the inverse of the matrix. a_{ij} is the entry in column j and row i of the matrix. On the other hand, the pivot ratio is defined as the ratio of magnitude of the first to the last pivot elements chosen in the solution of the system of linear equations using a Gaussian elimination procedure and a complete pivoting strategy [111] .

Figures (VI.7, VI.8 and VI.9) and also Tables (VI.5 and VI.6) show that both the condition number and the pivot ratio constitute a valid criterion for determining the occurrence of internal resonance when either the E-field or H-field equations, or any of their modified forms is considered. The calculation of the pivot ratio, however, is much easier, and is obtained at the same time when the matrix equation is solved using the Gauss algorithm. The calculation of the condition number, on the other hand, needs the explicit evaluation of a matrix inverse, which is about three times less efficient in terms of computer time or number of operations, when compared with the factorization method [112] . In Figures (VI.7) and (VI.8) we have shown the behaviour of both the condition number and the pivot ratio for the matrices corresponding to the original E-field equation and its first derivative, when the cylinder radius is changed from $ka = 1.5$ to $ka = 4.5$ with $kd = 0.001$. Curves for the original equation show peak values at $ka = 2.405$ and $ka = 3.832$ which correspond to the internal resonance of the scatterer. These values of ka actually determine the cutoff points of the lowest TM modes namely the TM_{01} and TM_{11} , which can propagate in the inner region of the scatterer. When the first derivative of the E-field equation is considered, it is found that the first peak at $ka = 2.405$ completely disappears, and splits, instead, into two other peaks around the original position. This resembles the resonance curves of the single and double tuned circuits. The splitting of the original peak into two peaks is of course due to the fact that the coefficient matrix considered in the second case is actually the sum of the original one obtained from the considera-

tion of the original E-field equation, plus another similar matrix which belongs to a smaller cylinder. This can be understood from the examination of equation (6.14) and (6.16). At ka = 3.832, both the original and the first derivative of the E-field equation show a peak in the condition number and the pivot ratio. The peak resulting from the derivative equation at this value of ka is explained with reference to equations (6.15) and (6.2) . There we can see that the first derivative of the E-field equation, has the same form as the unmodified H-field equation. The latter, however, possess a peak at this value of ka , which represents the cutoff point of the TE_{11} mode in the internal region. The additional peak at ka = 4.201 in the case of the derivative equation comes again because of the splitting of the peak at ka = 5.136 of the original E-field equation.

The effect of changing kd on the behaviour of the condition number for the coefficient matrix corresponding to the first derivative of the E-field equation is also shown in Figure (VI.9) for the range of ka = 1.5 to 4.5 and for three values of kd . It is noticed that changing kd has almost no effect on the value of ka where ill-conditioning occurs. Increasing kd, however, results in the dampening of those peaks and resonance effects therefore, can be completely eliminated from the solution by choosing a proper value for this parameter.

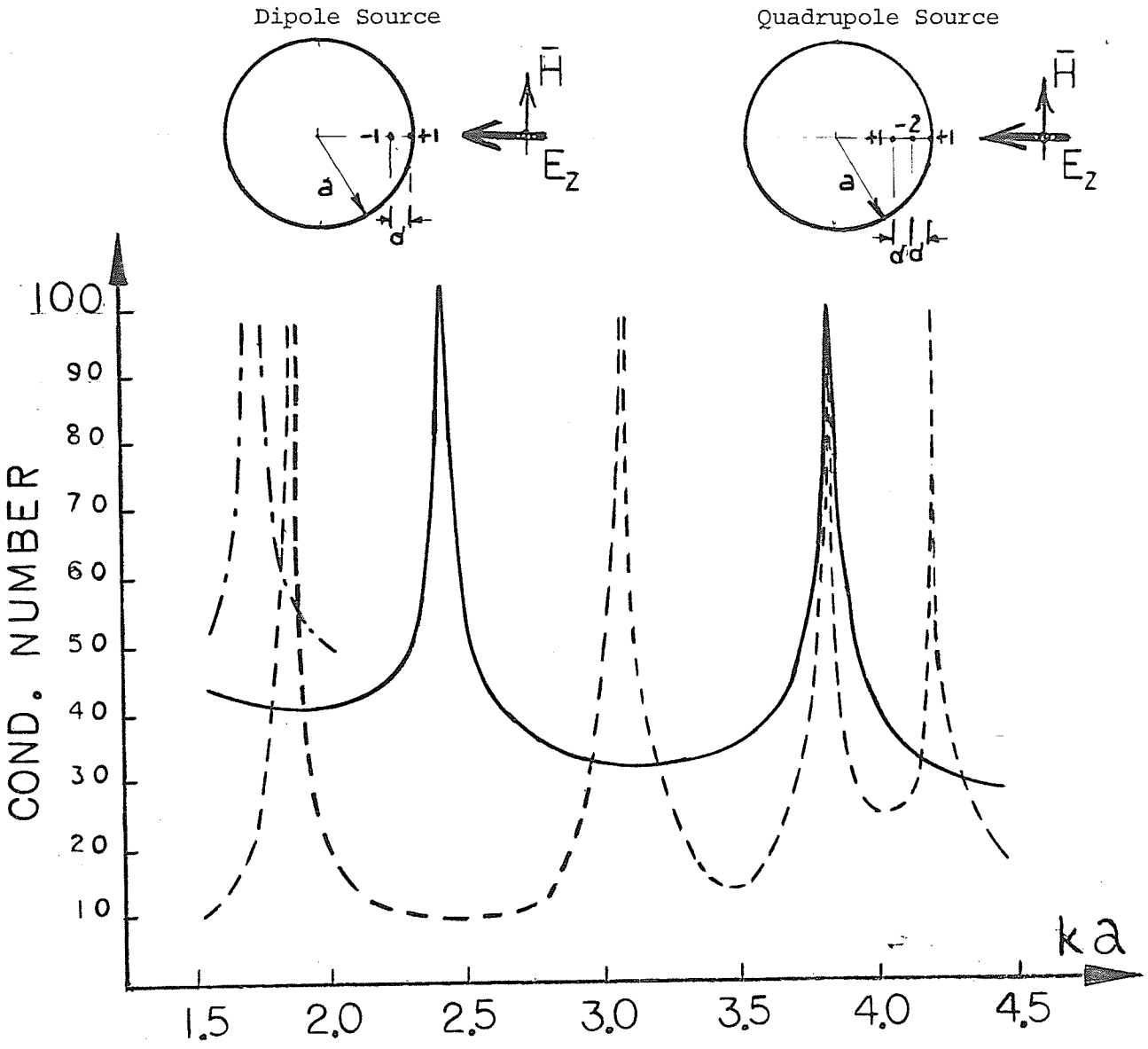

Fig. VI.7. Variation of condition number with ka for the EFIE and its modified forms (kd = 0.001).

——— Point Source;

------- Dipole Source;

-.-.-.- Quadrupole Source.

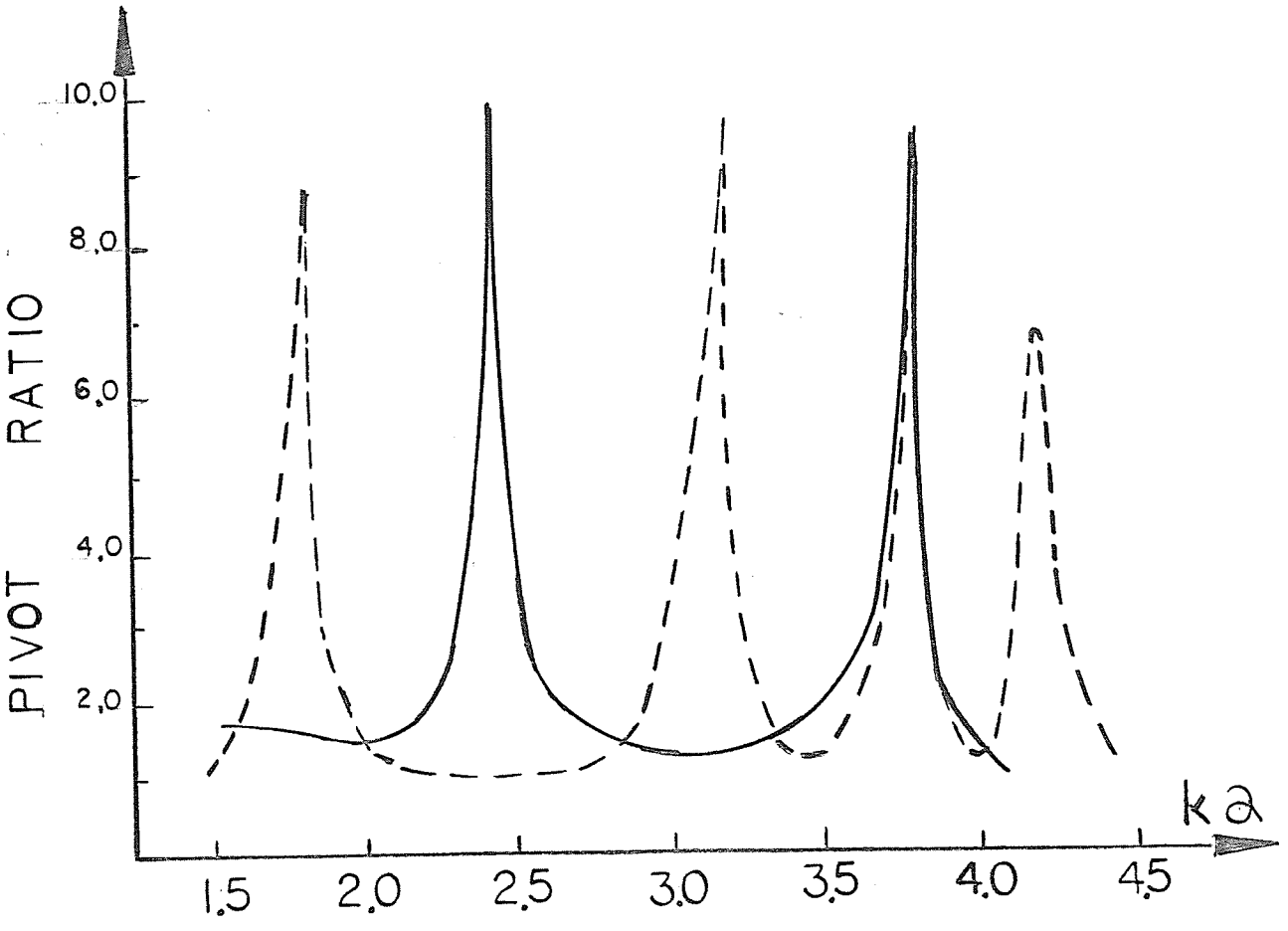

Fig. VI.8. Variation of the Pivot Ratio with ka for the EFIE and its modified form (Dipole Source).

———— Point Source; -------- Dipole Source (kd = 0.001).

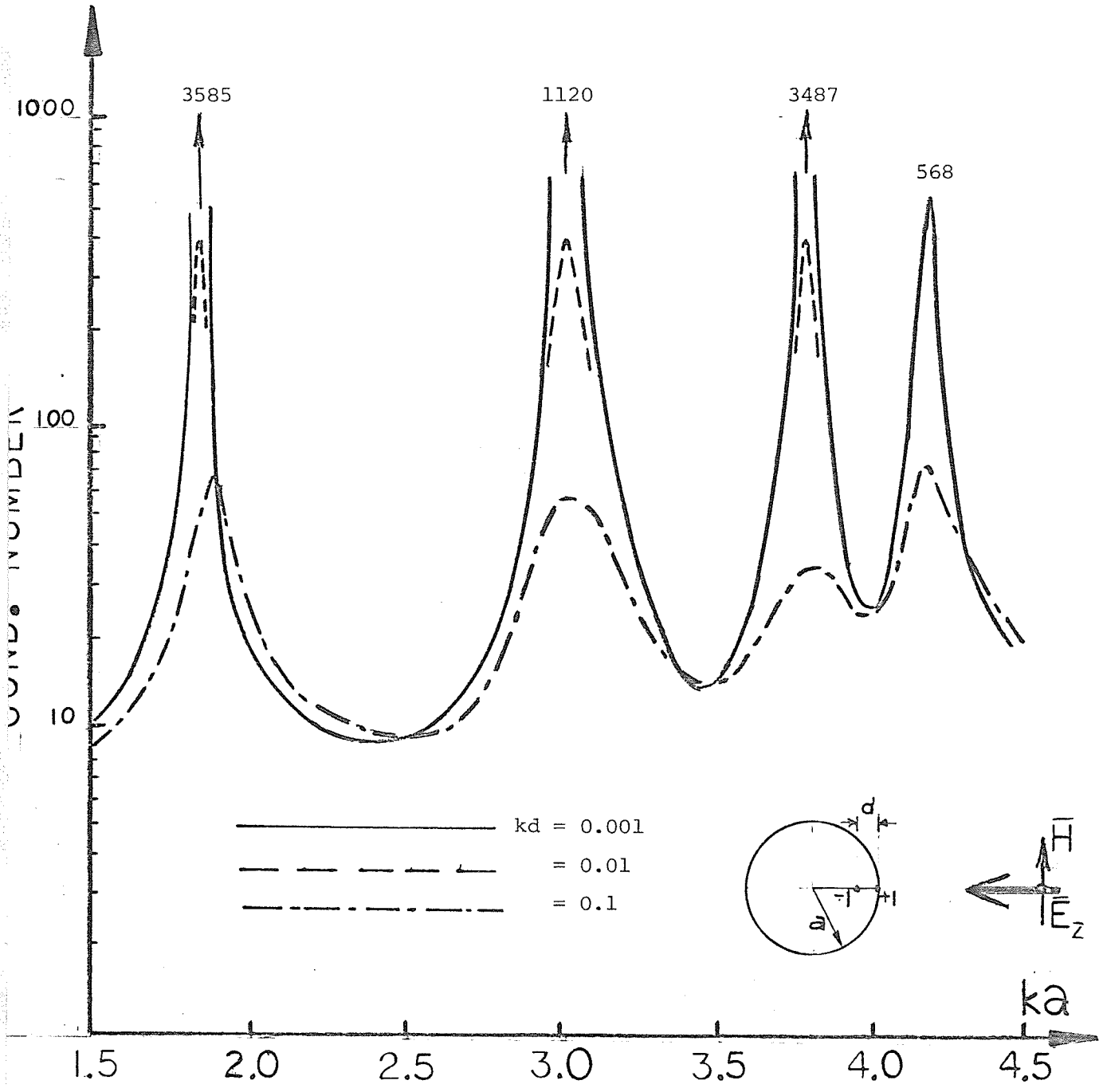

Fig. VI.9. Variation of condition number with ka for the EFIE and its modified form. (Dipole source with kd = 0.001, 0.01, 0.1).

TABLE VI.5

VARIATION OF CONDITION NUMBER AND PIVOT RATIO WITH ka .

EFIE AND ITS MODIFIED FORMS ARE CONSIDERED WITH SMALL VALUES OF kd .

ka	Moment Method	Modified Moment Solution (Dipole)			Modified Moment Solution (Quadrupole)			CONDITION NUMBER
		kd = 0.001	kd = 0.01	kd = 0.1	kd = 0.001	kd = 0.01	kd = 0.1	
1.500	42.95	9.042	8.875	8.862	49.34	172.0	52.79	
1.671	41.47	16.03	15.52	12.87	179.0	125.0	overflow	
1.780	40.79	41.74	38.39	22.73	81.61	121.6	91.19	
1.841	40.54	3583.	456.8	47.45	55.68	1154.	76.42	
1.930	40.36	31.28	32.45	62.56	52.69	83.35	469.6	
2.123	41.55	12.23	13.00	14.57	48.13	39.37	39.12	
2.405	.1200D+05	9.819	9.808	10.35	93.03	49.51	32.96	
2.730	36.46	12.62	12.47	11.83	65.35	127.2	176.5	
3.054	38.57	1120.	468.9	60.81	51.70	34.91	38.38	
3.443	34.64	13.44	13.47	14.21	62.67	74.63	38.99	
3.832	8417.	3487.	390.8	37.77	79.05	69.86	346.6	
4.016	39.67	24.54	24.10	22.12	232.2	38.02	54.47	
4.201	32.77	568.0	380.6	71.48	1.046	33.97	33.97	
4.500	30.62	17.18	17.94	19.56	413.4	54.28	34.18	

TABLE VI.5 (cont'd)

ka	Moment Method	Modified Moment Solution (Dipole)			Modified Moment Solution (Quadrupole)			PIVOT RATIO
		kd = 0.001	kd = 0.01	kd = 0.1	kd = 0.001	kd = 0.01	kd = 0.1	
1.500	1.753	1.041	1.041	1.042	2.276	3.807	1.634	
1.841	1.645	48.61	6.584	1.363	3.667	12.13	1.795	
2.123	1.561	1.133	1.191	1.189	2.916	3.547	3.138	
2.405	29.15	1.151	1.151	1.153	2.585	1.747	1.645	
2.730	1.451	1.095	1.095	1.099	2.310	2.315	3.324	
3.054	1.405	14.17	6.195	1.423	2.999	1.686	1.864	
3.443	1.558	1.240	1.239	1.234	2.476	1.903	1.337	
3.832	34.33	24.00	2.988	1.141	2.393	1.984	3.614	
4.016	1.280	1.263	1.265	1.317	2.380	2.704	2.518	
4.201	.7237D+76	6.899	4.805	1.406	1.000	1.933	2.143	
4.500	.7237D+76	1.182	1.227	1.212	3.278	1.560	1.493	

TABLE VI.6

VARIATION OF CONDITION NUMBER AND PIVOT RATIO WITH ka .

EFIE AND ITS MODIFIED FORMS ARE CONSIDERED WITH LARGE VALUES OF kd .

ka	Moment Method	Modified Moment Method (Dipole)			Modified Moment Method (Quadrupole)			CONDITION NUMBER
		kd = 0.2	kd = 0.4	kd = 0.8	kd = 0.2	kd = 0.4	kd = 0.8	
1.500	4.017	6.725	7.595	6.674	3.886	8.813	43.19	
1.780	3.966	4.142	5.413	5.483	2.521	4.938	46.14	
1.841	3.979	3.846	5.094	5.281	2.361	4.524	39.47	
1.930	4.005	3.500	4.708	5.029	2.170	4.041	29.11	
2.123	4.016	2.979	4.116	4.672	1.875	3.310	15.58	
2.405	3.582	2.524	3.606	4.584	1.609	2.665	8.328	
2.730	3.212	2.202	3.200	4.571	1.428	2.232	5.406	
3.054	3.098	1.981	2.839	4.110	1.316	1.968	4.252	
3.443	3.052	1.792	2.499	3.530	1.230	1.764	3.726	
3.832	2.862	1.662	2.272	3.209	1.174	1.620	3.503	
4.016	2.769	1.615	2.192	3.111	1.155	1.565	3.322	
4.201	2.703	1.575	2.123	3.022	1.138	1.517	3.094	
4.500	2.644	1.520	2.027	2.879	1.117	1.452	2.744	

TABLE VI.6 (cont'd)

ka	Moment Method	Modified Moment Method (Dipole)			Modified Moment Method (Quadrupole)		
		kd = 0.2	kd = 0.4	kd = 0.8	kd = 0.2	kd = 0.4	kd = 0.8
1.500	1.013	1.072	1.037	1.068	1.143	1.204	1.237
1.841	1.009	1.040	1.018	1.036	1.059	1.100	1.621
2.123	1.012	1.027	1.020	1.017	1.031	1.064	1.189
2.405	1.011	1.020	1.022	1.012	1.018	1.043	1.069
2.730	1.006	1.014	1.019	1.016	1.010	1.029	1.032
3.054	1.008	1.009	1.012	1.005	1.005	1.020	1.025
3.443	1.004	1.005	1.006	1.008	1.003	1.014	1.028
3.8317	1.006	1.004	1.005	1.005	1.002	1.010	1.030
3.832	1.006	1.004	1.005	1.004	1.002	1.010	1.030
4.016	1.002	1.003	1.005	1.002	1.001	1.008	1.027
4.201	1.003	1.003	1.005	1.003	1.001	1.007	1.021
4.500	1.005	1.002	1.004	1.003	1.001	1.005	1.013

PIVOT RATIO

6.6 Conclusion

In this chapter, modified E-field and H-field integral equations were studied with the aim of eliminating ill-condition behaviour of their associated coefficient matrices resulting when a moment method of solution is applied to the integral equation. The modified equations are obtained by differentiating the original equation ℓ times, (ℓ = 1, 2, 3 ..), with respect to the normal n' to the contour c at a field point on the scatterer. This is equivalent to consider Green's functions of dipole or quadrupole line sources, etc. ... in the kernel of the integral equation. It was found that the ill-conditioning of the matrix associated with the original E-field equation can be made to occur at different frequencies than that of the true frequency of internal resonance. A proper value of kd for the separation between the line sources, might even eliminate completely any ill-conditioning at TM resonances. In addition, it was found that elements of the coefficient matrix near the diagonal, decay at a faster rate as the higher order derivatives of the equation are considered. Accordingly, we were able to approximate almost 12.5% of the total number of entries by zeros and still obtain an accurate estimate for the magnitude of the currents on the scatterer. This of course constitutes a first step towards reducing the coefficient matrix to a sparse one, and hence using sparse matrix techniques for inversion in the case of large scatterers.

The modified H-field equations also resulted in matrices which are less dense than those associated with the original H-field equa-

tion. For small ka , the solution converged for small values of kd. For this case, the matrix elements for the first and second order derivatives of the equation were of the same order of magnitude as those resulting from the original H-field equation. On the other hand, larger values of kd were needed for the convergence of the solution when ka is large. It was concluded therefore that an optimum value of kd/ka should be determined in this case to obtain accurate results. The determination of this optimum value becomes important when the technique is applied to bodies of revolution with impedance boundary conditions. This of course is due to the fact that the relevant integral equation in this case are in effect formulated from the combination of the H-field and E-field equations of perfectly conducting scatterers.

Derivatives for both E-field and H-field equations of orders higher than those considered in this chapter, might show some ranges of kd where both equations result in a predominantly diagonal matrix accompanied with accurate solutions. In this case, the equations can be combined successfully to study impedance boundary value problems. This, however, is left for a future investigation.

CHAPTER VII

DISCUSSION AND CONCLUSION

The principal aim of the present work was to provide a new tool for the design of corrugated electromagnetic horns. Such horns have already proved to possess many desirable features, mainly, a rotational symmetric pattern, a low level of cross-polarization, a well defined phase centre, etc.

Previous analytical investigations related to the design of such radiators were based on particular mathematical approximations and treated only a limited range of variation for some of the important design parameters. Hence, studies based on modal analysis or geometrical theory of diffraction were generally assuming long horn walls and resonant corrugation slots. Radiation pattern were usually determined using aperture integration technique, hence neglecting the effect of the currents on the outer surface of the horn walls.

Due to the basic assumptions adopted in these theories, many important facts associated with the radiation characteristics of these horns could not be explained. According to these studies, square corrugations with groove depths (d/λ) in the range of $0 \leq d/\lambda \leq 1/4$ provide an inductive surface and cannot deflect the electromagnetic energy away from the horn walls. In such cases, diffraction effects at the aperture edges will be responsible for deteriorating the symmetry of the radiation

pattern. This, however, was contradicting some experimental results obtained by Shafai [85] who designed a corrugated horn with similar E- and H-plane radiation patterns, and having corrugations which are 0.2λ deep.

The procedure adopted in this thesis was to substitute for the corrugations a smooth surface with impedance boundary conditions. The excitation was provided by a lumped source whose polarization and location, together with the proper waveguide dimensions, provide the correct type of field incident at the horn-waveguide junction. An integral equation for the induced currents on the waveguide and horn walls was then formulated and solved using the moment method of solution. Once these currents are known, the total electromagnetic field radiated from the horn can be determined as the sum of the field resulting from the induced currents plus that due to the exciting source. The use of the impedance boundary conditions reduces the effective outer surface of the waveguide-horn combination. The subsequent application of the moment method to the integral equation results therefore in matrices of reduced size which can be handled on today's generation of computers.

It is concluded from our study on corrugated surfaces that different types of corrugations are equivalent if they present the same surface impedance to the incident electromagnetic wave. Hence, equivalent corrugation types will have the same effect on the horn radiation pattern and can be interchanged without affecting the directivity of the

horn. The value of the surface impedance is determined by studying the possible type of electromagnetic field which can exist in the grooves of the corrugations and is, therefore, independent of the field existing above the corrugated surface. Usually, the characteristic impedance of the dominant mode in the corrugations was providing reasonably accurate results in our study of corrugated horns using numerical methods. The dominant radial waveguide mode can be used to determine the surface impedance representing the V-type corrugations, while the dominant parallel plate waveguide mode is used in conjunction with rectangular corrugated surfaces. In the latter case, the effect of zero impedance of the teeth can be taken into consideration by weighting the impedance at the top of the groove by the ratio $g/(g+\delta)$, where g and δ are the slot and tooth widths respectively. This averaging process is useful since it needs less matching points in a moment method of solution. Although it was reported [33] that this average impedance should be used only when $\delta \leq 0.1g$, it was found, however, that the expression works satisfactorily in our numerical solution for cases where $\delta \simeq 0.5g$.

Due to the equivalence of the different types of corrugations, manufacturing costs and ease of production for each type become, therefore, important criteria in the design stage. In addition, corrugations with minimum surface area must be generally used to reduce ohmic losses in places where surface current is large. Proper machining and silver coating of these areas help in further reduction of losses.

It was also concluded that for a low VSWR, a smooth transition is needed between the waveguide and the corrugated walls of the horn. Such transitions could be achieved by varying a proper geometrical parameter determining the impedance of the corrugations. It can also be achieved by inserting a number of dielectrics in the grooves. In all these cases, the impedance is a varying function of position and the integral equation formulation using impedance boundary conditions can be solved without further complication. On the other hand, the application of modal analysis or geometrical theory of diffraction to non-uniform corrugations, is not clear at the present time.

In the case of rotationally symmetric corrugated horns, the integral equation for the induced currents was obtained by combining the electric field integral equation (EFIE) and the dual form of the magnetic field integral equation (MFIE) of a perfectly conducting counterpart with no corrugations. Symmetry properties of bodies of revolution were used to reduce surface integrals to line integrals for the surface currents. By applying the moment method to the final equation, it was found that the coefficient matrix can be represented as the combination of three matrices. One of these matrices represents the surface impedance over the waveguide and horn, while the other two depend only on the geometry of the smooth wall counterpart. The entries of the last two matrices are generally determined by numerical integration. Separation of the coefficient matrix into three matrices as mentioned above results in substantial saving in computer time when different surface impedances are investigated.

Reliable results could be obtained only when the horn walls are assigned a non-zero thickness. This was attributed to the fact that the integral equation was formulated in terms of the dual form of the MFIE of smooth conductors. The latter is known to be useless in the numerical solution of very thin scatterers.

It is also worthwhile to note that the integral equation formulation using impedance boundary conditions permitted the simultaneous consideration of the effect of corrugation parameters, wall length and horn flare angle on the radiation properties of the horn. It was found that for short horns, optimum performance is not necessarily obtained when the corrugations are resonant or capacitive in nature. Resonant corrugations do indeed result in the fastest decay of surface currents on the horn walls, hence reducing wave diffraction at the horn aperture. At the same time, however, they result in a high VSWR at the horn-waveguide junction. Furthermore, rays diffracted at this junction might interfere destructively with other rays and hence deteriorate the radiation pattern when wall lengths and flare angles are not properly matched with the value of the corrugation impedance.

The same formulation used to investigate the radiation properties of corrugated horns proved useful also in the study of the scattering properties of electromagnetic horns. For rotationally symmetric horns, the inner surface at the bottom of the waveguide section was assigned a uniform impedance value in both directions tangential to the surface. For

circular waveguides with $1.841 < ka < 2.405$, this value is equal to the characteristic impedance of the dominant TE_{11} mode in the guide.

In general, it was found that 7 to 8 matching points per wavelength were needed in the investigation of the radiation properties of corrugated horns. When studying the scattering properties, a higher density was needed, in particular at the bottom of the waveguide section, for a convergent solution to be obtained. Accordingly, matrix sizes of the order of 100 x 100 were normally inverted during the investigation. The total length of the generating line of the horn did not exceed 6λ in any case we have studied.

Chapters III to V determined the aspects of the numerical solution associated with the impedance representation of corrugations and matched terminations in horns when studied separately. The application of the analysis to study the scattering properties of corrugated electromagnetic horns becomes a straight forward extension.

Our formulation can also be used to study the radiation properties of corrugated horns when the feeding waveguide is carrying a combination of dominant plus higher order modes. This is usually useful in problems of beam synthesis and requires only the consideration of proper lumped sources for excitation.

The same formulation could also be extended to study the scattering properties of bodies of revolution with impedance boundary conditions

when the incident wave is not in the axial direction. In this case higher order azimuthal modes have to be considered in the numerical evaluation of the scattered field.

Investigations of these new topics, however will result in large coefficient matrices to be inverted when the moment method is applied to the integral equation. Hence, apart from the excessive computer time and storage required for the solution, the accumulation of round off error during inversion also becomes a limiting factor in the numerical investigation. In an attempt to overcome these difficulties, we investigated the formulation of integral equations for the currents using new Green's functions. Hence Green's functions which are in effect the field of a dipole or a quadrupole source were used to obtain integral equations for cylindrical scatterers. The modified integral equations could also be obtained by successive differentiation of the equation obtained by conventional moment method with respect to the normal to the contour of the scatterer at the field point. By applying the moment method, the peak condition number of the new coefficient matrix in the TM case was found to occur at frequencies different from those of internal resonance. It was concluded, therefore, that the modified integral equation can be used to reduce the error in the solution resulting from the ill-conditioned matrices of the original moment method. In addition, it was found that the off-diagonal elements of the coefficient matrix obtained through the application of the new Green's function decay at a faster rate when the multiplicity of the elementary source was increased. When elements

far from the diagonal were assigned zero value, the solution for the current magnitudes was still close to the exact current obtained analytically. The scattered field, however, was less accurate.

It was also concluded that an optimum multiple source could be determined and used in the modified integral equation. For this optimum source, all elements in the coefficient matrix smaller than a predetermined percentage of the diagonal element can then be approximated to zero. When the number of zeros becomes reasonably high, sparse matrix techniques can be used to invert the matrix. This of course will increase the maximum size of the scatterer which can be handled by moment methods.

A parametric study can also be conducted to determine the optimum multiple source (i.e., its degree of multiplicity, the separation between its components) for which both the magnetic and the electric fields integral equations would possess, at the same time, a predominantly diagonal coefficient matrix and an accurate solution. If this optimum source is determined, the two modified equations can then be combined in a proper ratio and still give accurate results. The combined equation can then be studied when applied in three dimensions and could be useful in investigating scattering from bodies of revolution with impedance boundary conditions. Extensions for these studies was left for possible future research.

Some of the above mentioned results and conclusions have been documented in [82, 115, 116, 117, 118, and 119].

APPENDIX A

INTEGRAL FUNCTIONS USED IN APERTURE INTEGRATION AND GTD ANALYSIS OF CORRUGATED HORNS

A.1 The function $F(\theta,\theta_0,kr')$ appearing in equation (2.12a and b) is given by

$$F(\theta,\theta_0,kr') = \int_0^{\theta_0} \{(\cos\theta + \cos\theta')\,[J_0(kr'\sin\theta\,\sin\theta') + J_2(kr'\sin\theta\,\sin\theta')]$$

$$+ (1+\cos\theta\,\cos\theta')\,[J_0(kr'\sin\theta\,\sin\theta') - J_2(kr'\sin\theta\,\sin\theta')]$$

$$+ 2j\,\sin\theta\,\sin\theta'\,J_1(kr'\sin\theta\,\sin\theta')\}\,x$$

$$x\,f_{1\nu}^{(1)}(\theta')\,\exp(jkr'\,\cos\theta\,\cos\theta')\,\sin\theta'\,d\theta'$$

where

$$f_{1\nu}^{(1)}(\theta') = \frac{dP_\nu'(\cos\theta')}{d\theta'} + \frac{P_\nu'(\cos\theta')}{\sin\theta'}$$

A.2 Expressions for I_1, I_2, I_3 and I_4 appearing in (2.19a and b) and in (2.20a and b) are given by

$$I_1 = \int_{-b/2}^{b/2} I_{x1}^e(x')\,\exp\left[jk\,\sin\theta\,\left(x'\cos\phi + \frac{a}{2}\sin\phi\right)\right]\,dx'$$

$$I_2 = \int_{-b/2}^{b/2} I_{x2}^e(x')\,\exp\left[jk\,\sin\theta\,\left(x'\cos\phi - \frac{a}{2}\sin\phi\right)\right]\,dx'$$

$$I_3 = \int_{-a/2}^{a/2} I_{y3}^{m}(y') \exp\left[jk \sin\theta \left(b/2\cos\phi + y'\sin\phi\right)\right] dy'$$

$$I_4 = \int_{-a/2}^{a/2} I_{y4}^{m}(y') \exp\left[jk \sin\theta \left(-b/2\cos\phi + y'\sin\phi\right)\right] dy'$$

where

$I_{x1}^{e}(x')$ = $\hat{x}$-directed equivalent electric current on the H-plane edge at y=a/2

$$= -2\sqrt{2\pi k}\, e^{j(\pi/4)}\, H_{\rho}^{i}\, D_s(\pi - \theta_H + \theta, 2)$$

$I_{x2}^{e}(x')$ = $\hat{x}$- directed equivalent electric current on the H-plane edge y= -a/2

$$= -2\sqrt{2\pi k}\, e^{j(\pi/4)}\, H_{\rho}^{i}\, D_s(\pi - \theta_H - \theta, 2)$$

$$H_{\rho}^{i} = -\frac{1}{j\omega\mu_0}\, \hat{a}_{\rho} \cdot (\nabla \times \bar{E}^{a})\Big|_{edge}$$

$I_{y3}^{m}(y')$ = $\hat{y}$-directed equivalent current on the H-plane edge at x=b/2

$$= -2\sqrt{2\pi k}\, e^{j(\pi/4)}\, (-E_{\rho}^{i})\, D_s(\pi - \theta_E + \theta, 2)$$

$I_{y4}^{m}(y')$ = $\hat{y}$-directed equivalent current on the H-plane edge at x= -b/2

$$= -2\sqrt{2\pi k}\, e^{j(\pi/4)}\, (-E_{\rho}^{i})\, D_s(\pi - \theta_E - \theta, 2)$$

and

$$E_{\rho}^{i} = \frac{1}{j\omega\varepsilon_0}\, \hat{a}_{\rho} \cdot (\nabla \times \bar{H}^{a})\Big|_{edge} .$$

A.3 Expression for $K(\alpha)$, $E_s(\alpha)$ and v_B appearing in (2.21) are given by

$$K(\alpha) = \begin{cases} 2, & \text{if } 180^\circ < \alpha < 270^\circ \\ 0, & \text{otherwise .} \end{cases}$$

$E_s(\alpha)$ = slope diffracted field from the model of Figure (II.3b)

$$= \eta H^d = jk\eta\ (-E^i_\rho)\ D_s(\alpha, 2)$$

$$E^i_\rho \simeq \frac{1}{j\omega\varepsilon_0}\ \hat{a}_\rho \cdot (\nabla \times \bar{H})\Big|_{\text{at the edge}}$$

= normal derivative of the vanishing incident tangential field along the edge

$$v_B = \frac{2\, e^{j(\pi/4)}}{\sqrt{\pi}}\ \frac{1}{n}\ \sin\frac{\pi}{n}\ \frac{\cos\left(\frac{\alpha-90^\circ}{n}\right)}{\cos\left(\frac{\pi}{n}\right) - \cos\left(\frac{\alpha-90^\circ}{n}\right)}$$

$$\cdot\ e^{jkd\cos(\alpha-90^\circ)} \int_{\sqrt{kd\,(1+(\cos\alpha-90^\circ))}}^{\infty} \exp\left(-j\tau^2\right) d\tau$$

and $n = 3/2$ for the corner [114] .

A.4 Expressions for I_5 and I_6 appearing in (2.22) are given by:

$$I_5 = \int_{-a/2}^{a/2} I_{y5}^{m}(y') \cdot \exp\,[jk(b/2 + d\cos\theta_E)\sin\theta\cos\phi]$$

$$\cdot \exp\,[-jkd\sin\theta_E\cos\theta]\exp\,[jk\sin\theta\, y'\sin\phi]\,dy'$$

and

$$I_6 = \int_{-a/2}^{a/2} I_{y6}^{m}(y') \cdot \exp\,[jk(-b/2 - d\cos\theta_E)\sin\theta\cos\phi]$$

$$\cdot \exp\,[-jkd\sin\theta_E\cos\theta]\exp\,[jk\sin\theta\, y'\sin\phi]\,dy'$$

$$I_{y5}^{m} = I_{y6}^{m} = -2\sqrt{2\pi k}\, e^{j(\pi/4)}\,(-E_{\rho}^{i})\, D_s(3\pi/2, 2)$$

$$\cdot v_B(\alpha - 90^{\circ}, d, 3/2)\exp\,(jkd\sin\theta_E)\,.$$

APPENDIX B

DERIVATION OF EQUATION (3.2)

By defining a system of cylindrical coordinates $(\hat{\ell}, \hat{n}, \hat{z})$ such that

$$\hat{\ell} \times \hat{n} = \hat{z} \tag{B.1}$$

Then, one can write [113]

$$\bar{H}_t = \frac{-jk_z}{k^2 - k_z^2} \left(\frac{\partial H_z}{\partial n} \hat{n} + \frac{\partial H_z}{\partial \ell} \hat{\ell}\right) \tag{B.2}$$

and

$$\bar{E}_t = - \sqrt{\frac{\mu}{\varepsilon}} \frac{k}{k_z} (\hat{z} \times \bar{H}_t) \tag{B.3}$$

where the subscript t denotes the component in the direction transverse to z, and k_z is the z variation in the field.

By substituting for $\bar{H}_t$ from (B.2) and using the vector relationship defined in (B.1), equation (B.3) takes the form

$$\bar{E}_t = \frac{j\sqrt{\mu/\varepsilon}\, k}{k^2 - k_z^2} \left\{\frac{\partial H_z}{\partial n} (-\hat{\ell}) + \frac{\partial H_z}{\partial \ell} \hat{n}\right\} \tag{B.4}$$

From which we can deduce

$$\frac{\partial H_z}{\partial n} = \frac{jk}{\eta} E_\ell \tag{B.5}$$

for a field with no variation in the z direction.

APPENDIX C

DERIVATION OF EQUATION (4.38)

Since the surface of the scatterer s is closed, then

$$\int\int_s \nabla_s \cdot (V \bar{W}^p_{mi}) \, ds = 0 \tag{C.1}$$

Now, the representations (4.8a and b) for the surface gradient and the surface divergence imply that

$$\nabla_s \cdot (V \bar{W}^p_{mi}) = V \nabla_s \cdot \bar{W}^p_{mi} + \bar{W}^p_{mi} \cdot \nabla_s V \tag{C.2}$$

In (C.2), the surface gradient of V can be replaced by the ordinary three-dimensional gradient of V because (4.8a) is the component of the three-dimensional gradient tangential to s and $\bar{W}$ is tangential to s.

Substitution of (C.2) into (C.1) and then (C.1) into (4.36) yields to the equation (4.38).

APPENDIX D

DERIVATION OF EQUATION (4.41)

The scalar potential V appearing in (4.38) is given by (4.16) in terms of the unknown charge density σ. The latter, however, is related to $\nabla_s \cdot \bar{J}$ through (4.19). If now we use (4.8b) for the surface divergence and (4.24 and 4.25) for the expansion of the current $\bar{J}$, we obtain in analogy to (4.40), the expressions

$$\sigma^{t}_{nj} = \frac{-1}{j\omega\rho'} \frac{\partial}{\partial t'} (\rho' f_j(t')) e^{jn\phi'} \tag{D.1a}$$

$$\sigma^{\phi}_{nj} = \frac{-n}{\omega\rho'} f_j(t') e^{jn\phi'} \tag{D.1b}$$

which specialize the variation of σ in (4.16) along the t and ϕ coordinates, respectively.

Accordingly, the more general expression corresponding to (4.38), would include $\bar{W}^{p}_{mi}$ and $\bar{J}^{q}_{nj}$ and would be written as:

$$(Z^{pq,\bar{J}}_{mn})_{ij} = j\omega \int\int_{s} [\bar{W}^{p}_{mi} \cdot \bar{A} (\bar{J}^{q}_{nj}) + v^{p}_{mi} V (\bar{J}^{q}_{nj})] \, ds' \tag{D.2}$$

Substituting for $\bar{W}^{p}_{mi}$, $\bar{A}(\bar{J}^{q}_{nj})$, v^{p}_{mi} from (4.24 and 4.25), (4.29) and (4.40) and considering the substitution of σ^{p}_{nj} as given in (D.1a and b) in the representation of V, one then obtains

$$\begin{bmatrix} (Z_{mn}^{tt,\bar{J}})_{ij} \\ (Z_{mn}^{\phi t,\bar{J}})_{ij} \\ (Z_{mn}^{t\phi,\bar{J}})_{ij} \\ (Z_{mn}^{\phi\phi,\bar{J}})_{ij} \end{bmatrix} = \int_0^{t_u} dt \int_0^{t_u} dt' \int_0^{2\pi} d\phi \int_0^{2\pi} d\phi' \quad \frac{e^{-jk|\bar{r}-\bar{r}'|}\, e^{j(n\phi'-m\phi)}}{4\pi|\bar{r}-\bar{r}'|}$$

$$\times \begin{bmatrix} jk\rho\, f_i(t)\, \rho' f_j(t')\, \hat{u}_t \cdot \hat{u}_t' - \frac{j}{k} \frac{\partial}{\partial t}(\rho f_i(t))\, \frac{\partial}{\partial t'}(\rho' f_j(t')) \\ jk\rho\, f_i(t)\, \rho' f_j(t')\, \hat{u}_\phi \cdot \hat{u}_t' - \frac{m}{k\rho}\, \rho f_i(t)\, \frac{\partial}{\partial t'}(\rho' f_j(t')) \\ jk\rho\, f_i(t)\, \rho' f_j(t')\, \hat{u}_t \cdot \hat{u}_\phi' + \frac{n}{k\rho'} \frac{\partial}{\partial t}(\rho f_i(t))\, \rho' f_j(t') \\ j\rho f_i(t)\, \rho' f_j(t')\, (k\hat{u}_\phi \cdot \hat{u}_\phi' - \frac{mn}{k\rho\rho'}) \end{bmatrix} \quad (D.3)$$

Using (4.2), (4.3) and (4.4), for $\hat{u}_t$, $\hat{u}_t'$ and $\hat{u}_\phi'$, we obtain the dot products

$$\hat{u}_t \cdot \hat{u}_t' = \sin\nu \sin\nu' \cos(\phi'-\phi) + \cos\nu \cos\nu'$$

$$\hat{u}_\phi \cdot \hat{u}_t' = \sin\nu' \sin(\phi'-\phi)$$

$$\hat{u}_t \cdot \hat{u}_\phi = -\sin\nu \sin(\phi'-\phi)$$

$$\hat{u}_\phi \cdot \hat{u}_\phi = \cos(\phi'-\phi) \quad (D.4)$$

while the distance $|\bar{r}-\bar{r}'|$ is given in (4.7) .

In view of (D.4) and (4.7), the integrands of (D.3) are periodic functions of ϕ' with period 2π. Hence we can replace ϕ' by $(\phi'+\phi)$ without changing the values of the integrals. When this is done, the ϕ dependence of the integrands becomes $e^{j(n-m)\phi}$ which when integrated gives 2π for $m=n$ and zero otherwise.

APPENDIX E

ON THE DERIVATION OF EQUATION (4.47)

We start from the H-field integral equation for the electric current induced on the surface of a scatterer with perfect conducting boundaries (equation (4.46)). Then let $\bar{J}(r')$ be the current on an infinitesimal area Δs plus the current on s minus Δs. The area Δs is that portion of s inside a sphere of radius δ centered at the point of s nearest $\bar{r}$. δ is so small that Δs is essentially flat and the current $\bar{J}$ on it is a constant. If the infinitesimal distance Δ of equation (4.46) is appreciably less than δ, then, from Ampere's law, the contribution to $\hat{n} \times \bar{H}^{sc}$ from the current on Δs is $\frac{-\bar{J}}{2}$, where $\bar{J}$ is the value of the current on Δs. This contribution to $\hat{n} \times \bar{H}^{sc}$ comes exclusively from a small portion of Δs in the immediate vicinity of $\bar{r}$. The current on that portion of Δs for which the distance to the field point $\bar{r}$ is appreciably greater than Δ does not contribute to $\hat{n} \times \bar{H}^{sc}$. Now we let $\Delta \to 0$, in which case $\bar{r}$ becomes a point of s, the contribution $-\bar{J}/2$ comes from the value of $\bar{J}$ at the single point $\bar{r}$, and the current on any portion of Δs which does not contain $\bar{r}$ contributes nothing to $\hat{n} \times \bar{H}^{sc}$. In view of the above considerations Mautz and Harrington [73] obtained equation (4.47) in which $\bar{r}$ lies exactly on s.

APPENDIX F

DERIVATION OF EQUATION (4.53)

To obtain equation (4.53) from (4.52), we first evaluate the cross product $(\bar{r}-\bar{r}') \times \bar{M}(\bar{r}')$. Hence using (4.23) to express $\bar{M}$ in terms of its t and ϕ components, we get:

$$(\bar{r}-\bar{r}') \times \bar{M}(\bar{r}') = (\bar{r}-\bar{r}') \times \hat{u}_{t'} M^{t}(t',\phi') + (\bar{r}-\bar{r}') \times \hat{u}_{\phi} M^{\phi}(t',\phi') \tag{F.1}$$

Substitution from (4.2, 3, 5, and 6) in (F.1) yields

$$\begin{aligned}(\bar{r}-\bar{r}') \times \bar{M}(\bar{r}') = {} & \{\hat{u}_{\rho}[-\rho' \cos\nu' + (z'-z) \sin\nu'] \sin(\phi'-\phi) \\ & - \hat{u}_{\phi}[(\rho-\rho' \cos(\phi'-\phi)) \cos\nu' + (z'-z) \sin\nu' \cos(\phi'-\phi)] \\ & + \hat{u}_{z} \rho \sin\nu' \sin(\phi'-\phi)\} M^{t}(t',\phi') \\ & + \{\hat{u}_{\rho} (z'-z) \cos(\phi'-\phi) + \hat{u}_{\phi}(z'-z) \sin(\phi'-\phi) \\ & + \hat{u}_{z} [-\rho'+\rho \cos(\phi'-\phi)]\} M^{\phi}(t',\phi')\end{aligned} \tag{F.2}$$

To evaluate the $\hat{u}_t$ and $\hat{u}_\phi$ components of (4.52) we use

$$\hat{u}_t \cdot \hat{n} \times [(\bar{r}-\bar{r}') \times \bar{M}(\bar{r}')] = \hat{u}_{\phi} \cdot [(\bar{r}-\bar{r}') \times \bar{M}(\bar{r}')] \tag{F.3a}$$

and

$$\hat{u}_\phi \cdot \hat{n} \times [(\bar{r}-\bar{r}') \times M(r')] = - \hat{u}_t \cdot [(\bar{r}-\bar{r}') \times \bar{M}(\bar{r}')] \qquad (F.3b)$$

When (4.2a) and (F.2) are used, equation (F.3a and b) become

$$\begin{aligned} \hat{u}_t \cdot \hat{n} \times [(\bar{r}-\bar{r}') \times \bar{M}(\bar{r}')] &= \{[(\rho'-\rho)\cos\nu' - (z'-z)\sin\nu']\cos(\phi'-\phi) \\ &\quad - 2\rho\cos\nu'\sin^2(\tfrac{\phi'-\phi}{2})\} M^t(t',\phi') \\ &\quad + (z'-z)\sin(\phi'-\phi) M^\phi(t',\phi') \qquad (F.4a) \end{aligned}$$

and

$$\begin{aligned} \hat{u}_\phi \cdot \hat{n} \times [(\bar{r}-\bar{r}') \times \bar{M}(\bar{r}')] &= [\rho'\sin\nu\cos\nu' - \rho\sin\nu'\cos\nu \\ &\quad - (z'-z)\sin\nu\sin\nu'] \sin(\phi'-\phi) M^t(t'_\phi) \\ &\quad + \{[(\rho'-\rho)\cos\nu - (z'-z)\sin\nu]\cos(\phi'-\phi) \\ &\quad + 2\rho'\cos\nu\sin^2(\tfrac{\phi'-\phi}{2})\} M^\phi(t',\phi') \qquad (F.4b) \end{aligned}$$

The surface integral in (4.52) include an integration with respect to ϕ'. Since the integrand is a periodic function of ϕ' with period 2π, while the integration is carried from 0 to 2π in ϕ', then a replacement of ϕ' by $\phi'+\phi$ will not change the value of the integral. When this is considered, the substitution of (F.4a and b) in (4.52) then leads to the integral equation (4.53).

APPENDIX G

DERIVATION OF EQUATION (4.68)

When we considered the equation

$$\hat{n} \times \bar{E}^{sc} = \frac{-1}{\varepsilon} \hat{n} \times \nabla \times \bar{F}$$

$$= - \lim_{\Delta \to 0} \hat{n} \times \nabla \times \int\int_{s} \bar{M} \Phi \, ds' \qquad (G.1)$$

we obtained, through the application of the moment method and the expansion of $\bar{M}$ in equation (4.55), a matrix equation of the form

$$\begin{bmatrix} [\tilde{Z}^{tt}_{m}, \bar{F}] & [\tilde{Z}^{t\phi}_{m}, \bar{F}] \\ [\tilde{Z}^{\phi t}_{m}, \bar{F}] & [\tilde{Z}^{\phi\phi}_{m}, \bar{F}] \end{bmatrix} \begin{bmatrix} [b^{t}_{m}] \\ [b^{\phi}_{m}] \end{bmatrix} = \begin{bmatrix} < W^{t}_{m}, \hat{n} \times \bar{E}^{sc} > \\ < W^{\phi}_{m}, \hat{n} \times \bar{E}^{sc} > \end{bmatrix} \qquad (G.2)$$

Hence, if we now consider the following equation (instead of G.1)

$$- \underset{\bar{F}}{\bar{E}^{sc}} = \frac{1}{\varepsilon} \nabla \times \bar{F} = \lim_{\Delta \to 0} \nabla \times \int\int_{s} \bar{M} \Phi \, ds' \qquad (G.3)$$

and we assume the same expansion for $\bar{M}$ as before, one should get:

$$\begin{bmatrix} [\tilde{Z}_m^{\phi t,\bar{F}}] & [\tilde{Z}_m^{\phi\phi,\bar{F}}] \\ -[\tilde{Z}_m^{tt,\bar{F}}] & -[\tilde{Z}_m^{t\phi,\bar{F}}] \end{bmatrix} \begin{bmatrix} [b_m^t] \\ [b_m^\phi] \end{bmatrix} = \begin{bmatrix} < W_m^t, -\bar{E}^{sc}_{\bar{F}} > \\ < W_m^\phi, -\bar{E}^{sc}_{\bar{F}} > \end{bmatrix} \tag{G.4}$$

Accordingly, when the relation between M^t, M^ϕ and J^t, J^ϕ are used from (4.27), one should make the following changes in (G.4).

$$[b_m^t] \longrightarrow [Z^\phi \; I_m^\phi] \tag{G.5a}$$

and

$$[b_m^\phi] \longrightarrow [-\, Z^t \; I_m^t] \tag{G.5b}$$

In this case, (G.4) becomes:

$$\begin{bmatrix} -[\tilde{Z}_m^{\phi\phi,\bar{F}}] & [\tilde{Z}_m^{\phi t,\bar{F}}] \\ [\tilde{Z}_m^{t\phi,\bar{F}}] & -[\tilde{Z}_m^{tt,\bar{F}}] \end{bmatrix} \begin{bmatrix} [Z^t \; I_m^t] \\ [Z^\phi \; I_m^\phi] \end{bmatrix} = \begin{bmatrix} < W_m^t, -\bar{E}^{sc}_{\bar{F}} > \\ < W_m^\phi, -\bar{E}^{sc}_{\bar{F}} > \end{bmatrix} \tag{G.6}$$

from which (4.68) can be directly deduced.

APPENDIX H

ELEMENTS OF THE MATRIX [B] OF EQUATION (4.102)

Examination of the equation (4.68) shows that the matrix [B] appearing in (4.102) can be put in the form

$$[B] = \begin{bmatrix} [B_1] & -[B_1] \\ [B_2] & -[B_2] \end{bmatrix} \tag{H.1}$$

Both $[B_1]$ and $[B_2]$ are square matrices of order Nl. In each of them, the rows are all the same. Any row of $[B_1]$ would be given by

$$(B_1)_{i,j}\Big|_{j=1,Nl} = -[Z_1^t \quad Z_2^t \quad Z_3^t \quad .... \quad Z_{Nl}^t] \tag{H.2}$$

which are the values of the surface impedance Z^t evaluated at the segments $n=1$ to Nl.

Similarly, any row of $[B_2]$ would be given in terms of the surface impedance Z^ϕ at these segments. Hence

$$(B_2)_{i,j}\Big|_{j=1,Nl} = [Z_1^\phi \quad Z_2^\phi \quad Z_3^\phi \quad .... \quad Z_{Nl}^\phi] \tag{H.3}$$

APPENDIX I

NEAR FIELD AND FAR FIELD COMPONENTS OF AN X-DIRECTED HERTZIAN DIPOLE

Consider an x-directed Hertzian dipole centered at (x',y',z'). The electric field at a field point (x,y,z) is given by

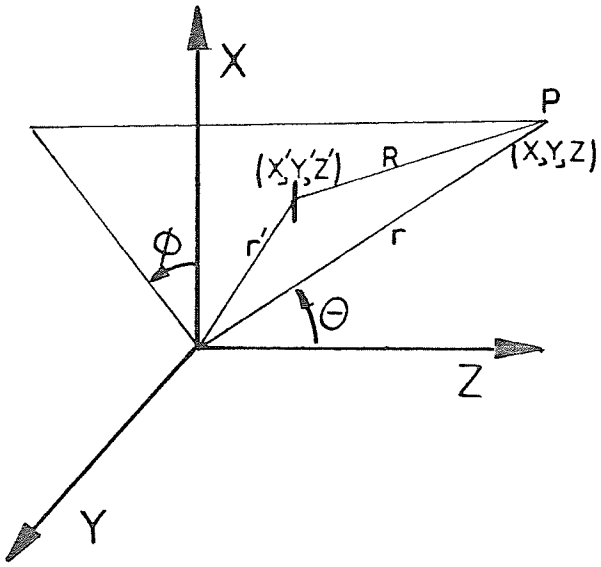

$$\bar{E} = -j\omega\mu\,\bar{A} + \frac{1}{j\omega\varepsilon}\nabla\,(\nabla\cdot\bar{A}) \qquad (I.1)$$

where

$$\bar{A} = \frac{\overline{I\ell}}{4\pi}\,\frac{e^{-jkR}}{R}\,\hat{a}_x \qquad (I.2)$$

$\overline{I\ell}$ is the dipole moment, R is the distance between the two points (x',y',z') and (x,y,z) and $k^2 = \omega^2\mu\varepsilon$.

The exact expressions for the rectangular field components are obtained from (I.1) and (I.2) as:

$$E_x = \frac{-j}{\omega\varepsilon}\,\frac{I\ell}{4\pi}\,\frac{e^{-jkR}}{R}\left\{k^2 - \frac{jk}{R} - \frac{1}{R^2} - (x-x')^2\left(\frac{k^2}{R^2} - \frac{3jk}{R^3} - \frac{3}{R^4}\right)\right\}$$

$$E_y = \frac{j}{\omega\varepsilon}\,\frac{I\ell}{4\pi}\,(x-x')(y-y')\,\frac{e^{-jkR}}{R}\left(\frac{k^2}{R^2} - \frac{3jk}{R^3} - \frac{3}{R^4}\right)$$

$$E_z = \frac{j}{\omega\varepsilon}\,\frac{I\ell}{4\pi}\,(x-x')(z-z')\,\frac{e^{-jkR}}{R}\left(\frac{k^2}{R^2}-\frac{3jk}{R^3}-\frac{3}{R^4}\right) \tag{I.3}$$

When the dipole is centered on the z-axis, $x' = 0 = y'$. In this case, the spherical components of the far field can be obtained from (A.3) by neglecting terms in R^{-2} or smaller. Hence,

$$E_r = 0$$

$$E_\theta = -j\omega\mu\,\left(\frac{I\ell}{4\pi}\right)\cos\theta\,\cos\phi\,e^{jkz'\cos\theta}\,\frac{e^{-jkr}}{r}$$

$$E_\phi = j\omega\mu\,\left(\frac{I\ell}{4\pi}\right)\sin\phi\,e^{jkz'\cos\theta}\,\frac{e^{-jkr}}{r} \tag{I.4}$$

REFERENCES

[1] POTTER, P.D., "A New Horn Antenna with Suppressed Sidelobes and Equal Beamwidths", Microwave Journal, Vol.6, pp. 71-78, June 1963.

[2] POTTER, P.D., and LUDWIG, A.C., "Beamshaping by Use of Higher Order Modes in Conical Horns", Northeast Electron. Res. and Eng. Meeting, pp. 92-93, Nov. 1963.

[3] JENSEN, P.A., "A Low-Noise Multimode Cassegrain Monopulse Feed with Polarization Diversity", Northeast Electron. Res. and Eng. Meeting, pp. 94-95, Nov. 1963.

[4] DRABOWITZ, S., "Multimode Antennas", Microwave Journal, Vol. 9, pp. 41-51, Jan. 1966.

[5] LUDWIG, A.C., "Radiation Pattern Synthesis for Circular Horn Antennas", IEEE Trans. Antennas Propagat., Vol. AP-14, pp. 434-440, July 1966.

[6] TURRIN, R.H., "Dual Mode Small Aperture Antennas", IEEE Trans. Antennas Propagat., Vol. AP-15, pp. 307-308, March 1967.

[7] COHN, S.B., "Flare-Angle Changes in a Horn as a Means of Pattern Control", Microwave Journal, Vol. 13, pp. 41, 42, 44, 46, Oct. 1970.

[8] HAN, C.C., and WICKERT, A.N., "A New Multimode Rectangular Horn Antenna Generating a Circularly Polarized Elliptical Beam", IEEE Trans. Antennas Propagat., Vol. AP-22, pp. 746-751, Nov. 1974.

[9] BARTLETT, H.E., and MOSELEY, R.E., "Dielguides - Highly Efficient Low Noise Antennas Feeds", Microwave Journal, Vol. 9, pp. 53-58, Dec. 1966.

[10] TSANDOULAS, G.N., and FITZGERALD, W.D., "Aperture Efficiency Enhancement in Dielectrically Loaded Horns", IEEE Trans. Antennas Propagat., Vol. AP-21, pp. 69-74, Jan. 1972.

[11] HAMID, M.A.K., TOWAIJ, S.J., and MARTENS, G.O., "A Dielectric Loaded Circular Waveguide Antenna", IEEE Trans. Antennas Propagat., Vol. AP-20, pp. 96-97, Jan. 1972.

[12] KAY, A.F., "The Scalar Feed", U.S. Air Force Cambridge Research Laboratory Report 62-347, March 1964.

[13] SIMMONS, A.J. and KAY, A.F., "The Scalar Feed - A High Performance Feed for Large Paraboloid Reflectors", Instn. Elect. Engrs. Conference Publication 21, pp. 213-317, 1966.

[14] MINNET, H.C., and THOMAS, B. MacA., "A Method of Synthesizing Radiation Patterns with Axial Symmetry", IEEE Trans. Antennas Propagat., Vol. AP-14, pp. 654-656, Sept. 1966.

[15] RUMSEY, V.H., "A New Way of Solving Maxwell's Equations", IRE Trans. Antennas Propagat., Vol. AP-9, pp. 461-465, Sept. 1961.

[16] RUMSEY, V.H., "Horn Antennas with Uniform Power Patterns Around their Axes", IEEE Trans. Antennas Propagat., Vol. AP-14, pp. 556-558, Sept. 1966.

[17] CLARRICOATS, P.J.B., and SAHA, P.K., "Propagation and Radiation Behaviour of Corrugated Feeds", Parts I and II , Proc. Inst. Elect. Eng., Vol. 118, No. 9, pp. 1167-1186, Sept. 1971.

[18] JANSEN, J.K.M., JENKEN, M.E.J., and LAMBRECHTSE, C.W., "The Scalar Feed", Arch. Elek. Übertragung. Vol. 26, pp. 22-30, Jan. 1972.

[19] LOVE, A.W., Ed., Electromagnetic Horn Antennas , New York; IEEE Press, 1976.

[20] SHAFAI, L., "A High Performance Feed for a Low Cost Earth Terminal", Communications Research Centre, Tech. Memorandum, No. 59/77, February 1977.

[21] DRAGONE, C., "An Improved Antenna for Microwave Radio Systems Consisting of Two Cylindrical Reflectors and a Corrugated Horn", The Bell System Technical Journal, Vol. 53, No. 7, pp. 1351-1377, Sept. 1974.

[22] PRICE, R., "High Performance Corrugated Feed Horn for the Unattended Earth Terminal", Comsat Technical Review, Vol. 4, No. 2, pp. 283-302, Fall 1974.

[23] HARRINGTON, R.F., "Field Computation by Moment Methods", The MacMillan Company, New York, 1968.

[24] FRANDSEN, A., "Computation of Scattering and Radiation from Open Ended Waveguides and Small Horns", IEEE International Symposium on Antennas and Propagation, University of Washington, pp. 360-363, June 1979.

[25] SIMMONS, A.J. and KAY, A.F., "The Scalar Feed - A High Performance Feed for Large Paraboloid Reflectors", Op. cit.

[26] MINNET, H.C., and THOMAS, B. MacA., "A Method of Synthesizing Radiation Patterns with Axial Symmetry", Op. cit.

[27] CLARRICOATS, P.J.B., and Saha, P.K., "Propagation and Radiation Behaviour of Corrugated Feeds", Op. cit .

[28] JANSEN, J.K.M., JENKEN, M.E.J., and LAMBRECHSTE, C.W., "The Scalar Feed", Op. Cit.

[29] NARASIMHAN, M.S., "Corrugated Conical Horns with Arbitrary Corrugation Depth", Radio Electron. Eng., Vol. 43, pp. 188-192, March 1973.

[30] NARASIMHAN, M.S., and RAO, B.V., "Radiation Characteristics of Corrugated E-Plane Sectoral Horns", IEEE Trans. Antennas Propagat., Vol. AP-21, No. 3, pp. 320-327, May 1973.

[31] NARASIMHAN, M.S., and RAO, B.V., "Hybrid Modes in Corrugated Conical Horns", Electron. Lett., No. 6, pp. 32-34, 1970.

[32] NARASIMHAN, M.S., and RAO, B.V., "Diffraction by Wide-Flare-Angle Corrugated Conical Horns", Elect. Lett., No. 6, pp. 469-471, 1970.

[33] LAWRIE, R.F., and PETERS, L.J.R., "Modification of Horn Antennas for Low Sidelobe Levels", IEEE Trans. Antennas Propagat., Vol. AP-14, pp. 605-610, Sept. 1966.

[34] MENTZER, C.A., and PETERS, L.J.R., "Pattern Analysis of Corrugated Horn Antennas", IEEE Trans. Antennas Propagat., Vol. AP-24, No. 3, pp. 304-309, May 1976.

[35] MENTZER, C.A., and PETERS, L.J.T., "Properties of Cutoff Corrugated Surfaces for Corrugated Horn Design", IEEE Trans. Antennas Propagat., Vol. AP-22, No.2, pp. 191-196, March 1974.

[36] MENTZER, C.A., and PETERS, L.J.R., "A Corrugated Horn Antenna Using V-Shape Corrugations", IEEE Trans. Antennas Propagat., Vol. AP-23, No.1, pp. 93.97, Jan. 1975.

[37] TERZUOLI, A.J.JR., and PETERS, L.JR., "VSWR Properties of E-Plane Dihedral Corrugated Horns", IEEE Trans. Antennas Propagat., Vol. AP.26, No. 2, pp. 239-243, March 1978.

[38] TERZUOLI, A.J.JR., RICHMOND, J.H., and PETERS, L.JR., "Shielding Effectiveness in Corrugated Horns", IEEE Trans. Antennas Propagat., Vol. AP.26, No.5, pp. 654-658, Sept. 1978.

[39] ELLIOT, R.D., and HOCKHAM, G.A., "Optimised Design of Choked Waveguide Feeds", IEE International Conference on Antennas and Propagation, pp. 369-371, Nov. 1978.

[40] SHAFAI, L, and HANSEN, J.E., "Matrix Formulation of Corrugated Feeds by Using Impedance Boundary Conditions", Electron. Lett., Vol. 13, No. 11, pp. 310-311, 1977.

[41] SHAFAI, L. and HANSEN, J.E., "Correction to: Matrix Formulation of Corrugated Feeds by Using Impedance Boundary Conditions", Electron. Lett., Vol. 13, p. 491, 1977.

[42] VU, T.B., and VU, Q.H., "Optimum Feed for Large Radio-Telescopes: Experimental Results", Electron. Lett., Vol. 6, pp. 159-160, 1970.

[43] VU, T.B., and HIEN, N.V., "A New Type of High-Performance Monopulse Feed", IEEE Trans. Antennas Propagat., Vol. AP-21, pp. 855-857, Nov. 1973.

[44] THOMAS, B.MacA., "Mode Conversion Using Circumferentially Corrugated Cylindrical Waveguide", Electron Lett., Vol. 8, pp. 394-396, 1972.

[45] Jenken, M.E.J., "Experimental Radiation Pattern of the Corrugated Conical-Horn Antenna with Small Flare Angle", Electron. Lett., Vol. 5, pp. 484-485, 1969.

[46] JENKEN, M.E.J., and LAMBRECHTSE, C.W., "Small Corrugated Conical-Horn Antenna with Wide Flare Angle", Electron. Lett., Vol. 5, pp. 489-490, 1969.

[47] THOMAS, B. MacA., "Design of Corrugated Conical Horns", IEEE Trans. Antennas Propagat., Vol. AP-26, No. 2, pp. 367-372, March 1978.

[48] JANSEN, J.K.M., JENKEN, M.E.J. and LAMBRECHTSE, C.W., "The Scalar Feed", T.H. Report 70-E-12, Eindhoven University of Technology, Netherlands.

[49] MENTZER, C.A., and PETERS, L.JR., "GTD H-Plane Horn Pattern Analysis Using Slope Wave Diffraction", 1974 IEEE/AP-S Symposium Program and Digest, June 10 - 12, 1974.

[50] MENTZER, C.A., PETERS, L.J.R., and RUDDUCK, R.C., "Slope Diffraction and its Application to Horns", IEEE Trans. Antennas Propagat., Vol. AP-22, pp. 191-196, March 1974.

[51] KELLER, J.B., "Geometrical Theory of Diffraction", J. Opt. Soc. Amer., Vol. 52, Feb. 1962.

[52] RYAN, C.E., and PETERS, L.JR., "Evaluation of Edge Diffracted Fields Including Equivalent Current for the Caustic Regions", IEEE Trans. Antennas Propagat., Vol. AP-17, pp. 292-299, May 1969.

[53] CLARRICOATS, P.J.B., and SAHA, P.K., "Propagation and Radiation Behaviour of Corrugated Feeds", Op. cit.

[54] JANSEN, J.K.M., JENKEN, M.E.J., and LAMBRECHTSE, C.W., "The Scalar Feed", Op. cit.

[55] NARASIMHAN, M.S., "Corrugated Conical Horns with Arbitrary Corrugation Depth", Op. cit.

[56] ELLIOT, R.D., and HOCKHAM, G.A., "Optimized Design of Choked Waveguide Feeds", Op. cit.

[57] MENTZER, C.A., PETERS, L.JR., and RUDDUCK, R.C., "Slope Diffraction and its Application to Horns", Op. cit.

[58] MENTZER, C.A., and PETERS, L.JR., "Properties of Cutoff Corrugated Surfaces for Corrugated Horn Design", Op. cit.

[59] MENTZER, C.A., and PETERS, L.JR., "A Corrugated Horn Antenna Using V-Shape Corrugations", Op. cit.

[60] MITTRA, R., Ed., Computer Techniques for Electromagnetics, Pergamon Press, 1973.

[61] CARNAHAN, B., LUTHER, H.A., and WILKES, J.O., Applied Numerical Methods, John Wiley & Sons, N.Y., 1969.

[62] HARRINGTON, R.F., Time Harmonic Electromagnetic Fields, McGraw-Hill Book Company, 1961.

[63] WALTER, C.H., Traveling Wave Antennas, McGraw-Hill Book Company, 1965.

[64] HARRINGTON, R.F., Field Computation by Moment Methods, Op. cit.

[65] IMSL (International Mathematical and Statistical Libraries), Inc., 7500 Bellaire Boulevard, Sixth Floor, GNB Building, Houston, Texas 77036.

[66] RALSTON, A., and WILF, H.S., Mathematical Methods for Digital Computers, Vol. II, John Wiley & Sons, 1968.

[67] ABROMOWITZ, M., and STEGUN, I.A., Handbook of Mathematical Functions, Appl. Math. Ser., Washington, D.C., NBC, 1964.

[68] POGGIO, A.J., and MILLER, E.K., "Integral Equation Solutions of Three-Dimensional Scattering Problems", Chap. 4 of Computer Techniques for Electromagnetics, edited by R. Mittra, Pergamon Press, 1973.

[69] ANDREASEN, M.G., "Scattering from Bodies of Revolution", IEEE Trans., Antennas Propagat., Vol. AP-13, pp. 303-310, March 1965.

[70] THIELE, G.A., "Wire Antennas", Chapter 2 of Computer Techniques Techniques for Electromagnetics, edited by R. Mittra, Pergamon Press, 1973.

[71] MILLER, E.K., and DEADRICK, F.J., "Some Computational Aspects of Thin Wire Modeling", Chapter 4 of Numerical and Asymptotic Techniques in Electromagnetics, edited by R. Mittra, Springer Verlag, New York, 1975.

[72] HARRINGTON, R.F., Field Computation by Moment Methods, Op. cit.

[73] MAUTZ, J.R., and HARRINGTON, R.F., "H-Field, E-Field, and Combined Field Solution for Bodies of Revolution", Technical Report TR-77-2, Dept. of Elect. and Comp. Engg., Syracuse University, N.Y. 13210, Ferb. 1977.

[74] SHAFAI, L. and HANSEN, J.E., "Matrix Formulation of Corrugated Feeds by Using Impedance Boundary Conditions", Op. cit.

[75] HARRINGTON, R.F., Field Computation by Moment Methods, Op. cit.

[76] MAUTZ, J.R., and HARRINGTON, R.F., "Generalized Network Parameters for Bodies of Revolution", Technical Report TR-68-7, Electrical Engineering Department, Syracuse University, Syracuse, N.Y., June 1968.

[77] MAUTZ, J.R., and HARRINGTON, R.F., "H-Field, E-Field, and Combined Field Solution for Bodies of Revolution", Op. cit.

[78] HARRINGTON, R.F., Time Harmonic Electromagnetic Fields, Op. cit.

[79] RYDAHL, O., "Scattering from Small Bodies of Revolution", M.Sc. Thesis, Electromagnetic Institute, Tech. University of Denmark, Lyngby, Sept. 1974.

[80] SILVER, S. (Ed.), Microwave Antenna Theory and Design, McGraw-Hill Book Co., New York, 1949.

[81] ABROMOWITZ, M., and STEGUN, I.A., Handbook of Mathematical Functions, Op. cit.

[82] ISKANDER, K.A., and SHAFAI, L., "Scattering from Bodies of Revolution with Impedance Boundary Condition, Computer Program Description", Univ. of Manitoba Report, Department of Electrical Engineering, August 1980.

[83] LUDWIG, A.C., "The Definition of Cross Polarization", IEEE Trans., Antennas Propagat., Vol. AP-21, No. 1, pp. 116-119, Jan. 1973.

[84] JANSEN, J.K.M., JENKEN, M.E.J., and LAMBRECHTSE, C.W., "The Scalar Feed", Op. cit.

[85] SHAFAI, L., "A High Performance Feed for a Low Cost Earth Terminal", Op. cit.

[86] COLLIN, R.E., and ZUCKER, F.J., Antenna Theory, McGraw-Hill Book Co., 1979.

[87] HARRINGTON, R.F., "Theory of Loaded Scatterers", Proc. IEEE, Vol. III, pp. 617-623, April 1964.

[88] KING, R.W.P., The Theory of Linear Antennas, Chap. IV, pp. 456-521, Harvard University Press, Cambridge, Mass. 1956.

[89] CHEN, K.M., and LIEPA, V., "The Minimization of Back Scattering of a Cylinder by Central Loading", IEEE Trans. Antennas Propagat., Vol. AP-12, pp. 576-582, Sept. 1964.

[90] CHEN, K.M., "Minimization of Back Scattering of a Cylinder by Double Loading", IEEE Trans. Antennas Propagat., Vol. AP-13, pp. 262-270, March 1965.

[91] FRANDSEN, A., "Computation of Scattering and Radiation from Open Ended Waveguides and Small Horns", Op. cit.

[92] MITZNER, K.M., "Electromagnetic Scattering from Symmetric Bodies", Spring URSI Meeting, Washington, D.C., 1969.

[93] TSAI, L.L., DUDLEY, D.G., and WILTON, D.R., "Electromagnetic Scattering by a Three-Dimensional Conducting Rectangular Box", Journal of Applied Physics, Vol. 45, No. 10, pp. 4393-4400, October 1974.

[94] WU, C.Y., and CHENG, D.K., "A Method for Symmetrizing Generalized Impedance Matrices", IEEE Trans. Electromagnetic Compatibility, Vol. EMC-19, No. 2, pp. 81-88, May 1977.

[95] ANDREASEN, H.G., "Scattering from Bodies of Revolution", Op. cit.

[96] MAUTZ, J.R., and HARRINGTON, R.F., "Generalized Network Parameters for Bodies of Revolution", Op. cit.

[97] TEW, M.D., and TSAI, L.L., "A Method Towards Improving Convergence of Moment Method Solutions", Proc. IEEE, Vo. 20, pp. 1436-1437, 1972.

[98] AZARBAR, B. and SHAFAI, L., "Application of Moment Method to Large Cylindrical Reflector Antennas", IEEE Trans. Antennas Propagat., Vol. AP-26, No. 3, pp. 500-502, May 1978.

[99] POGGIO, A.J., and MILLER, E.K., "Integral Equation Solutions of Three-Dimensional Scattering Problems", Chap. 4 of Computer Techniques for Electromagnetics, Op. cit.

[100] BURNSIDE, W.D., YU, C.L., and MARHEFKA, R.J., "A Technique to Combine the Geometrical Theory of Diffraction and the Moment Method", IEEE Trans. Antennas Propagat., Vol. AP-23, No. 4, pp. 551-558, July 1975.

[101] THIELE, G.A., and NEWHOUSE, T.H., "A Hybrid Technique for Combining Moment Methods with the Geometrical Theory of Diffraction", IEEE Trans. Antennas Propagat., Vol. AP-23, No. 1, pp. 62-69, Jan. 1975.

[102] KINZEL, J.A., "Large Reflector Antenna Pattern Computation Using Moment Method", IEEE Trans. Antennas Propagat., Vol. AP-22, No. 1, pp. 116-118, Jan. 1974.

[103] SHAFAI, L., "An Improved Integral Equation for Numerical Solution of Two-Dimensional Diffraction Problems", Can. J. Phys., Vol. 48, pp. 954-963, 1970.

[104] KLEIN, C., and MITTRA, R., "Stability of Matrix Equations Arising in Electromagnetics", IEEE Trans. Antennas Propagat., Vol. AP-21, pp. 902-905, Nov. 1973.

[105] MITTRA, R., and KLEIN, C.A., "The Use of Pivot Ratios as a Guide to Stability Arising in the Method of Moments", IEEE Trans. Antennas Propagat., Vol. AP-23, pp. 448-450, May 1975.

[106] BOLOMEY, J.C. and TABBARA, W., "Numerical Aspects on Coupling Between Complementary Boundary Value Problems", IEEE Trans. Antennas Propagat., Vol. AP-21, No. 3, pp. 356-363, May 1973.

[107] WATERMAN, P.C., "Matrix Formulation of Electromagnetic Scattering", Proc. IEEE, Vol. 53, pp. 805-512, Aug. 1965.

[108] MAUTZ, J.R., and HARRINGTON, R.F., "H-Field, E-Field, and Combined-Field Solutions for Conducting Bodies of Revolution", AEU, Baud 32, Heft 4, pp. 157-164, 1978.

[109] HARRINGTON, R.F., Time Harmonic Electromagnetic Fields, Op. cit.

[110] HARRINGTON, R.F., Field Computation by Moment Methods, Op. cit.

[111] MITTRA, R., and KLEIN, C.A., "Stability and Convergence of Moment Method Solutions", Chap. 5 of Numerical and Asymptotic Techniques in Electromagnetics, edited by R. Mittra, Springer Verlag, N.Y., 1975.

[112] POGGIO, A.J., and MILLER, E.K., "Integral Equation Solutions of Three-Dimensional Scattering Problems", Chap. 4 of Computer Techniques for Electromagnetics, Op. cit.

[113] JOHNSON, C.C., Field and Wave in Electrodynamics, McGraw-Hill Book Co., N.Y., 1965.

[114] PAULI, W., "An Asymptotic Series for Functions in the Theory of the Diffraction of Light", Phys. Rev., Vol. 54, pp. 924-931, Dec. 1938.

[115] SHAFAI, L., ISKANDER, K.A., and HANSEN, J.E., "Investigation of Scattering By Corrugated Structures Using Impedance Boundary Conditions", Elect. Letters, 1978, Vol.114, No.5, pp.144-146

[116] ISKANDER, K.A., and SHAFAI, L., "Numerical Investigation of Scattering By Corrugated Surfaces Using Impedance Boundary Conditions", International Symposium on Antennas and Propagation, Sendai, Japan, August 1978.

[117] ISKANDER, K.A., and SHAFAI, L., "Application of Impedance Boundary Conditions To Numerical Solution of Corrugated and Receiver Horns With Rotational Symmetry", Fourth Annual Antenna Applications Symposium, College of Engineering, Dept. of Elect. Engg., Urbana 61801, Sept. 24-26, 1980.

[118] ISKANDER, K.A., SHAFAI, L., FRANDSEN, A., and HANSEN, J.E., "Application of Impedance Boundary Conditions To Numerical Solution of Corrugated And Receiver Horns With Rotational Symmetry", Submitted for Publication, IEEE Trans. on Antennas and Propagation.

[119] Shafai, L., and ISKANDER, K.A., "Investigation On New Green's Functions For Numerical Solution of Field Problems", IEEE International Symposium on Antennas and Propagat., University of Washington, pp.175-176, June 1979.